Mathematical modeling and optimization for real life phenomena

Edited by
Cristiana J. Silva, Guillermo Huerta Cuellar
and Monique Chyba

About Frontiers

Frontiers is more than just an open access publisher of scholarly articles: it is a pioneering approach to the world of academia, radically improving the way scholarly research is managed. The grand vision of Frontiers is a world where all people have an equal opportunity to seek, share and generate knowledge. Frontiers provides immediate and permanent online open access to all its publications, but this alone is not enough to realize our grand goals.

Frontiers journal series

The Frontiers journal series is a multi-tier and interdisciplinary set of open-access, online journals, promising a paradigm shift from the current review, selection and dissemination processes in academic publishing. All Frontiers journals are driven by researchers for researchers; therefore, they constitute a service to the scholarly community. At the same time, the *Frontiers journal series* operates on a revolutionary invention, the tiered publishing system, initially addressing specific communities of scholars, and gradually climbing up to broader public understanding, thus serving the interests of the lay society, too.

Dedication to quality

Each Frontiers article is a landmark of the highest quality, thanks to genuinely collaborative interactions between authors and review editors, who include some of the world's best academicians. Research must be certified by peers before entering a stream of knowledge that may eventually reach the public – and shape society; therefore, Frontiers only applies the most rigorous and unbiased reviews. Frontiers revolutionizes research publishing by freely delivering the most outstanding research, evaluated with no bias from both the academic and social point of view. By applying the most advanced information technologies, Frontiers is catapulting scholarly publishing into a new generation.

What are Frontiers Research Topics?

Frontiers Research Topics are very popular trademarks of the *Frontiers journals series*: they are collections of at least ten articles, all centered on a particular subject. With their unique mix of varied contributions from Original Research to Review Articles, Frontiers Research Topics unify the most influential researchers, the latest key findings and historical advances in a hot research area.

Find out more on how to host your own Frontiers Research Topic or contribute to one as an author by contacting the Frontiers editorial office: frontiersin.org/about/contact

Mathematical modeling and optimization for real life phenomena

Topic editors

Cristiana J. Silva – University of Aveiro, Portugal

Guillermo Huerta Cuellar – Univeristary Center of Lagos, University of Guadalajara, Mexico

Monique Chyba – University of Hawaii, United States

Table of contents

Editorial: Mathematical modeling and optimization for real life phenomena

Cristiana J. Silva[1], Monique Chyba[2] and
Guillermo Huerta Cuellar[3]*

[1]Department of Mathematics, University of Aveiro, Aveiro, Portugal, [2]Department of Mathematics,
University of Hawaii, Honolulu, HI, United States, [3]University Center of Lagos, University of
Guadalajara, Lagos de Moreno, Mexico

Editorial on the Research Topic
Mathematical modeling and optimization for real life phenomena

In today's world, where complexity abounds and challenges are multifaceted, mathematical modeling and optimization emerge as essential tools for addressing real-life phenomena. These disciplines not only enhance our understanding of intricate systems but also empower us to devise efficient solutions for a wide array of problems. By representing real-world phenomena through equations and algorithms, mathematical modeling enables us to simulate and predict the behavior of complex systems. When combined with optimization techniques, we can seek the best solutions for challenges ranging from logistical planning to natural resource management.

In the realm of mathematical modeling and optimization, statistical processes like Markov Chain Monte Carlo methods play a crucial role in estimating posterior distributions for Bayesian computations. However, these methods often face challenges with slow run times when dealing with large datasets or complex parameter distributions. To address this, Suchoski et al. introduce the Multiple-Try Metropolis variant, optimizing the algorithm for faster convergence by running more parallel likelihood calculations to approach a parameter estimation for a Susceptible-Exposed-Infectious-Removed (SEIR) model and forecasting new cases of COVID-19. The recent pandemic situation highly affected our world, then the study of epidemic spread, exemplified by COVID-19, has attracted significant attention from scholars. By proposing the SEIRD (Susceptible-Exposed-Infected-Recovered-Dead) model based on the SIR (Susceptible-Infected-Recovered) propagation model, Chen et al. introduce specific parameters to simulate virus spread through objects, providing valuable insights for epidemic analysis and prediction.

Amid the current emphasis on sustainability, efficiency, and innovation, mathematical modeling and optimization are also indispensable in fields that include applications in humans and animal health. Netshikweta and Garira present a nested multiscale model that integrates within-host and between-host disease dynamics for Paratuberculosis in ruminants. Their study explores the influence of the initial infective inoculum dose on disease dynamics, revealing insights into pathogen replication and super-infection effects. Also, results on mathematical modeling in the case of health risk, for animals and humans in the agriculture exposed by pesticides result in an interesting topic. Aksüt and Eren studied the significance of personal protective equipment using a multi-criteria

decision-making approach to mitigate the risks of injuries and illnesses stemming from pesticide use. Emphasizing the utilization of personal protective equipment, particularly during pesticide application, will enhance the adoption rate of protective measures. Another real life phenomenon needing mathematical modeling and optimization arise in the formation of hydroxyapatite in biological tissues which is regulated by physicochemical factors not fully understood. In that sense, Poorhemati and Komarova utilize mathematical modeling to depict the intricate environment conducive to hydroxyapatite precipitation, enabling *in silico* studies of complex clinical scenarios.

The modeling of dynamical systems in the area of neural behavior and new technological devices, as new logical gates, has been growing in the last decade. Dynamical behavior in neural burst patterns is characterized by temporal heterogeneity across various domains. Lee et al. propose a Burst and Memory-aware Transformer (BMT) model designed to address bursty temporal patterns effectively, enhancing predictive performance. In the field of communications systems, new devices and logical gates are continually evolving to meet technological advancements. Dynamical systems displaying chaotic behavior are utilized to emulate logic gates for general-purpose computing. Rivera-Durón et al. present a methodology based on unstable dissipative systems capable of generating multi-scrolls and multi-stability, leading to the development of dynamic logic gates.

In the area of controlling dynamical systems, some examples about control and synchronization are mentioned, for which it is well known that when the synchronization topic is studied, it can develop emergent phenomena depending on the number of elements of the system. Research on optimal control using fractional calculus by Hailu and Teklu explores dynamics of rail passengers' negative attitudes, aiming to prevent and treat negative attitudes through optimal control strategies. The synchronization transition in the Shinomoto-Kuramoto model on networks of fruit-fly and human connectomes is investigated by Ódor et al. shedding light on critical behavior in the presence of external excitation. Their numerical solutions provide insights into non-universal scaling tails and compare well with experimental results obtained by fMRI. The Particle Swarm Optimization (PSO) algorithm is an effective optimization method known for its impressive performance in problem-solving. Research on the convergence analysis of this method is still ongoing, in that sense, Nigatu et al. introduce a method for regulating particle swarm velocity by incorporating a constriction factor into the standard swarm optimization algorithm, known as CSPSO. They also present a mathematical model of CSPSO with the time step attractor to analyze convergence conditions and stability. This adaptation of the standard particle swarm optimization aims to enhance the balance between exploration and exploitation, thus mitigating premature convergence issues commonly seen in PSO algorithms.

Fostering research and development in mathematical modeling and optimization is crucial for addressing current challenges effectively across diverse fields. By integrating these disciplines into our problem-solving approaches, we can advance toward a more sustainable, efficient, and impactful future. This Research Topic gathers important recent developments with promising future perspectives on mathematical models for real life phenomena.

Author contributions

CS: Supervision, Validation, Writing—review & editing. MC: Supervision, Validation, Writing—review & editing. GH: Supervision, Validation, Writing—original draft, Writing—review & editing.

Funding

Conflict of interest

The authors declare that the research was conducted in the absence of any commercial or financial relationships that could be construed as a potential conflict of interest.

Publisher's note

GPU Accelerated Parallel Processing for Large-Scale Monte Carlo Analysis: COVID-19 Parameter Estimation and New Case Forecasting

Brad Suchoski[1], Steve Stage[2], Heidi Gurung[1] and Prasith Baccam[1*]

[1] IEM, Inc., Bel Air, MD, United States, [2] IEM, Inc., Baton Rouge, LA, United States

Markov Chain Monte Carlo methods have emerged as one of the premier approaches to estimating posterior distributions for use in Bayesian computations. Unfortunately, these methods often suffer from slow run times when the data become large or when the parameter values come from complex distributions. This speed issue has prevented MCMC analysis from being used to solve some of the most interesting problems for which its technique is a good fit. We used the Multiple-Try Metropolis variant of the basic Metropolis Hastings algorithm, which trades off running more parallel likelihood calculations in favor of a higher acceptance rate and faster convergence compared to traditional MCMC. We optimized our algorithm to parallelize it and to take advantage of GPU processing. We applied our approach to parameter estimation for a Susceptible-Exposed-Infectious-Removed (SEIR) model and forecasting new cases of COVID-19. In comparison to a fully parallelized CPU implementation, using a single GPU to execute the simulations resulted in more than a 13x speedup in wall clock time, running on multiple GPUs resulted in a 36.3x speedup in wall clock time, and using a cloud-based server consisting of 8 GPUs resulted in a 56.5x speedup in wall clock time. Our approach shows that MCMC methods can be utilized to tackle problems that were previously thought to be too computationally intensive and slow.

Keywords: COVID-19, GPU, mathematical modeling, compartment model, markov chain monte carlo, parameter estimation

1. INTRODUCTION

This paper explores the use of computer algorithm optimization and parallelization to accelerate large-scale Markov Chain Monte Carlo (MCMC) analyses which were applied to parameter estimation for a Susceptible-Exposed-Infectious-Removed (SEIR) model and forecasting new cases of COVID-19. A large quantity of simulations was run to estimate the parameter values in the SEIR model and increase their accuracy through optimization via graphics processing unit (GPU) processing and parallelization of both the likelihood function and multiple MCMC chains using a multiple-try Metropolis (MTM) MCMC algorithm. The key accomplishment of this project was the application of optimization and parallelization techniques to speed up the MCMC analysis to the point that it could be used in a large, real-world situation, demonstrating that theoretical

improvements are now achievable with existing computer hardware, parallel programming, and GPU acceleration.

MCMC methods have emerged as one of the premier approaches to estimating posterior distributions for use in Bayesian computations, which have been useful in a number of fields, including machine learning [1], physics [2], and systems biology [3]. Unfortunately, these methods often suffer from slow run times when the data become large or when the parameter values come from complex distributions. This speed issue has prevented MCMC analysis from being used to solve some of the most interesting problems for which its technique is a good fit. Finding methods to improve the speed while maintaining accuracy without bias has been a topic many researchers have investigated [4, 5]. Other methods have been proposed to improve the convergence rate, resulting in more accurate results for the same number of iterations of the MCMC algorithm [6, 7]. The Multiple-Try Metropolis algorithm is one technique that has arisen that can improve computation speeds through parallel processing because the algorithm itself is highly parallelizable [8]. While parallelizing computations will inevitably reduce computational time, we have sought to increase speed further by optimizing the code to also leverage hardware advances to decrease the time it takes for analysis by running on GPUs.

The idea for the MCMC method used in this example comes from a source-reconstruction plume dispersion model currently in development. This original work takes a time series of chemical concentration signals recorded by field sensors at known locations. It then works backwards from those signals to estimate the most likely source of the chemical release. An MCMC chain is used to run the plume model in a forward direction, and the similarity of the real sensor data to the estimates from the plume model is used as the likelihood function to infer the most likely parameter values that describe the chemical release.

In this paper we instead start with a time series of COVID-19 cases. We then use MCMC to work backward to estimate SEIR parameter values which works in a similar manner plume model case. In both cases, the computation of the likelihood function involves running a complex physics-based simulation in the forward direction and then using the simulation's results to calculate a likelihood. The inclusion of the physics-based simulation in the likelihood function makes it impractical to use any MCMC variants, such as Hamiltonian Monte Carlo, which require the gradient of the likelihood function. At the same time, these particular physics simulations are simple enough that running a single instance of them does not require enough work to fully utilize the hardware of even a single modern GPU.

This creates a particularly challenging problem, because MCMC methods are inherently sequential algorithms. Calculating each step of the chain requires knowing the state of the chain from the previous step as input. This can make them computationally expensive when analyzing large datasets and complex parameter sets, making them impractical in those situations [9]. Many approaches to parallelizing and accelerating MCMC algorithms have been proposed that mainly fall into two categories. One approach is to divide the problem into smaller pieces that can be run independently and in parallel.

The other approach is to use knowledge of the posterior, priors or other information to accelerate the convergence rate and reduce the number of iterations required [4, 5]. For example, the simplest of these approaches is to just run several independent chains in parallel and then average the results. Alternatively, one can run multiple interacting chains that share information at certain points in the step to reduce the number of iterations required for convergence. Other methods such as Hamiltonian Monte Carlo (HMC) and No U-Turn Sampling (NUTS) use auxiliary parameters combined with Hamiltonian dynamics and the ability to calculate the likelihood function's gradients to accelerate convergence [10, 11].

Our approach to accelerating the SEIR-based MCMC chains was twofold. First, we used multiple parallel chains that synchronize on each iteration before the next proposal point is drawn. During the drawing of the proposal point, each chain uses the other chain locations as samples to estimate the local parameter covariances. This allows us to use a multivariate Gaussian proposal distribution that more closely estimates the target posterior at each step. Second, we used the MTM variant of the basic Metropolis Hastings (MH) algorithm [8, 12]. The MTM algorithm trades off running more parallel likelihood calculations in favor of a higher acceptance rate, faster convergence, and fewer total iterations compared to traditional MCMC. We then optimized our algorithm to parallelize it from the top down with a synchronization point in the likelihood function just prior to starting the SEIR model simulations. This allowed us to simultaneously launch an entire ensemble of SEIR simulations that need to be run on GPU. The entire ensemble could then be solved in parallel using the fine-grained data parallel execution model of GPUs as opposed to the independent course-grained task parallel model of central processing units (CPUs).

2. MATERIALS AND METHODS

2.1. Background
2.1.1. SEIR Applications
Prior to this research, IEM had developed a tool (BioSim) that allows users to quickly and efficiently build epidemiological compartment models with any number of compartments and connections, and leverages the computational power of Nvidia GPUs to significantly accelerate solving ensembles of compartment model problems in parallel. The application of this research was to explore methods for applying parallel solutions of compartment models to estimating parameters and forecasting new cases of the COVID-19 pandemic using recent confirmed case counts.

The BioSim tool was built with three key unique components over existing and traditional SEIR models. First, the model itself has been parallelized and optimized to run ensembles of simulations multi-threaded on CPU, or on GPU for additional speedup, allowing large numbers of simulations to be run quickly. This aspect is important for MCMC and other analyses that require large volumes of data. Next, BioSim supports aged transitions. That is, individuals move from compartments, but also with reference to their time in the compartment. This blends the standard compartment model concept with an

agent-based approach, as transitions between compartments are controlled at the agent level. A third addition to BioSim which is not found in existing SEIR modeling tools is the ability to allocate resources and have those resource allocations impact the outbreak. Resources include things like vaccines, hospital beds, and treatment availability.

A number of other SEIR tools and packages are currently available. They include: for R, the plotSIRModel package [13] that plots Markov chain SEIR models; for Python, the SEIR package [14] for building SEIR models within Python, and the Cornell multi-region SEIR model with mobility [15], a web page that allows users to build and observe SEIR models online. Many researchers also use ordinary differential equation (ODE) solvers available as packages in several different languages (such as Python, R, and C++) to build their own SEIR models.

2.1.2. GPU Accelerated MCMC Applications

In 2013, Hall et al. proposed a Metropolis Monte Carlo (MMC) method for running molecular simulations [16]. Their approach used CUDA to run their CPU-GPU algorithm, with special manipulation of the GPU memory to decrease the use of system memory and swapping across devices. The system is designed with one GPU per CPU process. The GPU is tasked with parallelizing parts of the likelihood function asynchronous to the CPU, and the CPU is responsible for running the parts of the likelihood function that cannot be efficiently parallelized before synchronizing with the GPU and combining the results. This approach parallelizes only portions of the inner likelihood function running the molecular simulations while each step of the MCMC algorithm is computed sequentially on the CPU. This is feasible in their use case because the molecular dynamics simulations run during the likelihood function calculation were sufficiently complex to provide enough parallel work that the GPU was fully utilized.

Our use case involves solving an SEIR model during the likelihood function calculation. In our case, and many like it, the amount of work required for a single simulation is not sufficient to completely utilize even a single GPU. Running ensembles of many independent simulations simultaneously and in parallel can increase GPU utilization. Even so, it may still require several hundreds to several thousands of independent simulations in an ensemble before GPU acceleration becomes beneficial. In order to efficiently use the GPUs in these cases, the parallelization cannot be limited to just the likelihood function as in Hall et al [16]. It must rather be moved up a level to include portions of the MCMC algorithm itself.

2.2. Methods

In this section we introduce our method, which can be broken into four separate tasks:

1. Choosing an epidemiological model for taking a set of input parameter values and modeling data such as cumulative case counts over time
2. Implementing a parallelized modified MCMC analysis to estimate epidemiological model parameter values that best fit historic reported data

3. Developing an epidemiological model 'restart' method which allows tracking changes in epidemiological model parameters over time by using MTM-MCMC to fit parameters in a series of overlapping windows of historical data
4. Applying these techniques to first estimate the best model parameters to fit historic values and then using those parameters to project future parameter values and case counts.

Optimizing the epidemiological model and MCMC analysis algorithms to run on GPU hardware is also included in the activities of the first two tasks.

2.2.1. Epidemiological Model

The IEM BioSim tool was used to build the standard SEIR model defined by the system of ordinary differential (Equation 1) [17].

$$
\begin{aligned}
S' &= -\frac{\beta I S}{N}, \\
E' &= \frac{\beta I S}{N} - \mu E, \\
I' &= \mu E - \gamma I, \\
R' &= \gamma I
\end{aligned} \tag{1}
$$

We begin each of the simulations with the entire population susceptible, except for a single person in exposed. The simulation start date that this occurs on is one of our inferred MCMC parameters. We used an estimate of 5.2 days as both the latent period $1/\mu$ and infectious period $1/\gamma$ [18]. We then allow the transmissibility $\beta(t)$ to be a function of time instead of a constant as is typical with SEIR models. The rationale behind this is that while the biological factors affecting transmissibility are unlikely to change much over time, there are a multitude of social, behavioral and political factors that do. Mask wearing, social distancing, school closings and vaccinations, to name a few, can all dramatically change the transmissibility on very short time scales. They tend to not stay constant over the course of an outbreak. Rather than attempt to account for all of these factors, we simply used a general parameterized function $\beta(t; \theta_\beta)$ for the transmissibility and then used case data and MCMC to work backward to infer the parameter θ_β.

While the BioSim tool is capable of being generalized to any number of compartments and supports resource constraints and aged transitions between compartments, for this problem we chose to use a simple SEIR model to minimize the assumptions in the epidemiological model. All of the methods discussed are applicable to arbitrarily complex epidemiological models. We have successfully tested the methods using epidemiological models that include factors such as hospitalization and ICU admission, deaths, asymptomatic cases, and vaccinations, for instance. For the context of the current discussion however, a simple SEIR model illustrates all of the important issues.

2.2.2. Multiple-Try Metropolis Markov Chain Monte Carlo Method

In order to find the most likely values of our epidemiological model parameters that explain the observed data and to quantify the uncertainty in those values, we employ the use of an MCMC

method. MCMC provides several important benefits over other optimization algorithms, including but not limited to

- MCMC can locate not only the optimal solution to some likelihood function but also estimates the shape of the entire posterior probability function $\pi(\theta|y)$ of some parameters θ given some observed data y.
- There are versions of the algorithm that do not rely on the ability to calculate or estimate any derivatives of the likelihood function, allowing for more complicated functions to be used. In our case, the likelihood function uses the solution to our SEIR model.
- The MTM variant of the standard MCMC method that we use provides a significant level of parallel computation well suited for execution on GPUs.

We used a variation of the MTM algorithm [12] that is similar to the methods described in Martino et al. [19], Calderhead et al. [20], and Corander et al. [6]. The core idea of MTM is that instead of evaluating a single proposal parameter set at each iteration it evaluates multiple proposals in parallel. Once the likelihood of each proposal is calculated, it can be shown that the likelihood values can be used to choose a single proposal and an acceptance rate in a way such that the stationary distribution of the chain matches the target posterior. The reason we chose the MTM variant over the traditional MH is that it trades parallelism for total likelihood function evaluations. The MTM variant will typically have to perform more total likelihood function evaluations to achieve the same level of convergence as compared to the standard MH. However, because the likelihood evaluations at each iteration of MTM can be computed in parallel, and fewer MTM iterations are required to reach convergence, the MTM algorithm can more effectively utilize a multi-core CPU or GPU.

The variation of MTM-MCMC analysis listed in **Algorithm 1** is used in this paper and can be generalized to any problem by simply changing the likelihood function. Most of **Algorithm 1** is run on the CPU with no optimization, the exception being the likelihood calculation $\mathcal{L}(y|\theta)$. Even so, the CPU portion is still responsible for less than 6% of the total runtime in all of our GPU benchmark tests. However, the problem-specific likelihood function is both optimized and parallelized to run on GPU and is responsible for the remaining compute time in our benchmarks.

The likelihood function $\mathcal{L}(y|\theta)$ and prior probability pdf $g(\theta)$ are problem specific. The proposal pdf $Q(\theta|\Theta)$ can be chosen for the specific problem being solved, but there are generalizable options available. In the tests for this paper, we chose to use the simple and generalized form of a multivariate normal distribution

$$Q(\theta|\Theta) = \mathcal{N}(\theta, \Lambda) \qquad (2)$$

where Λ is the estimated sample covariance matrix of the N_c chain samples $\Theta = [\theta^{(1)}, \ldots, \theta^{(N_c)}]$.

2.2.3. Time Varying SEIR Model Parameters

One of the main aspects of the COVID-19 outbreak we are trying to capture is the time-varying nature of the model parameters. In particular, we know that the effective reproductive number,

Algorithm 1: Variation of the Multiple-Try Metropolis Algorithm with N_t tries and N_c chains. It is identical to the traditional Metropolis Hastings MCMC algorithm in the case where $N_t = 1$ and $N_c = 1$, and is identical to the Multiple-Try Metropolis Algorithm in the case where $N_t > 1$ and $N_c = 1$. Increasing either N_t or N_c will also increase the amount of computational work required per outer N_{MTM} loop. However, increasing either should result in faster convergence thus requiring fewer total N_{MTM} iterations. Also, the inner N_c and N_t loops can be computed in parallel using a single barrier synchronization point.

Data:
Observed data y
Initial Parameters $\Theta^{(0)} = [\theta^{(0,1)}, \ldots, \theta^{(0,N_c)}]$, one for each chain
Likelihood pdf $\mathcal{L}(y|\theta)$
Prior probability pdf $g(\theta)$
Proposal pdf $Q(\theta|\Theta)$
Importance weight function $w(\theta|\Theta) = \frac{\mathcal{L}(y|\theta)g(\theta)}{Q(\theta|\Theta)}$
Result: Parameter samples
$\quad \Theta^{(i)} = [\theta^{(i,1)}, \ldots, \theta^{(i,N_c)}], \forall i \in [1, \ldots, N_{MTM}]$
for $i = 1, \ldots, N_{MTM}$ **do**
  parfor $c = 1, \ldots, N_c$ **do**
    parfor $t = 1, \ldots, N_t$ **do**
      Draw test sample $\theta_s^{(t,c)} \sim Q(\theta_s^{(t,c)}|\Theta^{(i-1)})$
      Calculate the test importance weight
      $I^{(t,c)} = w(\theta_s^{(t,c)}|\Theta^{(i-1)})$
    end
    Select a single $\bar{\theta}^{(c)}$ from $[\theta_s^{(1,c)}, \ldots, \theta_s^{(N_t,c)}]$ with probabilities proportional to $[I^{(1,c)}, \ldots, I^{(N_t,c)}]$
    Barrier
    Let $\bar{\Theta} = [\bar{\theta}^{(1)}, \ldots, \bar{\theta}^{(N_c)}]$
    parfor $t = 1, \ldots, N_t$ **do**
      if $t < N_t$ **then**
        Draw reference sample $\theta_s^{(t,c)} \sim Q(\theta_s^{(t,c)}|\bar{\Theta})$
      else
        Let reference sample $\theta_s^{(t,c)} = \theta^{(i-1,c)}$
      end
      Calculate the reference importance weight
      $J^{(t,c)} = w(\theta_s^{(t,c)}|\bar{\Theta})$
    end
    Draw $\alpha \sim \mathcal{U}(0,1)$
    if $\alpha < \frac{I^{(1,c)}+\ldots+I^{(N_t,c)}}{J^{(1,c)}+\ldots+J^{(N_t,c)}}$ **then**
      Accept: $\theta^{(i,c)} = \bar{\theta}^{(c)}$
    else
      Reject: $\theta^{(i,c)} = \theta^{(i-1,c)}$
    end
  end
  Let $\Theta^{(i)} = [\theta^{(i,1)}, \ldots, \theta^{(i,N_c)}]$
end

$R_e(t)$, (or equivalently the transmissibility $\beta(t) = R_e(t)/\gamma$) is not constant but changes over the course of an outbreak due to many

factors including physical distancing, vaccination, quarantining, masking, sufficient and appropriate use of personal protective equipment (PPE), and contact tracing. We want to capture the dynamic nature of the changing reproductive number without making too many assumptions that would restrict the exact shape of the change and instead allow data to dictate its shape.

To accomplish this, we model the outbreak over time using a series of overlapping constant size windows W_i spanning time $t_{b,i} \leq t \leq t_{e,i}$, with the beginning of each window being the center of the previous window $t_{b,i+1} = \frac{1}{2}(t_{b,i} + t_{e,i})$. Within each window we model the transmissibility as changing linearly over time $\beta_i(t) = A_i t + B_i$, and use **Algorithm 1** to find the best estimate values for A_i and B_i that match the reported data for window W_i. By allowing A_i and B_i to change from one window to the next we can capture the time varying nature of the outbreak.

One obvious problem with this method is that the likelihood function for window W_i involves using the solution to our SEIR model during the current window's time range $t_{b,i} \leq t \leq t_{e,i}$. However, to step the SEIR model forward in time through that time period we need to know the initial conditions at some point prior to the beginning of the window $t_{b,i}$. The only time that we know the model state with any certainty is at the start of the outbreak $t_{b,0}$ where we assume that the entire population is susceptible with the exception of a single person who has been exposed. To calculate the likelihood we have to either run each SEIR model instance from $t_{b,0}$ up to $t_{e,i}$ using samples of A_j and B_j $\forall j \leq i$, or come up with a method for initializing the SEIR model at the beginning of the current window $t_{b,i}$ and solve it only for the current window's time range $t_{b,i} < t \leq t_{e,i}$. We chose the latter approach.

The key insight needed to accomplish this is to realize that the initial state of the SEIR model for window W_i at time $t_{b,i}$ does not take on a single well-defined value. It is instead itself a random variable. Samples of it can be drawn by capturing the SEIR model state of the chains from the previous window W_{i-1} at time $t_{b,i}$ in the middle of that window's time range. Ideally, to get a truly random sampling of the initial state, we would run the chains for window W_{i-1} and W_i simultaneously. Applying this approach recursively though would then require us to run all of the windows back to W_0 simultaneously, which would increase computational complexity. We instead decided to store a finite set of samples of the model state in the middle of each window when running those chains. Then we then can draw a random sample from that finite set for window W_{i-1} when running the window W_i as an approximation to the truly randomly drawn initial conditions.

2.2.4. Application of Optimization and Parallelization to the SEIR Model for *R(t)* Value and New Case Projections

The parameter search space used by our MTM algorithm consists of a set of three parameters when running the first window and then as sets of two parameters for each subsequent window. The two common parameters are the linear coefficients A_i and B_i that describe $\beta(t) = A_i t + B_i$, and for the first window only the additional third parameter is the start date on which the first person was exposed. The prior probability, $g(\theta)$

from **Algorithm 1**, used for these parameters was a rectangular distribution. That is, they are uniformly distributed if the parameter lies within feasible bounds and have a zero probability outside those bounds. In our particular case, the feasibility region is where the parameters result in a transmissibility $\beta(t)$ that is positive for all times in the current window $\beta(t) > 0$, $\forall t$ where $t_{b,i} \leq t \leq t_{e,i}$.

All of the likelihood function $\mathcal{L}(y|\theta)$ evaluations in **Algorithm 1** are located inside parallel loops over the N_c chains and N_t tries. All iterations of those loops are advance forward to the likelihood function evaluation before any iteration starts evaluating the likelihood. We can then setup an ensemble of all the forward SEIR simulations needed and solve them in parallel using BioSim. The simulated number of incident new cases each day $c^{(t)}$ is recorded from the BioSim SEIR runs. Our model assumes the historical reported number of new cases each day $C^{(k)}$ provided by Johns Hopkins University [21] includes a normally distributed reporting error $\varepsilon^{(k)} = C^{(k)} - C^{(k)}_{true}$ with mean 0 and variance σ^2_{rep}. The likelihood $\mathcal{L}(C|\theta)$ is then supposed to be calculating the probability of reported values being $C^{(k)}$ under the assumption that our simulated values $c^{(k)}$ are the true values $C^{(k)}_{true}$. So that is simply

$$\mathcal{L}(C|\theta) = \prod_k \varphi(C_k; c_k, \sigma_{rep}) \qquad (3)$$

where $\varphi(x; \mu, \sigma)$ is the normal distribution pdf with mean μ and variance σ^2. The reporting error variance σ_{rep} is not known, but because the likelihood function is assuming that $c^{(k)} = C^{(k)}_{true}$ we can approximate it as the estimated sample variance of the set of residuals $\varepsilon^{(k)} = C^{(k)} - c^{(k)}$. Then for each stored parameter output $\theta^{(i,c)}$ from **Algorithm 1** we can also store $\sigma^{(i,c)}_{rep}$ as the sample of the reporting error posterior.

For the last window W_n, the projections (c_n at times $t > t_{e,n}$) are theoretically separate from the historical estimations (c_n a times $t_{b,n} \leq t \leq t_{e,n}$). However, for computational efficiency, both the historical and projected values are calculated and stored while running the forward SEIR simulations for the likelihood calculation in the final window. The historical case values are only dependent on the time-varying value of $\beta_n(t)$ within window W_n for which we have data. The accuracy of projected case values though is dependent on how we extrapolate $\beta(t)$ past time $t_{e,n}$, for which we have no data. This is an active area of our research. Currently we use the constant value $\beta(t) = \beta_n(t_{e,n})$, which is to say the value of $\beta(t)$ today will continue to the end of our projection window (1–4 weeks in the future).

3. RESULTS

Our data source to test the method was cumulative case timeseries data collected at the county level across the US provided by the Johns Hopkins University Systems Science & Engineering [21]. We used a selection of 385 individual counties as well as the aggregate cases for all 50 states, 3 US territories, and the US as a whole for a total of 439 jurisdictions. We started each jurisdiction on March 8th, 2020, and ran 21-day

windows W_i through March 23rd, 2021. To test the speedup, we measured and compared the wall clock time under different hardware configurations for running $N_{MTM} = 250$ iterations of the modified MTM (**Algorithm 1**), with $N_c = 32$ chains and $N_t = 128$ tries, for a single window on all 439 jurisdictions. With 2 likelihood function calls per iteration, that required running a total of 899,072,000 complete SEIR simulations, covering a 20 day window at 2.4 h timesteps.

3.1. Software Configuration

The IEM BioSim library used to execute the SEIR models is written in C++/OpenMP/CUDA. It is fully capable of running either optimized for single node multi-core CPU execution or for optimized single GPU acceleration, with that option being configurable through an argument on a single API call. The MCMC code is written in Julia with a few computationally intensive portions, such as the likelihood calculation from Equation (3), being offloaded to the GPUs using CUDA.jl when running in GPU mode [22, 23].

A majority of the MCMC algorithm, including drawing the proposal, calculating acceptance rates, and sample recording, is run on CPU in both the CPU and GPU configurations. Some of it could be offloaded to the GPUs for acceleration, but it currently accounts for less than 6% of the overall runtime even in the 8xGPU HPC node configuration. Julia's built-in distributed processing was used to split the SEIR model runs across multiple GPUs or CPUs, with each process responsible for executing an ensemble of SEIR models on a single CPU or GPU through the BioSim API, and then synchronizing with the rest of the MCMC algorithm. In the CPU configuration tests, each process' CPU threads were locked to a single local NUMA node. For these tests we scaled the solution up to multiple GPUs on a single node, but Julia's distributed processing interface is capable of being scaled up to multi-node/multi-GPU without code modifications.

3.2. Hardware Configuration

All tests were run in both CPU and GPU configurations on one of three hardware configurations meant to be representative of either a high-end developer's workstation, a single-node CPU optimized HPC server, or a single-node GPU optimized HPC server. The CPU optimized HPC server tests were run on the top tier Amazon EC2 x86 compute optimized instance (c5.metal), and the GPU optimized HPC server tests were run on the top tier EC2 accelerated computing instance (p4d.24xlarge). The detailed specifications of each hardware configuration are listed in **Table 1**, and the timing results of running our test on each hardware configuration are listed in **Table 2**.

3.3. Accuracy of the Results

The accuracy of the test results was assessed by using the MCMC chain samples to calculate prediction intervals for the number of reported daily incident cases. We then compared the coverage of the actual reported data against those prediction intervals. Doing this comparison for days in the projection

TABLE 1 | Benchmark test hardware configurations.

Configuration	CPU	Main memory	GPUs
Workstation	1x Intel Core i9-10920X	128 GiB	4x Nvidia RTX 2080 Ti
CPU HPC Node	2x Intel Xeon Platinum 8275CL	192 GiB	
GPU HPC Node	2x Intel Xeon Platinum 8275CL	1024 GiB	8x Nvidia Tesla A100-SXM4-40GB

TABLE 2 | Benchmark timing tests results.

Configuration	Wall time (seconds)	Speedup (Rel to WS)	Speedup (Rel to HPC)
Workstation 1xCPU	8,469	1.0x	0.67x
Workstation 1xGPU	624	13.6x	9.06x
Workstation 4xGPU	233	36.3x	24.30x
HPC Node 2xCPU	5,654	1.5x	1.00x
HPC Node 1xGPU	387	21.9x	14.60x
HPC Node 8xGPU	100	84.7x	56.50x

time range, that is at times $t > t_{e,n}$, would introduce errors caused by the $\beta(t)$ extrapolation method used in addition to any errors in the MCMC analysis itself. In order to isolate the MCMC analysis errors, we decided to calculate this coverage for days within the final windows time range $t_{b,n} \leq t \leq t_{e,n}$.

The reported number of cases on any given day, $C_{rep} = C_{true} + \varepsilon_{rep}$, is assumed to be the sum of the true number of cases C_{true} and some normally distributed reporting error ε_{rep} with 0 mean and variance of σ^2_{rep}. The MCMC process produces samples of the true number of cases C_{true} from the SEIR model output, and samples of the reporting error variance σ^2_{rep} from the likelihood Equation (3). Under these assumptions, if we knew the exact value of σ_{rep}, then the probability density function $f_{C_{rep}}(x) = \left(f_{C_{true}} * \Phi_{0,\sigma_{rep}}\right)(x)$ could be calculated as the convolution of $f_{C_{true}}(x)$ with the normal probability density function $\Phi_{0,\sigma_{rep}}(x)$. However, because we do not know the exact value of σ_{rep}, we have to integrate over all possible values of σ_{rep}

$$f_{C_{rep}}(x) = \int_0^\infty \left[(f_{C_{true}} * \Phi_{0,\sigma_{rep}})(x) \right] f_{\sigma_{rep}}(\sigma_{rep}) \, d\sigma_{rep} \quad (4)$$

Due to the complexity of directly calculating (4), we chose instead to estimate the distribution by generating samples of C_{rep} from the samples of C_{true} and σ_{rep} that were stored while running **Algorithm 1**. To do so, we first randomly select a set $\{c_i \in C_{true}\}$ from the set of true values and a set $\{\sigma_i \in \sigma_{rep}\}$ from the set of reporting error variances. We can then draw samples of the reporting error $\{\varepsilon_i \sim \mathcal{N}(0, \sigma_i^2)\}$, let C_{rep} be the set $\{c_i + \varepsilon_i\}$, and estimate f_{rep} directly from those samples.

Prediction intervals were estimated from the samples by first applying a Box-Cox power transformation $y_\lambda(C_{rep})$ to the

chain samples C_{rep} so that y_λ would be approximately normally distributed in the transformed domain [24]. From the normally distributed samples we could then calculate quantiles of interest from the inverse normal CDF $\Phi_{y_\lambda}^{-1}(p)$, and apply a reverse transform to get those points in the original domain. Those points were then used to estimate the prediction intervals $PI(p)$ from the inverse CDF points as

$$PI(p) = \left[y_\lambda^{-1}(\Phi_{y_\lambda}^{-1}(.5 - p/2)), \, y_\lambda^{-1}(\Phi_{y_\lambda}^{-1}(.5 + p/2)) \right] \quad (5)$$

Each point in **Figure 1** shows the prediction interval vs. coverage rate calculated on the set of 439 test jurisdictions. This value was calculated on the 29 different time windows and 50 prediction interval percentages for 1,450 points total.

FIGURE 1 | Prediction intervals of incident cases vs. coverage of reported data. Subfigures show this calculated on day 10 and day 20 of each 20-day window W_i. We can see that while we have good agreement on day 10 near the middle of each window, day 20 at the end of each window predicts too large of an interval resulting in a higher than expected coverage.

FIGURE 2 | Synthetically generated test case illustrating why calculated confidence near the beginning and end of a window may tend to overpredict their range.

4. DISCUSSION

We can see that although there is good agreement between the prediction interval and measured coverage for the middle of each window, the final day tends to over-predict the range. We hypothesize that the reason for this is at least in part that the likelihood Equation (3) does not take into account the autocorrelation of the residual $\varepsilon^{(k)} = C^{(k)} - C_{true}^{(k)}$ from day to day. The real world reported case data does contain some time-dependent correlations in the reporting error. For instance, cases reported over the weekend tend to be lower than on weekdays when reporting staff are more likely to be working and processing the data. Similarly, Mondays and Tuesdays tend to report higher numbers as the backlog of cases not reported over the weekend is processed. On long enough time scales we expect this error to be nearly a stationary process, meaning that there should be almost no correlation in the values for days $i \neq j$.

To illustrate the concept we ran the MCMC algorithm with the same loss Equation (3), but using a set of synthetically generated, time independent data, and also a simple linear model instead of an SEIR model. **Figure 2** shows the timeseries plots of the samples selected from the MCMC algorithm along with the true values and reported data provided as input to the MCMC algorithm. The samples selected by the algorithm can be categorized as follows

1. The model output c_i begins much lower than the true value for days near the beginning of the window, crosses over the true value somewhere near the middle, and ends up much higher than the true value for days near the end
2. The model output c_i begins much higher than the true value for days near the beginning of the window, crosses over the true value somewhere near the middle, and ends up much lower than the true value for days near the end
3. Everything else

Because the samples from categories 1 and 2 overlap and both cross the true value near the middle of the window, the sample density closer to the middle of the window tends to be slightly higher than it is near the ends. Some preliminary testing of adding a Box Pierce Q test [25] term into the loss Equation (3) to test for the independence of the residual timeseries has shown to effectively reduce the severity of this over estimation in some synthetic test cases. At this time however, more research and testing would need to be done before any conclusions could be made about the correctness, general applicability, and effectiveness of such a method.

We presented a Multiple-Try Metropolis MCMC algorithm that can be parallelized and optimized to run on GPU and accelerate solving problems where the likelihood function involves running complex physics-based simulations. Examples of such problems include the original inspiration for our model, the plume reconstruction problem, the epidemiological model presented in this paper, problems from computational chemistry, and many more.

We presented as an example a simple SEIR model solved using IEM's BioSim simulator. The BioSim simulator itself features the capability to add additional compartments, aged transitions, and resource constraints to build a model that more closely matches real-world scenarios providing more accurate estimates of resource needs, such as hospital beds, ventilators, medication requirements, etc. Any of these features could be added to the underlying epidemiological model while maintaining the parallelization and acceleration provided by the GPUs.

In our testing, using a single GPU to execute the simulations resulted in more than a 13x speedup in wall clock time compared to a fully parallelized CPU implementation. The algorithm is also able to scale up to run on multiple GPUs. Using 4 Nvidia RTX 2080 Ti GPUs in a high-end developer's workstation resulted in a 36.3x speedup in wall clock time compared to running fully parallelized on the single Intel Core-i9-10920X CPU with 12 physical cores using 24 hyperthreads. The same tests on an AWS HPC server consisting of 8 Nvidia Tesla A100-SMX4-40GB GPUs resulted in a 56.5x speedup in wall clock time compared to running on the dual socket Intel Xeon Platinum 8275CL CPUs with a combined 48 physical cores and 96 hyperthreads.

DATA AVAILABILITY STATEMENT

The raw data supporting the conclusions of this article will be made available by the authors, without undue reservation.

AUTHOR CONTRIBUTIONS

BS developed the initial model idea and implemented the CPU and GPU optimized code to run the SEIR models and MCMC algorithm. BS and SS designed the main algorithms and developed the theoretical model formalism. PB supervised the project and provided oversight. All authors contributed to developing tests and analysis of the results and contributed to developing the manuscript and approved of its publication.

REFERENCES

1. Andrieu C, Freitas N, Doucet A, Jordan M. An introduction to MCMC for machine learning. *Mach Learn.* (2003) 50:5–43. doi: 10.1023/A:1020281327116
2. Dunkley J, Bucher M, Ferreira PG, Moodley K, Skordis C. Fast and reliable markov chain monte carlo technique for cosmological parameter estimation. *Mon Not R Astron Soc.* (2005) 356:925–36. doi: 10.1111/j.1365-2966.2004.08464.x
3. Valderrama-Bahamóndez GI, Fröhlich H. MCMC techniques for parameter estimation of ODE based models in systems biology. *Front Appl Math Stat.* (2019) 5:55. doi: 10.3389/fams.2019.00055
4. Craiu RV, Lemieux C. Acceleration of the multiple-try metropolis algorithm using antithetic and stratified sampling. *Stat Comput.* (2007) 17:109. doi: 10.1007/s11222-006-9009-4
5. Robert CP, Elvira V, Tawn N, Wu C. Accelerating MCMC algorithms. *Wiley Interdiscip Rev Comput Stat.* (2018) 10:e1435. doi: 10.1002/wics.1435

6. Corander J, Gyllenberg M, Koski T. Bayesian model learning based on a parallel MCMC strategy. *Stat Comput*. (2006) 16:355–362. doi: 10.1007/s11222-006-9391-y

7. Martino L, Elvira V, Luengo D, Corander J, Louzada F. Orthogonal parallel MCMC methods for sampling and optimization. *Digit Signal Process*. (2016) 58:64–84. doi: 10.1016/j.dsp.2016.07.013

8. Bédard M, Douc R, Moulines E. Scaling analysis of multiple-try MCMC methods. *Stochastic Process Appl*. (2012) 03;122:758–786. doi: 10.1016/j.spa.2011.11.004

9. Cotter SL, Roberts GO, Stuart AM, White D. MCMC methods for functions: modifying old algorithms to make them faster. *Stat Sci*. (2013) 28:424–46. doi: 10.1214/13-STS421

10. Girolami M, Calderhead B. Riemann manifold langevin and hamiltonian monte carlo methods. *J R Stat Soc B*. (2011) 73:123–214. doi: 10.1111/j.1467-9868.2010.00765.x

11. Neal RM. *MCMC Using Hamiltonian Dynamics*. Boca Raton, FL: Chapman & Hall/CRC. (2012).

12. Liu JS, Liang F, Wong WH. The multiple-try method and local optimization in metropolis sampling. *J Am Stat Assoc*. (2000) 95:121–34. doi: 10.1080/01621459.2000.10473908

13. Bartz-Beielstein T, Stork J, Zaefferer M, Rebolledo M, Lasarczyk C, Rehbach F. *CRAN SPOT plotSIRModel. Plot of Continuous Time Markov Chains SIR Models*. (2020). Available online at: https://rdrr.io/cran/SPOT/man/plotSIRModel.html.

14. team B. *SEIR 0.2.3. Python Package for Modeling Epidemics Using the SEIR Model*. (2020). Availablable online at: https://pypi.org/project/SEIR/.

15. Mori JCM, Barbour W, Gui D, Piccoli B, Work D, Samaranayake S. *A Multi-Region SEIR Model With Mobility*. (2020). Available online at: https://seir.cee.cornell.edu/index.html.

16. Hall C, Ji W, Blaisten-Barojas E. The metropolis monte carlo method with CUDA enabled graphic processing units. *J Comput Phys*. (2014) 258:871–9. doi: 10.1016/j.jcp.2013.11.012

17. Anderson RM, Anderson B, May RM. *Infectious Diseases of Humans: Dynamics and Control*. Oxford: Oxford University Press (1992).

18. Li Q, Guan X, Wu P, Wang X, Zhou L, Tong Y, et al. Early transmission dynamics in wuhan, china, of novel coronavirus-infected pneumonia. *N Engl J Med*. (2020) 382:1199–207. doi: 10.1056/NEJMoa2001316

19. Martino L. A review of multiple try MCMC algorithms for signal processing. *Digit Signal Process*. (2018) 75:134–52. doi: 10.1016/j.dsp.2018.01.004

20. Calderhead B. A general construction for parallelizing metropolis-hastings algorithms. *Proc Natl Acad Sci USA*. (2014) 111:17408–13. doi: 10.1073/pnas.1408184111

21. Ensheng Dong HD, Gardner L. An interactive web-based dashboard to track COVID-19 in real time. *Lancet Infect Dis*. (2020) 20:533–4. doi: 10.1016/S1473-3099(20)30120-1

22. Besard T, Foket C, De Sutter B. Effective extensible programming: unleashing julia on GPUs. *IEEE Trans Parallel Distribut Syst*. (2018) 30: 827–41. doi: 10.1109/TPDS.2018.2872064

23. Besard T, Churavy V, Edelman A, De Sutter B. Rapid software prototyping for heterogeneous and distributed platforms. *Adv Eng Softw*. (2019) 132:29–46. doi: 10.1016/j.advengsoft.2019.02.002

24. Box GEP, Cox DR. An analysis of transformations. *J R Stat Soc B*. (1964) 26:211–52. doi: 10.1111/j.2517-6161.1964.tb00553.x

25. Box GEP, Pierce DA. Distribution of residual autocorrelations in autoregressive-integrated moving average time series models. *J Am Stat Assoc*. (1970) 65:1509–26. doi: 10.1080/01621459.1970.10481180

Generation of a Dynamical Logic Gate From Unstable Dissipative Systems of Type 1

Roberto R. Rivera-Durón[1]*, Ricardo Sevilla-Escoboza[2] and Qui-Ling Wang[3]

[1] Unmanned System Research Institute, Northwestern Polytechnical University, Xi'an, China, [2] Centro Universitario de los Lagos, Universidad de Guadalajara, Lagos de Moreno, Mexico, [3] College of Transportation, Chang'an University, Xi'an, China

The obtainment of a dynamical logic gate (DLG), which is a device capable of implementing several logic functions using the same model, has been one of the goals of the scientific community. Dynamical systems, specifically those that display chaotic behavior, have been widely used to emulate different logic gates which are the basis of general-purpose computing. In this study, we present a methodology based on unstable dissipative systems of type 1 (UDS-1), a kind of dynamical system capable of generating multi-scrolls and multi-stability. Using these two features, we codify inputs, subsequently, we get the adequate output, developing in this way a dynamical (reconfigurable) logic gate that performs any of the sixteen possible logic functions of two inputs. A highlight of the proposed methodology is that the selection of the desired logic gate is realized just by varying a couple of parameters.

Keywords: unstable dissipative systems, multi-stability, reconfigurable computing, reconfigurable logic gate, dynamical logic gate

1. INTRODUCTION

In the last decades, a vast quantity of budget and effort has been invested to design and construct a unique device capable of implementing several logic gates into the same structure. In 1998, Sinha and Ditto showed the capacity of lattices of coupled logistic maps to emulate NOR gates, resulting in chaos computing [1]. From this pioneering study, several schemes have been exploited, these include chaotic continuous and discrete dynamical systems [2–7]; piece-wise linear (PWL) systems [8, 9]; resonators controlled by noise intensity [10]; cellular neuronal networks [11]; memristive devices [12, 13], and doping-free bipolar junction transistors controlled by polarity [14]. In chaos computing, chaotic elements are exploited to act as different logic functions by changing parameters so that these devices are more flexible than the silicon-based architectures.

On the other hand, multi-stability is intrinsically present in physics, chemistry, biology, among other fields [15]. It is defined as the coexistence of multiple possible final stable states. The final state to which the system will converge depends on the initial conditions [16]. In the dynamical systems field, multi-stability is an important feature related to dissipative systems. Unstable dissipative systems are those that have a focus-saddle equilibrium point responsible for stable and unstable manifolds, but also, the sum of their eigenvalues is negative [17].

In most of the previously presented approaches related to chaos computing, the sensitivity to the initial conditions of chaotic elements is exploited to obtain logic gates; however, it could be a disadvantage when an experimental implementation is realized due to small variations in the voltages or a little differences in the tolerance of components. In this study, we present a

methodology based on the capacity of displaying multi-stability of unstable dissipative systems of type 1 (UDS-1) to implement a dynamical logic gate (DLG), also known as a reconfigurable logic gate. In our proposed method, logic zeros and logic ones are codified through one of the clearly distinguishable possible final states of the multi-stable USD-1. Although we obtain logic gates using multi-stability, which is closely related to the initial conditions, we take advantage of the concept of the basin of attraction, so that a vast set of initial conditions will produce the same response in our system. This gives the advantage to our model of being easily reliable and repeatable. An important aspect of our methodology is that by just varying two parameters, we can get the complete spectrum of two-input logic functions (16 logic gates), which represents an advantage in terms of time and resources for the future electronic implementation of the model.

The remaining of this article is structured as follows: In Section 2, we provide the fundamental theory of UDS-1. Our proposed methodology is explained in Section 3. Results for the DLG are shown and discussed in Section 4. Finally, in Section 5, some conclusions about this article are given.

2. UNSTABLE DISSIPATIVE SYSTEMS FUNDAMENTALS

In the same spirit of Campos-Cantón et al. [18], let us consider the following dynamical system:

$$\dot{x} = Ax, \tag{1}$$

where $x = [x_1, x_2, x_3]^T \in \mathbb{R}^3$ is the state vector, $A = [a_{ij}] \in \mathbb{R}^{3 \times 3}$ denotes a linear operator and it is a non-singular matrix. Also, let $\Lambda = \{\lambda_1, \lambda_2, \lambda_3\}$ be the set of eigenvalues of matrix A.

The system given by Equation (1) is called an UDS-1, if the following two statements are satisfied:

1. Focus-saddle equilibrium condition. The matrix A must possess one negative pure real eigenvalue λ_1, whereas $\lambda_{2,3}$ are complex conjugate with a positive real part.
2. Dissipativity condition. The system is dissipative, if $\sum_{i=1}^{3} \text{Re}(\lambda_i) < 0$.

Moreover, a UDS-1 is capable of displaying multi-scrolls if an adequate commutation control law is applied to it. A simple way to generate multi-scrolls consists of applying a PWL function to modify the system dynamics by changing the position of equilibrium points. Thus, if an additive term B is applied to Equation (1), it can be rewritten as:

$$\dot{x} = Ax + B, \tag{2}$$

where $B = [b_1, b_2, b_3]^T \in \mathbb{R}^3$ is a real vector, and it works as a discrete commutation function dependent on the state x. B changes depending on which domain $\mathcal{D}_i \subset \mathbb{R}^3$ the trajectory is located. The main idea is dividing the full phase space into domains, in other words, $\mathbb{R}^3 = \cup_{i=1}^{k} \mathcal{D}_i$. With this last regard, and supposing $B = [0, 0, b_3]^T$, then the switching function is given by:

$$b_3 = \begin{cases} \beta_1, & \text{if } x \in \mathcal{D}_1; \\ \beta_2, & \text{if } x \in \mathcal{D}_2; \\ \vdots & \vdots \\ \beta_k, & \text{if } x \in \mathcal{D}_k. \end{cases} \tag{3}$$

Because A is a non-singular matrix, the equilibrium point of the system given by Equation (2) is located at $x^* = -A^{-1}B$. Specifically, equilibrium points are $x_i^* = -A^{-1}\beta_i$ with $i = 1, 2, \ldots, k$. In this way, the system will have as equilibrium points as domains $\mathcal{D}_i$ are defined.

3. METHODS

In order to design a DLG, we start considering the following system in its canonical form:

$$\dot{x} = Ax = \begin{bmatrix} 0 & 1 & 0 \\ 0 & 0 & 1 \\ -0.5 & -0.7 & -0.5 \end{bmatrix} \begin{bmatrix} x_1 \\ x_2 \\ x_3 \end{bmatrix}, \tag{4}$$

whose eigenvalues are $\Lambda = \{\lambda_1 = -0.6358, \lambda_2 = 0.0679 + 0.8842i, \lambda_3 = 0.0679 + 0.8842i\}$; and $\sum_{i=1}^{3} \text{Re}(\lambda_i) = -0.5 < 0$. Thus, system of Equation (4) satisfies the two conditions mentioned in Section 2 to classify it as a USD-1.

The next step in our methodology consists of forcing the system in Equation (4) to generate n scrolls. It is important to mention that the number of scrolls n to be generated can be arbitrarily chosen and increased, the only requirement is that $n \geq 2$. In our case, we decide to generate three scrolls. Therefore, we add the commutation vector B to Equation (4) and we can rewrite it as:

$$\dot{x} = Ax + B = \begin{bmatrix} 0 & 1 & 0 \\ 0 & 0 & 1 \\ -0.5 & -0.7 & -0.5 \end{bmatrix} \begin{bmatrix} x_1 \\ x_2 \\ x_3 \end{bmatrix} + \begin{bmatrix} 0 \\ 0 \\ b_3 \end{bmatrix}, \tag{5}$$

as we desire to generate three scrolls, then the same quantity of equilibrium points are necessary and we want them arbitrarily located at $x_{e1}^* = (-3, 0, 0)$, $x_{e2}^* = (0, 0, 0)$, $x_{e3}^* = (3, 0, 0)$, which are equispaced only along the x_1 plane. Also, let us remember that each equilibrium point is located in $x_i^* = -A^{-1}\beta_i$, this leads to $x_i^* = -2\beta_i$. Hence, we need to define the switching function b_3 and each β_i, which are described as:

$$b_3 = \begin{cases} 1.5 & \text{if} & x_1 < -1.5, \\ 0 & \text{if} & -1.5 \leq x_1 \leq 1.5, \\ -1.5 & \text{if} & x_1 > 1.5 \end{cases} \tag{6}$$

where the commutation surfaces among domains are located at -1.5 and 1.5 to preserve the shape and symmetry of the scrolls.

Up to now, we have constructed a UDS-1 with the capability of generating three scrolls. In **Figure 1** are plotted projections of the states of the system given by Equations (5) and

(6) for several planes. The plot in **Figure 1A** corresponds to the x_1x_2 plane, where it is possible to distinguish the three scrolls clearly. **Figure 1B** is the projection onto the x_1x_3 plane; whereas **Figure 1C** shows the projection in the x_2x_3 plane.

The following step is controlling the system described by Equations (5) and (6) with the aim of transforming it into a multi-stable system. To achieve this goal, first, let us define the negative reciprocal of element a_{33} as $\mu = -1/a_{33}$, and second, let us multiply the last row of matrix A and the switching function b_3 times μ.

$$\dot{x} = Ax + B = \begin{bmatrix} 0 & 1 & 0 \\ 0 & 0 & 1 \\ -\frac{0.5}{0.5} & -\frac{0.7}{0.5} & -\frac{0.5}{0.5} \end{bmatrix} \begin{bmatrix} x_1 \\ x_2 \\ x_3 \end{bmatrix} + \begin{bmatrix} 0 \\ 0 \\ -\frac{1}{0.5}b_3 \end{bmatrix}, \quad (7)$$

The parameter μ induces multi-stability to the system but leaves the dissipativity unchanged. Now, each scroll we previously generated with the system described by Equations (5) and (6) have become a possible final stable state to which the system will converge depending on the initial conditions. In other words, the system will converge to one of these three scrolls depending on whether its initial condition belongs to the basin of attraction of the scroll. **Figure 2** shows these possible final states to which the system can converge. **Figure 2A** corresponds to the initial condition $x(0) = (-2.5, -1, 0)$; **Figure 2B** to $x(0) = (1.1, -1, 0)$; and finally, **Figure 2C** to $x(0) = (2.5, -1, 0)$.

To develop a system capable of emulating all possible two-input logic functions, we have built a simple three-node network in which each node is a multi-stable UDS-1 governed by Equation (7). The topology of this network is shown in **Figure 3**. Node 1 and node 2 act as inputs, whereas node 3 works as the output of the DLG. In the example, we are using to explain our methodology, the number of scrolls matches with the number of nodes in the network, but there is no relationship between these two quantities.

As it was previously explained, the multi-stable UDS-1 of Equation (7) can converge to three final attractors depending on the initial conditions, in such a way that we can choose two of these attractors to codify logical zeros and ones. Arbitrarily, we decide that if the multi-stable UDS-1 is converging to the left attractor (**Figure 2A**), then it will represent a logical zero. On the other hand, if the multi-stable UDS-1 is converging to the right attractor (**Figure 2C**), then this will be coded as a logical one. The initial condition $(x_0, y_0, z_0) = (-3, 0, 0)$ and $(x_0, y_0, z_0) = (3, 0, 0)$ belong to the basin of attraction of the left and right attractor, respectively. Thus, we can define the target point $(x, y, z) = (I_{1,2} \in \{-3, 3\}, 0.001, 0)$ to be reached through feedback control. Taking these assumptions into consideration, the dynamics of node 1 acting as the first input is described by:

$$\dot{x}_1 = y_1 - k(x_1 - I_1), \quad (8)$$
$$\dot{y}_1 = z_1 - k(y_1 - 0.001), \quad (9)$$
$$\dot{z}_1 = -0.5\mu x_1 - 0.7\mu y_1 - 0.5\mu z_1 + \mu b_{n1}, \quad (10)$$

where the switching function b_{n1} is:

$$b_{n1} = \begin{cases} 1.5 & \text{if } x_1 < -1.5, \\ 0 & \text{if } -1.5 \le x_1 \le 1.5, \\ -1.5 & \text{if } x_1 > 1.5 \end{cases} \quad (11)$$

The dynamics of node 2 which works as the second input is given by:

$$\dot{x}_2 = y_2 - k(x_2 - I_2), \quad (12)$$
$$\dot{y}_2 = z_2 - k(y_2 - 0.001), \quad (13)$$
$$\dot{z}_2 = -0.5\mu x_2 - 0.7\mu y_2 - 0.5\mu z_2 + \mu b_{n2}, \quad (14)$$

whose commutation function is:

$$b_{n2} = \begin{cases} 1.5 & \text{if } x_2 < -1.5, \\ 0 & \text{if } -1.5 \le x_2 \le 1.5, \\ -1.5 & \text{if } x_2 > 1.5 \end{cases} \quad (15)$$

How input node 1 and node 2 interconnect with the output node 3 considers the following linear affined system:

$$h(I_1, I_2) = \boldsymbol{\alpha} \cdot \mathbf{i} + \gamma, \quad (16)$$

where $\mathbf{i} = (I_1, I_2)^T$ is a column vector whose elements $I_{1,2} \in \{-3, 3\}$; $\boldsymbol{\alpha} = (\alpha_1, \alpha_2) \in \mathbb{R}^2$ and $\gamma \in \mathbb{R}$ are system parameters to be adjusted to obtain the desired logic gate. Function h results from summing the scalar product $\boldsymbol{\alpha} \cdot \mathbf{i}$ plus an offset given by γ. The output of the system is ruled by:

$$I_3(h) = \begin{cases} 3, & \text{if } |h| < \kappa; \\ -3, & \text{otherwise}. \end{cases} \quad (17)$$

where $\kappa \in \mathbb{R}$ is defined as a threshold.

Therefore, the dynamics of node 3 behaving as output is governed by:

$$\begin{aligned} \dot{x}_3 &= y_3 - k(x_3 - I_3), \\ \dot{y}_3 &= z_3 - k(y_3 - 0.001), \\ \dot{z}_3 &= -0.5\mu x_3 - 0.7\mu y_3 - 0.5\mu z_3 + \mu b_{n3}, \end{aligned} \quad (18)$$

with the function b_{n3} governed by:

$$b_{n3} = \begin{cases} 1.5 & \text{if } x_3 < -1.5, \\ 0 & \text{if } -1.5 \le x_3 \le 1.5, \\ -1.5 & \text{if } x_3 > 1.5 \end{cases} \quad (19)$$

The networked system described by Equations (10)–(19) emulates any of the possible sixteen two-input logic functions whose truth tables appear in **Table 1**. $\perp$ represents the contradiction or null; I_1I_2, AND; I_1I_2', inhibition of I_2; I_1, transfer of I_1; $I_1'I_2$, inhibition of I_1; I_2, transfer of I_2; $I_1 \oplus I_2$, XOR; $I_1 + I_2$, OR; $(I_1 + I_2)'$, NOR; $(I_1 \oplus I_2)'$, XNOR; I_2', complement
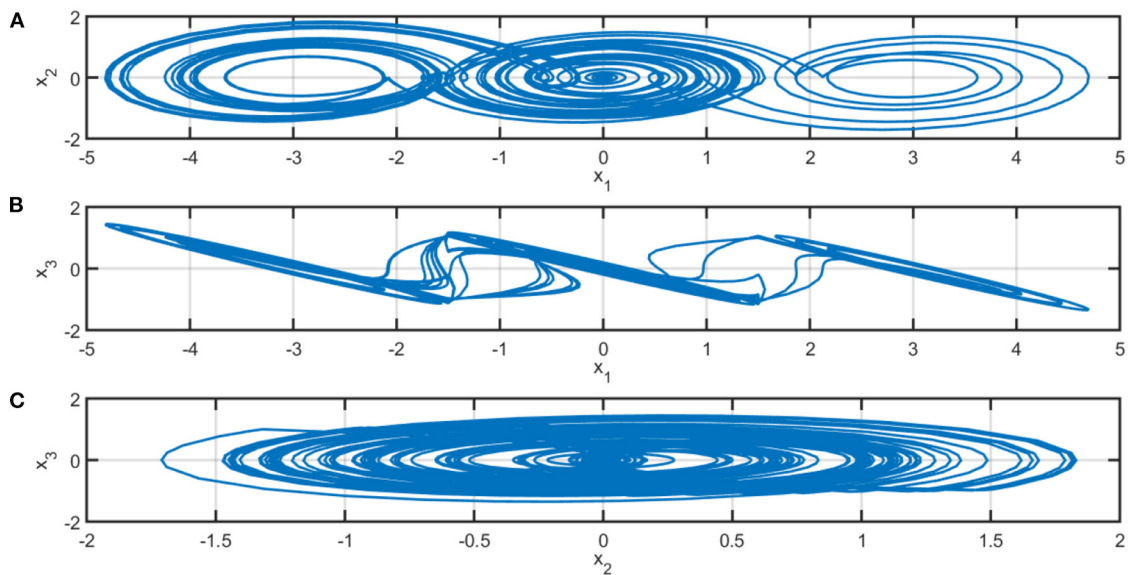
FIGURE 1 | Projections of the system given by equations. axplusbmethod and b3method onto the planes of R^3. The plot **(A)** corresponds to x_1x_2 plane; **(B)** is the projection onto x_1x_3 plane; and **(C)** is the projection in x_2x_3 plane.
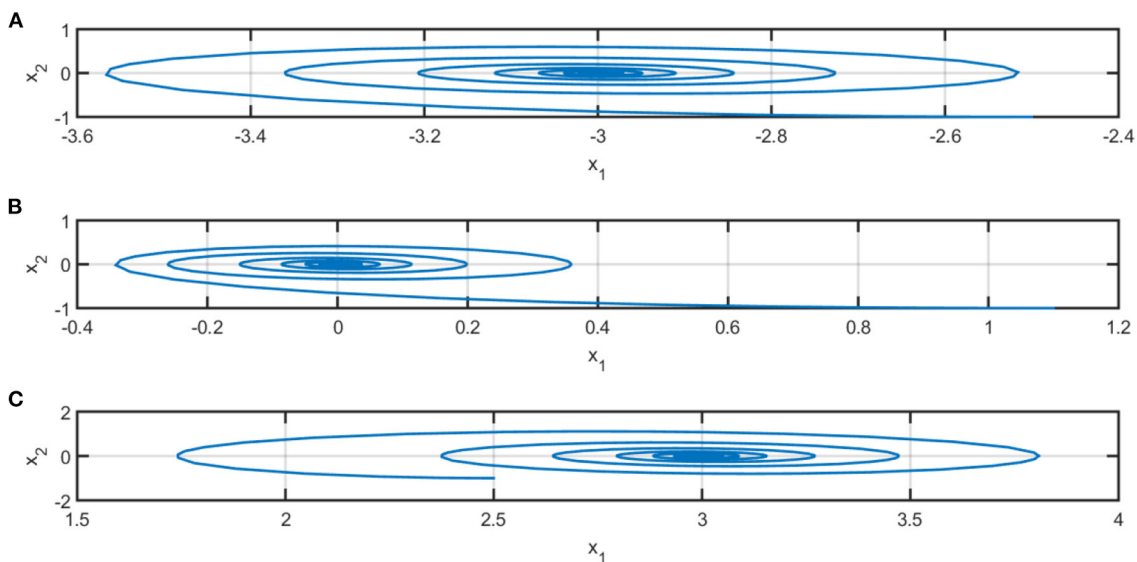
FIGURE 2 | Projections onto the x_1x_2 plane of the three final possible attractors of the multi-stable system of equation (7). axplusbmultimethod. Plot **(A)** corresponds to the initial condition $x(0) = (-2.5, -1, 0)$; Plot **(B)** to $x(0) = (1.1, -1, 0)$; and Plot **(C)** to $x(0) = (2.5, -1, 0)$.

of I_2; $I_1 + I'_2$, implication (I_2 implies I_1); I'_1, complement of I_1; $I'_1 + I_2$, implication (I_1 implies I_2); $(I_1I_2)'$, NAND; $\top$, tautology or identity.

The selection of logic gate functionality is realized by adjusting system parameters α_1, α_2, γ, and κ so that Equations (16) and (17) are satisfied simultaneously. Depending on the values of I_1 and I_2, Equation (16) will have one of the results shown in the third column of **Table 2**. These results will fall or will not be inside

the interval $(-\kappa, \kappa)$ according to the truth table of the desired logic function we desire to obtain. If h of Equation (16) falls in the open interval $(-\kappa, \kappa)$ defined in Equation (17), then $I_3 = 3$ which represents a logical one and the output node 3 will converge to the left attractor; otherwise, $I_3 = -3$ what is defined as a logical zero and the output node 3 will converge to the right attractor.

In the following lines, we briefly explain the selection of parameters for the case of the AND (I_1I_2) gate, but an analog
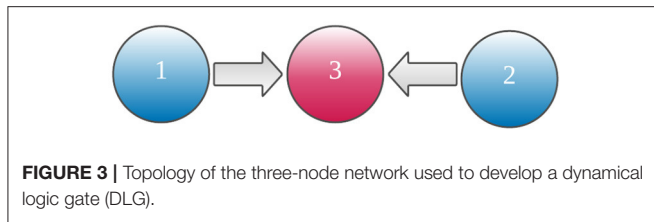
FIGURE 3 | Topology of the three-node network used to develop a dynamical logic gate (DLG).

TABLE 1 | Truth tables for all the sixteen possible two-input logic functions expressed in Boolean variables (0 and 1).

I_1	I_2	$\perp$	I_1I_2	I_1I_2'	I_1	$I_1'I_2$	I_2	$I_1 \oplus I_2$	$I_1 + I_2$
0	0	0	0	0	0	0	0	0	0
0	1	0	0	0	0	1	1	1	1
1	0	0	0	1	1	0	0	1	1
1	1	0	1	0	1	0	1	0	1
I_1	I_2	$(I_1 + I_2)'$	$(I_1 \oplus I_2)'$	I_2'	$I_1 + I_2'$	I_1'	$I_1' + I_2$	$(I_1I_2)'$	$\top$
0	0	1	1	1	1	1	1	1	1
0	1	0	0	0	0	1	1	1	1
1	0	0	0	1	1	0	0	1	1
1	1	0	1	0	1	0	1	0	1

TABLE 2 | Values of $h(I_1, I_2)$ in Equation 16.

I_1	I_2	$h(I_1, I_2)$
-3	-3	$-3\alpha_1 - 3\alpha_2 + \gamma$
-3	3	$-3\alpha_1 + 3\alpha_2 + \gamma$
3	-3	$3\alpha_1 - 3\alpha_2 + \gamma$
3	3	$3\alpha_1 + 3\alpha_2 + \gamma$

TABLE 3 | List of the system parameters α_2 and γ used to emulate each logic function.

Logic function	$\perp$	I_1I_2	I_1I_2'	I_1	$I_1'I_2$	I_2	$I_1 \oplus I_2$	$I_1 + I_2$
α_2	0.0	0.5	-0.5	0.0	-0.5	0.5	0.8	0.5
γ	4.5	-4.0	-4.0	-3.0	4.0	-3.0	0.0	-2.0
Logic function	$(I_1 + I_2)'$	$(I_1 \oplus I_2)'$	I_2'	$I_1 + I_2'$	I_1'	$I_1' + I_2$	$(I_1I_2)'$	$\top$
α_2	0.5	-0.8	0.5	-0.5	0.0	-0.5	0.5	0
γ	4.0	0.0	3.0	-2.0	3.0	1.0	2.0	0

procedure is necessary for the rest of the logic gates. First, we fix the threshold $\kappa = 3$. According to the truth table of AND gate shown in the fourth upper column of **Table 1**, only when $I_1 = 3$ and $I_2 = 3$, the sum h must fall inside the interval $(-3, 3)$; the remaining combinations of I_1 and I_2 will fall outside $(-3, 3)$. In such a way, the following inequalities must be accomplished simultaneously:

$$
\begin{aligned}
-3\alpha_1 - 3\alpha_2 + \gamma < -3 \quad &\vee \quad 3 < -3\alpha_1 - 3\alpha_2 + \gamma, \\
-3\alpha_1 + 3\alpha_2 + \gamma < -3 \quad &\vee \quad 3 < -3\alpha_1 + 3\alpha_2 + \gamma, \\
3\alpha_1 - 3\alpha_2 + \gamma < -3 \quad &\vee \quad 3 < 3\alpha_1 - 3\alpha_2 + \gamma, \\
3\alpha_1 + 3\alpha_2 + \gamma > -3 \quad &\wedge \quad 3 > 3\alpha_1 + 3\alpha_2 + \gamma.
\end{aligned}
\tag{20}
$$
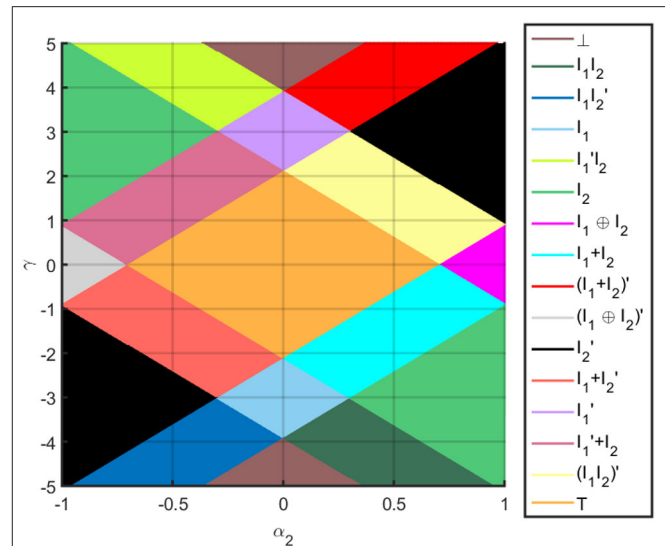
FIGURE 4 | Map of regions for parameters α_2 and γ of DLG.

TABLE 4 | Comparative frame among several approaches already presented and our proposal of DLG.

Reference	Number of obtained logic gates	Number of parameters to configure
Li et al. [7]	11	1
Peng et al. [8]	7	3
Peng et al. [9]	16	2
Guerra et al. [10]	2	1
Rivera-Durón *et al.*	16	2

After algebraic calculations, it is possible to determine that $\alpha_1 = 0.3$, $\alpha_2 = 0.5$, and $\gamma = -4.0$ are one of the several combinations that satisfy the corresponding inequalities in the system Equation (20).

4. RESULTS

The parameter selection is not unique, there are several combinations of $\alpha_1, \alpha_2, \gamma$, and κ that can satisfy Equations (16) and (17). For this reason, we utilized a computer code to determine the set of system parameters to obtain each of the sixteen two-input logic functions for a constant value of $\kappa = 3$. After inspecting the results, we noticed that the value of $\alpha_1 = 0.3$ appeared in all the cases, therefore, we can assume that α_1 is constant too. This last represents an advantage because the functionality of the DLG only depends on the values of α_2 and γ, which can result in the optimization of time and resources in the future experimental realization of the DLG. A map for parameters α_2 and γ to select functionality of DLG is shown in **Figure 4**. The complete list of the system parameters that we used to emulate each logic function is shown in **Table 3**, it is important to remark that in all the cases $\kappa = 3$ and $\alpha_1 = 0.3$.
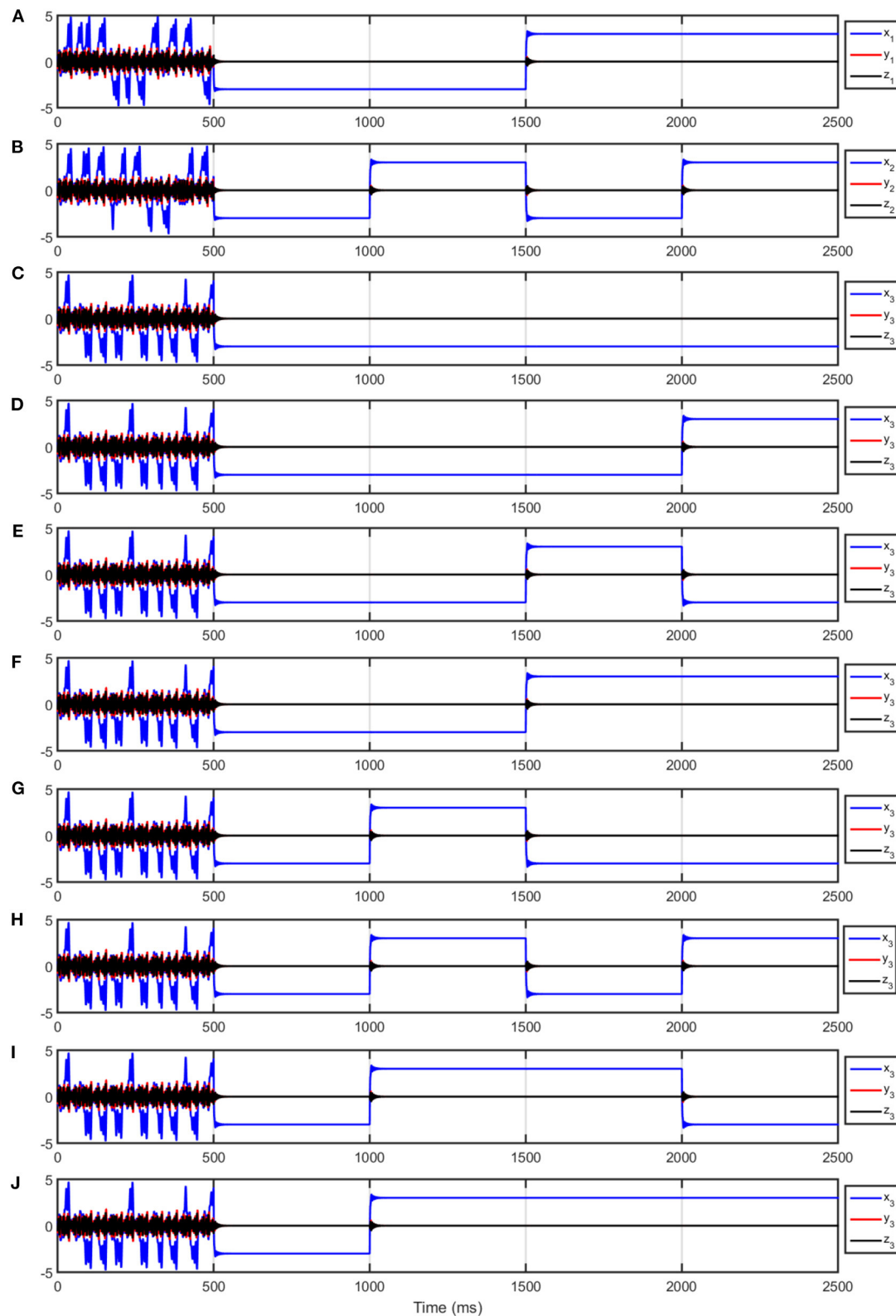
FIGURE 5 | Temporal evolution of the input nodes and for the output node emulating the logic functions shown in the upper part of Table Truth Tables. The plot in **(A)** corresponds to the input node 1. Plot **(B)** corresponds to the temporal evolution of input node 2. bot is represented in plot **(C)**; $I_1 I_2$ in plot **(D)**; $I_1 I_2$' in plot **(E)**; I_1 in plot **(F)**; I_1'I_2 in plot **(G)**; I_2 in plot **(H)**; I_1 plus I_2 in plot **(I)**; $I_1 + I_2$ in plot **(J)**.
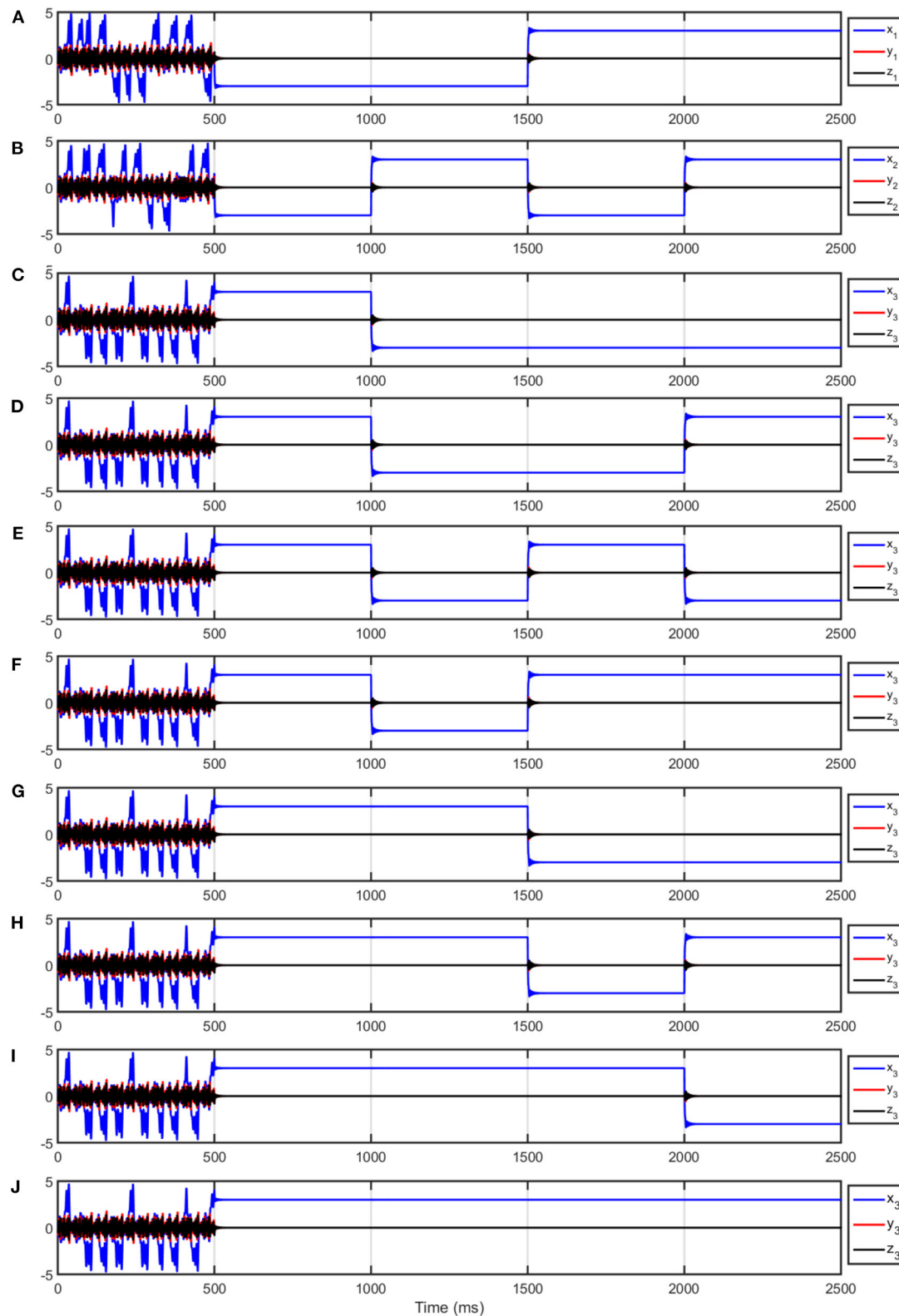
FIGURE 6 | Temporal evolution of the input nodes and for the output node emulating the logic functions shown in the lower part of Table TruthTables. The plot in **(A)** corresponds to the input node 1. Plot **(B)** corresponds to the temporal evolution of input node 2. $(I_1 + I_2)'$ in plot **(C)**; $(I_1 \oplus I_2)'$ in plot **(D)**; I_2' in plot **(E)**; $I_1 + I_2'$ in plot **(F)**; I_1' in plot **(G)**; $I_1' + I_2$ in plot **(H)**; $(I_1 I_2)'$ in plot **(I)**; top in plot **(J)**.

TABLE 5 | The truth table for the full adder.

C_{in}	I_1	I_2	C_{out}	S
0	0	0	0	0
0	0	1	0	1
0	1	0	0	1
0	1	1	1	0
1	0	0	0	1
1	0	1	1	0
1	1	0	1	0
1	1	1	1	1

The three first columns correspond to the inputs, whereas the remaining ones, to the outputs.
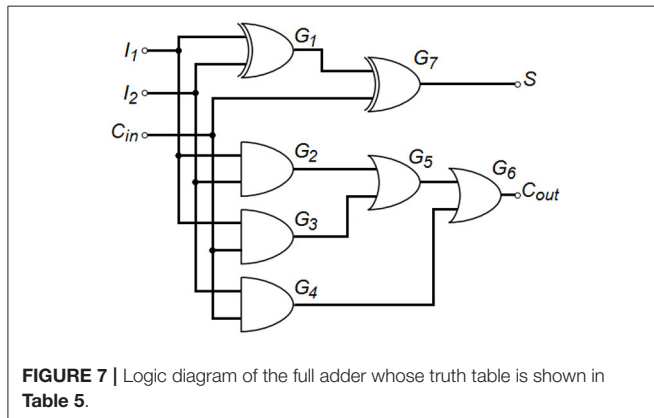
FIGURE 7 | Logic diagram of the full adder whose truth table is shown in **Table 5**.

We can compare our proposal with respect to other approaches to measure the benefits between the achieved logic gates and the number of parameters to be configured. In this sense, **Table 4** shows a comparative frame among previously presented studies and our proposal of DLG. From this table, it is possible to observe that [10] achieves only a pair of logic gates (AND, OR) by varying the resonator's operation parameters. The study in Peng et al. [8] obtains seven logic gates ($\perp$, AND, OR, NAND, NOR, XOR, $\top$) by tuning three parameters. Eleven logic gates ($\perp$, AND, OR, NAND, NOR, XNOR, I_2, I_2', $I_1' + I_2$, $I_1 + I_2'$, $\top$) were achieved in Li et al. [7] by varying a single parameter. Special mention deserves the work done in Peng et al. [9], in which authors got all the possible two-input logic gates as well as we did in our approach through the tuning of a pair of parameters.

Numerical simulations were realized to prove the correct performance of the developed DLG. We started simulations letting the three nodes behave freely so that $\mu = 1$ and they are not in a multi-stable regime for time $0 \leq t \leq 500$. Then, we set $\mu = -1/0.5$ to get multi-stability in all the nodes, and we configured I_1 of node 1 to be $I_1 = -3$ for $500 < t \leq 1500$ and $I_1 = 3$ for $1500 < t \leq 2500$; in analogous way, I_2 of the node 2 was configured to be $I_2 = -3$ for $t \in \{(500, 1000] \cup (1500, 2000]\}$, and $I_2 = 3$ for $t \in \{(1000, 1500] \cup (2000, 2500]\}$. In this way, the four possible combinations of I_1 and I_2 shown in the first two columns of **Table 2** were accomplished. The plots of the temporal evolution of the input node 1 are shown in **Figures 5A**, **6A**, whereas the plots in **Figures 5B**, **6B** correspond to the temporal evolution of input node 2. The behavior of the output node 3

is plotted in **Figures 5**, **6**. $\perp$ is represented in **Figure 5C**; $I_1 I_2$ in **Figure 5D**; $I_1 I_2'$ in **Figure 5E**; I_1 in **Figure 5F**; $I_1' I_2$ in **Figure 5G**; I_2 in **Figure 5H**; $I_1 \oplus I_2$ in **Figure 5I**; $I_1 + I_2$ in **Figure 5J**; $(I_1 + I_2)'$ in **Figure 6C**; $(I_1 \oplus I_2)'$ in **Figure 6D**; I_2' in **Figure 6E**; $I_1 + I_2'$ in **Figure 6F**; I_1' in **Figure 6G**; $I_1' + I_2$ in **Figure 6H**; $(I_1 I_2)'$ in **Figure 6I**; $\top$ in **Figure 6J**. From **Figures 5**, **6** is possible to note the fast response time of the output node, this is because of the control law we added which yields the system to an initial condition into the basin of attraction of the desired attractor but also, this control law avoids falling in any of the equilibrium points of the system.

Now, let us implement a full adder to prove the performance of the DLG when it is executing compound functions. The full adder is a combinational circuit that realizes the arithmetical sum of three bits. I_1 and I_2 are the bits to be added, whereas C_{in} is the input carry bit coming from a previous sum. Due to the sum of three bits varies from 0 to 3, the circuit needs two bits to correctly represent the addition; these bits are S and C_{out}, which are the sum and the output carry, respectively. The truth table for the full adder is shown in **Table 5**. From the truth table is possible to determine the logic functions $S = C_{in} \oplus I_1 \oplus I_2$ and $C_{out} = C_{in} I_1 + C_{in} I_2 + I_1 I_2$. The logic diagram to configure the full adder consists of seven logic gates (G_1 to G_7), and it is displayed in **Figure 7**. Again, we launched the numerical simulations with all the nodes behaving freely so that $\mu = 1$ and they are not in a multi-stable regime for time $0 \leq t \leq 250$, after this time, we set $\mu = -1/0.5$ to get multi-stability in all the nodes. To achieve the eight possible combinations in the inputs of the full adder, we proceeded as follows: first, we configured C_{in} at node 1 to be $C_{in} = -3$ for $250 < t \leq 1250$ and $C_{in} = 3$ for $1250 < t \leq 2250$; second, I_1 at the node 2 was configured to be $I_1 = -3$ for $t \in \{(250, 750] \cup (1250, 1750]\}$, and $I_1 = 3$ for $t \in \{(750, 1250] \cup (1750, 2250]\}$; finally, I_2 at node 3 was fixed to be $I_2 = -3$ for $t \in \{(250, 500] \cup (750, 1000] \cup (1250, 1500] \cup (1750, 2000]\}$, and $I_2 = 3$ for $t \in \{(500, 750] \cup (1000, 1250] \cup (1500, 1750] \cup (2000, 2250]\}$. The temporal evolution of the full adder is plotted in **Figure 8**. The plots in **Figures 8A–C** correspond to C_{in}, I_1, and I_2, respectively. **Figure 8D** displays the behavior of G_1 which is configured as XOR gate ($I_1 \oplus I_2$). **Figure 8E** shows the evolution of the AND gate G_2 ($I_1 I_2$). In **Figure 8F** is plotted the AND gate G_3 ($I_1 C_{in}$). **Figure 8G** is showing the evolution of the AND gate G_4 ($I_2 C_{in}$). **Figure 8H** shows the temporal evolution of G_5 configured as OR gate and which receives in its inputs the signals coming from G_2 and G_3. The signal coming from G_4 and G_5 are received by G_6 and whose output corresponds to C_{out}, this is shown in **Figure 8I**. Finally, G_7 processes the signal coming from G_1 and C_{in} and its output results in the sum S, which is plotted in **Figure 8J**.

Our proposal of DLG can be taken into an electronic realization through currently available electronic components. Since the core of DLG is composed of three ordinary differential equations, they can be implemented using operational amplifiers (OP-AMP) in the basic configurations (integrator, inverted adder, and inverted), resistors, and capacitors. From an engineering viewpoint, the computational complexity and hardware cost to implement a DLG through a three-node network could be elevated compared with the current logic devices. For this reason, we have as future work to achieve the same results here reported
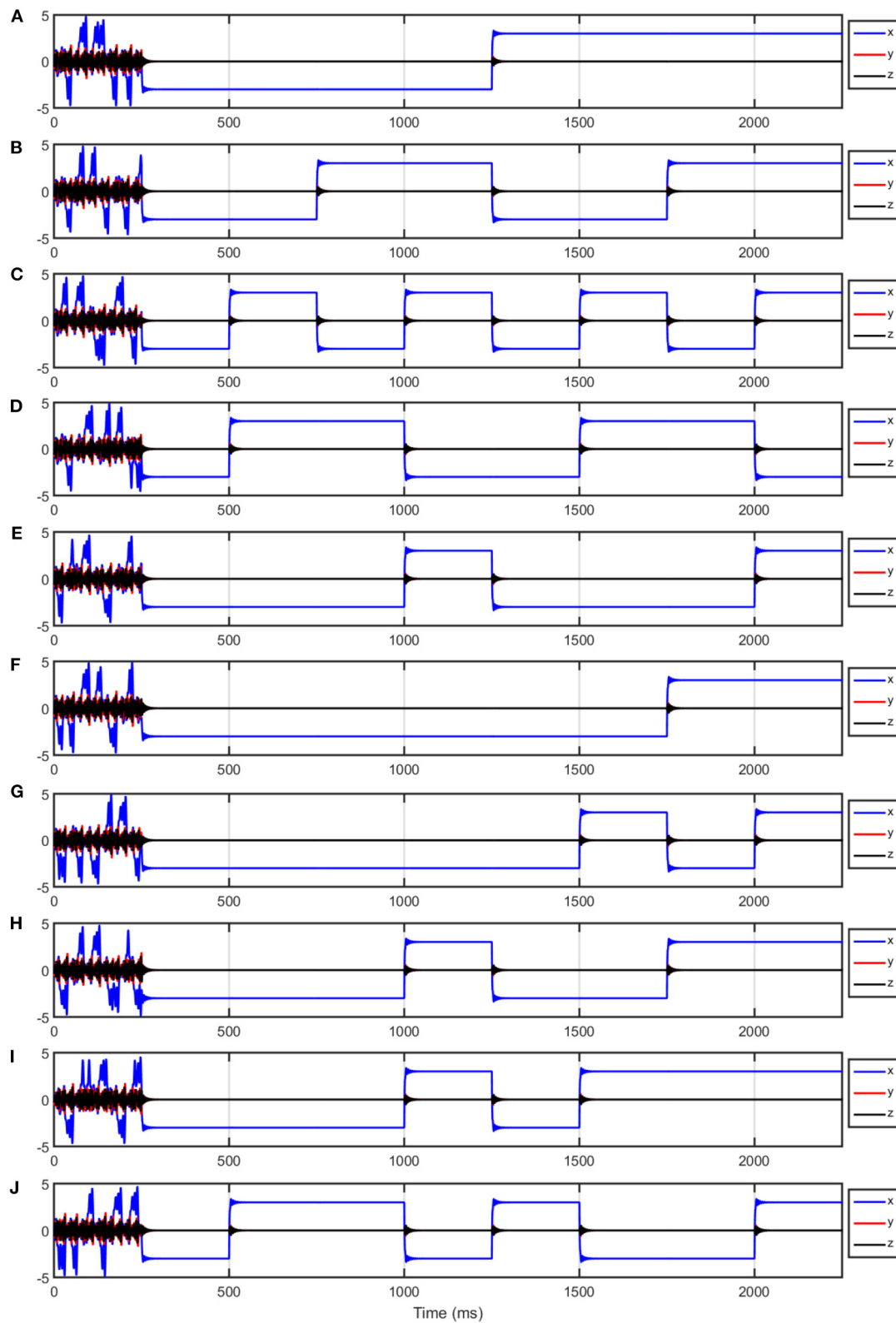
FIGURE 8 | Temporal evolution of the nodes in the full adder. The plot **(A)** corresponds to C_{in}; **(B)** to I_1; **(C)** to I_2; **(D)** to G_1; **(E)** to G_2; **(F)** to G_3; **(G)** to G_4; **(H)** to G_5; **(I)** to G_6 which is C_{out}; and **(J)** to G_7 which is the sum S.

but just using a single UDS-1 for each DLG, which will decrease the prices and the design tasks. However, our approach has the advantage that the programming to implement several functions can be quite quick and it can be done on the fly. Also, another advantage we can elucidate is related to a research issue; whereas in the traditional digital logic devices, as the FPGAs, the states updating is governed by a master clock so that the updating occurs in a synchronous way; in our device, we can add a delay element to investigate autonomous Boolean networks, a kind of dynamical system where the state updating happens when there exists a transition in any input. In this way, we can study the effect of delays in autonomous Boolean networks.

5. CONCLUSION

We presented a methodology to design a DLG using a multi-stable UDS-1. We constructed a three-node network of multi-stable UDS-1. In this topology, a couple of nodes act as inputs of the logic gate, whereas the remaining node is the output or response. Using a pair of the different final states (attractors) of the multi-stable system, we were able to codify Boolean ones and zeros, and subsequently, we obtain the adequate response to emulate all the possible two-input logic functions (16 logic gates). We are sure that our results are relevant because we just need to adjust a pair of parameters to select the functionality of the DLG,

this could be important in terms of time and cost in the future experimental realization of this DLG.

DATA AVAILABILITY STATEMENT

The original contributions presented in the study are included in the article/supplementary material, further inquiries can be directed to the corresponding author/s.

AUTHOR CONTRIBUTIONS

RR-D was involved in methodology conceptualization, numerical simulations, writing the original draft, reviewing and editing the manuscript. RS-E is responsible for numerical simulations, validation, reviewing and editing the manuscript. Q-LW responsible for numerical simulations, validation, data visualization, and reviewing and editing the manuscript. All authors contributed to the article and approved the submitted version.

FUNDING

REFERENCES

1. Sinha S, Ditto W. Dynamics based computation. *Phys Rev Lett.* (1998) 81:2156–9.

2. Sinha S, Ditto W. Computing with distributed chaos. *Phys Rev E.* (1999) 60:363–77. doi: 10.1103/PhysRevE.60.363

3. Munakata T, Sinha S, Ditto W. Chaos computing: implementation of fundamental logical gates by chaotic elements. *IEEE Trans Circ Syst I Fundam Theory Appl.* (2002) 49:1629–33. doi: 10.1109/TCSI.2002.8 04551

4. Murali K, Sinha S, Ditto W. Implementation of NOR gate by a chaotic chua's circuit. *Int J Bifurcat Chaos.* (2003) 13:2669–72. doi: 10.1142/S0218127403008053

5. Murali K, Sinha S, Ditto W. Construction of a reconfigurable dynamic logic cell. *Pramana.* (2005) 64:433–41. doi: 10.1007/BF02704569

6. Murali K, Miliotis A, Ditto W, Sinha S. Logic from nonlinear dynamical evolution. *Phys Lett A.* (2009) 373:1346–51. doi: 10.1016/j.physleta.2009.02.026

7. Li L, Yang C, Hui S, Yu W, Kurths J, Peng H, et al. A reconfigurable logic cell based on a simple dynamical system. *Math Probl Eng.* (2013) 2013:735189. doi: 10.1155/2013/735189

8. Peng H, Yang Y, Li L, Luo H. Harnessing piecewise-linear systems to construct dynamic logic architecture. *Chaos Interdiscip J Nonlin Sci.* (2008) 18:033101. doi: 10.1063/1.2953494

9. Peng H, Liu F, Li L, Yang Y, Wang X. Dynamic logic architecture based on piecewise-linear systems. *Phys Lett A.* (2010) 374:1450–6. doi: 10.1063/5.0046968

10. Guerra D, Bulsara A, Ditto W, Sinha S, Murali K, Mohanty P. A noise-assisted reprogrammable nanomechanical logic gate. *Nano Lett.* (2010) 10:1168–71. doi: 10.1021/nl9034175

11. Yuan X, Liu W. Implementation and improvement of dynamic logic gates based on cellular neural networks. In: *2012 Fifth International Workshop on Chaos-fractals Theories and Applications.* (Dalian) (2012). p. 99–103.

12. Rothenbuhler A, Tran T, Smith E, Saxena V, Campbell K. Reconfigurable threshold logic gates using memristive devices. In: *2012 IEEE Subthreshold Microelectronics Conference (SubVT).* Waltham, MA (2012). p. 1–3.

13. James A, Krestinskaya O, Maan A. Recursive threshold logica bioinspired reconfigurable dynamic logic system with crossbar arrays. *IEEE Trans Biomed Circ Syst.* (2020) 14: 1311–22. doi: 10.1109/TBCAS.2020.3027554

14. Sahu A, Kumar A, Tiwari S. Performance investigation of universal gates and ring oscillator using doping-free bipolar junction transistor. In: *2020 IEEE Silicon Nanoelectronics Workshop (SNW).* Honolulu, HI (2020). p. 125–6.

15. Hens C, Dana S, Feudel U. Extreme multistability: attractor manipulation and robustness. *Chaos Interdiscipl J Nonlin Sci.* (2015) 25:053112. doi: 10.1063/1.4921351

16. Pisarchik A, Feudel U. Control of multistability. *Phys Rep.* (2014) 540:167–218. doi: 10.1016/j.physrep.2014.02.007

17. Campos-Cantón E, Femat R, Chen G. Attractors generated from switching unstable dissipative systems. *Chaos: Interdis J Nonlin Sci.* (2012) 22:033121. doi: 10.1063/1.4742338

18. Campos-Cantón E, Barajas-Ramírez J, Solís-Perales G, Femat R. Multiscroll attractors by switching systems. *Chaos: Interdis J Nonlin Sci.* (2010) 20:013116. doi: 10.1063/1.3314278

| Frontiers in Applied Mathematics and Statistics

A nested multiscale model to study paratuberculosis in ruminants

Rendani Netshikweta and Winston Garira*

Modelling Health and Environmental Linkages Research Group, Department of Mathematics and Applied Mathematics, University of Venda, Thohoyandou, South Africa

In this study, we present a nested multiscale model that integrates the within-host scale and the between-host scale disease dynamics for Paratuberculosis in ruminants (e.g., cattle, goats, and sheep), with the aim of ascertaining the influence of initial infective inoculum dose on its dynamics. Ruminant paratuberculosis is often characterized as an environmentally-transmitted disease and it is caused by bacteria called *Mycobacterium avium subspecies paratuberculosis* that can survive in the physical environment for a considerable period of time. In the context of nested multiscale models developed at host level, a key feature is that the within-host scale and the between-host scale disease dynamics influence each other in a reciprocal way, with the between-host scale influencing the within-host scale through initial infective inoculum dose which susceptible ruminants may consume from the environment. The numerical results of the nested multiscale model presented in this study demonstrate that once the minimum infectious dose is consumed, then the infection at the within-host scale is sustained more by pathogen replication than by super-infection. From these results we conclude that super-infection might have an insignificant effect on the dynamics of PTB in ruminants. However, at this stage we cannot precisely conclude if super-infection does not effect on the dynamics of the disease. This would be investigated further using an embedded multiscale model, which is more appropriate in giving us conclusive results. We further demonstrate the need to use nested multiscale models over single-scale modeling approach by estimating a key parameter for pathogen replication that cannot be estimated using single-scale models.

KEYWORDS

multiscale modeling of disease, nested multiscale models, environmentally-transmitted diseases, multiscale modeling of paratuberculosis, infectious disease systems

1. Introduction

Paratuberculosis (PTB) infection, also known as Johne's disease, is an important disease in ruminants such as cattle, goats, and sheep [see [1–3] and references therein] that cannot be easily ignored as its cases continue to be reported throughout the world, more especially in countries with temperate climates. Ruminant Paratuberculosis is often characterized as an environmentally-transmitted disease.

PTB is caused by bacteria called *Mycobacterium avium subspecies paratuberculosis* (MAP) which infects the intestine of ruminants [4]. This organism is most commonly widespread in dairy cattle and can lead to serious economic burdens in livestock industries due to the reduction of milk production and the productive life of cattle as well [5]. The main clinical outcomes of PTB infection in cattle are failure of growth, increase in weight loss, and chronic diarrhea. Although PTB has not been classified as a zoonotic disease, clinical studies show that most human patients with Crohn's disease are found with MAP [6]. Crohn's disease is an inflammatory bowel disease characterized by a persisting, painful, and diarrheal inflammatory disease of the intestinal tract in humans [6]. Ruminants usually acquire PTB infection through ingestion of the infective bacteria in colostrum, and from the faeces of infected ruminants contaminating food and surface water/water troughs. The disease can also be transmitted vertically from an infected pregnant ruminant to its foetus. However, following the ingestion of MAP bacteria contained in faecal material, and reaching the gut of an infected ruminant, MAP are engulfed by macrophages in the submucosal of the ruminant, and the submucosal macrophages become infected [2]. In general, the dynamics of MAP among submucosal macrophages within an infected ruminant can be controlled by the ruminant immune response (such as T-helper immune response cells). Yet, currently there is no meaningful treatment that has been made available for PTB in ruminants, and control programs implemented in many countries have had limited success [7]. It is important to note that at the ruminant host level both the two PTB disease processes: (i) the infection of a ruminant by free-living MAP in the environment and (ii) the shedding of MAP into the environment by an infected ruminant interlink the transmission process of MAP among the ruminants which often happens at a slow time scale and the replication process of MAP within an infected ruminant which often occur at a fast time scale to close the complete multiscale cycle (i.e., the replication-transmission cycle) dynamics of PTB [25].

Multiscale models that characterize infectious disease processes across different scales at different levels of organization of an infectious disease have been developed recently to study disease dynamics [3, 8–14, 21–24]. Some of these multiscale models have further been used to evaluate the comparative effectiveness of different preventive and treatment health interventions that operate at different scales against infections [13, 14]. Based on the categorization in [15, 16], there are five main different categories of multiscale models of infectious disease systems that can be developed at different levels of organization of an infectious disease system (the cell level, the tissue level, the host level, etc.) which are: (i) individual-based multiscale models (IMSMs), (ii) nested multiscale models (NMSMs), (iii) embedded multiscale models (EMSMs), (iv) hybrid multiscale models (HMSMs), and (v) coupled multiscale models (CMSMs). In multiscale modeling of infectious disease

systems, knowledge of the different categories of multiscale models is important to understand which multiscale model is most suitable for characterizing disease dynamics at particular levels of organization of an infectious disease system. It is also important for the description of the structure of the multiscale model. It enables authors to describe the structure of the multiscale model in brief by referring to the generic description of the structure of the category of the multiscale model concerned without the need to repeatedly discuss its structure whenever a multiscale model of an infectious disease system is being developed and focus instead on issues peculiar to that multiscale model [16]. In this study we develop a nested multiscale model to study the multiscale dynamics of PTB in ruminants and further use it to enhance a single-scale model that can be developed at host/population/herd level. Nested multiscale models of infectious diseases are mathematical models in which the macroscale sub-model influences the microscale sub-model through the initial value of the inoculum of the infective pathogen. In these nested multiscale models, the microscale also influences the macroscale through pathogen excretion. Further, the macroscale sub-model and the microscale sub-model must be described by the same formalism or mathematical representation for this category of multiscale models. We can identify three main classes in the category of nested multiscale models which are [15, 16]:

(a) *Class 1 - Transformation based nested multiscale models (TRAN-NMSMs)*: Here the microscale scale submodel is formally transformed into a macroscale model. They are formulated through developing microscale structured macroscale submodels. At host level this task is accomplished by subdividing the entire host population into various sub-classes corresponding to the different levels of microscale traits: naive or completely susceptible, completely or partially immune, vaccinated, immune compromised or protected from infection due to certain genetic factors.

(b) *Class 2 - Unidirectional coupling based nested multiscale models (UNID-NMSMs)*: The nature of the multiscale model in this class is such that there is strictly one-way inter-scale information flow among the two submodels (from the microscale submodel to the macroscale submodel).

(c) *Class 3 - Simplification based nested multiscale models (SIMP-NMSMs)*: These are multiscale models of infectious disease systems which are formulated by simplifying or reducing the order/dimensions of UNID-MSMs in class 2 of this category. The simplification or reduction of order is sometimes achieved by using methods such as slow and fast time scale analysis [12] or dynamical systems based methods such as centre manifold theory [17].

In this article, we first develop a class 2 nested multiscale model of PTB disease dynamics in ruminants at host level, and then derive a class 3 nested multiscale model through

fast-and-slow time scale analysis of the class 2 nested multiscale model. For the host level of organization of an infectious disease system, the within-host scale (the microscale) sub-model and the between-host scale (the macroscale) sub-model serve as building blocks in the development of the complete nested multiscale model [16]. For PTB infection in ruminants, the within-host scale on one hand is associated with the interaction of MAP with ruminant macrophages (target cells) and other immune response cells that happens inside an infected ruminant. It is at this scale where the outcomes of infection within a single infected ruminant determine if, when and how much the ruminant will further transmit the bacteria into the environment, and in turn affecting the spread of the disease for the ruminant at between-host scale. The processes of PTB infection at the within-ruminant-host can be modified by the within-host conditions and medical interventions. The between-host scale disease processes on the other hand, however, are associated with the transmission dynamics of MAP bacteria that typically occurs between ruminants and their environment. This takes place when ruminants feed from contaminated pasture with fecal material containing infective MAP, or drink from contaminated surface water/water troughs with the bacteria. The processes of disease transmission at the between-ruminant-host scale can be modified by control measures such as reducing fecal contamination of food, water and pasture (which can be achieved by raising feed and water troughs, strip grazing, or use of mains/piped water rather than surface/pond water); avoid spreading yard manure on pasture; and maintain proper hygiene practices particularly in buildings/yards and calving boxes [18].

To date, most of PTB disease dynamics models in the literature have been devoted to study the dynamics of PTB infection in ruminants and evaluating the effect of control measures aimed at controlling, eliminating, and even eradicating this disease using a single-scale modeling approach [1, 19, 20]. This is despite the fact that PTB infection is a complex and multiscale disease system. However, we have to date, witnessed the development of few models in the literature that consider the complexity and multiscale nature of PTB infection in attempting to study its dynamics [3, 21–23]. The multiscale models in [3, 21] use the time-since-infection approach to link the within-host sub-model with the between-host sub-model for PTB infection as well as the dependence of some epidemiological parameters on the within-host MAP bacteria load. This coupling principle employed in [3, 21] was suggested for the first time by Gilchrist and Sasaki [24]. In addition, it is also worthy to note that the multiscale models in [3, 21] are categorized as hybrid multiscale models [15, 16]. Although the multiscale models in [3, 21] and the multiscale model developed in this study all characterize the reciprocal influence between the within-host scale and the between-host scale disease dynamics, there are important differences between these multiscale models. Specifically, in the current nested multiscale model, both the within-host scale and the between-host scale sub-models are all described by the

same formalism or mathematical representation (i.e., a system of ODEs). However, the multiscale models in [3, 21] are hybrid multiscale models, where only the within-host scale sub-models are represented by ODEs, while their between-host sub-models are represented by partial differential equations (PDEs). The hybrid multiscale models in [3, 21] are more difficult to analyze than nested multiscale models because apart from the fact they incorporate different time scales for the within-host scale and the between-host scale, they also do not use a common metric of disease transmission across scales. At within-host scale, pathogen load is used as the metric for disease transmission while at between-host scale, disease class (i.e., infected class) is used as the metric for disease transmission.

The rest of this paper is organized as follows. In Section 2, we derive and analyze the nested multiscale model for PTB multiscale dynamics. It is in this section where we evaluate the influence of initial infective inoculum on the dynamics of PTB. In Section 3, we estimate a parameter of pathogen replication that cannot be estimated using single-scale models. In Section 4, we analyze the simplified multiscale model of PTB and show that the model is mathematically and epidemiologically well-posed. We also perform a sensitivity analysis of the two ruminant population health measures derived from the simplified multiscale model. The paper ends up with discussion and conclusions in Section 5.

2. Derivation of nested multiscale model for the dynamics of ruminant paratuberculosis (PTB)

For infectious disease systems at host level, the between-host scale sub-model and the within-host scale sub-model are the building blocks upon which multiscale models are developed. In this case, we derive a nested multiscale model that integrates the between-host sub-model associated with the transmission dynamics of PTB disease and the within-host sub-model associated with the replication dynamics of MAP bacteria within an infected ruminant at the site of infection. In the following sections, we begin by presenting two independent sub-models for PTB disease dynamics at two distinct scales, one at the between-host scale and other at the within-host scale and then integrate them into a single multiscale model.

2.1. The between-host scale submodel for the PTB multiscale model dynamics

The between-host scale submodel for the multiscale dynamics of PTB in ruminants is described by a susceptible-infected-susceptible-infected, *SIS*, model coupled with the

TABLE 1 A summary of the variables associated with the transmission cycle of PTB at the between-host scale.

No.	Variable	Description
1.	$S_C(t)$	Population of susceptible ruminant hosts at time t
2.	$I_C(t)$	Population of infected ruminant hosts at time t
3.	$B_C(t)$	Population of MAP bacteria in the environment at time t

compartment of the MAP environmental dynamics, B_C, that depicts the evolution of bacteria in the environment. The description of model variables associated with the transmission cycle of PTB at the between-host scale are tabulated in Table 1. We make the following assumptions for this sub-model:

(a) The transmission of the infection is only through contact with MAP bacterial load (B_C) in the physical environment. However, if there is any direct transmission, it can be estimated by indirect transmission in terms of environmental MAP bacterial load (B_C).

(b) The dynamics of S_C, I_C, and B_C are assumed to occur at slow time scale, t, compared to the within-host scale PTB transmission dynamics variables that occur at fast time scale, τ, so that $S_C = S_C(t)$, $I_C = I_C(t)$, and $B_C = B_C(t)$.

(c) The different classes that the infected ruminant progresses through (e.g., the exposed class, the chronically infected class, etc.) are accounted for by the within-host scale sub-model.

(d) The average extracellular MAP bacteria in each infected ruminant is modeled phenomenologically by $\widehat{N_c}$, which is a proxy for individual ruminant infectiousness.

(e) The environmental MAP bacterial (B_C) do not replicate in the environment (outside-host environment).

(f) ruminant with MAP can recover from PTB infection.

Based on these assumptions the sub-model for the PTB transmission dynamics at the between-host scale becomes:

$$
\begin{cases}
(i) \ \dfrac{dS_C(t)}{dt} = \Lambda_C - \dfrac{\beta_C B_C(t)}{B_0 + B_C(t)} S_C(t) - \mu_C S_C(t) + \widehat{\gamma_C}(B_c) I_C(t), \\[2ex]
(ii) \ \dfrac{dI_C(t)}{dt} = \dfrac{\beta_C B_C(t)}{B_0 + B_C(t)} S_C(t) - [\mu_C + \widehat{\delta_C}(B_c) + \widehat{\gamma_C}(B_c)] I_C(t), \\[2ex]
(iii) \ \dfrac{dB_C(t)}{dt} = \widehat{N_c} \alpha_c I_C(t) - \alpha_C B_C(t),
\end{cases}
\quad (2.1)
$$

The between-host scale submodel given by Equation (2.1) is based on monitoring the dynamics of three populations which are susceptible ruminants (S_C), infected ruminants (I_C), and MAP bacterial load (B_C) in the physical environment. The first equation of the model system (2.1) describes the dynamics of susceptible ruminants. At any time t, new recruits of susceptible ruminants enter the ruminant population through birth and

incoming ruminants from different farms/geographical regions at a constant rate Λ_C and is also increased through recovery of infected individuals at a rate $\widehat{\gamma_C}(B_c)$, with B_c being the population of the within-ruminant-host MAP bacteria at time τ. This population losses individuals due to natural death at a constant rate μ_C. The susceptible population also decreases through infection at a rate $\beta_C B_C(t)/(B_0 + B_C(t))$ with β_C being the exposure rate to infective MAP bacterial load (B_C) in the environment and B_0 is the saturation parameter of the bacteria that yield 50 percent chance of a ruminant getting infected with PTB infection after ingesting the bacteria. The infection happens when susceptible ruminants feed from contaminated pasture with faecal material containing infective MAP, or drink from contaminated surface water/water troughs with the bacteria. The second equation in the model system (2.1) describes the dynamics of PTB infected ruminants. This population increases through infection of susceptible ruminants and decreases through natural death at a constant rate μ_C as well as through recovery at a rate $\widehat{\gamma_C}(B_c)$. There is additional death at a rate $\widehat{\delta_C}(B_c)$ in the population of infected ruminants due to disease, so that an average lifespan of PTB infected ruminant in the population is $1/(\mu_C + \widehat{\delta_C}(B_c) + \widehat{\gamma_C}(B_c))$. We assume that infected ruminants spread the disease through contaminating the environment at a rate $\widehat{N_c} \alpha_c I_C$, where $\widehat{N_c}$ models phenomenologically the average number of the within-host scale MAP bacterial load available for excretion into the environment by each infected ruminants at a rate α_c. Therefore, the population dynamics of MAP bacilli in the environment, described by the last equation of the model system (2.1), increases following excretion of MAP bacteria by infected ruminant hosts in faecal material into the environment at a rate $\widehat{N_c} \alpha_c I_C$. This population of MAP bacilli in the environment is assumed to decrease due to natural death at a rate α_C. However, from the single model system (2.1), we note that $\widehat{N_c}$ is treated as a single value parameter. But in reality $\widehat{N_c}$ is a composite parameter that summaries the bacterial dynamics within an infected individual ruminant, and this makes the single-scale model system (2.1) to be unrealistic. We also note that it is not easy to estimate $\widehat{N_c}$ using a single-scale models. However, an alternative approach for estimating $\widehat{N_c}$ is to use a nested multiscale model. In the next section, we derive a within-host scale submodel for estimating $\widehat{N_c}$. The description of model variables associated with the transmission cycle of PTB at the between-host scale are tabulated in Table 1.

2.2. The within-host scale submodel for the PTB multiscale model dynamics

For the derivation of the current nested multiscale model for PTB in ruminants considered in this study,

the within-host submodel dynamics is adopted from a more elaborative single-scale model framework from the work by Magombedze et al. [2] with minor modifications which are based on multiscale considerations. However, the main multiscale consideration incorporated into the model in [2] is the excretion/shedding rate α_c, which is an important multiscle consideration since in general the within-host scale sub-model is linked to the between-host scale sub-model through pathogen shedding/excretion [15]. The resulting within-host model describes the interactions of six populations: susceptible macrophages (M_ϕ) which are target cells, infected macrophages (I_m) which are macrophages which have internalized extracellular MAP bacteria cells, MAP bacterial load (B_c) at the extracellular environment, naive CD4+ T cells (T_0), Th1 immune response cells (T_1), and Th2 phenotype immune response cells (T_2) [see the work in [2]]. We also modify the model in [2] by making the following assumptions:

(a) Transmission of the infection between cells is only through contact with the extracellular MAP bacterial load B_c in the extracellular environment at the site of infection.

(b) The within-host scale disease processes happen at fast time scale, τ, compared to the between-host scale PTB submodel variables so that $M_\phi = M_\phi(\tau)$, $I_m = I_m(\tau)$, $B_c = B_c(\tau)$, $T_0 = T_0(\tau)$, $T_1 = T_1(\tau)$, and $T_2 = T_2(\tau)$.

(c) The extracellular MAP bacterial load modeled mechanistically by $B_c = B_c(\tau)$ is a proxy for individual ruminant infectiousness.

(d) The extracellular MAP bacteria does not replicate outside the macrophage cells of an individual ruminant.

(e) The depletion of MAP bacteria in the extracellular environment through engulfment by macrophages is negligible.

These assumptions lead to the following submodel of ordinary differential equations for the within-host scale PTB transmission dynamics:

$$
\begin{cases}
i. & \dfrac{dM_\phi(\tau)}{d\tau} = \Lambda_\phi - \beta_\phi M_\phi(\tau) B_c(\tau) - \mu_\phi M_\phi(\tau), \\[2mm]
ii. & \dfrac{dI_m(\tau)}{d\tau} = \beta_\phi M_\phi(\tau) B_c(\tau) - \gamma_m T_1(\tau) I_m(\tau) - (k_m + \mu_\phi) I_m(\tau), \\[2mm]
iii. & \dfrac{dB_c(\tau)}{d\tau} = N_m k_m I_m(\tau) - (\mu_c + \alpha_c) B_c(\tau), \\[2mm]
iv. & \dfrac{dT_0(\tau)}{d\tau} = \Lambda_0 - (\delta_m I_m(\tau) + \delta_b B_c(\tau)) T_0(\tau) - \mu_0 T_0(\tau), \\[2mm]
v. & \dfrac{dT_1(\tau)}{d\tau} = \theta_1 \delta_m I_m(\tau) T_0(\tau) - \mu_1 T_1(\tau), \\[2mm]
vi. & \dfrac{dT_2(\tau)}{d\tau} = \theta_2 \delta_b B_c(\tau) T_0(\tau) - \mu_2 T_2(\tau).
\end{cases}
\tag{2.2}
$$

In the within-host scale sub-model (2.2), the first two equations describe the dynamics of the within-ruminant-host macrophage population which is divided into two groups. The first group is of susceptible macrophage cells $M_\phi(\tau)$ (these are macrophages which are healthy and are susceptible to the Paratuberculosis at the site of infection). The second group is of infected macrophage cells $I_m(t)$ (these are macrophages which are infected by the MAP bacteria). We assume that, at any time τ, new macrophage recruits enter the population of susceptible macrophages through the supply of macrophage cells from progenitor monocytes that are recruited from the blood to the site of infection at a constant rate Λ_ϕ and this population loses individuals due to natural death at a constant rate μ_ϕ. Susceptible macrophages acquire infection through engulfing extracellular MAP bacilli bacteria at a rate β_ϕ. We assume that in the population of infected macrophages experiences additional death due to bursting of infected cells at a rate k_m and due to cell removal by T_1 immune response at a rate γ_m. In addition, when infected macrophages burst at constant rate k_m, they are assumed to release an average number of intracellular MAP bacilli N_m into the extracellular environment, so that the total number of intracellular bacteria released into the extracellular environment is $N_m k_m I_m$. The third equation of the model system (2.2) describes the changes in time of the population size of MAP bacteria in the extracellular environment which is generated following the release of the intracellular MAP bacilli into the extracellular environment when each infected macrophage bursts. We assume that the population of MAP bacteria in the extracellular environment decays naturally at a constant rate μ_c and are excreted out of the body of infected ruminant into the physical environment through feces at a constant rate α_c. The last three equations of the model system (2.2) describe the evolution in time of the population of ruminant immune response cells at the site of infection in the gut which are naive CD4+ T cells (T_0), and the two subsets of the MAP specific immune response, Th1 (T_1) and Th2 (T_2) cells [see [2] and reference therein]. The population of naive CD4+ T cells (T_0) for MAP bacilli are produced at a constant rate Λ_0 from the thymus. We assume that these naive CD4+ T cells decay naturally at a rate μ_0. Following the work in [2], we assume that T_0 cells become T_1 or T_2 immune response cells at per capita rates δ_m and δ_b, respectively. Thus, the population of T_1 and T_2 immune response cells are proliferated at a rate $\theta_1 \delta_m I_m T_0$ and $\theta_1 \delta_b B_m T_0$, respectively. We assume that both the population of T_1 and T_2 immune response cells decay naturally at rates μ_1 and μ_2, respectively. The description of model variables associated with the replication cycle of PTB at the within-host scale are tabulated in Table 2.

2.3. Integration of the between-host and within-host submodels of PTB dynamics into a nested multiscale model

In the previous two subsections we presented the two submodels for the dynamics of PTB infection [between-host submodel (2.1) and within-host submodel (2.2)] that separately describe the two key processes of PTB disease dynamics (transmission and replication of MAP bacteria processes) which occur at two distinct scales (within-host scale and between-host scale). We now integrate them into a single multiscale model as shown in flow diagram in Figure 1. We achieve this by replacing the parameter $\widehat{N_c}$ which phenomenologically models within-host scale pathogen replication by a variable $B_c(\tau)$ which mechanistically models the within-host scale pathogen replication to get:

$$
\begin{cases}
i. \ \dfrac{dS_C(t)}{dt} &= \Lambda_C - \dfrac{\beta_C B_C(t)}{B_0 + B_C(t)} S_C(t) - \mu_C S_C(t) + \widehat{\gamma_C}(B_c) I_C(t), \\[2mm]
ii. \ \dfrac{dI_C(t)}{dt} &= \dfrac{\beta_C B_C(t)}{B_0 + B_C(t)} S_C(t) - [\mu_C + \widehat{\delta_C}(B_c) + \widehat{\gamma_C}(B_c)] I_C(t), \\[2mm]
iii. \ \dfrac{dB_C(t)}{dt} &= \alpha_c B_c(\tau) I_C(t) - \alpha_C B_C(t), \\[2mm]
iv. \ \dfrac{dM_\phi(\tau)}{d\tau} &= \Lambda_\phi - \beta_\phi M_\phi(\tau) B_c(\tau) - \mu_\phi M_\phi(\tau), \\[2mm]
v. \ \dfrac{dI_m(\tau)}{d\tau} &= \beta_\phi M_\phi(\tau) B_c(\tau) - \gamma_m T_1(\tau) I_m(\tau) - (k_m + \mu_\phi) I_m(\tau) \\[2mm]
vi. \ \dfrac{dB_c(\tau)}{d\tau} &= N_m k_m I_m(\tau) - (\mu_c + \alpha_c) B_c(\tau), \\[2mm]
vii. \ \dfrac{dT_0(\tau)}{d\tau} &= \Lambda_0 - (\delta_m I_m(\tau) + \delta_b B_c(\tau)) T_0(\tau) - \mu_0 T_0(\tau), \\[2mm]
viii. \ \dfrac{dT_1(\tau)}{d\tau} &= \theta_1 \delta_m I_m(\tau) T_0(\tau) - \mu_1 T_1(\tau), \\[2mm]
ix. \ \dfrac{dT_2(\tau)}{d\tau} &= \theta_2 \delta_b B_c(\tau) T_0(\tau) - \mu_2 T_2(\tau).
\end{cases} \quad (2.3)
$$

Based on the categorization of multiscale models of infectious disease systems presented in [15, 16], the multiscale model for PTB disease dynamics given by (2.3) falls in the category of nested multiscale models of class 2.

2.4. Analysis of the multiscale model using fast-low time-scale analysis

We note from the full nested multiscale model system given by (2.3) has two different time scales involved which are the between-host time scale (t) associated with the transmission dynamics of PTB at the population level and the within-host time scale (τ) associated with the replication dynamics

TABLE 2 A summary of the variables associated with the replication cycle of PTB at the within-host scale.

No.	Variable	Description
1.	$M_\phi(\tau)$	Population of susceptible macrophages within an infected ruminant host at time τ
2.	$I_m(\tau)$	Population of infected macrophages within an infected ruminant host at time τ
3.	$T_0(\tau)$	Population of naive CD4 T cells within an infected ruminant host at time τ
4.	$T_1(\tau)$	Population of specific immune response, Th1 within an infected ruminant host at time τ
5.	$T_2(\tau)$	Population of specific immune response, Th2 within an infected ruminant at time τ
6.	$B_c(\tau)$	Population of extracellular MAP bacteria within an infected ruminant host at time τ

of PTB infectious agent at an individual ruminant level. This makes the analysis of the full nested multiscale model system (2.3) more difficult to perform. However, the analysis of the multiscale model system (2.3) can be simplified by expressing the slow time-scale and the fast time-scale in terms of each other by using the relationship $t = \epsilon\tau$, where $0 < \epsilon \ll 1$ and ϵ being a constant highlighting the fast time-scale dynamics of the within-host model compared to the slow time-scale of the between-host scale dynamics. We further assume the constant rate of recovery and constant disease-induced death rate of infected ruminants so that $\widehat{\gamma_C}(B_c) = \gamma_C$ and $\widehat{\delta_C}(B_c) = \delta_C$, so that the full nested multiscale model system (2.3) becomes:

$$
\begin{cases}
i. \ \dfrac{dS_C(t)}{dt} &= \Lambda_C - \dfrac{\beta_C B_C(t)}{B_0 + B_C(t)} S_C(t) - \mu_C S_C(t) + \gamma_C I_C(t), \\[2mm]
ii. \ \dfrac{dI_C(t)}{dt} &= \dfrac{\beta_C B_C(t)}{B_0 + B_C(t)} S_C(t) - (\mu_C + \delta_C + \gamma_C) I_C(t), \\[2mm]
iii. \ \dfrac{dB_C(t)}{dt} &= \alpha_c B_c(t) I_C(t) - \alpha_C B_C(t), \\[2mm]
iv. \ \epsilon \dfrac{dM_\phi(t)}{dt} &= \Lambda_\phi - \beta_\phi M_\phi(t) B_c(t) - \mu_\phi M_\phi(t) \\[2mm]
v. \ \epsilon \dfrac{dI_m(t)}{dt} &= \beta_\phi M_\phi(t) B_c(t) - \gamma_m T_1(t) I_m(t) - (k_m + \mu_\phi) I_m(t) \\[2mm]
vi. \ \epsilon \dfrac{dB_c(t)}{dt} &= N_m k_m I_m(t) - (\mu_c + \alpha_c) B_c(t) \\[2mm]
vii. \ \epsilon \dfrac{dT_0(t)}{dt} &= \Lambda_0 - (\delta_m I_m(t) + \delta_b B_c(t)) T_0(t) - \mu_0 T_0(t) \\[2mm]
viii. \ \epsilon \dfrac{dT_1(t)}{dt} &= \theta_1 \delta_m I_m(t) T_0(t) - \mu_1 T_1(t) \\[2mm]
ix. \ \epsilon \dfrac{dT_2(t)}{dt} &= \theta_2 \delta_b B_c(t) T_0(t) - \mu_2 T_2(t).
\end{cases} \quad (2.4)
$$

FIGURE 1
A schematic representation of the nested multiscale model of paratuberculosis disease in ruminants, with $\lambda_C = \beta_C B_C/(B_0 + B_C)$.

In the next two sub-sections, we assess through numerical simulations the full nested multiscale model system given by equation (2.4) to ascertain the reciprocal influence between the between-host scale and the within-host scale dynamics of PTB infection. We achieve this by demonstrating (i) the influence of the between-host scale on the within-host scale through the initial infective inoculum that susceptible ruminants may acquire by interacting with MAP bacteria in contaminated environment, and (ii) the influence of the within-host scale parameters on the between-host disease dynamics. The parameter values used for simulations are tabulated in Table 3. In addition, initial values used for simulations for the full nested multiscale model system (2.4) are as follows: $S_C(0) = 2,000$, $I_C(0) = 5$, $B_c(0) = 10$, $M_\phi(0) = 500$, $I_m(0) = 0$, $T_0(0) = 0$, $T_1(0) = 0$, $T_2(0) = 0$, $B_C(0) = 1,000$.

2.4.1. The influence of initial inoculum on the within-host scale of PTB infection dynamics

In this subsection, we demonstrate through numerical simulations of the full nested multiscale model system (2.4) the influence of between-host scale dynamics on within-host scale variables for PTB infection dynamics. This is achieved by varying the initial value condition of the infective inoculum $B_c(0)$ that susceptible ruminants may acquire by interacting with MAP bacteria in contaminated environment for different values and assess its impact on the dynamics of four selected key within-host variables, I_m, B_c, T_1, and T_2. Figure 2 shows the effect of varying $B_c(0)$ for different values on the within-host variables (I_m, B_c, T_1, T_2). $B_c(0)$: $B_c(0) = 10$, $B_c(0) = 1,000$, and $B_c(0) = 1,000,000$. The used values are plausible largely because of the scarcity of multiscale empirical data for PTB. We used the multiscale model as an experimental

TABLE 3 Model parameter values used for simulations.

Parameter	Description	Unit	Value (Range explored)	References
Λ_C	Ruminants birth rate	day^{-1}	0.27 [0.14–0.27]	[1, 3]
β_C	Ruminants infection rate	day^{-1}	0.00027 [0.0–0.008]	Assumed
μ_C	Natural death rate of Ruminants	day^{-1}	0.0001 [0.001–0.0001]	[1]
δ_C	Cattle removal rate due to PTB infection	day^{-1}	0.0008 [0.005–0.0008]	[1]
γ_C	Ruminant recovery rate	day^{-1}	0.0014 [0.014–0.0008]	Assumed
α_C	Environmentally bacteria death rate	day^{-1}	0.0018 [0.01–0.0008]	[1]
B_0	Saturation rate of bacteria	day^{-1}	1,000 [0 - 1,000]	[3]
Λ_ϕ	Macrophages supply rate	day^{-1}	10 [8.0–10.0]	[2]
β_ϕ	Macrophages infection rate	day^{-1}	0.002 [0.0–0.01]	[2]
μ_ϕ	Macrophages natural death rate	day^{-1}	0.02 [0.11–0.025]	[2]
N_m	Burst size	day^{-1}	100 [80–100]	[2]
k_m	Burst rate	day^{-1}	0.00075 [0.00–0.0001]	[2]
γ_m	T_1 lytic effect	day^{-1}	0.01 [0.0–0.2]	[2]
μ_c	Bacteria's death rate	day^{-1}	0.03 [0.0–1.0]	[2]
α_c	Excretion rate	day^{-1}	0.01 [0.0–1.0]	[3]
Λ_0	T_0 supply rate	day^{-1}	0.001 [0.00001–0.001]	[2]
μ_0	T_0 death rate	day^{-1}	0.01 [0.1–0.01]	[2]
μ_1	T_1 death rate	day^{-1}	0.03 [0.1–0.01]	[2]
μ_2	T_2 death rate	day^{-1}	0.02 [0.1–0.01]	[2]
δ_m	T_0 differentiation into T_1 cells	day^{-1}	0.01 [0.0–0.1]	[2]
δ_b	T_0 differentiation into T_2 cells	day^{-1}	0.01 [0.0–0.1]	[2]
θ_1	T_1 cells clonal expansion	day^{-1}	9,000 [1.0–10,000]	[2]
θ_2	T_2 cells clonal expansion	day^{-1}	9,000 [1.0–10,000]	[2]

tool to investigate a range of model variables initial inoculum. From the numerical results in Figure 2, we notice that as the initial infective inoculum $B_c(0)$ increases beyond the minimum infectious dose (MID), there is a noticeable but minimal changes in the dynamics of the within-host scale variables I_m, B_c, T_1, T_2. This is because, once the host is infected, the replication of the MAP bacteria at the within-host scale sustains the disease dynamics at this scale.

Figure 2 shows the solution profiles of the population of (Figure 2A) infected macrophage population (I_m), (Figure 2B) within-host MAP bacteria population (B_c), (Figure 2C) MAP-Specific Th1 response cells (T_1), and (Figure 2D) MAP-Specific Th2 response cells for different values of initial inoculum of MAP bacterial load $B_c(0)$: $B_c(0) = 10$, $B_c(0) = 1,000$, and $B_c(0) = 1,000,000$ at within-host scale. The results in Figure 2 illustrate that the variation in the initial inoculum influence the dynamics of the disease at the within-host scale only within a period of 50 days. But, after that the

dynamics of the disease reach an endemic level. Therefore, this implies that different initial inoculum values converge to the same endemic state after a period of about 50 days. Overall, this confirms that once the minimum infectious dose is consumed, the long term disease dynamics is independent of the initial inoculum. And also confirms that as the initial inoculum increases, the time to reach the endemic state also increases.

2.4.2. The influence of within-host scale parameters on the between-host scale PTB infection dynamics

In this subsection, we illustrate through numerical simulations of the full nested multiscale model system (2.4) the influence of within-host scale parameters on between-host scale variables for PTB infection dynamics. We vary the within-host

FIGURE 2
Graphs of numerical solutions of the multiscale model system (2.4) showing changes of **(A)** infected macrophage population (I_m), **(B)** within-host MAP bacteria population (B_c), **(C)** MAP-Specific Th1 response cells (T_1), and **(D)** MAP-Specific Th2 response cells (T_2) for different values of initial value condition of the within-host MAP bacterial load $B_c(0)$: $B_c(0) = 10$, $B_c(0) = 1,000$, and $B_c(0) = 1,000,000$.
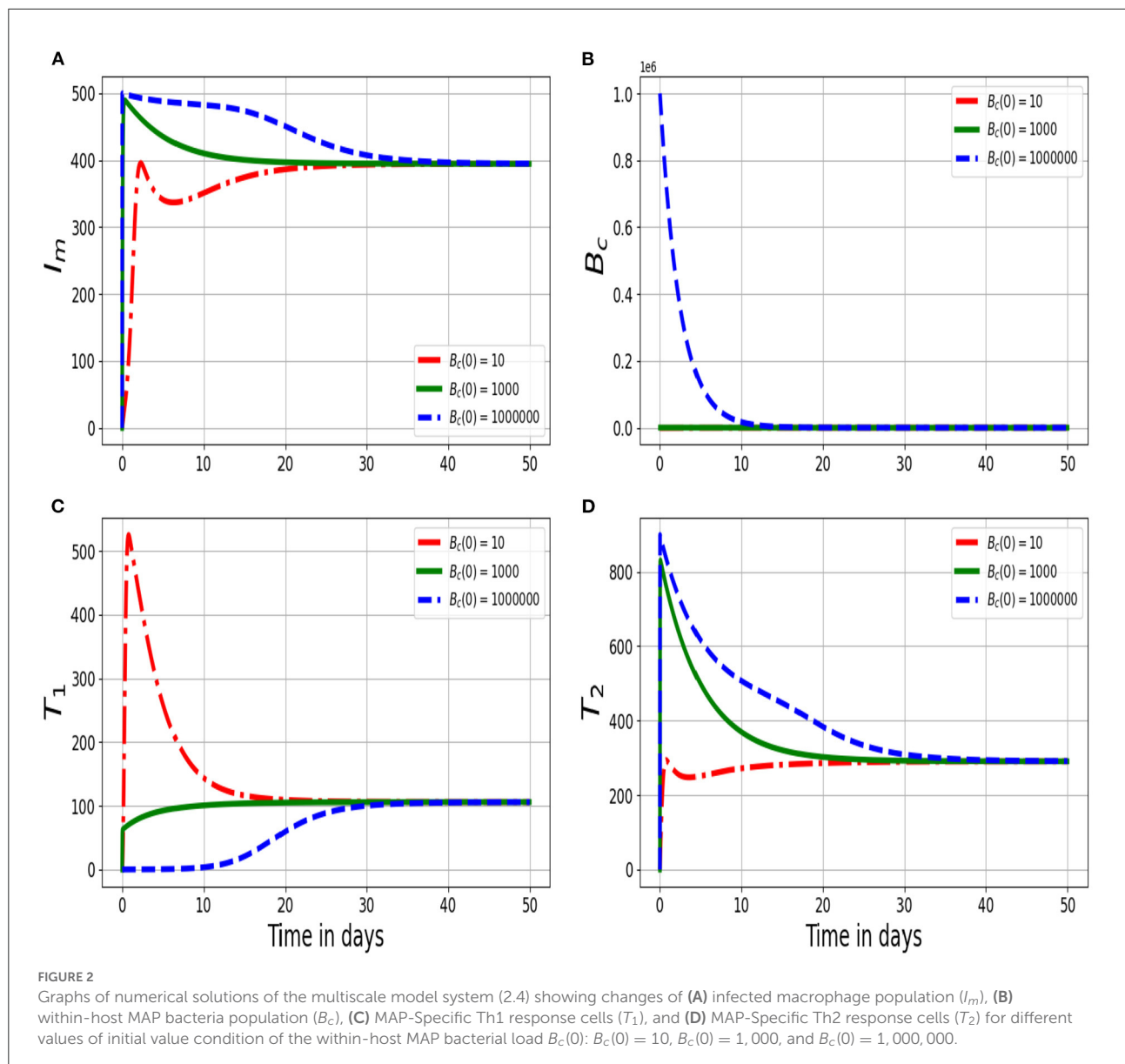
scale parameters, α_c, μ_c, and N_m and assess their impact on the dynamics of the between-host scale variables S_C, I_C, and B_C.

Figure 3 shows graphs of numerical solutions of the model system (2.4) showing dynamics of (Figure 3A) population of susceptible ruminants (S_C), (Figure 3B) population of infected ruminants (I_C), and (Figure 3C) environmental MAP bacteria load (B_C) for different values of excretion rate of the within-host scale MAP bacilli into the environment α_c: $\alpha_c = 0.1$, $\alpha_c = 0.01$, and $\alpha_c = 0.001$. The results show that an increase in the excretion rate of the within-host scale bacterial load into the physical environment by each infected ruminant

individual has important ruminant population health effects at the between-host scale dynamics of PTB infection as there is a noticeable increase in the population of environmental MAP bacteria B_C and the population of infected ruminants I_C as well as a decrease in the population of susceptible ruminants S_C.

Figure 4 shows changes in (Figure 4A) population of susceptible ruminants (S_C), (Figure 4B) population of infected ruminants (I_C), and (Figure 4C) population of environmental MAP bacteria load (B_C) for different values of natural decay rate of the within-host scale MAP bacteria cells: μ_c: $\mu_c = 0.3$, $\mu_c = 0.03$, and $\mu_c = 0.003$. The results in Figure 4 show that as the

FIGURE 3
Graphs of numerical solutions of the multiscale model system (2.4) showing the evolution in time of **(A)** population of susceptible ruminants (S_C), **(B)** population of infected ruminants (I_C), and **(C)** between-host MAP bacterial load (B_C) for different values of excretion rate of the within-host MAP bacterial load into the environment α_c: $\alpha_c = 0.1$, $\alpha_c = 0.01$, and $\alpha_c = 0.001$.

death rate of the within-host scale bacterial load increases, there is also a noticeable reduction in the population of environmental MAP bacteria B_C and the population of infected ruminants I_C as well as an increase in the population of susceptible ruminants S_C at between-host scale. Therefore, development of any treatment measures that target MAP bacteria at within-host scale such as antibiotics [28] are equally good for both the individual ruminant and the population because a single infected ruminant will no longer pose a threat for transmitting infection in the population/herd which consequently reduces the transmission risk of the disease among the ruminants in the population/herd.

Figure 5 shows the dynamics in the (Figure 5A) population of susceptible ruminants (S_C), (Figure 5B) population of infected ruminants (I_C), and (Figure 5C) population of environmental MAP bacterial load (B_C) for different values of within-host scale bursting size of each infected macrophage cell N_m: $N_m = 100$, $N_m = 1,000$, $N_m = 10,000$. The numerical results in Figure 5 show that as the average replication rate of the within-host MAP bacteria within infected macrophage cells at the site of infection increases, transmission of PTB infection at the population/herd level of ruminants also increases. Therefore, these results demonstrate the benefit of treatment that can restrict the replication of MAP bacteria at

FIGURE 4
Graphs of numerical solutions of the multiscale model system(2.4) showing changes in **(A)** population of susceptible ruminants (S_C), **(B)** population of infected ruminants (I_C), and **(C)** population of environmental MAP bacterial load (B_C) for different values of death rate of the within-host MAP bacterial load μ_c: $\mu_c = 0.3$, $\mu_c = 0.03$, and $\mu_c = 0.003$.

individual ruminant level on the transmission of the disease at the population/herd level of ruminants. Collectively, we note from the results in Figures 3–5, that the between-host scale variables (S_C, I_C, B_C) are significantly sensitive to the variation of the three selected within-host scale parameters (α_c, μ_c, and N_m), particularly the decay rate μ_c of the within-host scale MAP bacteria.

Overall, the results in Figures 2–5 show that:

(a) The between-host scale influences the within-host scale through the initial inoculum of the infectious agent.

(b) Once the initial inoculum has been introduced from the between-host scale, then the infection at within-host scale is sustained by pathogen replication.

(c) As the initial inoculum acquired from the between-host scale increases beyond the MID, the time taken for the infection at within-host scale to reach equilibrium increases.

(d) The between-host scale variables (S_C, I_C, B_C) are significantly sensitive to the variation of the three selected within-host scale parameters (α_c, μ_c, and N_m), particularly the decay rate μ_c of the within-host scale MAP bacteria.
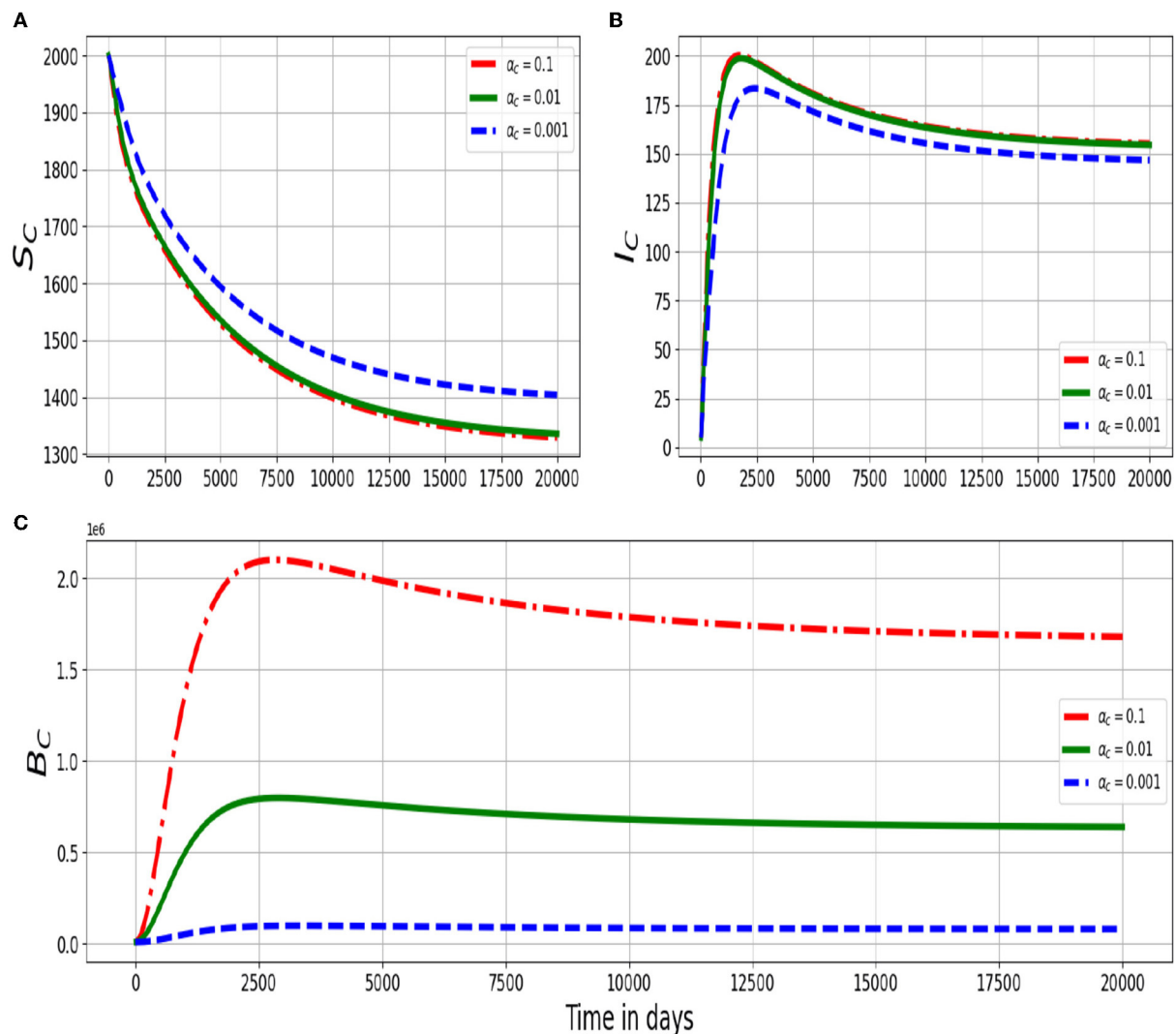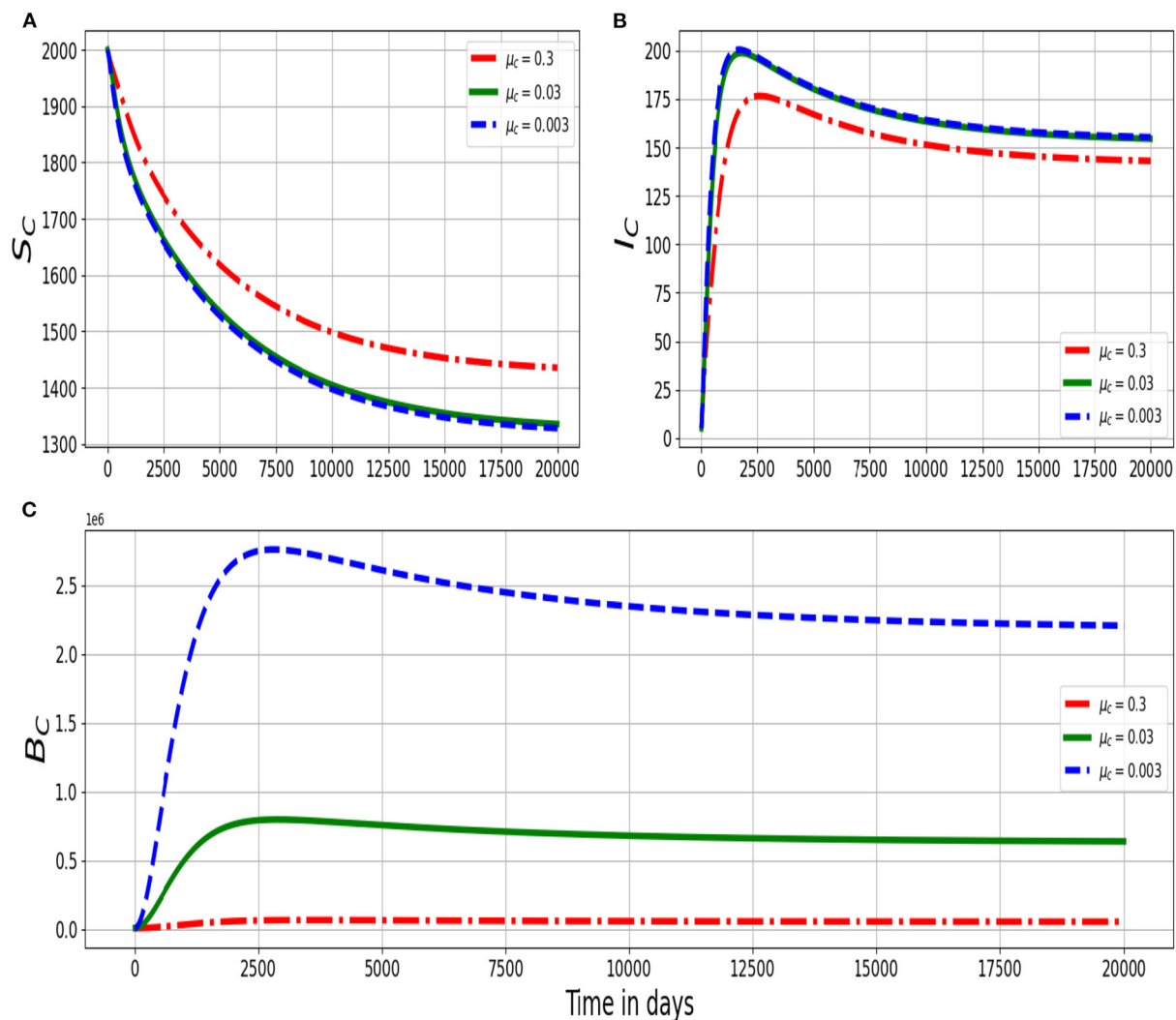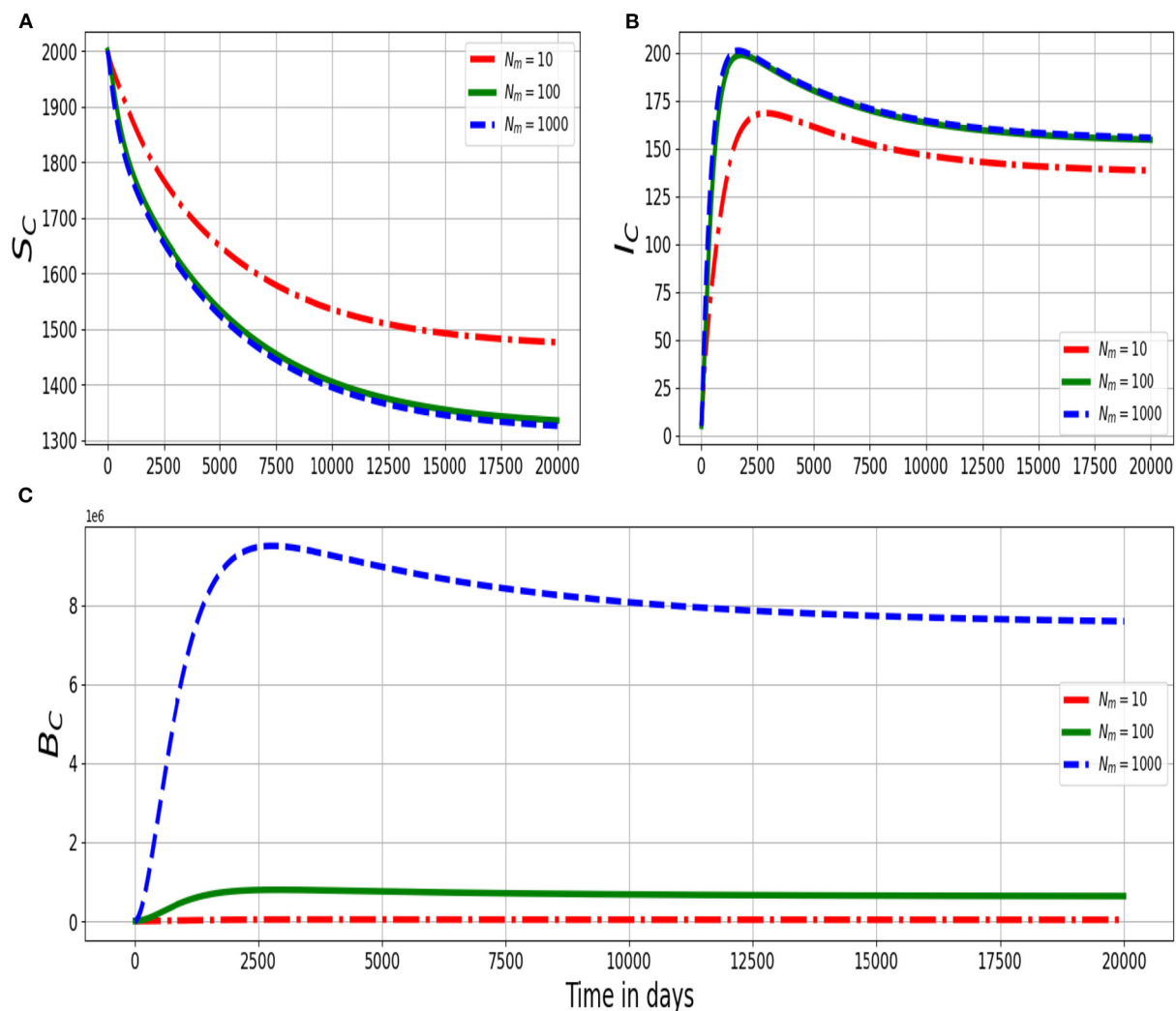
FIGURE 5
Graphs of numerical solutions of the multiscale model system (2.4) showing dynamics in **(A)** population of susceptible ruminants (S_C), **(B)** population of infected ruminants (I_C), and **(C)** population of environmental MAP bacterial load (B_C) for different values of within-host scale MAP bacteria produced per bursting infected macrophage cell N_m: $N_m = 100$, $N_m = 1,000$, $N_m = 10,000$.

This indeed indicates that during the dynamics for PTB infection in ruminants once the infection has successfully established at the within-host scale, the contribution of initial infective inoculum to the total pathogen load becomes negligible compared to the contribution of the replication of the pathogen. Further, the results in Figures 3–5 seem to have a threshold effect. This is because there no significant differences between S_C and I_C for low values of α, μ, and N_m and yet these quantities are significantly different for higher values of these parameters. It may be just the values of parameters used, but further work to be reported elsewhere will investigate this as it could be utilized for control measures.

3. Estimation of $\widehat{N_c}$ from the full nested multiscale model

In this section, we estimate $\widehat{N_c}$ parameter in the single scale model for the dynamics of PTB infection using the nested multiscale model system (2.4). This is achieved by assuming that $0 < \epsilon \ll 1$, so that to reasonable approximation we can set $\epsilon = 0$ in the full nested multiscale model system (2.4). Thus, we consider the last six equations of the PTB full nested multiscale model system (2.4) re-written here as a quick reference

$$\begin{cases} i. \ \epsilon \dfrac{dM_\phi(t)}{dt} &= \Lambda_\phi - \beta_\phi M_\phi(t)B_c(t) - \mu_\phi M_\phi(t), \\ ii. \ \epsilon \dfrac{dI_m(t)}{dt} &= \beta_\phi M_\phi(t)B_c(t) - \gamma_m T_1(t)I_m(t) - (k_m + \mu_\phi)I_m(t), \\ iii. \ \epsilon \dfrac{dB_c(t)}{dt} &= N_m k_m I_m(t) - (\mu_c + \alpha_c)B_c(t), \\ iv. \ \epsilon \dfrac{dT_0(t)}{dt} &= \Lambda_0 - (\delta_m I_m(t) + \delta_b B_c(t))T_0(t) - \mu_0 T_0(t), \\ v. \ \epsilon \dfrac{dT_1(t)}{dt} &= \theta_1 \delta_m I_m(\tau)T_0(\tau) - \mu_1 T_1(t), \\ vi. \ \epsilon \dfrac{dT_2(t)}{dt} &= \theta_2 \delta_b B_c(t)T_0(t) - \mu_2 T_2(t). \end{cases} \quad (3.5)$$

Since $0 < \epsilon << 1$, we can set ϵ to zero so that the within-host scale PTB replication dynamics submodel becomes independent of time and we obtain:

$$\begin{cases} i. \quad \Lambda_\phi - \beta_\phi M_\phi^* B_c^* - \mu_\phi M_\phi^* = 0, \\ ii. \quad \beta_\phi M_\phi^* B_c^* - \gamma_m T_1^* I_m^* - (k_m + \mu_\phi)I_m^* = 0, \\ iii. \quad N_m k_m I_m^* - (\mu_c + \alpha_c)B_c^* = 0, \\ iv. \quad \Lambda_0 - (\delta_m I_m^* + \delta_b B_c^*)T_0^* - \mu_0 T_0^* = 0, \\ v. \quad \theta_1 \delta_m I_m^* T_0^* - \mu_1 T_1^* = 0, \\ vi. \quad \theta_2 \delta_b B_c^* T_0^* - \mu_2 T_2^* = 0. \end{cases} \quad (3.6)$$

From (3.6) we get

$$\begin{cases} i. \ M_\phi^* &= \dfrac{2\Lambda_\phi(\mu_c + \alpha_c)}{\beta_\phi N_m k_m M + 2\mu_\phi(\mu_c + \alpha_c)}, \\ ii. \ I_m^* &= \dfrac{M}{2}, \\ iii. \ B_c^* &= \dfrac{N_m k_m M}{2(\mu_c + \alpha_c)}, \\ iv. \ T_0^* &= \dfrac{2\Lambda_0(\mu_c + \alpha_c)}{2\mu_0(\mu_c + \alpha_c) + [\delta_m(\mu_c + \alpha_c) + \delta_b N_m k_m]M}, \\ v. \ T_1^* &= \dfrac{\theta_1 \delta_m \Lambda_0(\mu_c + \alpha_c)M}{2\mu_0\mu_1(\mu_c + \alpha_c) + \mu_1[\delta_m(\mu_c + \alpha_c) + \delta_b N_m k_m]M}, \\ vi. \ T_1^* &= \dfrac{\theta_2 \delta_b \Lambda_0 N_m k_m M}{2\mu_2\mu_0(\mu_c + \alpha_c) + \mu_2[\delta_m(\mu_c + \alpha_c) + \delta_b N_m k_m]M}. \end{cases} \quad (3.7)$$

In the expression (3.7),

$$\begin{cases} M &= -\phi_1 + \sqrt{\phi_1^2 + 4\phi_2} \\ \phi_1 &= \dfrac{k_3 + \mu_1\mu_0 k_2 - k_1 Q}{k_2 k_1}, \\ \phi_2 &= \dfrac{\mu_1\mu_0 Q}{k_2 k_1}, \end{cases} \quad (3.8)$$

with

$$\begin{cases} Q &= \mu_\phi(\mu_\phi + \delta_\phi)(R_{0_W} - 1), \\ k_1 &= \dfrac{\mu_1\delta_m(\mu_c + \alpha_c) + \mu_1\delta_b N_m k_m}{(\mu_c + \alpha_c)}, \\ k_2 &= \dfrac{\beta_\phi N_m k_m(\mu_\phi + k_m)}{(\mu_c + \alpha_c)}, \\ k_3 &= k_0 + \mu_\phi\gamma_m\theta_1\delta_m\Lambda_0, \\ k_0 &= \dfrac{\beta_\phi N_m k_m\gamma_m\theta_1\delta_m\Lambda_0}{(\mu_c + \alpha_c)}, \\ R_{0_W} &= \dfrac{\beta_\phi \Lambda_\phi N_m k_m}{\mu_\phi(\mu_\phi + k_m)(\mu_c + \alpha_c)}. \end{cases} \quad (3.9)$$

Further, in the expression (3.9) the quantity

$$R_{0_W} = \frac{\beta_\phi \Lambda_\phi N_m k_m}{\mu_\phi(\mu_\phi + \delta_\phi)(\mu_c + \alpha_c)},$$

is the within-host scale basic reproductive number. Therefore, the fast-slow analysis reduces the within-host scale submodel system (2.2) to the algebraic equations given in (3.7) which can be fed into the parameters of the between-host scale submodel and become

$$\begin{cases} i. \ \dfrac{dS_C(t)}{dt} &= \Lambda_C - \dfrac{\beta_C B_C(t)}{B_0 + B_C(t)}S_C(t) - \mu_C S_C(t) + \gamma_C I_C(t), \\ ii. \ \dfrac{dI_C(t)}{dt} &= \dfrac{\beta_C B_C(t)}{B_0 + B_C(t)}S_C(t) - (\mu_C + \delta_C + \gamma_C)I_C(t), \\ iii. \ \dfrac{dB_C(t)}{dt} &= \alpha_c B_c^* I_C(t) - \alpha_C B_C(t). \end{cases} \quad (3.10)$$

We note that from the model system given by (3.10) that the total number of extracellular MAP bacilli excreted by each infected ruminant into the physical environment $B_c I_C$ is now approximated by $B_c^* I_C$. Using the notation that $\widehat{N_c} = B_c^*$, a composite parameter which can be interpreted as the average number of the within-host scale MAP bacterial load (B_c) at the endemic equilibrium that is available for excretion into the environment by each infected ruminant, the full multiscale model (2.4) of PTB transmission dynamics is simplified to become

$$\begin{cases} i. \ \dfrac{dS_C(t)}{dt} &= \Lambda_C - \dfrac{\beta_C B_C(t)}{B_0 + B_C(t)}S_C(t) - \mu_C S_C(t) + \gamma_C I_C(t), \\ ii. \ \dfrac{dI_C(t)}{dt} &= \dfrac{\beta_C B_C(t)}{B_0 + B_C(t)}S_C(t) - (\mu_C + \delta_C + \gamma_C)I_C(t), \\ iii. \ \dfrac{dB_C(t)}{dt} &= N_c\alpha_c I_C(t) - \alpha_C B_C(t) \end{cases} \quad (3.11)$$

where the composite parameter N_c which estimates $\widehat{N_c}$ is given by

$$N_c = \frac{N_m k_m}{2(\mu_c + \alpha_c)}\left[-\phi_1 + \sqrt{\phi_1^2 + 4\phi_2}\right]. \qquad (3.12)$$

In the expression for N_c given by equation (3.12), the expressions ϕ_1 and ϕ_2 are defined by (3.8) and (3.9). Based on the categorization of the multiscale models of infectious disease systems in [15, 16], the multiscale model system given by (3.11) is a nested multiscale model of class 3. After estimating N_c as well as establishing the simplified nested multiscale model system given by (3.11), we now analyze the behavior of this nested multiscale model system (3.11). In the next section, we present some results from mathematical analysis and numerical simulations of the behavior of the simplified nested multiscale model (3.11).

4. Mathematical analysis of the simplified nested multiscale model for PTB infection in ruminants

The PTB dynamics multiscale model system (3.11) can be analyzed in a region $\Gamma \subset \mathbb{R}_+^3$ of biological interest, which is given by

$$\begin{aligned}\Gamma = \{(S_C; I_C; B_C) \in \mathbb{R}_+^3 : \\ 0 \le S_C + I_C \le S_1, \; 0 \le B_C \le S_2\}\end{aligned} \qquad (4.13)$$

where the constant S_1 and S_2 are such that

$$\begin{cases} S_1 = \dfrac{\Lambda_C}{\mu_C}, \\[2mm] S_2 = \dfrac{N_c \alpha_c \Lambda_C}{\alpha_C \mu_C}. \end{cases} \qquad (4.14)$$

It can be easily shown that all solutions for the simplified multiscale model system (3.11) with positive initial conditions remain bounded within the invariant region Γ given by (4.13). Therefore, it is sufficient to consider the dynamics of the flow generated by the simplified nested model system (3.11) in Γ.

In the following three subsections, we evaluate global stability of both the disease-free and endemic equilibrium states for the PTB dynamics multiscale model system (3.11) as well as evaluating sensitivity of the two main between-host transmission metrics which are the basic reproductive number (R_0) and the endemic value of the nested multiscale model (3.11) MAP bacteria (B_C^*).

4.1. Disease-free equilibrium and reproductive number of the simplified nested multiscale model

The disease-free equilibrium of the nested multiscale model system (3.11) was obtained by setting the left-hand side of the model to zero and further assume that $I_C = B_C = 0$ to get

$$\widehat{E}_0 = (X^*, 0) = \left(\frac{\Lambda_C}{\mu_C}, 0, 0\right), \qquad (4.15)$$

where $\widehat{E}_0$ denotes the disease-free equilibrium of the simplified nested multiscale model system (3.11).

4.1.1. Derivation of the reproductive number of the simplified multiscale model

The basic reproduction number denoted by R_0, is a threshold value that is often used as a public health measure to determine whether a disease will persist or die out. In this study, we computed the basic reproductive number of the simplified multiscale model system (3.11) by using the next generation operator approach in [26] to obtain

$$R_0 = \frac{\beta_C \Lambda_C N_c \alpha_c}{\mu_C(\mu_C + \delta_C + \gamma_C)B_0\alpha_C}. \qquad (4.16)$$

Details of the derivation of the basic reproductive number given by expression (4.16) are given in Appendix A. This expression of the basic reproductive number can be re-written as

$$R_0 = R_{0_a} R_{0_b} \qquad (4.17)$$

where the quantity R_{0_a} is explained as follows:

a. Consider a single newly infected ruminant entering a contaminated-free environment at an equilibrium point. The expected number of bacteria cells produced by this ruminant and contaminate the environment is approximately

$$R_{0_a} = \frac{N_c \alpha_c}{\mu_C(\mu_C + \delta_C + \gamma_C)}. \qquad (4.18)$$

From the expression (4.18) we deduce that the quantity R_{0_a} depends on the average MAP bacterial load within an infected ruminant N_c which is excreted into the physical environment at a rate α_c, where it becomes infectious to other ruminants during feeding from contaminated food or water with MAP bacterial load. In this study, we consider N_c as a composite parameter which is interpreted as the endemic value of the within-host scale MAP bacterial load B_c^* which we have already determined from the within-host PTB disease dynamics sub-model as given in equation (3.12). Therefore, the

quantity R_{0_a} quantifies how much an infected ruminant can contribute to the spread of the disease in the herd during its entire period of infectiousness, with $1/(\mu_C + \delta_C + \gamma_C)$ describes the average life span of an infected ruminant.

b. Similarly, consider a newly bacterial infectious dose of MAP bacilli cells entering a disease-free population of a ruminant population at an equilibrium point. The expected number of ruminants infected by this dose of bacteria cells is approximately

$$R_{0_b} = \frac{\beta_C \Lambda_C}{\alpha_C B_0}. \tag{4.19}$$

We can also deduce that the quantity R_{0_b} in (4.19) depends on the supply rate of susceptible ruminants Λ_C, the rate at which susceptible ruminants contract MAP bacteria in the physical environment domains during feeding β_C, the average life span of each susceptible ruminant host $1/\mu_C$, the average life span of MAP bacteria load in the physical environment domains and the susceptibility coefficient to PTB infection in the ruminant community/herd, where B_0 is the bacterial load that results in 50% chance of ruminants being infected.

Collectively, based on the two expressions R_{0_a} and R_{0_b}, we conclude that the epidemiological (between-host scale) transmission parameters and the immunological (within-host scale) parameters all contribute to the transmission of ruminant paratuberculosis disease.

4.1.2. Global stability of the disease-free equilibrium

In this subsection, we determine the global stability of DFE of the simplified multiscale model system (3.11) by further using a next generation operator [26]. Thus the model system (3.11) can be re-written in the form

$$\begin{cases} \dfrac{dX}{dt} = F(X, Z), \\[2mm] \dfrac{dZ}{dt} = G(X, Z), \end{cases} \tag{4.20}$$

where

- $X = S_C$ represents a compartment of uninfected ruminants, and
- $Z = (I_C, B_C)$ represents compartments of infected ruminants and Infective MAP bacteria in the physical environment.

We let

$$E_0 = (X^*, 0) = \left(\frac{\Lambda_C}{\mu_C}, 0, 0 \right), \tag{4.21}$$

denote the disease-free equilibrium (DFE) of the model system (3.11). For X^* to be globally asymptotically stable, the following conditions (H1) and (H2) must be satisfied.

H1. $\dfrac{dX}{dt} = F(X, 0)$ is globally asymptotically stable (GAS),

H2. $G(X, Z) = AZ - \hat{G}(X, Z)$, $\hat{G}((X, Z) \geq 0$ for $(X, Z) \in \mathbb{R}^3_+$ where $A = D_Z G(X^*, 0)$ is an M-matrix and $\mathbb{R}^3_+$ is the region where the model makes biological sense.

In this case,

$$F(X, 0) = \left[\Lambda_C - \mu_C S_C \right], \tag{4.22}$$

and the matrix A is given by

$$A = \begin{bmatrix} -(\mu_C + \delta_C + \gamma_C) & \dfrac{\beta_C \Lambda_C}{\mu_C B_0} \\[3mm] N_c \alpha_c & -\alpha_C \end{bmatrix} \tag{4.23}$$

and

$$\hat{G}(X, Z) = \begin{bmatrix} \left(\dfrac{\Lambda_C}{\mu_C B_0} - \dfrac{S_C}{B_0 + B_C} \right) \beta_C B_C \\[3mm] 0 \end{bmatrix}. \tag{4.24}$$

Since $S_C^0 = \dfrac{\Lambda_C}{\mu_C B_0} \geq \dfrac{S_C}{B_0 + B_C}$, it is clear that $\hat{G}(X, Z) \geq 0$ for all $(X, Z) \in \mathbb{R}^3_+$. It is also clear that A is a M-matrix, since the off diagonal elements of A are non-negative.

We state a theorem which summarizes the above results:

Theorem 1. *The fixed point*

$$E_0 = (X^*, 0) = \left(\frac{\Lambda_C}{\mu_C}, 0, 0 \right)$$

of the multiscale model system (3.11) is globally asymptotically stable (GAS) if $R_0 \leq 1$ and the assumptions (H1) and (H2) are satisfied.

4.2. Endemic equilibrium and its global stability

In the subsection, we determine the endemic equilibrium state of the simplified nested multiscale model system (3.11)

by setting the left-hand side of the simplified nested multiscale model system (3.11) to zero but assuming that I_C and B_C are non-zero, so that

$$E^* = \left(S_C^*, I_C^*, B_C^*\right) \qquad (4.25)$$

where

$$
\begin{cases}
S_C^* = \dfrac{\Lambda_C[(\mu_C + \delta_C + \gamma_C)R_0 + \beta_C(\delta_C + \mu_C)]}{\mu_C[(\beta_C + \mu_C)(\mu_C + \delta_C) + \mu_C\gamma_C]R_0}, \\[2mm]
I_C^* = \dfrac{\beta_C \Lambda_C[R_0 - 1]}{(\mu_C + \delta_C + \gamma_C)(\beta_C + \mu_C)R_0}, \\[2mm]
B_C^* = \dfrac{\mu_C(\mu_C + \delta_C + \gamma_C)[R_0 - 1]}{(\beta_C + \mu_C)(\mu_C + \delta_C) + \mu_C\gamma_C}, \\[2mm]
R_0 = \dfrac{\beta_C \Lambda_C N_c \alpha_c}{\mu_C(\mu_C + \delta_C + \gamma_C)B_0 \alpha_C}.
\end{cases}
\qquad (4.26)
$$

We deduce that only a single positive endemic equilibrium point exists whenever $R_0 > 1$. To this effect, we conclude that there exists only one unique endemic equilibrium point for model system (3.11) whenever $R_0 > 1$. We can then further determine the global stability of the endemic equilibrium for the simplified multiscale model system (3.11) since we have established the existence of E^* without providing any information about its stability. The global stability of the endemic equilibrium E^* of the multiscale model system (3.11) is summarized in the following theorem:

Theorem 2. *The Endemic Equilibrium E^* of the model system (3.11) is global asymptotically stable (GAS) whenever $R_0 > 1$.*

Proof: Let's consider a Volterra-type Lyapunov function given by

$$
\begin{aligned}
L_1 &= L(S_C, I_C, B_C), \\
&= S_C^* g\left(\frac{S_C}{S_C^*}\right) + I_C^* g\left(\frac{I_C}{I_C^*}\right) + \frac{\lambda_C^* S_C^*}{N_c \alpha_c I_C^*} B_C^* g\left(\frac{B_C}{B_C^*}\right),
\end{aligned}
\qquad (4.27)
$$

and further taking advantage of the properties of the function

$$g(x) = x - 1 - \ln(x) \qquad (4.28)$$

which is positive in $(0, \infty)$ except at x = 1 where it vanishes. We note that L_1 is non-negative in the interior of Γ and attain zero at E^*. We now need to show that $\dot{L}_1$ is negative definite. Differentiating L_1 along the trajectories of the model system (2.1), we obtain

$$
\begin{aligned}
\dot{L}_1 &= \frac{dS_C}{dt}\left[1 - \frac{S_C^*}{S_C}\right] + \frac{dI_C}{dt}\left[1 - \frac{I_C^*}{I_C}\right] + \frac{\lambda_C^* S_C^*}{N_c \alpha_c I_C^*}\frac{dB_C}{dt}\left[1 - \frac{B_C^*}{B_C}\right], \\
&= \left[1 - \frac{S_C^*}{S_C}\right][\Lambda_C - \lambda_C S_C - \mu_C S_C + \gamma_C I_C] \\
&\quad + \left[1 - \frac{I_C^*}{I_C}\right][\lambda_C S_C - (\mu_C + \delta_C + \gamma_C)I_C] \\
&\quad + \frac{\lambda_C^* S_C^*}{N_c \alpha_c I_C^*}\left[1 - \frac{B_C^*}{B_C}\right][N_c \alpha_c I_C - \alpha_C B_C].
\end{aligned}
\qquad (4.29)
$$

Since E^* is an equilibrium point, the following relations hold

$$
\begin{cases}
\Lambda_C = \lambda_C^* S_C^* + \mu_C S_C^*, \quad (\mu_C + \delta_C + \gamma_C) = \dfrac{\lambda_C^* S_C^*}{I_C^*}, \\[3mm]
\alpha_C = \dfrac{N_c \alpha_c I_C^*}{B_C^*}.
\end{cases}
\qquad (4.30)
$$

Using the relations in (4.30), $\dot{L}_1$ becomes

$$
\begin{aligned}
\dot{L}_1 &= \left[1 - \frac{S_C^*}{S_C}\right][\lambda_C^* S_C^* + \mu_C S_C^* - \lambda_C S_C - \mu_C S_C + \gamma_C I_C \\
&\quad - \gamma_C I_C^*] + \left[1 - \frac{I_C^*}{I_C}\right]\left[\lambda_C S_C - \frac{\lambda_C^* S_C^* I_C}{I_C^*}\right] \\
&\quad + \frac{\lambda_C^* S_C^*}{N_c \alpha_c I_C^*}\left[1 - \frac{B_C^*}{B_C}\right]\left[N_c \alpha_c I_C - \frac{N_c \alpha_c I_C^* B_C}{B_C^*}\right].
\end{aligned}
\qquad (4.31)
$$

By direct calculations from equation (4.31), we have that the first term at the right hand side of Equation (4.31) is as follows

$$
\begin{aligned}
&\left[1 - \frac{S_C^*}{S_C}\right][\lambda_C^* S_C^* + \mu_C S_C^* - \lambda_C S_C - \mu_C S_C + \gamma_C I_C - \gamma_C I_C^*] \\
&= \left[1 - \frac{S_C^*}{S_C}\right]\left(\lambda_C^* S_C^* - \lambda_C S_C\right) \\
&\quad + \left[1 - \frac{S_C^*}{S_C}\right]\left(\mu_C S_C^* - \mu_C S_C\right) + \left[1 - \frac{S_C^*}{S_C}\right]\left(\gamma_C I_C - \gamma_C I_C^*\right) \\
&= -\mu_C\left[1 - \frac{S_C^*}{S_C}\right]^2
\end{aligned}
\qquad (4.32)
$$

$$
\begin{aligned}
&- \gamma_C\left[1 - \frac{S_C^*}{S_C}\right]\left[1 - \frac{I_C}{I_C^*}\right] + \lambda_C^* S_C^*\left[1 - \frac{S_C^*}{S_C}\right]\left[1 - \frac{\lambda_C S_C}{\lambda_C^* S_C^*}\right] \\
&\leq \lambda_C^* S_C^*\left[1 - \frac{S_C^*}{S_C}\right]\left[1 - \frac{\lambda_C S_C}{\lambda_C^* S_C^*}\right].
\end{aligned}
$$

The second term at the right hand side of Equation (4.31) is

$$
\begin{aligned}
&\left[1 - \frac{I_C^*}{I_C}\right]\left[\lambda_C S_C - \frac{\lambda_C^* S_C^* I_C}{I_C^*}\right] \\
&= \lambda_C^* S_C^*\left[1 - \frac{I_C^*}{I_C}\right]\left[\frac{\lambda_C S_C}{\lambda_C^* S_C^*} - \frac{I_C}{I_C^*}\right],
\end{aligned}
\qquad (4.33)
$$

and the third term at the right hand side of Equation (4.31) is as follows

$$
\begin{aligned}
&\frac{\lambda_C^* S_C^*}{N_c \alpha_c I_C^*}\left[1 - \frac{B_C^*}{B_C}\right]\left[N_c \alpha_c I_C - \frac{N_c \alpha_c I_C^* B_C}{B_C^*}\right] \\
&= \lambda_C^* S_C^*\left[1 - \frac{B_C^*}{B_C}\right]\left[\frac{I_C}{I_C^*} - \frac{B_C}{B_C^*}\right].
\end{aligned}
\qquad (4.34)
$$

Therefore,

$$
\begin{aligned}
\dot{L}_1 \leq\ & \lambda_C^* S_C^* \left[1 - \frac{S_C^*}{S_C} \right] \left[1 - \frac{\lambda_C S_C}{\lambda_C^* S_C^*} \right] \\
& + \lambda_C^* S_C^* \left[1 - \frac{I_C^*}{I_C} \right] \left[\frac{\lambda_C S_C}{\lambda_C^* S_C^*} - \frac{I_C}{I_C^*} \right] \\
& + \lambda_C^* S_C^* \left[1 - \frac{B_C^*}{B_C} \right] \left[\frac{I_C}{I_C^*} - \frac{B_C}{B_C^*} \right], \quad (4.35) \\
\leq\ & \lambda_C^* S_C^* \left[2 - \frac{\lambda_C S_C I_C^*}{\lambda_C^* S_C^* I_C} + \frac{\lambda_C}{\lambda_C^*} - \frac{S_C^*}{S_C} - \frac{I_C}{I_C^*} \right] \\
& + \lambda_C^* S_C^* \left[1 - \frac{I_C B_C^*}{I_C^* B_C} + \frac{I_C}{I_C^*} - \frac{B_C}{B_C^*} \right]
\end{aligned}
$$

By using the function $g(x)$ defined in (4.28), we get

$$
\begin{aligned}
\dot{L}_1 \leq\ & \lambda_C^* S_C^* \left[-g\left(\frac{S_C^*}{S_C} \right) - g\left(\frac{\lambda_C S_C I_C^*}{\lambda_C^* S_C^* I_C} \right) + \frac{\lambda_C}{\lambda_C^*} - \ln\left(\frac{B_C}{B_C^*} \right) \right. \\
& \left. - \frac{I_C}{I_C^*} + \ln\left(\frac{I_C}{I_C^*} \right) + \ln\left(\frac{B_0 + B_C}{B_0 + B_C^*} \right) \right] \\
& + \lambda_C^* S_C^* \left[-g\left(\frac{I_C B_C^*}{I_C^* B_C} \right) - \ln\left(\frac{I_C}{I_C^*} \right) + \frac{I_C}{I_C^*} + \ln\left(\frac{B_C}{B_C^*} \right) - \frac{B_C}{B_C^*} \right], \\
\leq\ & \lambda_C^* S_C^* \left[-g\left(\frac{S_C^*}{S_C} \right) - g\left(\frac{\lambda_C S_C I_C^*}{\lambda_C^* S_C^* I_C} \right) + \frac{B_C}{B_C^*} - \ln\left(\frac{B_C}{B_C^*} \right) - \frac{I_C}{I_C^*} \right. \\
& \left. + \ln\left(\frac{I_C}{I_C^*} \right) \right] \quad (4.36) \\
& + \lambda_C^* S_C^* \left[\frac{B_C(B_0 + B_C^*)}{B_C^*(B_0 + B_C)} - \frac{B_0 + B_C}{B_0 + B_C^*} - g\left(\frac{B_0 + B_C}{B_0 + B_C^*} \right) - \frac{B_C}{B_C^*} - 1 \right] \\
& + \lambda_C^* S_C^* \left[-g\left(\frac{I_C B_C^*}{I_C^* B_C} \right) - \ln\left(\frac{I_C}{I_C^*} \right) + \frac{I_C}{I_C^*} + \ln\left(\frac{B_C}{B_C^*} \right) - \frac{B_C}{B_C^*} \right], \\
\leq\ & \lambda_C^* S_C^* \left[\frac{B_C}{B_C^*} - \ln\left(\frac{B_C}{B_C^*} \right) - \frac{I_C}{I_C^*} + \ln\left(\frac{I_C}{I_C^*} \right) \right] \\
& + \lambda_C^* S_C^* \left[\frac{I_C}{I_C^*} - \ln\left(\frac{I_C}{I_C^*} \right) + \ln\left(\frac{B_C}{B_C^*} \right) - \frac{B_C}{B_C^*} \right] = 0
\end{aligned}
$$

From (4.36), we have that the largest invariant subset, where $\dot{L}_1 = 0$, is E^*. Therefore, we conclude from the LaSelle's Invariance Principle that E^* is globally asymptotically stable (*GAS*) when $R_0 > 1$.

4.3. Sensitivity analysis

In this sub-section, we conduct a sensitivity analysis of the two PTB transmission metrics derived from the simplified nested multiscale model given by (3.11) to the parameters of the model variation. As mentioned previously, the two PTB transmission metrics derived from the baseline PTB multiscale model system (3.11) are: the reproductive number, R_0, which generally describes the dynamics of a disease at the beginning of an infection and the endemic value of the environmental bacteria load, B_C^*, which generally describes the dynamics of a disease at the endemic level. For any epidemic model that describes the dynamics of any diseases in a population, a sensitivity analysis study is an essential to perform as it helps to identify model's parameters which can be targeted for disease control, elimination, or even eradication, and also be monitored and controlled during an

outbreak of the disease. In this case, sensitivity analysis of both the PTB multiscale transmission metrics (R_0 and B_C^*), with respect to the variation of the baseline PTB multiscale model system (3.11)'s parameters is conducted using Latin Hypercube Sampling and partial rank correlation coefficients (PRCCs). We used 1,000 simulations per run to investigate the impact of each model parameter on both the basic reproduction numbers (R_0) and the endemic value of the environmental bacteria load (B_C^*). The sensitivity results of R_0 and B_C^* to the model parameters are given in the Tornado plots, Figures 6, 7, respectively.

Figures 6, 7 show the results of the evaluation of the sensitivity of the two PTB transmission metrics derived from the PTB simplified multiscale model (3.11) which are the basic reproductive number R_0 and the value of MAP environmental bacteria at the endemic level B_C^*. From the sensitivity analysis results of both R_0 and B_C^* to baseline PTB multiscale model (3.11)'s parameters in Figures 6, 7, we deduce that some of the baseline PTB multiscale model (3.11)'s parameters have positive PRCCs and some have negative PRCCs. This indicates that, parameters with positive PRCCs will increase the value of both R_0 and B_C^* when they are increased, while parameters with negative PRCCs will decrease the value of R_0 and B_C^* when they are increased. For instance, increasing a parameter like bacteria transmission rate β_C at the between-host scale eventually increases the value of R_0 and B_C^*, and also increasing parameters like μ_c will lead to a reduction in the value of both R_0 and B_C^*. Therefore, since R_0 characterizes transmission of PTB infection at the start of the epidemic while B_C^* characterizes transmission of PTB when the disease is now endemic in a herd, we make the following conclusions regarding the sensitivity of both R_0 and B_C^*:

(a) On one hand, the PTB transmission metric R_0 is highly sensitive to the variation of the within-host scale parameters of the multiscale model system (3.11), in particular to the three within-host scale parameters (μ_c, N_m, β_ϕ). From the results of the sensitivity analysis of R_0, we can easily notice that the influence of the between-host scale parameters on the changes of R_0 is negligible.

(b) On the other hand, the PTB transmission metric B_C^* is highly sensitive to the variation of two of the between-host scale parameters (β_C, γ_C) and only one within-host scale parameter (μ_c) of the multiscale model system (3.11).

Overall, since R_0 describes the dynamics of the disease at the start of the infection, this means that at the start of PTB, pharmaceutical interventions such as drugs that target the killing of the within-host bacteria as well as restricting the replication of bacteria within an infected macrophage cells are required to be highly considered as they are likely to have the highest benefits in reducing the transmission of PTB among ruminants in the herd. Moreover, since B_C^* describes the dynamics of the disease when it
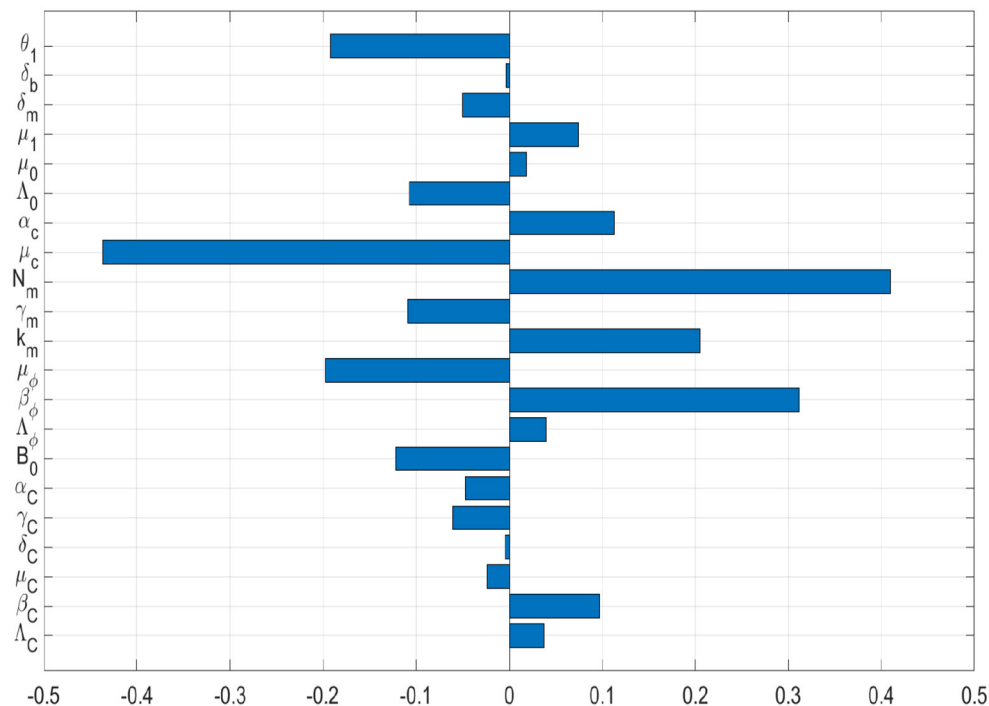
FIGURE 6
Tornado plot of partial rank correlation coefficients (PRCCs) of the model parameters that influence the PTB transmission metric R_0.

has already reached an endemic level when PTB is at the endemic level, this means that the combination of non-pharmaceutical interventions such as environmental hygiene management that reduces the risk of a ruminant to interact with environmental MAP bacterial cells in the environment and the pharmaceutical interventions such as drugs that target the killing of the within-host bacteria need to be highly considered as they are likely to have the highest benefits in reducing the transmission of PTB among ruminants in the herd.

5. Discussion and conclusions

Paratuberculosis disease in ruminants, like other environmentally transmitted diseases which threaten our food security urgently needs renewed attention and sustainable interventions. Paratuberculosis infection has been and continues to be a public health concern in ruminants, impacting on the development of many ruminant industries, especially those that are in the developing world. More efforts have been put in place in order to completely eradicate this disease, yet few countries in the developing world are on track to eliminate PTB. However, some countries in the developing world, particularly EU countries have nearly eliminated PTB [27]. To date, many mathematical models have been developed

and used as an important tool for studying the dynamics of a number of infectious diseases. Some of these mathematical models have further been used to evaluate the effectiveness of various intervention strategies intended to control, eliminate, or even eradicate most of these infectious diseases including environmental transmitted diseases. However, the major innovation in this paper to scientific knowledge is the use of a nested multiscale model to investigate if the initial infective inoculum increases beyond the minimum infectious dose (MID) has an impact on the dynamics of an infectious disease system in which the pathogen replication-cycle occurs only at the microscale. The numerical results in this study demonstrate that once the minimum infectious dose is consumed, then the infection at the within-host scale is sustained by pathogen replication. These results also show that as the initial inoculum increases, the time to reach the endemic state also increases at this scale domain. From these results it seems likely super-infection (i.e., repeated infection of the host before it recovers from the initial infectious episode) might have an insignificant effect on the dynamics of PTB in ruminants. However, at this stage we cannot precisely conclude if super-infection does not effect on the dynamics of the disease. This could only be investigated using an embedded multiscale model. Furthermore, the reduction of the dimensions of full nested multiscale model enabled us to estimate a composite parameter,
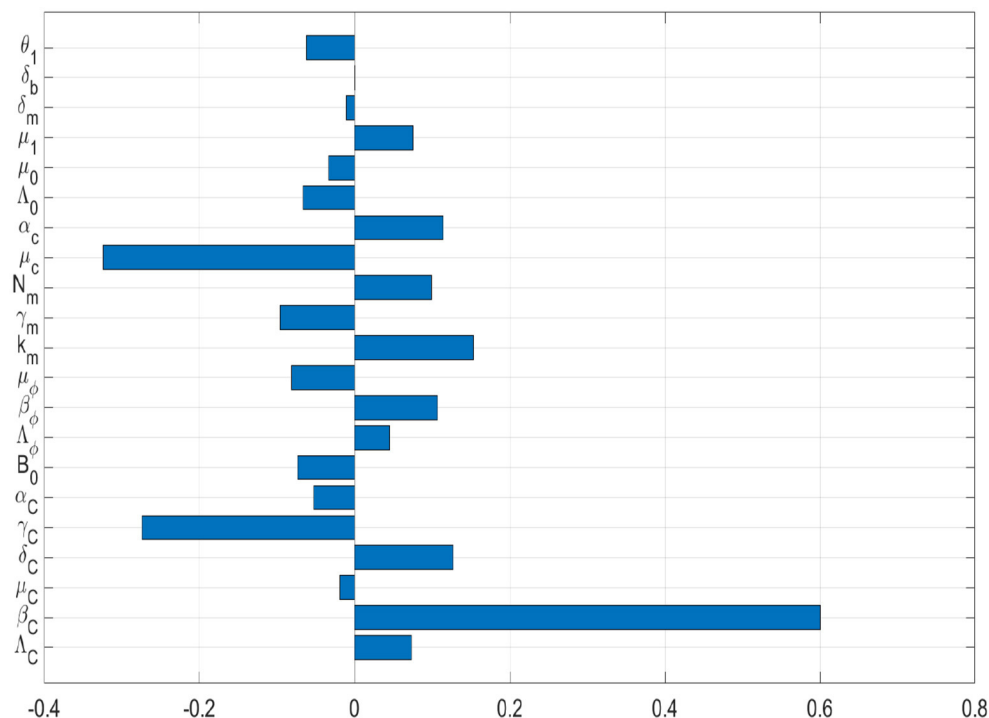
FIGURE 7
Tornado plot of partial rank correlation coefficients (PRCCs) of the model parameters that influence the PTB transmission metric B_C^*.

N_c, that is difficult to estimate using single-scale models. The estimation of N_c facilitate in enhancing single-scale model framework that can be developed at host level to predict the dynamics of paratuberculosis in ruminants at within-host scale. This is largely because single-scale models consider pathogen transmission as the only major disease process, while multiscale models consider both pathogen transmission and pathogen replication as the two major disease processes [25]. We also perform a sensitivity analysis to the two main disease dynamics metrics of the simplified nested multiscale model, namely the basic reproductive number and the endemic value of the MAP bacteria in the environment to determine important parameters of paratuberculosis disease dynamics. The sensitive analysis results show that at the start of PTB infection and when it has reach at the endemic level, the key within-host parameters μ_c is relatively sensitive to PTB disease dynamics. This would be hard to obtain from a single-scale modeling approach, which would only provide a general indication about the influential of the within-host dynamics on spread of the PTB disease at the population level, but not specifically indicating parameters that have potential influence on the disease dynamics.

Data availability statement

Author contributions

Funding

Acknowledgments

Conflict of interest

The authors declare that the research was conducted in the absence of any commercial or financial relationships that could be construed as a potential conflict of interest.

Publisher's note

All claims expressed in this article are solely those of the authors and do not necessarily represent those of their affiliated organizations, or those of the publisher, the editors and the reviewers. Any product that may be evaluated in this article, or claim that may be made by its manufacturer, is not guaranteed or endorsed by the publisher.

References

1. Magombedze G, Ngonghala CN, Lanzas C. Evalution of the "iceberg phenomenon" in Johne's disease through mathematical modelling. *PLoS ONE*. (2013) 8:e76636. doi: 10.1371/journal.pone.0076636

2. Magombedze G, Eda S, Ganusov VV. Competition for antigen between th1 and th2 responses determines the timing of the immune response switch during *Mycobaterium avium* subspecies *paratuberulosis* infection in ruminants. *PLoS Comput Biol*. (2014) 10:e1003414. doi: 10.1371/journal.pcbi.1003414

3. Martcheva M, Lenhart S, Eda S, Klinkenberg D, Momotani E, Stabel J. An immuno-epidemiological model for Johne's disease in cattle. *Vet Res*. (2015) 46:69. doi: 10.1186/s13567-015-0190-3

4. Chacon O, Bermudez L, Barletta R. Johne's disease, inflammatory bowel disease, *Mycobacterium paratuberculosis*. *Annu Rev Microbiol*. (2004) 58:329–63. doi: 10.1146/annurev.micro.58.030603.123726

5. Ott S, Wells S, Wagner B. Herd-level economic losses associated with Johne's disease on US dairy operations. *Prev Vet Med*. (1999) 40:179–92. doi: 10.1016/S0167-5877(99)00037-9

6. Chiodini RJ, Chamberlin WM, Sarosiek J, McCallum RW. Crohn's disease and the mycobacterioses: a quarter century later. Causation or simple association? *Crit Rev Microbiol*. (2012) 38:52–93. doi: 10.3109/1040841X.2011.638273

7. koets AP, Grohn YT. Within- and between-host mathematical modeling of *Mycobacterium avium* subspecies *paratuberculosis* (MAP) infections as a tool to study the dynamics of host-pathogen interactions in bovine paratuberculosis. *Vet Res*. (2015). 46:60. doi: 10.1186/s13567-015-0205-0

8. Wang X, Wang J. Disease dynamics in a coupled cholera model linking within-host and between-host interactions. *J Biol Dyn*. (2017) 11(Suppl 1):238–62. doi: 10.1080/17513758.2016.1231850

9. Netshikweta R, Garira W. A multiscale model for the world's first parasitic disease targeted for eradication: guinea worm disease. *Comput Math Methods Med*. (2017) 2017:1473287. doi: 10.1155/2017/1473287

10. Garira W, Mathebula D, Netshikweta R. A Mathematical modelling framework for linked within-host and between-host dynamics for infections with free-living pathogens in the environment. *Math Biosci*. (2014) 256:58–78. doi: 10.1016/j.mbs.2014.08.004

11. Feng Z, Velasco-Hernandez J, Tapia-Santo B. A mathematical model for coupling with-host and between-host dynamics in an environmental-driven infectious disease. *Math Biosci*. (2013) 241:49–55. doi: 10.1016/j.mbs.2012.09.004

12. Feng Z, Cen X, Zhao Y, Velasco-Hernandez JX. Coupled within-host and between-host dynamics and evolution of virulence. *Math Biosci*. (2015) 270:204–12. doi: 10.1016/j.mbs.2015.02.012

13. Garira W, Mathebula D. A coupled multiscale model to guide malaria control and elimination. *J Theret Biol*. (2019) 475:34–59. doi: 10.1016/j.jtbi.2019.05.011

14. Garira W, Mafunda MC. From individual health to community health: towards multiscale modelling of directly transmitted infectious disease systems. *J Biol Syst*. (2019) 27:131–66. doi: 10.1142/S0218339019500074

15. Garira W. A primer on multiscale modelling of infectious disease systems. *Infect Dis Modell*. (2018) 3:176–91. doi: 10.1016/j.idm.2018.09.005

16. Garira W. A complete categorization of multiscale models of infectious disease systems. *J Biol Dyn*. (2017) 11:378–435. doi: 10.1080/17513758.2017.1367849

17. Carr J. *Applications of Centre Manifold Theory*. vol. 35. New York, NY: Springer Science & Business Media (2012).

18. Bastida F, Juste RA. Paratuberculosis control: a review with a focus on vaccination. *J Immune Based Therap Vaccines*. (2011) 9:8. doi: 10.1186/1476-8518-9-8

19. Marce C, Ezanno P, Weber MF, Seegers H, Pfeiffer DU, Fourichon C. Invited review: modeling within-herd transmission of *Mycobacterium avium* subspecies *paratuberculosis* in dairy cattle: a review. *J Dairy Sci*. (2010) 93:4455–90. doi: 10.3168/jds.2010-3139

20. Mitchell R, Whitlock R, Stehman S, Benedictus A, Chapagain P, Grohn YT, et al. Simulation modeling to evaluate the persistence of *Mycobacterium avium* subsp. *paratuberculosis* (MAP) on commercial dairy farms in the United States. *Prev Vet Med*. (2008) 83:360–80. doi: 10.1016/j.prevetmed.2007.09.006

21. Martcheva M. *An Immuno-Epidemiological Model of Paratuberculosis*. (2011). Available online at: https://pdfs.semanticscholar.org/0090/c48945aedb167a146f32ab80bf6dd2c1e260.pdf

22. Robins J, Bogen S, Francis A, Westhoek A, Kanarek L, Lenhart S, et al. Agent-based model for Johne's disease dynamics in a dairy herd. *Vet Res*. (2015) 46:68 doi: 10.1186/s13567-015-0195-y

23. Konboon M, Bani-Yaghoub MM, Pithua PO, Rhee N, Aly SS. A nested compartment model to assess the efficacy of paratuberculosis control measures on U.S. dairy farms. *PLoS ONE*. (2018) 13:e0203190. doi: 10.1371/journal.pone.0203190

24. Gilchrist MA, Sasaki A. Modeling host-parasite co-evolution: a nested approach based on mechanistic models. *J Theor Biol*. (2002) 218:289–308. doi: 10.1006/jtbi.2002.3076

25. Garira W. The Replication-transmission relativity theory for multiscale modelling of infectious disease systems. *Sci Rep*. (2019) 9:1–17. doi: 10.1038/s41598-019-52820-3

26. Castillo-Chavez C, Feng Z., Huang W. On the computation of R_0 and its role in global stability. In: Castillo-Chavez C, Blower S, van den Driessche P, Kirschner D, editors. *Mathematical Approaches for Emerging and Re-emerging Infectious Diseases Part 1: An Introduction to Models, Methods Theory. The IMA Volumes in Mathematics Its Applications*. vol. 125. Berlin: Springer-Verlag (2002). p. 229–50. doi: 10.1007/978-1-4613-0065-6

27. Fanelli A, Buonavoglia D, Pleite CMC, Tizzani P. Paratuberculosis at European scale: an overview from 2010 to 2017. *Vet Ital*. (2020) 56:13–21. doi: 10.12834/VetIt.1829.9692.3

28. Kuenstner JT, Naser S, Chamberlin W, Borody T, Graham DY, McNees A, et al. The consensus from the *Mycobacterium avium* ssp. *paratuberculosis* (MAP) conference 2017. *Front Public Health*. (2017) 5:208. doi: 10.3389/fpubh.2017.00208

Appendix A

6. Derivation of the reproductive number of the PTB simplified multiscale model

To determine the reproduction number of the equations (3.11), we use the next generation operator approach in [26]. Thus the equations (3.11) can be written in this form

$$
\begin{cases}
\dfrac{dX}{dt} = f(X, Y, Z), \\[2mm]
\dfrac{dY}{dt} = g(X, Y, Z), \\[2mm]
\dfrac{dZ}{dt} = h(X, Y, Z).
\end{cases}
\tag{6.37}
$$

- $X = S_C$ represents the population of uninfected cattle.
- $Y = I_C$ represents the population of infected cattle.
- $Z = B_C$ represents the population of infected MAP bacilli in the environment.

Let

$$
U_0 = \left(\frac{\Lambda_C}{\mu_C}, 0, 0 \right)
\tag{6.38}
$$

denote the disease free-equilibrium state and further assume

$$
\tilde{g}(X^*, Z) = \frac{\beta_C \Lambda_C B_C}{\mu_C(\mu_C + \delta_C + \gamma_C)(B_0 + B_C)}.
\tag{6.39}
$$

A matrix

$$
A = D_Z h(X^*, \tilde{g}(X^*, 0), 0) = \frac{\beta_C \Lambda_C N_c \alpha_c}{\mu_C(\mu_C + \delta_C + \gamma_C)B_0} - \alpha_C
\tag{6.40}
$$

can be presented in the form $A = M - D$, where

$$
M = \frac{\beta_C \Lambda_C N_c \alpha_c}{\mu_C(\mu_C + \delta_C + \gamma_C)B_0}, \quad D = \alpha_C
\tag{6.41}
$$

Therefore, the basic reproduction number of the model system (3.11) is expressed by the following quantity,

$$
R_0 = \frac{\beta_C \Lambda_C N_c \alpha_c}{\mu_C(\mu_C + \delta_C + \gamma_C)B_0 \alpha_C}
\tag{6.42}
$$

Synchronization transitions on connectome graphs with external force

Géza Ódor[1], István Papp[1,2], Shengfeng Deng[1] and Jeffrey Kelling[3,4]*

[1]Centre for Energy Research, Institute of Technical Physics and Materials Science, Budapest, Hungary, [2]Wigner Research Centre for Physics, Budapest, Hungary, [3]Department of Information Services and Computing, Helmholtz-Zentrum Dresden-Rossendorf, Dresden, Germany, [4]Faculty of Natural Sciences, Chemnitz University of Technology, Chemnitz, Germany

We investigate the synchronization transition of the Shinomoto-Kuramoto model on networks of the fruit-fly and two large human connectomes. This model contains a force term, thus is capable of describing critical behavior in the presence of external excitation. By numerical solution we determine the crackling noise durations with and without thermal noise and show extended non-universal scaling tails characterized by the exponent $2 < \tau_t < 2.8$, in contrast with the Hopf transition of the Kuramoto model, without the force $\tau_t = 3.1(1)$. Comparing the phase and frequency order parameters we find different synchronization transition points and fluctuation peaks as in case of the Kuramoto model, related to a crossover at Widom lines. Using the local order parameter values we also determine the Hurst (phase) and β (frequency) exponents and compare them with recent experimental results obtained by fMRI. We show that these exponents, characterizing the auto-correlations are smaller in the excited system than in the resting state and exhibit module dependence.

KEYWORDS

Shinomoto-Kuramoto model, synchronisation, human connectome, fruit-fly, network

1 Introduction

The critical brain hypothesis has been confirmed experimentally many times since the pioneering electrode experiments in [1]. Power law (PL) distributed neuronal avalanches were shown in neuronal recordings (spiking activity and local field potentials, LFPs) of neural cultures *in vitro* [2–4], LFP signals *in vivo* [5], field potentials and functional magnetic resonance imaging (fMRI) blood-oxygen-level-dependent (BOLD) signals *in vivo* [6, 7], voltage imaging *in vivo* [8], 10–100 and single-unit or multi-unit spiking and calcium-imaging activity *in vivo* [9–12]. Furthermore, source reconstructed magneto- and electroencephalographic recordings (MEG and EEG), characterizing the dynamics of ongoing cortical activity, have also shown non-universal PL scaling in neuronal long-range temporal correlations [13, 14]. Optical methods, like light-sheet microscopy with GCaMP zebrafish larvae [15] or calcium imaging recordings of dissociated neuronal cultures [16] also show PL scaling.

From a theoretical point of view the hypothesis is also very attractive as critical systems possess optimal computational capabilities as well as provide efficient long range communications, memory and sensitivity [17–28].

Homogeneous critical systems exhibit universal scaling behavior and many experiments claim indeed a mean-field class behavior of the branching process [29, 30] generated by self-organized criticality [31]. However, neural systems are very non-homogeneous, thus it is natural to expect non-universal behavior, known in statistical physics within the field of quenched disordered models [32, 33]. Indeed some experiments [13, 14, 16] show that the measured exponents are not universal, significantly different from the mean-field class ones of the branching process.

Furthermore, external sources can move the system away from criticality [34, 35] or tune it to other classes, like the isotropic percolation [16, 36] or to tricritical points [37]. More complex models than the two-state branching process, can also exhibit hybrid type of phase transitions, like threshold models [38], models with inhibitory nodes [39] or models with oscillatory units [40]. Subsystems can also show different scaling behavior and may be within different distances from criticality [41].

For quenched disordered models it has recently been shown [42, 43], that even for weak time dependence the semi-critical, dynamical scaling, which occurs in an extended control parameter region of criticality, in the so called Griffihts Phases [44] (GP), remains stable. Furthermore, even when the network dimension is high, one does not find the usual mean-field behavior, but in the presence of modules a GP [36, 38, 45–48] or Griffihts effects [49] and a different, sometimes logarithmically slow scaling at the critical point [32].

The big advantage of critical universality is that more realistic models for the brain, like the integrate and fire models [50], can also show the same criticality as simpler ones like in a recent work [51], which derives Hopf bifurcation criticality or in a more experimental study [52] of neural cultures agreement with isotropic percolation avalanche size distributions is obtained. But of course the directed percolation criticality [53, 54], which occurs in branching processes [1] is the main example for the universality principle [55]. Therefore, the study of simpler models, for which numerical analysis can be done are very useful for the brain science [28, 33].

Recently threshold models and Kuramoto type of models have been analyzed on different, available connectome networks and GP behavior was reported [33, 43, 56–59]. This behavior is also called as frustrated synchronization [60–62] and has been analyzed within the framework of a Kuramoto like models, albeit lacking quenched self-frequencies.

From the experimental directions the different behavior in modules of brains of the mouse [41], by phenomenological renormalization-group analysis of the spectrum of electrode spikes, and humans [63], *via* Hurst and β exponents analysis of fMRI; quasi-critical (off-critical) scaling like behavior has been shown. Here we attempt to model this using the Shinomoto–Kuramoto (SK) model on connectomes of the fruit-fly (FF) and humans. This is an extension of the Kuramoto model [64], which itself does not have an external source, that can describe the resting state critical behavior at the Hopf transition towards a model with a periodic external driving force, thus may be appropriate to characterize criticality with an excitation [40].

2 Models and methods

In this Section we introduce the synchronization model, followed by an overview of different connectome graphs, on

which we run the numerical analysis. Finally we discuss the method of local synchronization to dig into the details of the spatio-temporal simulations of these brain systems.

2.1 The Shinomoto–Kuramoto (SK) model

We consider an extension of the Kuramoto model [64] of interacting oscillators sitting at the nodes of a network, whose phases $\theta_j(t)$, $j = 1, 2, \ldots N$ evolve according to the following set of dynamical equations

$$
\begin{aligned}
\dot{\theta}_j(t) = \omega_j^0 + K \sum_k W_{jk} \sin\left[\theta_k(t) - \theta_j(t)\right] \\
+ F \sin\left(\theta_j(t)\right) + \epsilon \eta_j(t).
\end{aligned}
\tag{1}
$$

Here, ω_j^0 is the so-called self-frequency of the jth oscillator, which is drawn from a Gaussian distribution with zero mean and unit variance. The summation is performed over adjacent nodes, coupled by the W_{jk} matrix. Up to this point we have the classical Kuramoto model [64]. In the Shinomoto extension [65], we have a Gaussian annealed noise term $\eta_j(t)$, with an amplitude ϵ, and to describe excitation, a site dependent periodic force term, proportional to a coupling F.

Sakaguchi [66] was the first to study the periodically forced Kuramoto model. In numerical simulations, however, he found that the state of forced entrainment was not always attained: macroscopic fractions of the system self-synchronized at a different frequency from that of the drive, indicating that this sub-population had broken away and established its own collective rhythm. Analytically improvements were provided in [67–69] and found a rich phase space of the SK model.

Recently, in [40] the avalanche behavior of the SK equation was investigated, albeit with site independent self-frequencies $\omega_j^0 = \omega$. The authors explored the phase diagram, besides the forceless Hopf transition a so-called saddle node invariant cycle (SNIC) and a hybrid type of bifurcation were compared. In a very recent publication [48], this numerical analysis has been continued on Erdős–Rényi (ER) and hierarchical modular networks, motivated by brain research. Considering quenched ω_j^0-s with bi-modal frequency distributions the authors claim the emergence of Griffiths effects by the broadening of the synchronization transition region.

Here we study the SK model using quenched ω_j^0-s with and without annealed noise $\eta_j(t)$ on real connectomes. In particular we test if the chaoticity, generated by the quenched ω_j^0-s generates the same phase transition behavior and avalanches as with the presence of the stochastic noise. We measured the Kuramoto phase order parameter:

$$
z(t) = r(t)\exp i\theta(t) = 1 \Big/ N \sum_j \exp\left[i\theta_j(t)\right],
\tag{2}
$$

by increasing the sampling time steps $\delta t = 0.01$. Here $0 \le r(t) \le 1$ gauges the overall coherence and $\theta(t)$ is the average phase. The set of Eq. 1 was solved by the steppers Runge–Kutta-4 (RK4), for the noisy, or by the Bulrisch–Stoer [70, 71] (BS) for the noiseless cases, because in the presence of noise the adaptive BS fails to work. Here and in earlier studies [58] we found that stronger stochastic noise makes the results non-reliable, while application of other steppers slows down

the numerical solution. For the noisy cases we also tried the Euler–Maruyama solver [72], which has a stronger mathematical foundation for stochastic differential equations. This had to be restricted to testing purposes only, as this first-order solver is orders of magnitude slower than the RK4 for the same precision.

We integrated the set of equations numerically for 10^3–10^4 independent initial conditions, by different ω_j^0-s and sample averages of the phases

$$R(t) = \langle r(t) \rangle \tag{3}$$

and of the variance of the frequencies

$$\Omega(t) = \langle \frac{1}{N} \sum_{j=1}^{N} (\bar{\omega}(t) - \omega_j(t))^2 \rangle \tag{4}$$

were calculated, where N denotes the number of nodes.

In the steady state, which we determined by visual inspection of $R(t)$ and $\Omega(t)$, we measured their half values and the standard deviations: $\sigma(R(t))$, $\sigma(\Omega(t))$ in order to locate the transition points. In the paper we plotted the $\sigma(R)$, $\sigma(\Omega)$ values, obtained by sample and time averaging in the steady state. Note, that $\sigma(R)$ is just a the so-called SK order parameter employed by [73] for discrete version of oscillatory models and is also used in [40] for the SK model. In case of the Kuramoto equation the fluctuations of both order parameters show a peak, albeit at different K_c^I (for phases) and K_c (for frequency) values in the case of the KKI-18 connectome [56]. For graph dimensions $3 < d < 4$, found for the human connectomes [78], a crossover transition is expected for R and phase transition for Ω. In the case of the FF, $d > 5$ [59], thus $K_c \simeq K_c^I$, which is expected for real phase transitions at large sizes, where both order parameters converge to a finite value in the infinite size limit [59].

2.2 Connectome graphs

The connectome is defined as the structural network of neural connections in the brain [74]. For the fruit-fly connectome, we used the hemibrain data-set (v1.0.1) from [75], which has $N_{FF} = 21,662$ nodes and $L_{FF} = 3,413,160$ edges, out of which the largest single connected component contains $N = 21,615$ and $L = 3,410,247$ directed and weighted edges. The number of incoming edges varies between 1 and 2,708. The weights are integer numbers, varying between 1 and 4,299. The average node degree is $\langle k \rangle = 315.129$ (for the in-degrees it is: 157.6), while the average weighted degree is $\langle w \rangle = 628$. The adjacency matrix, visualized in [59] where one can see a rather homogeneous, almost structureless network, however it is not random. For example, the degree distribution is much wider than that of a random ER graph and exhibits a fat tail. The analysis in [59] found a weight distribution $p(w)$ with a heavy tail and assuming a PL form, an exponent −2.9 (2) could be fitted for the $w > 100$ region.

The human brain has $\approx 10^{11}$ neurons, which current imaging techniques cannot comprehensively resolve at the scale of single neurons. We used graphs on the coarse-grained, level with $\approx 10^6$ nodes obtained by diffusion tensor imaging [76]. This method has generally been found to be in good agreement with ground-truth data from histological tract tracing [77]. Inferred networks of structural connections were made available by the Open

Connectome Project and previously analyzed by [78]. These graphs are symmetric, weighted networks, where the weights measure the number of fiber tracts between nodes. The network topology study found a certain level of universality in the topological features of the ten large human connectomes investigated: degree distributions, graph dimensions, clustering and small world coefficients. These can be observed in Tables 3 and 4 of [78]. Therefore, two networks, called KKI-18, and KKI-113 were selected to be the representatives in further studies. The graphs, downloaded in 2015 from the Open Connectome project repository [79], were generated *via* the MIGRAINE pipeline [80], publicly available from [81]. KKI-18 comprises a large component with $N = 804,092$ nodes connected *via* 41,523,908 undirected edges and several small disconnected sub-components, which were ignored in the modeling. Similarly, the extracted largest connected component of KKI-113 contains 799,133 nodes connected by 48,096,500 undirected and weighted edges. The large number of nodes is because of other parcellations closer to voxel resolution being used. For instance, there are approximately 1.8 million voxels in the brain mask of a 1 mm resolution standard-aligned MRI. The graphs exhibit a hierarchical modular structure, because they are constructed from cerebral regions of the Desikan–Killany–Tourville parcellations, which is standard in neuroimaging [82, 83] providing (at least) two different scales.

The modularity quotient of a network is defined by [84].

$$Q = \frac{1}{N\langle k \rangle} \sum_{ij} \left(A_{ij} - \frac{k_i k_j}{N\langle k \rangle} \right) \delta(g_i, g_j), \tag{5}$$

the maximum of this value characterizes how modular a network is, where A_{ij} is the adjacency matrix, k_i, k_j are the node degrees of i and j and $\delta(g_i, g_j)$ is 1 when nodes i and j are in the same community, or 0 otherwise. However, this value is not independent of the community detection method. If our detection method produces lower modularity than the maximum achieved by others, it means our algorithm needs to be improved. Community detection algorithms based on modularity optimization will get the closest to the actual modular properties of the network. We calculated the modularity using community structures detected by the Louvain method [85], the results for each network were: $Q_{FF} \approx 0.631$, $Q_{KKI-18} \approx 0.913$, $Q_{KKI-113} \approx 0.915$. The FF is a small-world network, according to the definition of the coefficient [86]:

$$\sigma^W = \frac{C^W/C_r}{L/L_r}, \tag{6}$$

because $\sigma_{FF} = 9.5$ is much larger than unity. Here C^W denotes the Watts clustering coefficient, and L the average path length. C_r and L_r are the reference values of random networks with the same sizes and average degrees. The same is true for the human connectomes, as their σ^W is in the range between 400 and 1,000 [78].

The effective graph (topological) dimension of the FF, obtained by the breadth-first search algorithm is $d = 5.4$ (5). This is defined by $N(r) \sim r^d$, where the number of nodes $N(r)$ with chemical distance r or less from the origin are counted and averages are calculated over many trials. For the Open Connectome data, power-law fits in the range $1 \leq r \leq 5$ suggest topological dimensions between $d = 3$ and $d = 4$ [78].

As these structural connectome graphs exhibit heavy-tailed weight distributions, probably as a result of learning, there exist hubs, which could fully determine the behavior of neighboring nodes and suppress the occurrence of critical behavior in the models [56]. In reality, on top of the structural weights, there exist inhibition/excitation mechanisms, which control the dynamics of the neural system and provide a local homeostasis. As we do not know the details of these mechanisms, in earlier studies [33, 43, 56–59], the weight normalization scheme

$$W'_{jk} = W_{jk} \Big/ \sum_k W_{jk} \tag{7}$$

was applied to achieve this artificially. This way we equalize the sensitivity of nodes of the incoming excitations. We do the same in the simulations presented here.

2.3 Analysis of the local synchronization

As the connectomes are very heterogeneous, built up from modules we also measured the local Kuramoto order parameter $R_i(t)$, defined as the partial sum of phases for the neighbors of node i

$$R_i(t) = \frac{1}{N_{i.\text{neigh}}} \left| \sum_j^{N_{i.\text{neigh}}} A_{ij} e^{i\theta_j(t)} \right|, \tag{8}$$

and the local $\Omega_i(t)$ defined as

$$\Omega_i(t) = \frac{1}{N_{i.\text{neigh}}} \left| \sum_j^{N_{i.\text{neigh}}} \left(\bar{\omega}(t) - \omega_j(t) \right)^2 \right|. \tag{9}$$

The local Kuramoto order parameter was initially suggested by [87, 88] to quantify the local synchronization of nodes, which allows us to follow the synchronization process by mapping the solutions on the connectome graphs.

The necessity of storing the states of the system at each time step requires large amount of hard drive storage. Thus we analyzed the local order parameters in a time period of 50 time-steps as stop time with time increment of $dt' = 0.1$, in the steady state. To study it in more detail we also separated the networks into communities. Although, these communities should be separated according to anatomical and/or functional properties [89], we chose as a first approximation a community detection method based on global optimization of the modularity [85]. This method yielded 9 modules in FF network, 130 communities in KKI-113 and 134 modules in the giant component of KKI-18. For detecting community structure that is closer to the real anatomical functional communities just by using the network topology, one might require other algorithms, which analyze the network with more depth, or even using fuzzy clustering methods [90, 91].

We studied the long-term persistence of the local order parameters with the Hurst and β exponents. The Hurst exponent measures the degree of self-similarity of a time series, based on the assumption of an Ornstein–Ulenbeck process, that the measured values will go back to its average in just a few time-steps. The Hurst exponent is defined as follows:
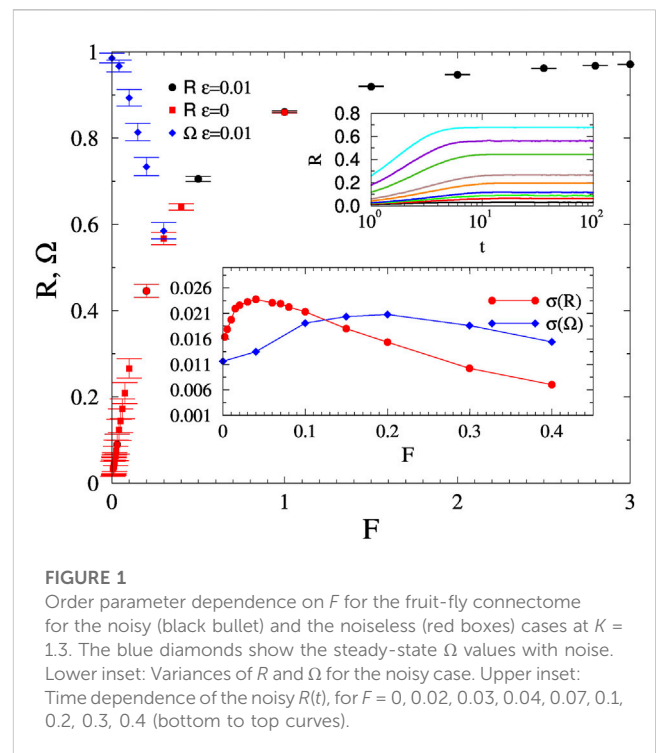
FIGURE 1
Order parameter dependence on F for the fruit-fly connectome for the noisy (black bullet) and the noiseless (red boxes) cases at $K = 1.3$. The blue diamonds show the steady-state Ω values with noise. Lower inset: Variances of R and Ω for the noisy case. Upper inset: Time dependence of the noisy $R(t)$, for $F = 0$, 0.02, 0.03, 0.04, 0.07, 0.1, 0.2, 0.3, 0.4 (bottom to top curves).

$$\mathbb{E}\left[\frac{Z(n)}{S(n)} \right] = Cn^H, \tag{10}$$

where $\mathbb{E}$ is the expectation value of the rescaled range Z/S and $Z(n)$ is the cumulative deviate of the series until the first number of n data points ($n = (t_{max} - t_0)/dt'$), while $S(n)$ is the sum of the standard deviations until that point. We averaged the first local parameter values within the communities and calculated the Hurst exponent over the n points in the time period t, where $S_j(n) = \sum_i^{M_{j,comm}} R_i(t)$ are community averages and $M_{j,comm}$ is the number of nodes in the community. We calculated the Hurst exponents for all communities.

Similarly, the power spectral scaling exponent, β, is used for quantifying long range correlations in time series. The power spectral density is the modulus of the Fourier transform, if the spectrum of the process satisfies a power-law scaling relation:

$$S(f) = \left| \sum_{j=0}^{N} \Omega_j(t) e^{-2\pi i f_j / N} \right|^2 \approx 1 / f^{\beta}, \tag{11}$$

where $f_j = \sum_j^{M_{i,comm}} \Omega_i(t)$ and β must be obtained by using a linear fit to the logarithmic axes of the Fourier transform periodigram [63].

3 Force driven synchronization transition

First we determined the synchronization transition behavior of the Shinomoto–Kuramoto model on different connectomes by calculating the global order parameters R and Ω as well as their fluctuations as the function of the force control parameter, which mimics the external excitation of the system. After that we measured

FIGURE 2
Order parameter dependence on F for the KKI-113 for the noisy and the noiseless cases at $K = 1$. Inset: Variances of R and Ω for the noisy case.

FIGURE 3
Fluctuations of R and Ω as the function of F for the KKI-18, for the noisy and the noiseless cases at $K = 1$. Inset: Order parameter R for the noisy and noiseless cases as well as Ω, denoted by the same symbols as in the main figure.
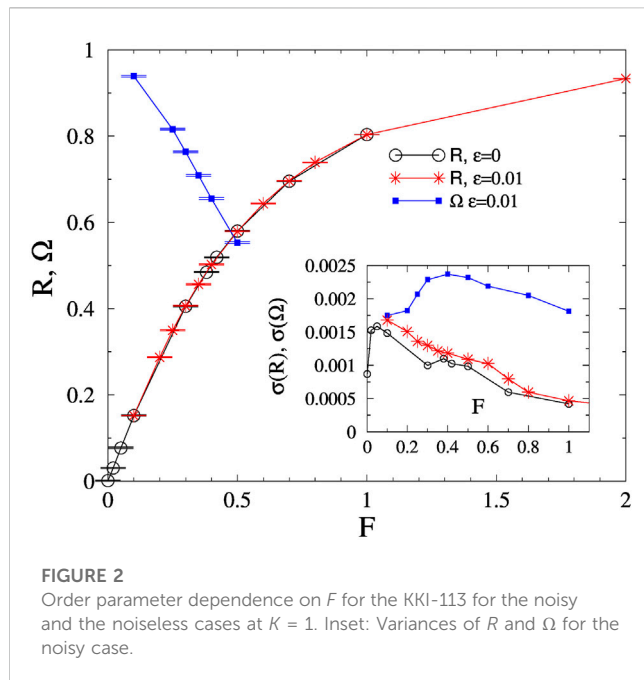
the crackling noise distributions within the neighborhood of these transitions.

3.1 Global order parameters

We started the numerical analysis of SK on the fruit-fly connectome at the global coupling value $K = 1.3$, which was found to be asynchronous without a force in [59]. For each F value we determined the steady state by following the evolution of the control parameters starting from random initial θ-s *via* visual inspection. Averaging was done over many independent samples, corresponding to different initial ω_j self-frequencies. The transient regimes were short, in the range of 10–100 time steps and we could not see PL growth as in case of the Hopf transition of the Kuramoto model. But the Kuramoto order parameter curves exhibit $R(t) \propto \ln(t)^{x(K)}$ type of growth (see upper inset of Figure 1), as in case of activated scaling in disordered systems [32].

To locate the transition we plotted the steady state values of R and Ω and their fluctuations on Figure 1. The half values provide estimates: $F_c \simeq 0.22$, for R and $F'_c \simeq 0.35$ for Ω. One can see smooth fluctuation peaks of $\sigma(R)$ at $F \simeq 0.05$ and of $\sigma(\Omega)$ at F' $\simeq 0.2$. Thus, the two different order parameters seem to exhibit different synchronization points. The frequency fluctuation peak agrees roughly with $F_c \simeq 0.22$, but the phase fluctuation peak occurs at a much lower value. This, in contrast with the Hopf transition of FF and the random network, where fluctuation peaks were roughly at the same position, where we knew that the dimension is $d > 4$. Plotting the results on log.-log. scale it turns out that the fluctuation growth can be fitted by $\sigma(R) \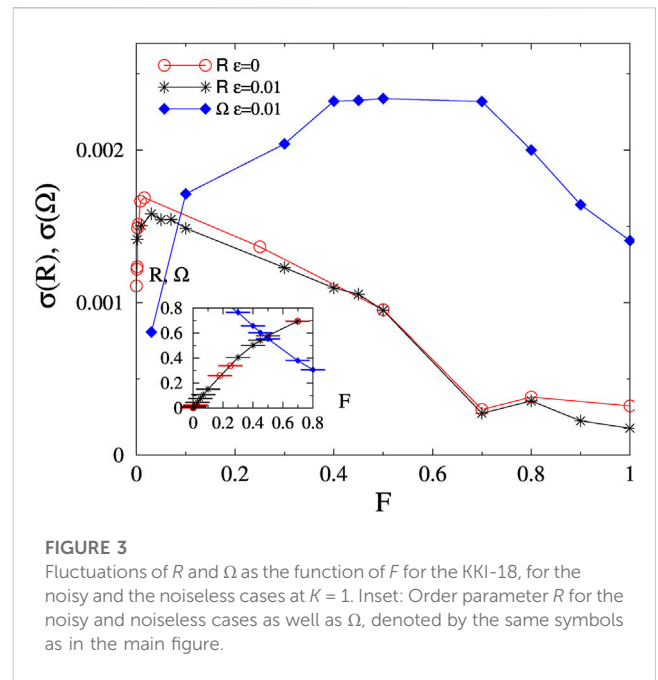propto F^{0.16(1)}$ for $F \leq 0.05$, while following the peak, for $F > 0.1$, it decays as $\sigma(R) \propto F^{-1.3(2)}$. Thus, we have susceptibility like exponents $\gamma' = 0.16(1) \neq \gamma = 1.3(2)$. Note, that in case of $K =$

2, when we started from a synchronous state by the addition of the force we obtained a very narrow growth region of the fluctuations, the decay is characterized by $\gamma = 1.34(1)$ (see Appendix).

As $\sigma(R)$ is also called SK order parameter, which characterizes the transition in excitable systems, its approach to zero as F increases agrees with the SNIC transition result of [40], albeit that was obtained in the synchronous phase. We have also run SK in the synchronous phase of FF, using $K = 2$, where we found similar results as in the asynchronous phase.

Results with and without a small noise with amplitude $\epsilon = 0.01$ did not show observable differences, so the chaotic noise from the quenched disorder is capable to compete with the ordering effect of the force. We have also determined the $\sigma(\Omega(K, F))$ for other K and F values, as they are close to the half values estimates of the transitions. As one can see on the inset of Figure 4 by increasing F the Kuramoto transition fluctuation peak becomes smoother and moves to smaller K values, similarly to the Widom line obtained in discrete brain models [34, 35].

As the next step we performed the same analysis of the human connectomes at $K = 1$, which is in the asynchronous phase without a force [57]. Figure 2 shows the steady state values both for R and Ω in case of $K = 1$ for KKI-113. Again the annealed noise does not modify the results and seems to be unnecessary to produce a synchronization transition. We estimated: $F'_c \simeq 0.4$ and $F_c \simeq 0.55$ by the half values or R and Ω respectively. The fluctuation peaks of the two order parameters are again far away from each other: $F \simeq 0.05$ versus $F' \simeq 0.4$. Again the fluctuation peak of Ω is close to $F'_c \simeq 0.4$.

For the connectome KKI-18 we enlarged the fluctuation peak results on Figure 3, by comparing the noiseless and the noisy R results. The smeared synchronization 'peaks' happen at similar values as for KKI-113: $F' \simeq 0.05$ and $F \simeq 0.5$ within numerical precision. The transition points, estimated by the half values of R is
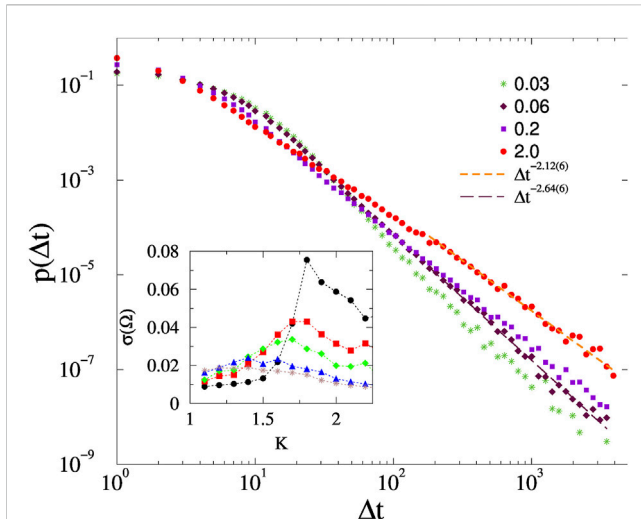
FIGURE 4
Avalanche duration distributions on the fruit-fly connectome for different forces, shown by the legends and at $K = 1.3$, $\epsilon = 0.01$. Dashed lines are PL fits for $\Delta t > 100$. The inset shows the steady state $\sigma(\Omega)$ as the function of K, for excitation values $F = 0.001, 0.0667, 0.1, 0.2, 0.3$ (top to bottom).
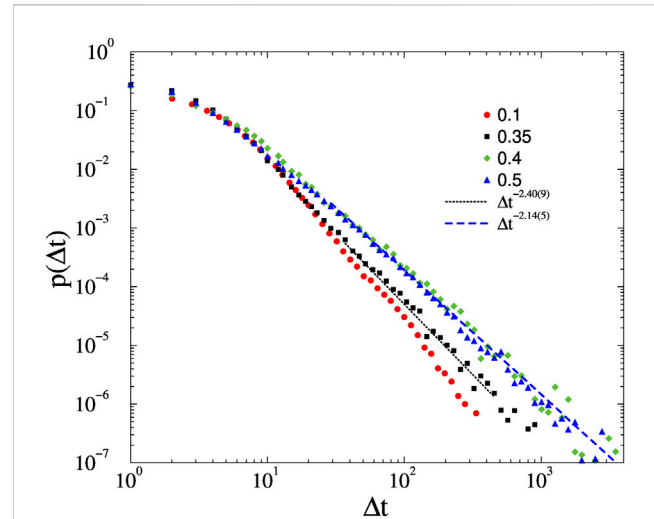

FIGURE 5
Avalanche duration distributions on the KKI-113 connectome for different forces, shown by the legends and at $K = 1$, $\epsilon = 0.01$. Dashed lines are PL fits for $\Delta t > 20$. The $F = 0.1$ case veers down on the log.-log. scale, but for $F = 0.35$ a more extended PL tail with exponent $\tau_t = 2.40(9)$ can be obtained. For $F = 0.4$, and $F = 0.5$ the slopes stabilize to $\tau_t = 2.14(5)$.

$F_c \simeq 0.4$ and of Ω is $F'_c \simeq 0.55$. As before, the $\sigma(R)$ peaks occur at much lower force values, than the other transition point estimates and the susceptibility exponents estimates have been estimated to be $\gamma' = 0.15(3)$ and $\gamma = 1.12(2)$.

3.2 Avalanche durations

We investigated avalanches similarly to the local field potential experiments and as it was done in simulations of spike-like events [40]. In critical systems avalanche sizes and durations exhibit PL tails, characterized by the exponents $p(S) \propto S^{-\tau}$ and $p(\Delta(t)) \propto \Delta(t)^{-\tau_t}$. However, we did not apply thresholds for the individual variables $\theta_i(t)$, but for the global order parameter $R(t)$. This has the advantage of a much faster algorithm, allowing us to consider larger statistics and the lack of ambiguity in the avalanche definitions [95–97]. The disadvantage is that spatially independent avalanches overlapping in time accidentally may be unified, thus the duration times can be larger and we do not have information on the spatio-temporal sizes, thus on the exponent τ. Still, we think that investigating this coarse-grained description of avalanches, which has also been measured in experiments, as a kind of crackling noise [98] in the case of zebrafish larvae [15], describes a possible critical behavior. Results of local characterization of the synchronization will be shown in Sections 3.3, 3.4, 4.2.

As in [40] here we also found that the choice of threshold $T(F)$ value did not change the scaling behavior of the duration distributions if it was chosen within the fluctuation range $R_{min} < T(F) < R_{max}$ corresponding to F, that was determined numerically after several runs on different initial conditions. For thresholds we used the mean value of $R(t)$, obtained in the steady state by sample and time averaging up to $t_{max} = 10^4$. By the integration we used
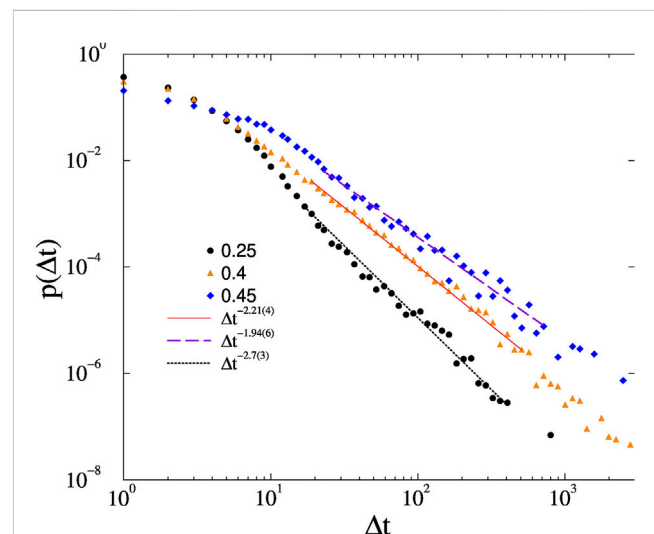
FIGURE 6
Avalanche duration distributions on the KKI-18 connectome for different forces, shown by the legends and at $K = 1$, $\epsilon = 0.01$. Dashed lines are PL fits for $\Delta t > 20$.

uniform random distributions $\theta_i(0) \in (0, 2\pi)$ and the initial frequencies were set to be $\dot{\theta}_i(0) = \omega_i^0$. Following measurements of the avalanche duration $\Delta(t) = t_i - t_{i'}$, defined between subsequent crossing of an up event: $R(t_i) > T$ and a down one: $R(t_i') < T$, we applied a histogramming to determine the probability distributions $p(\Delta(t))$.

Figure 4 shows the PDF $p(\Delta(t))$ results for the fruit-fly, in case of $K = 1.3$, $\epsilon = 0.01$ and different forces. We can see F dependent

FIGURE 7
Here we see the evolution of the local order parameters $R_i(t)$ of a sub-graph of the fruit-fly connectome at different time steps: $t = 12.6$, 36.6. The upper row shows R_i map without a force, the lowest one with $F = 1.0$. Color-coding at the bottom provides $R_i(t)$ for all sub-figures.

FIGURE 8
Hurst and β exponents of all fruit-fly connectome communities. In the forceless case at the critical Hopf transition coupling, the H exponent is the largest for every community. With forces these values drop for each community. This shows a resemblance with the rest and non-rest studies of different brain areas in [63], showing $\langle H \rangle \approx 1.0$ at resting state and $\langle H \rangle \approx 0.7$ at task driven states.

extended PL tails, with continuously changing exponents: $2.1 < \tau_t < 2.8$, which are somewhat smaller, but close to the experimental value reported for the zebrafish: $\tau_t = 3.0$ (1) [15] and to the random field Ising model duration values [99].

Similar results are obtained in case of the two human connectomes as shown on Figures 5, 6. Furthermore, the results do not change without the additive noise, or in case of a force in the synchronized phase (see graphs in the Appendix).

3.3 Local order parameters snapshots

We have plotted with Wolfram Mathematica [100] snapshots of the local order parameters of the FF at different force values in increasing order for the average local parameters (see Figure 7). The giant component of the graph was plotted with 21,615 nodes, however with a very few 75,657 edges for better visualization, where we sorted the links of each node by their weights in a decreasing manner and then randomly chose
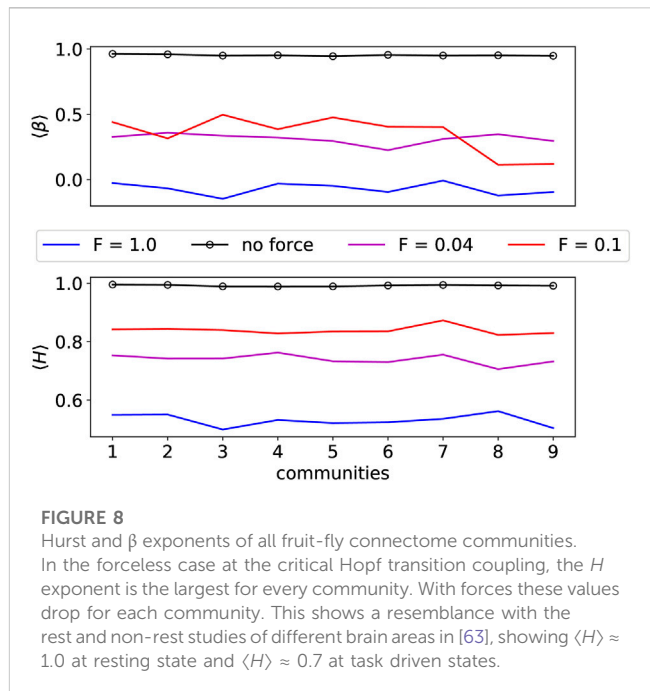
the first n_r links, where n_r is a random integer between 1 and $n_m = 6$. Since the graph is a modular small-world graph, this kind of representation can be a close visual representation of the actual network. The color coding on the figure is a logarithmic ($\log_3$) binned scale between 0 and 1 (0.01, 0.03, 0.09, 0.27, 0.81, 1.) representing the R_i values of each node at time step, indicated on the top left of each figure.

Top row plots are results without force, second row at $F = 0.04$, third row at $F = 0.1$ and last row is at $F = 1.0$. Similarly to the β exponent's case, we notice that the average local parameter R is not increasing linearly with the force at the same time-step. There is a maximum around 0.1, thus it does not have a linear correlation with the force. Without force the steady state has more fluctuations and the communities are more observable through visualization. By increasing the force every node comes into the same local state.

3.4 Hurst and β exponent results

The H and β exponents measure the self-similarity of a time series, when power-law behavior (10), (11) can be observed. H and β values lower than 0.5 describe anti-correlated signals. On the other hand, values between 0.5 and 1 mean signals with long range correlations in time.

First, we separated the communities in all FF, KK-18, KKI-113 connectomes with the Louvain modularity optimizing algorithm. Then, we calculated the H and β exponents for each community for the local parameters. In case of the FF the results (see Figure 8) with force could similarly be differentiated from the results without force as in the [63] experiments with rest and task driven measures. Simulation results without force seem to have longer correlations in time, resembling to the fMRI measurements at the rest phase.

The same conclusion however cannot be found in the case of the human connectomes (see Figure 9). It appears that even with
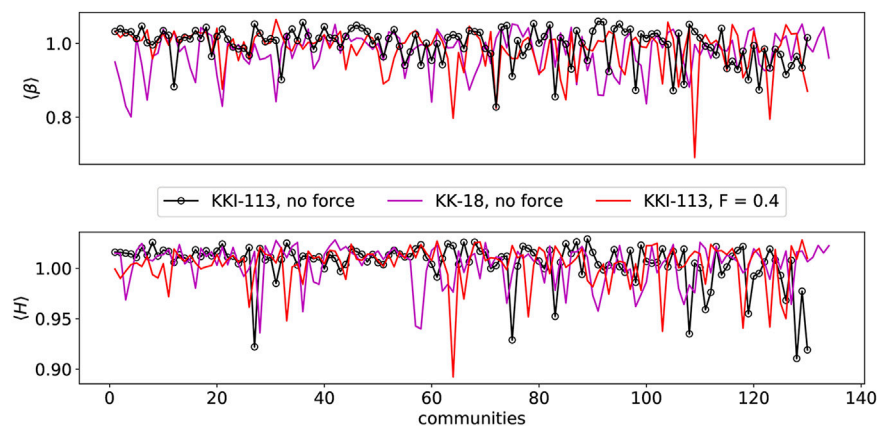
FIGURE 9
Hurst and β exponents of all human connectomes' communities. KKI-113 is presented with and without force terms and KK-18 without the force terms.
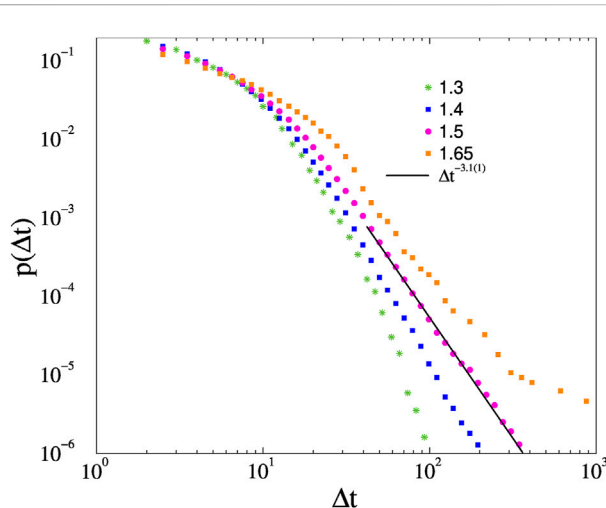

FIGURE 10
Avalanche duration distributions on the fruit-fly connectome without force for K different couplings. The line shows a PL fit for the $K = 1.5$ results, for $\Delta t > 30$.

a relatively high force the exponents remain close to each other and close to those of the "rest" phase. In the case of FF higher force led to less "rest" in the system resembling more like task driven behaviour.

Another very important result arose from the study of the two different human connectomes, where H exceeds the maximum value of 1. It is due to the fact that the brain at criticality is characterized by "crucial events." Crucial events are defined as abrupt changes in the signal amplitude, for example in electroencefalogramm (EEG) signals [92]. The waiting time (τ) distribution between events follows an inverse-power law $\psi(\tau) \approx \frac{1}{\tau^\mu}$ for $\tau \to \infty$. The intermittency index μ is an important measure in the interval $1 < \mu < 3$, with $H = (4 - \mu)/2$ and $\beta = 3 - \mu$. The condition $\mu < 2$ generates $H > 1$ with a possible maximum value $H = 1.5$. This is due to the fact that some non-stationary correlation could emerge in

crucial events, leading to $\mu < 2$, so that H exceeds the maximum value of 1 [93, 94]. As we can see on Figure 9, $H > 1$ and $\beta > 1$ occur in case of the human connectome results at certain communities, but we did not find it in the case of the FF (see Figure 8).

4 Hopf synchronization transition without force

We have rerun this analysis for the fruit-fly connectome using the standard Kuramoto equation for different couplings, i.e., near the Hopf synchronization transition discussed in [59].

4.1 Crackling noise analysis

Earlier mean-field type of phase transition was found at K_c 1.7(2). As we can see on Figure 10 the crackling noise duration analysis results in faster than PL decays of $p(\Delta t)$ for $K < 1.4$ and an inflection point with up veering decays for $K \geq 1.65$ couplings. At $K = 1.5$ we can observe a PDF, with PL decay for $30 < t < 300$, which can be fitted by the exponent $\tau_t = 3.1(1)$. Note, that in [59] an estimate for the synchronization transition $K_c = 1.70(2)$ was given, but in that work the RK4 solver was used mainly. Here the more precise Bulrisch-Stoer stepper was applied, which moves the $p(\Delta)$ tails slightly and provides a somewhat greater transition point estimate.

As in [59] we do not find an extended scaling region with non-universal exponents suggesting a GP. So, the crackling noise exponent, presumably the mean-field class exponent of the Hopf transition, describing the resting state, should be this value. This is a rather large exponent and is difficult to reproduce by simulations, because large systems are needed to see the scaling region before an exponential cutoff. We assume that this was not seen in [40], where $N = 500$ nodes were used. Another reason might be that in [40] an annealed Kuramoto model was simulated, lacking the quenched self-frequencies. Or perhaps because [40] used thresholds of the $\theta_i(t)$ variables and

identified avalanches by estimating the spatio-temporal size of the activity avalanches.

But indeed the scaling region we observe is rather narrow, even though we know that the Kuramoto model exhibits a critical synchronization transition here.

4.2 Hurst and β analysis of local variables

We cannot exclude the possibility that doing the avalanche analysis on the local angles $\theta_i(t)$, would lead to a lack of PL-s as it was claimed in [40]. Since identification of avalanches of local variables is a rather difficult and ambiguous task, requiring careful binning, to check the scaling of local phase and frequency data we performed auto-correlation measurements and estimated the Hurst and β exponents as before.

The "no-force" result on Figures 8, 9 show strong auto-correlations, indications of criticality as in the brain experiments [63]. In fact the exponents are larger (close to 1), than in case of the Shinomoto–Kuramoto model calculations. This suggests that the external excitation results in a less correlated scaling behavior of the neural systems than in the resting state. These results are in agreement with the experimental findings of [63].

5 Conclusion

In conclusion our numerical analysis of synchronization models on different connectome graphs show that in the case of excitation we can find PL scaling of duration of the crackling noise of the activity, defined by thresholds of R. By solving the Shinomoto-Kuramoto model numerically we concluded that even without the additive noise we can find similar synchronization transition as with the full Langevin equation.

The observed PL tails exhibit some dependence on the amplitude of the force, which may be related to GP heterogeneity effects, but can also arise as the consequence of quasi-critical, scaling like behavior reported in the discrete models of Ref. [35]. We estimated the extension of the synchronization transition region by the fluctuations of R and Ω and found an extended, smeared transition region. This makes it difficult to define the transition points. We attempted it in two different ways: half values and fluctuation peaks of the order parameters in the steady state. In general, the F_c'-s, obtained by the half values of Ω are greater than the F_c-s by the R-s and agree with the frequency fluctuation peaks. While the phase fluctuations peaks were found to be much smaller both for the FF and the human connectomes. This is very different from the Kuramoto Hopf transition results [59]. The susceptibility exponents are $\gamma' = 0.16(2)$ and $\gamma' = 1.3(1)$, but for the $K = 2$ case we could not measure γ', because $F_c = F_c' \simeq 0$ was found. The $\sigma(\Omega)$ results also show accordance with the Widom line, the peaks are flattened and shift by increasing the external force.

However, $\sigma(R)$ also describes the transition of the SK order parameter, introduced for excitable systems. Its decay seems to be faster than the one obtained by the SNIC bifurcation at $\omega_i^0 = 1$, $\epsilon = 0.275$ [40]. We have not reached a region, showing hybrid phase transition reported in [40], possibly by the lack of strong noise. We avoided to apply strong noise, because that makes the numerical solution less precise or very slow. A systematic finite-size scaling study of this transition would be necessary to settle this issue.

In case of initial conditions with random phase variables the $R(t)$ curves at the transition point do not show PL growth as in case of the Kuramoto model, but a logarithmic growth, similar to strong random fixed points of models of statistical physics.

We also investigated the local order parameters and found frustrated synchronization with Chimera like states, coexistence of synchronized and asynchronous domains. Performing auto-correlation analysis on the local order parameters we found strong auto-correlation in the resting (Kuramoto) state at criticality and somewhat weaker ones in presence of an external force. In the latter case the H and β exponents take their maximal values, where the fluctuations of $R(t)$ are maximal, i. e., at the transition.

We also investigated the module dependence of H and β by decomposing the connectomes *via* community detection algorithms. We observed variations amongst the communities suggesting different levels of criticality, but the identification of communities with real brain regions is a further task to be completed. Our simulated H and β exponents are in agreement with recent experimental findings [63].

Data availability statement

The raw data supporting the conclusion of this article will be made available by the authors, without undue reservation.

Author contributions

GÓ conceived of the presented idea, developed the theory. GÓ, IP, and SD performed the calculations, carried out the simulations. GÓ, IP, and SD drafted the manuscript and designed figures. JK developed the GPU codes for simulations and critically reviewed the manuscript.

Funding

Acknowledgments

Conflict of interest

The authors declare that the research was conducted in the absence of any commercial or financial relationships that could be construed as a potential conflict of interest.

Publisher's note

All claims expressed in this article are solely those of the authors and do not necessarily represent those of their affiliated organizations, or those of the publisher, the editors and the reviewers. Any product that may be evaluated in this article, or claim that may be made by its manufacturer, is not guaranteed or endorsed by the publisher.

References

1. Beggs J, Plenz D. Neuronal avalanches in neocortical circuits. *J Neurosci* (2003) 23: 11167–77. doi:10.1523/jneurosci.23-35-11167.2003

2. Mazzoni A, Broccard FD, Garcia-Perez E, Bonifazi P, Ruaro ME, Torre V. On the dynamics of the spontaneous activity in neuronal networks. *PLoS One* (2007) 2:e439. doi:10.1371/journal.pone.0000439

3. Pasquale V, Massobrio P, Bologna L, Chiappalone M, Martinoia S. Self-organization and neuronal avalanches in networks of dissociated cortical neurons. *Neuroscience* (2008) 153:1354–69. doi:10.1016/j.neuroscience.2008.03.050

4. Friedman N, Ito S, Brinkman BAW, Shimono M, DeVille REL, Dahmen KA, et al. Universal critical dynamics in high resolution neuronal avalanche data. *Phys Rev Lett* (2012) 108:208102. doi:10.1103/physrevlett.108.208102

5. Hahn G, Petermann T, Havenith MN, Yu S, Singer W, Plenz D, et al. Neuronal avalanches in spontaneous activity *in vivo*. *J Neurophysiol* (2010) 104:3312–22. pMID: 20631221. doi:10.1152/jn.00953.2009

6. Shriki O, Alstott J, Carver F, Holroyd T, Henson RN, Smith ML, et al. Neuronal avalanches in the resting MEG of the human brain. *J Neurosci* (2013) 33:7079–90. doi:10.1523/jneurosci.4286-12.2013

7. Tagliazucchi E, Balenzuela P, Fraiman D, Chialvo D. Criticality in large-scale brain FMRI dynamics unveiled by a novel point process analysis. *Front Physiol* (2012) 3:15. doi:10.3389/fphys.2012.00015

8. Scott G, Fagerholm ED, Mutoh H, Leech R, Sharp DJ, Shew WL, et al. Voltage imaging of waking mouse cortex reveals emergence of critical neuronal dynamics. *J Neurosci* (2014) 34:16611–20. doi:10.1523/jneurosci.3474-14.2014

9. Priesemann V, Wibral M, Valderrama M, Pröpper R, Le Van Quyen M, Geisel T, et al. *Front Syst Neurosci* (2014) 8:108.

10. Bellay T, Klaus A, Seshadri S, Plenz D. *Elife* (2015) 4:e07224.

11. Hahn G, Ponce-Alvarez A, Monier C, Benvenuti G, Kumar A, Chavane F, et al. Spontaneous cortical activity is transiently poised close to criticality. *PLOS Comput Biol* (2017) 13:e1005543. doi:10.1371/journal.pcbi.1005543

12. Seshadri S, Klaus A, Winkowski D, Kanold PO, Plenz D. Altered avalanche dynamics in a developmental NMDAR hypofunction model of cognitive impairment. *Transl Psychiatry* (2018) 8:3. doi:10.1038/s41398-017-0060-z

13. Palva J, Zhigalov A, Hirvonen J, Korhonen O, Linkenkaer-Hansen K, Palva S. Neuronal long-range temporal correlations and avalanche dynamics are correlated with behavioral scaling laws. *Proc Natl Acad Sci United States America* (2013) 110:3585–90. doi:10.1073/pnas.1216855110

14. Fuscà M, Siebenhühner F, Wang SH, Myrov V, Arnulfo G, Nobili L, et al. *Brain criticality predicts individual synchronization levels in humans*. bioRxiv (2022). doi:10.1101/2022.11.24.517800

15. Ponce-Alvarez A, Jouary A, Privat M, Deco G, Sumbre G. Whole-brain neuronal activity displays crackling noise dynamics. *Neuron* (2018) 100:1446–59.e6. doi:10.1016/j.neuron.2018.10.045

16. Yaghoubi M, De Graaf T, Orlandi J, Girotto F, Colicos M, Davidsen J. Neuronal avalanche dynamics indicates different universality classes in neuronal cultures. *Scientific Rep* (2018) 8:3417. doi:10.1038/s41598-018-21730-1

17. Chialvo D, Bak P. Learning from mistakes. *Neuroscience* (1999) 90:1137–48. doi:10.1016/s0306-4522(98)00472-2

18. Chialvo DR. complexity and criticality: In memory of per bak. *Physica A: Stat Mech its Appl* (2004) 340:7561947–2002.

19. Chialvo DR. Are our senses critical? *Nat Phys* (2006) 2:301–2. doi:10.1038/nphys300

20. Chialvo DR. The brain near the edge. *AIP Conf Proc* (2007) 887:1. doi:10.1063/1.2709580

21. Chialvo DR, Balenzuela P, Fraiman D. The brain: What is critical about it? *AIP Conf Proc* (2008) 1028:28. doi:10.1063/1.2965095

22. Fraiman D, Balenzuela P, Foss J, Chialvo DR. Ising-like dynamics in large-scale functional brain networks. *Phys Rev E* (2009) 79:061922. doi:10.1103/physreve.79.061922

23. Expert P, Lambiotte R, Chialvo DR, Christensen K, Jensen HJ, Sharp DJ, et al. Self-similar correlation function in brain resting-state functional magnetic resonance imaging. *J R Soc Interf* (2011) 8:472–9. doi:10.1098/rsif.2010.0416

24. Fraiman D, Chialvo D. What kind of noise is brain noise: Anomalous scaling behavior of the resting brain activity fluctuations. *Front Physiol* (2012) 3:307. doi:10.3389/fphys.2012.00307

25. Deco G, Jirsa VK. Ongoing cortical activity at rest: Criticality, multistability, and ghost attractors. *J Neurosci* (2012) 32:3366–75. doi:10.1523/jneurosci.2523-11.2012

26. Deco G, Ponce-Alvarez A, Hagmann P, Romani G, Mantini D, Corbetta M. How local excitation-inhibition ratio impacts the whole brain dynamics. *J Neurosci* (2014) 34: 7886–98. doi:10.1523/jneurosci.5068-13.2014

27. Senden M, Reuter N, van den Heuvel MP, Goebel R, Deco G. Cortical rich club regions can organize state-dependent functional network formation by engaging in oscillatory behavior. *NeuroImage* (2017) 146:561–74. doi:10.1016/j.neuroimage.2016.10.044

28. Muñoz MA. Colloquium: Criticality and dynamical scaling in living systems. *Rev Mod Phys* (2018) 90:031001. doi:10.1103/RevModPhys.90.031001

29. Plenz D, Ribeiro TL, Miller SR, Kells PA, Vakili A, Capek EL. Self-organized criticality in the brain. *Front Phys* (2021) 9:365. doi:10.3389/fphy.2021.639389

30. Kinouchi O, Copelli M. Optimal dynamical range of excitable networks at criticality. *Nat Phys* (2006) 2:348–51. doi:10.1038/nphys289

31. Bak P, Tang C, Wiesenfeld K. Self-organized criticality: An explanation of the 1/fnoise. *Phys Rev Lett* (1987) 59:381–4. doi:10.1103/physrevlett.59.381

32. Vojta T. Rare region effects at classical, quantum and nonequilibrium phase transitions. *J Phys A: Math Gen* (2006) 39:R143–205. doi:10.1088/0305-4470/39/22/r01

33. Ódor G, Gastner MT, Kelling J, Deco G. Modelling on the very large-scale connectome. *J Phys Complexity* (2021) 2:045002. doi:10.1088/2632-072x/ac266c

34. Williams-García RV, Moore M, Beggs JM, Ortiz G. Quasicritical brain dynamics on a nonequilibrium Widom line. *Phys Rev E* (2014) 90:062714. doi:10.1103/PhysRevE.90.062714

35. Fosque LJ, Williams-García RV, Beggs JM, Ortiz G. Evidence for quasicritical brain dynamics. *Phys Rev Lett* (2021) 126:098101. doi:10.1103/physrevlett.126.098101

36. Korchinski DJ, Orlandi JG, Son S-W, Davidsen J. Criticality in spreading processes without timescale separation and the critical brain hypothesis. *Phys Rev X* (2021) 11: 021059. doi:10.1103/PhysRevX.11.021059

37. Almeira J, Grigera TS, Chialvo DR, Cannas SA. Tricritical behavior in a neural model with excitatory and inhibitory units. *Phys Rev E* (2022) 106:054140. doi:10.1103/PhysRevE.106.054140

38. Ódor G, de Simoni B. Heterogeneous excitable systems exhibit Griffiths phases below hybrid phase transitions. *Phys Rev Res* (2021) 3:013106. doi:10.1103/physrevresearch.3.013106

39. Corral López R, Buendía V, Muñoz MA. Excitatory-inhibitory branching process: A parsimonious view of cortical asynchronous states, excitability, and criticality. *Phys Rev Res* (2022) 4:L042027. doi:10.1103/PhysRevResearch.4.L042027

40. Buendía V, Villegas P, Burioni R, Muñoz MA. Hybrid-type synchronization transitions: Where incipient oscillations, scale-free avalanches, and bistability live together. *Phys Rev Res* (2021) 3:023224. doi:10.1103/PhysRevResearch.3.023224

41. Morales GB, Di Santo S, Muñoz MA. *Unifying model for three forms of contextual modulation including feedback input from higher visual areas*. bioRxiv (2022). doi:10.1101/2022.05.27.493753v1

42. Ye X, Vojta T. Contact process with simultaneous spatial and temporal disorder. *Phys Rev E* (2022) 106:044102. doi:10.1103/PhysRevE.106.044102

43. Ódor G. Robustness of Griffiths effects in homeostatic connectome models. *Phys Rev E* (2019) 99:012113. doi:10.1103/PhysRevE.99.012113

44. Griffiths RB. Nonanalytic behavior above the critical point in a random ising ferromagnet. *Phys Rev Lett* (1969) 23:17–9. doi:10.1103/physrevlett.23.17

45. Moretti P, Muñoz MA. Griffiths phases and the stretching of criticality in brain networks. *Nat Commun* (2013) 4:2521. doi:10.1038/ncomms3521

46. Ódor G, Dickman R, Ódor G. Griffiths phases and localization in hierarchical modular networks. *Scientific Rep* (2015) 5:14451. doi:10.1038/srep14451

47. Cota W, Ódor G, Ferreira SC. Griffiths phases in infinite-dimensional, non-hierarchical modular networks. *Scientific Rep* (2018) 8:9144. doi:10.1038/s41598-018-27506-x

48. Buendí a V, Villegas P, Burioni R, Muñoz MA. The broad edge of synchronization: Griffiths effects and collective phenomena in brain networks. *Philos Trans R Soc A: Math Phys Eng Sci* (2022) 380:20200424. doi:10.1098/rsta.2020.0424

49. Cota W, Ferreira SC, Ódor G. Griffiths effects of the susceptible-infected-susceptible epidemic model on random power-law networks. *Phys Rev E* (2016) 93:032322. doi:10.1103/physreve.93.032322

50. Burkitt AN. A review of the integrate-and-fire neuron model: I. Homogeneous synaptic input. *Biol Cybernetics* (2006) 95:1–19. ISSN 1432-0770. doi:10.1007/s00422-006-0068-6

51. Liang J, Zhou T, Zhou C. Hopf bifurcation in mean field explains critical avalanches in excitation-inhibition balanced neuronal networks: A mechanism for multiscale variability. *Front Syst Neurosci* (2020) 14. ISSN 1662-5137. doi:10.3389/fnsys.2020.580011

52. Orlandi JG, Soriano J, Alvarez-Lacalle E, Teller S, Casademunt J. Noise focusing and the emergence of coherent activity in neuronal cultures. *Nat Phys* (2013) 9:582–90. doi:10.1038/nphys2686

53. Janssen HK. On the nonequilibrium phase transition in reaction-diffusion systems with an absorbing stationary state. *Z Phys B* (1981) 42:151–4. doi:10.1007/bf01319549

54. Grassberger P. On phase transitions in Schlögl's second model. *Z Phys B* (1982) 47:365–74. doi:10.1007/bf01313803

55. Ódor G. *Universality in nonequilibrium lattice systems: Theoretical foundations.* Singapore: World Scientific (2008).

56. Ódor G. Stochastic resetting in backtrack recovery by RNA polymerases. *Phys Rev E* (2016) 94:062411. doi:10.1103/PhysRevE.93.062411

57. Ódor G, Kelling J. Critical synchronization dynamics of the Kuramoto model on connectome and small world graphs. *Scientific Rep* (2019) 9:19621. doi:10.1038/s41598-019-54769-9

58. Ódor G, Kelling J, Deco G. The effect of noise on the synchronization dynamics of the Kuramoto model on a large human connectome graph. *J Neurocomputing* (2021) 461:696–704. doi:10.1016/j.neucom.2020.04.161

59. Ódor G, Deco G, Kelling J. Differences in the critical dynamics underlying the human and fruit-fly connectome. *Phys Rev Res* (2022) 4:023057. doi:10.1103/PhysRevResearch.4.023057

60. Villegas P, Moretti P, Muñoz M. Frustrated hierarchical synchronization and emergent complexity in the human connectome network. *Scientific Rep* (2014) 4:5990. doi:10.1038/srep05990

61. Villegas P, Hidalgo J, Moretti P, Muñoz M. *Proceedings of ECCS 2014: European conference on complex systems* (2016). p. 69–80.

62. Millán A, Torres J, Bianconi G. Complex network geometry and frustrated synchronization. *Scientific Rep* (2018) 8:9910. doi:10.1038/s41598-018-28236-w

63. Ochab JK, Wątorek M, Ceglarek A, Fafrowicz M, Lewandowska K, Marek T, et al. Task-dependent fractal patterns of information processing in working memory. *Scientific Rep* (2022) 12:17866. ISSN 2045-2322. doi:10.1038/s41598-022-21375-1

64. Kuramoto Y. *Chemical oscillations, waves, and turbulence, springer series in synergetics.* Berlin, Heidelberg: Springer Berlin Heidelberg (2012). ISBN 9783642696893.

65. Shinomoto S, Kuramoto Y. Phase transitions in active rotator systems. *Prog Theor Phys* (1986) 75:1105–10. ISSN 0033-068X. doi:10.1143/ptp.75.1105

66. Sakaguchi H. Cooperative phenomena in coupled oscillator systems under external fields. *Prog Theor Phys* (1988) 79:39–46. doi:10.1143/ptp.79.39

67. Antonsen TM, Faghih RT, Girvan M, Ott E, Platig J. External periodic driving of large systems of globally coupled phase oscillators. *Chaos: Interdisc J Nonlinear Sci* (2008) 18:037112. doi:10.1063/1.2952447

68. Ott E, Antonsen TM. Low dimensional behavior of large systems of globally coupled oscillators. *Chaos: Interdisc J Nonlinear Sci* (2008) 18:037113. doi:10.1063/1.2930766

69. Childs LM, Strogatz SH. Stability diagram for the forced Kuramoto model. *Chaos: Interdisc J Nonlinear Sci* (2008) 18:043128. doi:10.1063/1.3049136

70. Deuflhard P. Order and stepsize control in extrapolation methods. *Numerische Mathematik* (1983) 41:399–422. doi:10.1007/bf01418332

71. Hairer E, Norsett SP, Wanner G. Solving ordinary differential equations I. In: *Nonstiff problems.* In: *Vol. 8 of springer series in comput. Mathematics.* 2nd ed. Berlin, Heidelberg: Springer-Verlag (1987).

72. Maruyama G. Continuous Markov processes and stochastic equations. *Rendiconti Del Circolo Matematico di Palermo* (1955) 4:48. ISSN 1973-90. doi:10.1007/BF02846028

73. Lima Dias Pinto I, Copelli M. Oscillations and collective excitability in a model of stochastic neurons under excitatory and inhibitory coupling. *Phys Rev E* (2019) 100:062416. doi:10.1103/physreve.100.062416

74. Sporns O, Tononi G, Kötter R. The human connectome: A structural description of the human brain. *PLOS Comput Biol* (2005) 1:e42. doi:10.1371/journal.pcbi.0010042

75. The hemibrain dataset. *The hemibrain dataset (v1.0.1)* (2020). Available from: https://storage.cloud.google.com/hemibrain-release/neuprint/hemibrain_v1.0.1_neo4j_inputs.zip (Accessed January 23, 2020).

76. Landman BA, Huang AJ, Gifford A, Vikram DS, Lim IAL, Farrell JAD, et al. Multi-parametric neuroimaging reproducibility: A 3-T resource study. *NeuroImage* (2011) 54:2854–66. doi:10.1016/j.neuroimage.2010.11.047

77. Delettre C, Messé A, Dell L-A, Foubet O, Heuer K, Larrat B, et al. Comparison between diffusion MRI tractography and histological tract-tracing of cortico-cortical structural connectivity in the ferret brain. *Netw Neurosci* (2019) 3:1038–50. doi:10.1162/netn_a_00098

78. Gastner MT, Ódor G. The topology of large Open Connectome networks for the human brain. *Scientific Rep* (2016) 6:27249. doi:10.1038/srep27249

79. Neurodata. *Neurodata* (2015). Available from: https://neurodata.io (Accessed October 2, 2015).

80. Gray Roncal W, Koterba ZH, Mhembere D, Kleissas DM, Vogelstein JT, Burns R, et al. Migraine: MRI graph reliability analysis and inference for connectomics. In: 2013 IEEE Global Conference on Signal and Information Processing (2013). p. 313–6.

81. Docker Hub. *Neurodata/m2g* (2023). Available from: https://hub.docker.com/r/neurodata/m2g/builds.

82. Desikan RS, Ségonne F, Fischl B, Quinn BT, Dickerson BC, Blacker D, et al. An automated labeling system for subdividing the human cerebral cortex on MRI scans into gyral based regions of interest. *NeuroImage* (2006) 31:968–80. doi:10.1016/j.neuroimage.2006.01.021

83. Klein A, Tourville J. 101 labeled brain images and a consistent human cortical labeling protocol. *Front Neurosci* (2012) 6:171. doi:10.3389/fnins.2012.00171

84. Newman MEJ. Modularity and community structure in networks. *Proc Natl Acad Sci U S A* (2006) 103:8577–82. doi:10.1073/pnas.0601602103

85. Blondel VD, Guillaume J-L, Lambiotte R, Lefebvre E. Fast unfolding of communities in large networks. *J Stat Mech Theor Exp* (2008) 2008:P10008. doi:10.1088/1742-5468/2008/10/p10008

86. Humphries MD, Gurney K. Network 'small-world-ness': A quantitative method for determining canonical network equivalence. *PLoS One* (2008) 3:e0002051. doi:10.1371/journal.pone.0002051

87. Restrepo JG, Ott E, Hunt BR. Onset of synchronization in large networks of coupled oscillators. *Phys Rev E* (2005) 71:036151. doi:10.1103/physreve.71.036151

88. Schröder M, Timme M, Witthaut D. A universal order parameter for synchrony in networks of limit cycle oscillators. *Chaos: Interdisc J Nonlinear Sci* (2017) 27:073119. doi:10.1063/1.4995963

89. Sanchez-Rodriguez LM, Iturria-Medina Y, Mouches P, Sotero RC. Detecting brain network communities: Considering the role of information flow and its different temporal scales. *NeuroImage* (2021) 225:117431. ISSN 1053-8119. doi:10.1016/j.neuroimage.2020.117431

90. Deritei D, Lázár ZI, Papp I, Járai-Szabó F, Sumi R, Varga L, et al. Community detection by graph Voronoi diagrams. *New J Phys* (2014) 16:063007. doi:10.1088/1367-2630/16/6/063007

91. Lázár ZI, Papp I, Varga L, Járai-Szabó F, Deritei D, Ercsey-Ravasz M. Stochastic graph Voronoi tessellation reveals community structure. *Phys Rev E* (2017) 95:022306. doi:10.1103/PhysRevE.95.022306

92. Allegrini P, Paradisi P, Menicucci D, Gemignani A. Fractal complexity in spontaneous EEG metastable-state transitions: New vistas on integrated neural dynamics. *Front Physiol* (2010) 1. ISSN 1664-042X. doi:10.3389/fphys.2010.00128

93. Kalashyan AK, Buiatti M, Grigolini P. Ergodicity breakdown and scaling from single sequences. *Chaos, Solitons and Fractals* (2009) 39:895–909. doi:10.1016/j.chaos.2007.01.062

94. Buiatti M, Papo D, Baudonnière P-M, van Vreeswijk C. Feedback modulates the temporal scale-free dynamics of brain electrical activity in a hypothesis testing task. *Neuroscience* (2007) 146:1400–12. ISSN 0306-4522. doi:10.1016/j.neuroscience.2007.02.048

95. Touboul J, Destexhe A. Can power-law scaling and neuronal avalanches arise from stochastic dynamics? *PloS one* (2010) 5:e8982. doi:10.1371/journal.pone.0008982

96. Villegas P, Di Santo S, Burioni R, Muñoz MA. Time-series thresholding and the definition of avalanche size. *Phys Rev E* (2019) 100:012133. doi:10.1103/physreve.100.012133

97. Dalla Porta L, Copelli M. Modeling neuronal avalanches and long-range temporal correlations at the emergence of collective oscillations: Continuously varying exponents mimic M/EEG results. *PLoS Comput Biol* (2019) 15:e1006924. doi:10.1371/journal.pcbi.1006924

98. Sethna JP, Dahmen KA, Myers CR. Crackling noise. *Nature* (2001) 410:242–50. doi:10.1038/35065675

99. Sethna JP, Dahmen KA, Perkovic O. Random-field ising models of hysteresis. In: G Bertotti ID Mayergoyz, editors. *The science of hysteresis.* Oxford: Academic Press (2006). p. 107–79. ISBN 978-0-12-480874-4. doi:10.1016/B978-012480874-4/50013-0

100. Research W. *Graph* (2022). Available from: https://reference.wolfram.com/language/ref/Graph.html (Accessed June 29, 2022).

APPENDIX

Here we show avalanche duration PDF-s without noise in case of the KKI-113 connectome on Appendix figure A1. One see only a slight variation of the PL tail exponents around −2.2, but they are close to the noisy case results.

Similarly, in case of the FF with the application of force in the synchronized phase, i.e., $K = 2$ the PL tails fitted for $t > 20$ do not differ to much, they can be characterized by an exponent −2.21(1) as one can see on Appendix figure A2. The inset shows the rapid drop of the SK order parameter as the function of the force and the maximum both of $\sigma(R)$, $\sigma(\Omega)$ are at $F \simeq 0$. Plotting the F dependence of $\sigma(R)$ on log.-log. scale a PL tail arises, characterized by the exponent −1.34(1), which can be regarded a susceptibilty exponent of the Kuramoto equations. However, $\sigma(\Omega)$ falls exponentially fast as the function of F.

FIGURE A1
Avalanche duration distributions on the KKI-113 connectome for different forces, shown by the legends and at $K = 1$, without noise. Dashed lines are PL fits for $\Delta t > 20$.
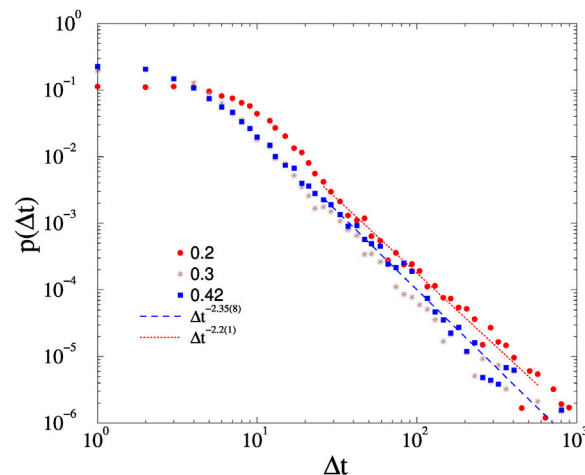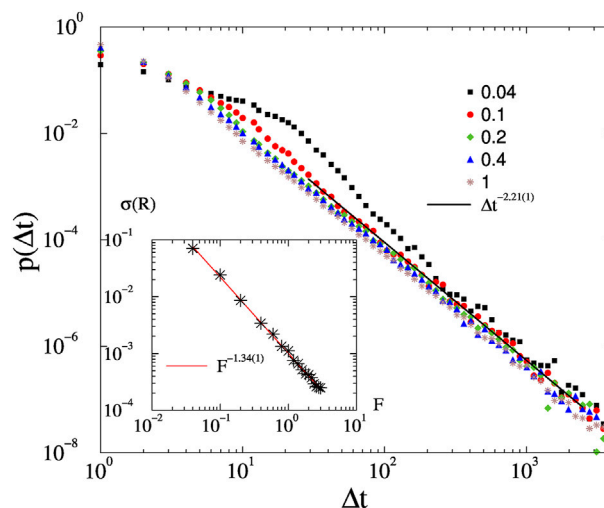

FIGURE A2
Avalanche duration distributions on the fruit-fly connectome for different forces, shown by the legends and at $K = 2$, $\epsilon = 0.01$. Dashed lines are PL fits for $\Delta t > 100$. The inset shows $\sigma(R)$ by increasing F on log. log. scale. The line corresponds to a PL fit.

Prediction of an epidemic spread based on the adaptive genetic algorithm

Bolun Chen[1,2], Shuai Han[1]*, Xiaoluan Liu[1], Zhe Li[1], Ting Chen[1] and Min Ji[1]

[1]Faculty of Computer and Software Engineering, Huaiyin Institute of Technology, Huaian, China, [2]Department of Physics, University of Fribourg, Fribourg, Switzerland

In recent years, coronavirus disease 2019 (COVID-19) has plagued the world, causing huge losses to the lives and property of people worldwide. How to simulate the spread of an epidemic with a reasonable mathematical model and then use it to analyze and to predict its development trend has attracted the attention of scholars from different fields. Based on the susceptible−infected−recovered (SIR) propagation model, this work proposes the susceptible−exposed−infected−recovered−dead (SEIRD) model by introducing a specific medium having many changes such as the self-healing rate, lethality rate, and re-positive rate, considering the possibility of virus propagation through objects. Finally, this work simulates and analyzes the propagation process of nodes in different states within this model, and compares the model prediction results optimized by the adaptive genetic algorithm with the real data. The experimental results show that the susceptible−exposed−infected−recovered−dead model can effectively reflect the real epidemic spreading process and provide theoretical support for the relevant prevention and control departments.

1 Introduction

Epidemic transmission is the spread of various infectious diseases between different individuals and in most cases endangers human health and safety. For example, the recent emergence of COVID-19 was caused by an epidemic virus that spread rapidly worldwide due to its high transmission capacity and difficulty in prevention, resulting in a large number of infected people and deaths, causing significant negative impacts and economic losses in countries worldwide. If trends in the number of infected people are predicted in advance by transmission models and methods, it will make a great contribution to the control of epidemics and the safety of people in all the countries worldwide [1]. Infectious disease models have always been an important basis for studying epidemics, and most scholars from different fields have used infectious disease models to study epidemics. Since the outbreak of COVID-19, the study of epidemic and infectious disease prediction models has once again become a hot topic of research. Due to the existence of certain unknowns and variability of viruses, the factors considered in prediction are gradually increasing, and it is difficult to obtain the complete details of virus infection by model prediction [2]. This paper introduces some other factors to the traditional epidemic model SIR so that the new model can be more applicable to the changes of the actual situation. The addition of latents and deaths to the original model makes the model more accurate in terms of prediction. Infectious disease

models focus on the state model and connectivity between individuals; the state model describes the impact of an infected person within a susceptible population in time, while connectivity determines the movement and contact between populations [3]. The variability of the virus can lead to changes in the mode of transmission and make outbreak protection more difficult. Through in-depth understanding of the virus, asymptomatic infections have also been identified in epidemic prevention and control. Such infections carry the transmitted virus but have no significant symptoms and are highly concealed, causing great inconvenience to the protection efforts [4]. With the advancement of medical treatment, self-healing patients have emerged during the treatment process, which also shows that the treatment greatly differs from patient to patient. This work proposes a new prediction model to predict the spread and trend of the epidemic, considering many factor changes, for example, mortality rate, self-healing rate, and repositive rate.

The choice of parameters in the model prediction has a large impact on the prediction results, and the parameter variables will continuously be adjusted using parameter optimization methods so that the prediction results are constantly close to the target values. Genetic algorithms are algorithms that provide optimal or near-optimal solutions to complex problems by simulating natural evolutionary processes. The algorithm uses computer simulation in a mathematical way to convert the process of problem solving into a process similar to the crossover and mutation of chromosomal genes in biological evolution. Adaptive genetic algorithms work better than conventional optimization algorithms in solving complex optimization problems. Therefore, this article uses the adaptive genetic algorithm to optimize the model parameters so that the predicted values of the model are closer to and match with the true values.

2 Current status of domestic and international research

2.1 Traditional epidemiological models

Traditional epidemic models are mainly based on the susceptible–infected–recovered (SIR) model for outbreak transmission studies. The traditional model can predict the trend of the number of infections in the short term and provide some theoretical support for subsequent outbreak prediction. The SIR model was proposed in 1927 by two epidemiologists, McKendric and Kenmack, and this model is one of the classical infectious disease models, specifically used to predict the change in the number of populations at different moments after an outbreak [5].

As a classical epidemiological model, many scholars have used the SIR model to predict the trend of infection changes in regional epidemics. [6] used kinetic differential equations for SIR to predict future trends in the development of the epidemic; first, deriving parameter data based on the number of previous infections and recoveries and obtaining the predictions by aggregating the parameters. To verify the validity of the pandemic modeling approach, [7] improved on the traditional SIR model by maintaining consistency in the total population size

to ensure that the number of susceptible individuals did not decline monotonically. A final comparative analysis of the modeling data demonstrates that disease transmission can be controlled with appropriate restrictions and strong policies, and likewise, COVID-19 transmission can be controlled in the communities under consideration. One of the most difficult problems in traditional infectious disease models is the presence of a large number of asymptomatic infected individuals. For this reason, [8] improved the SIR model, taking into account asymptomatic or undetected infected individuals in the new model. Furthermore, considering that the previous model took longer time in infectivity and non-isolation, it was somewhat shortened and finally agreed well with the epidemiological data. To study epidemics transmitted within different regions, [9] introduced a new control variable in the SIR model, namely, the effectiveness of the travel blocking operation. The authors also considered an epidemic model based on the vaccination control, using an asymptotic-regressive discrete scheme for numerical analysis, allowing this model to be applied to epidemics that spread within different regions. The exact solution of the classical SIR model is difficult to obtain in most cases, [10] and in order to obtain the exact solution more simply, the authors obtained the exact analytical solution of the model in a parametric form. The main proposals are the display model corresponding to the fixed values of parameters and the proof that numerical solutions can represent analytical solutions, showing that the general solutions of kinetic models can be represented in the exact parametric form. To better account for the dynamic behavior of epidemiology, [11] developed an SIR model with standardized incidence rates and non-linear recovery rates that takes into account the effect of resources available to the public health system. A three-dimensional model for the co-regulation of total population and disease incidence is also presented, explaining the epidemiological causes of endemic complex dynamic behaviors and concluding that adequate public health resources available are essential for epidemic prevention and control. To make the model more stable, [12] developed an epidemiological model of SIR with a latent period and saturation incidence. On the basis of ensuring that the susceptible population satisfies the logistic equation, the incidence rate is set with the susceptible population in a saturated form to find the threshold of whether the disease will die out automatically. According to the experimental results, if the threshold is less than 1, the disease-free equilibrium is globally progressively stable and the disease gradually disappears, whereas if the threshold exceeds 1, the disease does not gradually disappear.

2.2 Improved epidemiological model

The improved infectious disease model is mainly based on the susceptible–latent–infected–recovered (SEIR) model. The basic model is not applicable for complex epidemic studies in many aspects, and some scholars have improved the SIR model in order to be closer to the real spread of the epidemic, and the new improved SEIR adds latent to the original one, which is infected and carry the epidemic virus but do not have any evident symptoms themselves, and this stage is also known as the latent period.

Against the backdrop of the global outbreak COVID-19, countries worldwide are looking for better ways to curb the spread of the epidemic. [13] treated the functions in the model as fuzzy parameters, constructed the infection rate, recovery rate, etc., then applied the model parameters to the model, and finally used the matrix method to verify the stability of the model. Epidemic models are simplified methods used for describing the transmission of infectious diseases through individuals. To better investigate the predictive effect of models on epidemics and the conditions under which epidemics can spread, [14] applied the basics of models to real diseases, derived steady-state conditions, and showed that viruses spread only when the threshold parameter R exceeds 1. Furthermore, the transmission conditions of viruses were demonstrated by numerical simulations. Epidemic diseases can easily constitute a public safety problem, and in order to investigate whether pandemics will disappear automatically without human control, [15] modified the model by adding pathogen movements and human interventions to the model and using the next-generation matrix approach to determine the basic reproduction number, while solving the values yielded from the final result without strong control measures and social distance control. Since pandemics do not disappear automatically, [16] proposed a new improved model based on real data. This model applied the particle swarm optimization algorithm to estimate system parameters and finally concluded that the parameters of the SEIR model were different in different scenarios. By introducing seasonal and random infection, non-linear dynamics were discovered, and good results were obtained by using the model to demonstrate the real evolution situation. To numerically visualize the results, [17] studied a new stochastic epidemic model and quantified the behavior during an outbreak, then modeled the epidemic using Markov chains, and provided an effective computational program for the development of the distribution of outbreak duration. The expected ratio distribution of the number of individuals in each category of the model is used to study the evolution of the epidemic before it disappears, and the resulting results are visually presented in numbers. As the spread of the epidemic brings serious consequences and to better estimate the current spread of the epidemic and predict the change of the epidemic, [18] proposed a new conceptual mathematical model and took into account the impact of isolation, hospitalization, panic, and anxiety; established the boundary and balance; analyzed its stability; and verified the relevant predictions of the important models through research and comparison. [19] mainly studied the SEIR model with vaccination strategies, which determined the different morbidities of exposed and infected population, and proved the global asymptotically stable result of disease-free equilibrium using the Lyapunov function and LaSalle's invariant set theorem. Finally, the sufficient conditions for the global stability of local equilibrium are obtained using composite matrix theory. In addition, the direct numerical simulation of the system shows that there is a periodic solution when the system has three equilibrium points. In order to better judge whether the model is in a stable state theoretically, the new Lyapunov function constructed by [20] shows that the disease-free equilibrium of the model is globally asymptotically stable when the basic reproduction ratio is less than or equal to 1, and the local equilibrium of the model is also globally asymptotically stable when the basic reproduction ratio is greater than 1.

3 Model definition and stability analysis

3.1 Definition of the model

This article is based on the infectious disease model and helps improve the original model by adding some key elements to make it more consistent with the data changes in real life and taking into account not only the transmission of objects and self-healing but also the mortality rate. For real infectious diseases, there are often some death cases. The introduction of the mortality rate will bring the prediction result more in line with the actual situation. The new and improved model (SEIRD) divides the population into five categories, namely, susceptible (S), exposed(E), infected (I), recovered (R), and dead (D) [21], with the following meanings:

Susceptible(S) represents those who do not have the disease but have low immunity and are vulnerable to infection after contact with an infected person.

Exposed (E) represents a person who has been in contact with an infected person and has not yet developed significant symptoms but carries the virus in his or her body.

Infected (I) represents a person who has been infected and can be transmitted to a susceptible person to cause the disease.

Recovered (R) includes those who have been isolated or are now immune due to recovery from the illness.

Dead (D) represents a person who has been infected and cannot be cured in time, and hence, dies.

The SEIRD model contagion mechanism is shown in Figure 1, and the parameter definitions and explanations in the model are shown in Table 1.

According to the system modeling idea, the relationship between different populations in the SEIRD model can be described by a system of differential equations. The total number of users is set to N and satisfies $N(t) = S(t) + E(t) + I(t) + R(t) + D(t)$, and the system of equations for susceptible, exposed, infected, recovered, and dead people over time is as follows [22]:

$$\frac{ds}{dt} = -\eta S - \lambda SI - \lambda_1 SE + \theta R, \qquad (1)$$

$$\frac{dE}{dt} = \eta S + \lambda SI + \lambda_1 SE - \alpha E - \beta E, \qquad (2)$$

$$\frac{dI}{dt} = \alpha E - \gamma I - \omega I, \qquad (3)$$

$$\frac{dR}{dt} = \gamma I + \beta E - \theta R, \qquad (4)$$

$$\frac{dD}{dt} = \omega I. \qquad (5)$$

The initial conditions are $S(0) > 0$, $E(0) \geq 0$, $I(0) > 0$, $R(0) \geq 0$, $D(0) \geq 0$.

3.2 Equilibrium point solving and analysis

According to the actual background of the model, in order to analyze the stability of the model, the equilibrium point of the model should be considered in the bounded region. The equilibrium point is mainly the point with or without disease transmission and the local equilibrium point. When variables E and I are both 0 (there is no infected person or sleeper), we call such a point as the disease-free
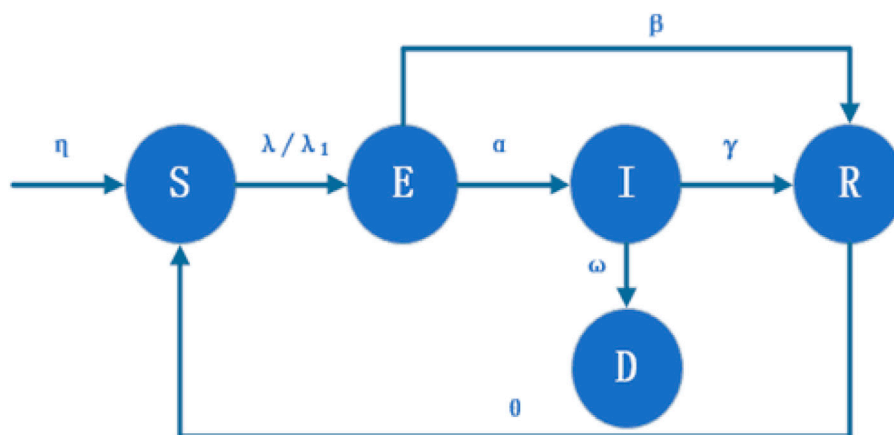
FIGURE 1
Diagram of the SEIRD model transmission mechanism.

TABLE 1 Definition and interpretation of model parameters.

Model parameter	Parameter interpretation
η	Infection rate of object transmission
λ	Infection rate of infected people
λ_1	Infection rate of latent people
α	Infection rate of the latent person to the infected person
γ	Recovery rate of infected individuals
θ	Recurrence rate in recovered individuals
β	Self-healing rate of latent individuals
ω	Mortality rate of infected individuals

equilibrium point. To determine the disease-free equilibrium point, we can make the set of equations as 0, $dS/dt = 0$, $dE/dt = 0$, $dI/dt = 0$, and $dR/dt = 0$, in which we obtain the system of equation non-zero solutions, from which it follows that

$$-\eta S - \lambda SI - \lambda_1 SE + \theta R = 0, \tag{6}$$

$$\eta S + \lambda SI + \lambda_1 SE - \alpha E - \beta E = 0, \tag{7}$$

$$\alpha E - \gamma I - \omega I = 0, \tag{8}$$

$$\gamma I + \beta E - \theta R = 0. \tag{9}$$

Then, by calculation, the solution of the system of equations is the equilibrium point of S, E, I, and R. For the case of the disease-free equilibrium point $E = I = 0$, according to Equations 6–9, we can obtain

$$S = \frac{\theta}{\theta + \eta}, \tag{10}$$

$$S = \frac{\eta}{\theta + \eta}. \tag{11}$$

Then, the disease-free equilibrium point of the model is

$$K_0 = (S, E, I, R) = \left(\frac{\theta}{\theta + \eta}, 0, 0, \frac{\eta}{\theta + \eta} \right). \tag{12}$$

However, the disease-free equilibrium is a disease-free state, which is not the case we are interested in the real world, so the internal equilibrium is not focused on in this article. When neither E nor I is 0 (i.e., there are infected persons and exposed persons), we use the local equilibrium point to represent the possibility of disease transmission, a relatively stable equilibrium point in the epidemic transmission. When $S \neq 0$, $E \neq 0$, $I \neq 0$, $R \neq 0$, we can obtain the solution of the internal equilibrium point through programming calculation, according to (6)–(9).

The Jacobi matrix is obtained according to Equations 1–4 [23]:

$$J = \begin{bmatrix} -\eta - \lambda I - \lambda_1 E & -\lambda_1 S & -\lambda S & \theta \\ \eta + \lambda I + \lambda_1 E & \lambda_1 S - \alpha - \beta & \lambda S & 0 \\ 0 & \alpha & -\gamma - \omega & 0 \\ 0 & \beta & \gamma & -\theta \end{bmatrix}. \tag{13}$$

In turn, the eigenvalues of the Jacobi matrix in the equation can be found from the aforementioned equation as

$$def (\mu I - J) = \begin{bmatrix} \mu + \eta + \lambda I + \lambda_1 E & \lambda_1 S & \lambda S & -\theta \\ -\eta - \lambda I - \lambda_1 E & \mu - \lambda_1 S + \alpha + \beta & -\lambda S & 0 \\ 0 & -\alpha & \mu + \gamma + \omega & 0 \\ 0 & -\beta & -\gamma & \mu + \theta \end{bmatrix}. \tag{14}$$

Then, we substitute (10) and $E = 0$ and $I = 0$ into Eq. 14 to obtain

$$\begin{bmatrix} \mu + \eta & \lambda_1 \dfrac{\theta}{\theta + \eta} & \lambda \dfrac{\theta}{\theta + \eta} & -\theta \\ -\eta & \mu - \lambda_1 \dfrac{\theta}{\theta + \eta} + \alpha + \beta & -\lambda \dfrac{\theta}{\theta + \eta} & 0 \\ 0 & -\alpha & \mu + \gamma + \omega & 0 \\ 0 & -\beta & -\gamma & \mu + \theta \end{bmatrix} = 0 \tag{15}$$

After simplifying, we can turn this equation into a polynomial. The polynomial on μ can be obtained after collation (see the appendix for details), with A denoting the coefficient of μ^3, B denoting the coefficient of μ^2, C denoting the coefficient of μ, and D denoting the algebraic equation without μ. Then, the equation can be transformed as follows:

$$\mu^4 + A\mu^3 + B\mu^2 + C\mu + D = 0. \tag{16}$$

Since the Cartesian sign rule can be used to determine the number of positive or negative roots of a polynomial, it follows from the Cartesian sign rule [24] that the number of negative roots of the characteristic equation is equal to the number of changes in the sign of the coefficients such that the equation satisfies the condition of Eq. 16 to have four negative values, i.e., $\mu_1 < 0, \mu_2 < 0, \mu_3 < 0, \mu_4 < 0$, and satisfy the conditions $A > 0, B > 0, C > 0$, and $D > 0$. The roots of the characteristic equations of the resulting model are all negative, so the model is globally convergent.

3.3 Basic regeneration number and equilibrium steady state

According to the research related to the infectious disease model, there exists a threshold value R_0 in the transmission of infectious diseases, and this threshold is also called the basic regeneration number; when $R_0 \leq 1$, the transmission of infectious diseases will die out naturally with time; while $R_0 > 1$, the infectious disease will break out within a certain period of time. Since the next-generation matrix method [25] is widely used in epidemiology and the calculation of the basic regeneration number, in dynamic populations, this paper mainly uses the next-generation matrix method to calculate R_0. There are two compartments in the model proposed in this paper, namely, $E(t)$ and $I(t)$. According to Eqs 1–5, the vector of X can be obtained by applying the next-generation matrix method, and then, the expressions on F, V are written based on the obtained vectors as follows:

$$X = \begin{bmatrix} E(t) \\ I(t) \end{bmatrix} = F_{1,2}(E, I) - V_{1,2}(E, I), \tag{17}$$

$$= \begin{bmatrix} \eta S + \lambda SI \\ 0 \end{bmatrix} - \begin{bmatrix} \lambda_1 SE - \alpha E - \beta E \\ \alpha E - \gamma I - \omega I \end{bmatrix}. \tag{18}$$

Finding the Jacobi matrix for F, V, we obtain

$$F = Jacobian(F_{1,2}(E, I)) = \begin{bmatrix} 0 & \lambda S \\ 0 & 0 \end{bmatrix}, \tag{19}$$

$$V = Jacobian(V_{1,2}(E, I)) = \begin{bmatrix} \lambda_1 S - \alpha - \beta & 0 \\ \alpha & -\gamma - \omega \end{bmatrix}. \tag{20}$$

The SEIRD model corresponding to R_0 is the maximum eigenvalue of FV^{-1}:

$$\rho(FV^{-1}) = \frac{\alpha \lambda S}{(\lambda_1 S - \alpha - \beta)(\gamma + \omega)}. \tag{21}$$

Furthermore, according to the next-generation matrix method, we can obtain

$$R_0 = \frac{\lambda \alpha \theta}{\lambda_1 \theta - (\alpha + \beta)(\theta + \eta)(\gamma + \omega)}. \tag{22}$$

Theorem 1: The system model in the system of Equations 1–4 is globally asymptotically stable if $R_0 \leq 1$. Theorem 2: If $R_0 > 1$, then the system model in the system of Equations 1–4 is not globally asymptotically stable. Proof: First, we assume that δ is an eigenvector of the matrix F and that

$$R_0 = \rho(FV^{-1}) = \rho(V^{-1}F). \tag{23}$$

Under the condition of $V^{-1}F = R_0$, we obtain

$$\delta R_0 = \delta V^{-1} F. \tag{24}$$

Let *Lyapunov* function [26] be

$$\dot{L} = \delta V^{-1} X. \tag{25}$$

So,

$$\frac{d\dot{L}}{dt} = \delta V^{-1} \frac{dX}{dt} = \delta V^{-1}(F - V)X. \tag{26}$$

Organize

$$\frac{d\dot{L}}{dt} = (\delta R_0 - \delta)X = \delta(R_0 - 1)X. \tag{27}$$

Here, if $R_0 \leq 1$, then $\frac{d\dot{L}}{dt} = 0$, that is, $\delta X = 0$. The result is $E = I = 0$, which is simply $\frac{dE}{dt} = \frac{dI}{dt} = 0$. From this equation, we obtain

$$\eta S + \lambda SI + \lambda_1 SE - \alpha E - \beta E - \alpha E - \gamma I - \omega I = 0. \tag{28}$$

If we substitute $E = 0$, then we can obtain

$$\eta S + \lambda SI - \gamma I - \omega I = 0, \tag{29}$$

$$\eta S + R_0 \frac{\lambda_1 \theta - (\alpha + \beta)(\theta + \eta)(\gamma + \omega)}{\alpha \theta} SI - \gamma I - \omega I = 0, \tag{30}$$

$$\eta S + I(\gamma + \omega)\left(R_0 \frac{\lambda_1 \theta - (\alpha + \beta)}{\alpha} - 1 \right) = 0, \tag{31}$$

namely,

$$R_0 - 1 \approx 0. \tag{32}$$

Then, it can further be obtained that when $R_0 \leq 1$, then $\frac{d\dot{L}}{dt} = 0$. This proves the global asymptotic stability of the model system. Conversely, if $R_0 > 1$, then within the defined neighborhood, $\frac{d\dot{L}}{dt} > 0$. According to *Lyapunov* stability theory, the system is not asymptotically stable under this condition.

4 Experimental results and analysis

4.1 Simulation

In order to get the experimental results closer to the real situation in the real world, at the same time, we can better observe the change trend and change quantity of each stage of the infection model. The simulation experiment [27] considers the number of people in a big city as the standard and sets the initial total population as $N = 10^7$. At the same time, considering the initial approximate number of each population, we set the initial population density as follows:

$$S(0) = 10^7 - 1, E(0) = 0, I(0) = 1, R(0) = 0, \text{ and } D(0) = 0.$$

At the same time, through observation, we found that when $E(t) = I(t) = 0$, there is no infection case in the model, and we can assume that the model has reached a stable state at this time. Figure 2 is a simulation diagram of the SEIRD model, through which we can witness the relationship between the density of five types of individuals and time in the propagation process. It can be seen from the following figure that at the beginning of the epidemic spread, the number of each population has hardly changed, which is quite consistent with the difficulty in
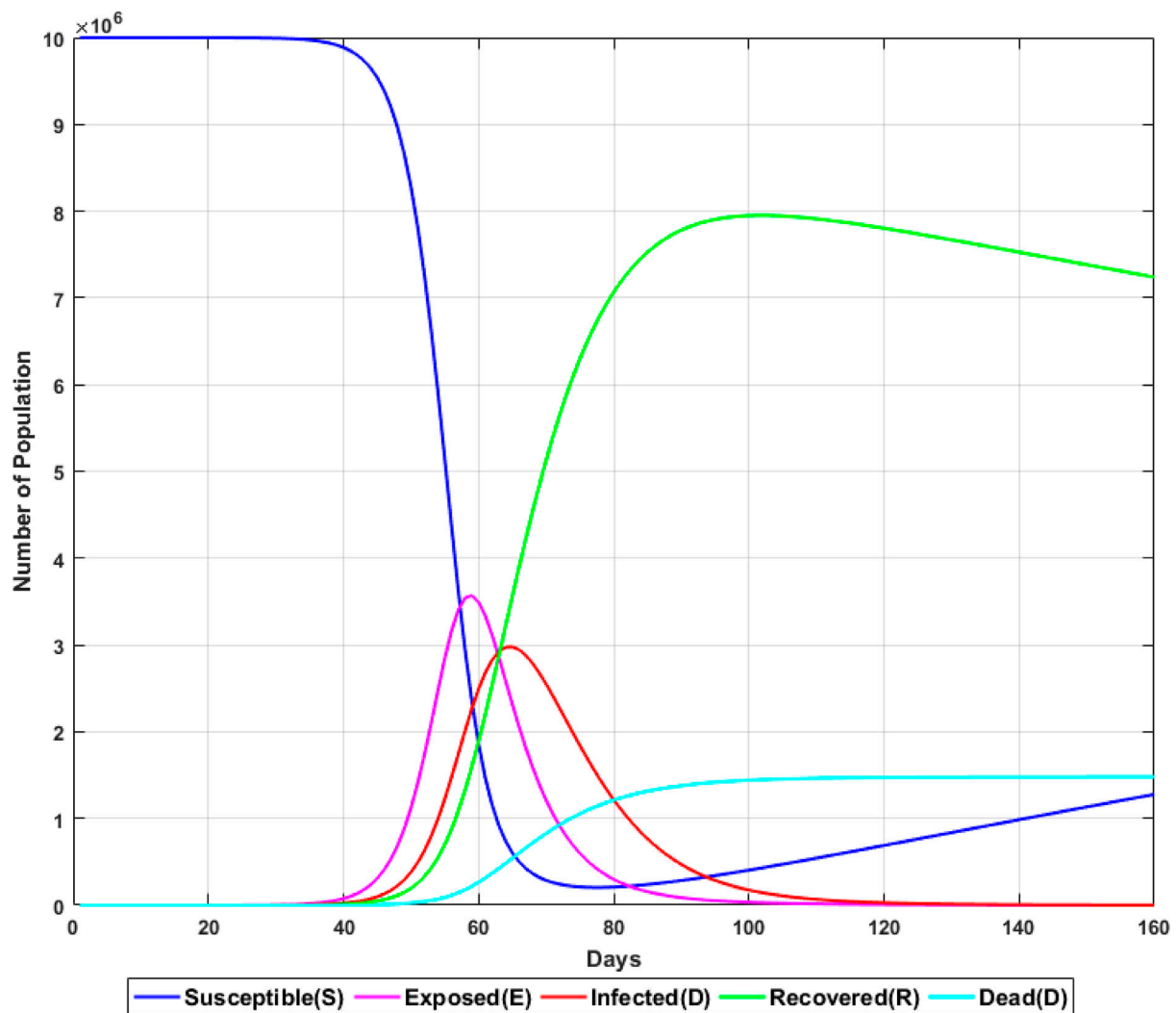
FIGURE 2
Simulation diagram of the SEIRD model simulation experiment.

finding the epidemic at the beginning. In the middle period of the epidemic spread, that is, the sudden period of epidemic, the number of people began to change significantly. In a short period of time, the number of susceptible people rapidly decreased, while the number of the infiltrator and infected people increased sharply. Mapped to reality, the epidemic situation has attracted the attention of government departments and the general public at this time, and began to carry out epidemic prevention and control in a strategic and organized way. The outbreak period was ushered in a short time after the outbreak period, the number of infected people reached its peak, and then, death cases began to appear. Because effective treatment and safety measures have been considered this time, the number of infected people begins to decrease after reaching the peak, and the number of recovered people is gradually increasing. Because the model also considers that the recovered patients may be re-infected after a period of recovery, the number of recovered patients will decrease and the number of susceptible people will increase in the later period. At the same time, the number of infected people will approach 0, the number of dead people will no longer increase, and the model will reach a stable state.

In the real process of spreading the epidemic, each factor is very important for the final result. Therefore, in simulation training, some important parameters should be simulated with different values, such as cold chain transmission probability, infected person transmission probability, rehabilitation rate, and recovery rate, and the results of numerical simulation should be compared and analyzed to achieve better prediction results. In the spread of the epidemic, the number of the lurker and infected people is very important for the prevention and control of the epidemic, so in the simulation experiment, we focus on observing the changing trend of the lurker and infected persons so as to obtain an ideal prediction result of the epidemic.

4.2 Influence of object propagation probability η on the epidemic spread

Object transmission [28] mainly means that viruses can also spread to various people along with external media. At the beginning of the epidemic, people did not realize that the virus could spread in

FIGURE 3
Simulation diagram of the influence of object propagation probability on the epidemic. **(A)** General map of simulated trends in different populations for different values of the parameters of object propagation; **(B)** trends in the number of susceptible persons for different parameter values of object 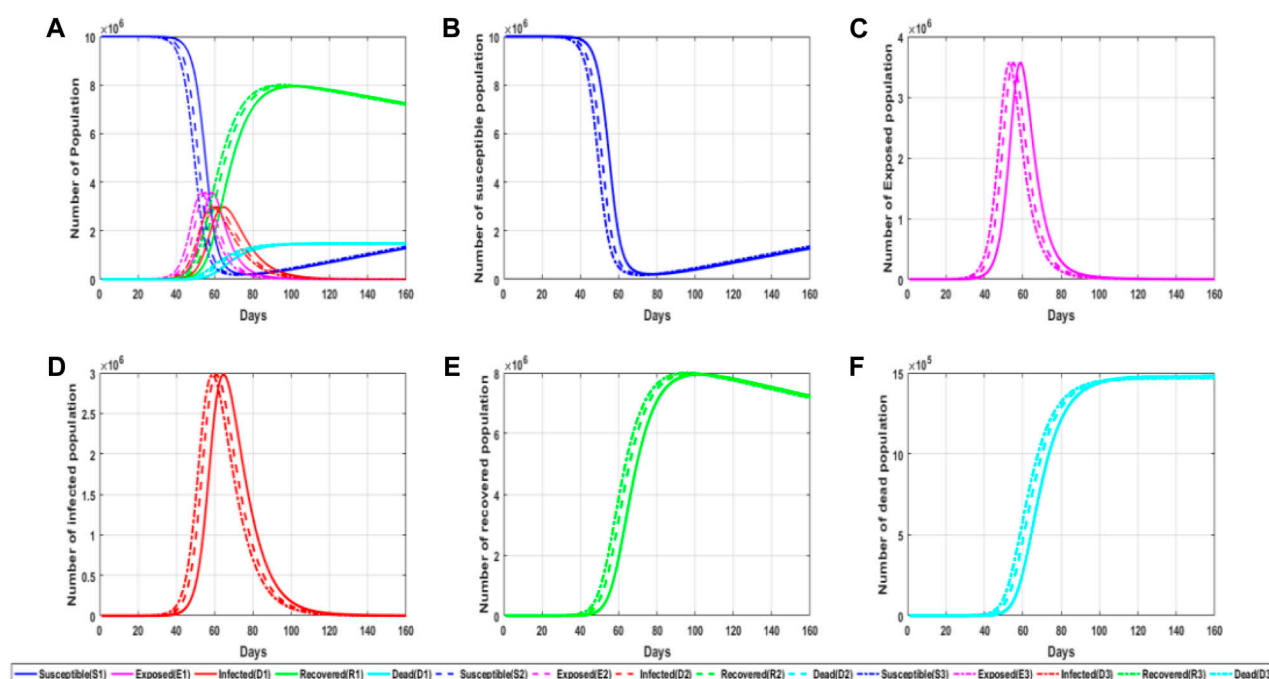propagation; **(C)** trends in the number of latent persons for different values of the parameters of object transmission; **(D)** trends in the number of infected persons for different values of the parameters of object transmission; and **(E)** trends in the number of recovered persons for the different values of the parameters of object transmission. **(F)** Trends in the number of fatalities for different values of object propagation parameters.

the cold chain. Later, after the local epidemic spread was blocked, many clustered epidemics occurred in various places. Finally, through investigation and study, novel coronavirus has strong viability on the surface of frozen products, and the continuous low temperature and humid cold chain environment also provide necessary conditions for the survival of novel coronavirus. Then, people began to pay attention to the prevention and control of object transmission. Figure 3 shows a simulation chart of the influence of object transmission probability η on epidemic transmission.

From the information observed in the figure, it can be found that different object transmission probability values will also have different impacts on the experiment. The greater the object transmission probability value, the faster the epidemic spread, and then the infiltrator and infected people will peak earlier, that is, enter the outbreak period faster. At the same time, we find that the increase in object propagation probability will lead to the peak appearing ahead of time, but it will not change the peak basically. It can be seen that reducing the spread of objects can help us slow down the spread of the epidemic. Usually, we strictly control overseas food and disinfect public places in order to reduce the spread probability of objects, thus slowing down the spread speed.

4.3 Influence of contact probability λ of infected persons on the epidemic spread

The virus infection rate is mainly divided into the infection rate of the infiltrator to the susceptible person and the infection rate of

the infected person to the susceptible person. Figure 4 shows a simulation chart of the influence of the virus infection probability λ on the spread of the epidemic situation.

It can be seen from the aforementioned figure that the infection rate has a significant impact on the epidemic situation. The probability of virus infection can not only affect the peak time of the lurker and infected people but also affect their peak value. It can also be observed from the figure that the number of infected people increases rapidly when the number of the infiltrator reaches its peak, so the growth trend of infected people can be judged by the number of the infiltrator. We found that the greater the value of infection probability, the earlier the change of each population, and the infection rate has different degrees of influence on each population, including the number of recovered patients and susceptible people in the later stage of infection. On one hand, this also explains the importance of wearing a mask because wearing a mask can effectively reduce the probability of infection as it not only reduces the number of infected people but also delays the onset time of infected people and reduces the probability of infection, which is more conducive to our prevention and control of the epidemic.

4.4 Influence of contact probability λ_1 of lurkers on the epidemic spread

In addition to the great influence of infection probability on the spread of the epidemic, the probability of contact with susceptible people in the infiltrator is also very important for the spread of the epidemic. Because the infected person is an individual who has been

FIGURE 4
Simulation diagram of the influence of object propagation probability on the epidemic. **(A)** General graph of simulated trends in the probability of viral infection for different populations at different parameter values; **(B)** trends in the number of susceptible persons at different parameter values of the probability of viral infection; **(C)** trends in the number of latent persons at different parameter values of the probability of viral infection; **(D)** trends in the number of infected persons at different parameter values of the probability of viral infection; and **(E)** trends in the number of convalescent persons at different parameter values of the probability of viral infection. **(F)** Trends in the number of deaths for different values of the probability of viral infection parameter.

diagnosed and has taken relevant isolation measures, this person does not have the ability of contact and transmission for the time being, and the contact probability is mainly for the infiltrator. Figure 5 shows a simulation chart of the influence of contact probability in the infiltrator on the epidemic spread.

From the aforementioned figure, it can be found that the greater the contact probability, the greater the probability of infection to susceptible persons. This also explains why once more infected people are found, measures such as reducing travel and isolating at home are adopted because some symptoms of the infiltrator have not been found yet, but it may spread to other people, so it is necessary to reduce the contact probability at this time. The greater the contact probability, the higher the possibility that the susceptible person will be infected. At the same time, the faster and shorter the time required for the susceptible person to become the infiltrator, which will eventually lead to a higher peak value in the infiltrator, that is, the number of the infiltrator will greatly increase. The sharp increase in the number of infected people will bring great challenges to the prevention and control of the epidemic, so when the outbreak is serious, travel is generally restricted and contact is reduced.

4.5 Influence of recovery probability γ on the epidemic spread

Recovery probability is one of the most important factors in epidemic prevention and control. As long as the recovery probability is relatively high in the process of epidemic spread, the epidemic can end

quicker, and the losses caused are relatively small. It can be seen that recovery probability is very important for us to study the spread of an epidemic. The recovery probability in this work means that the virus carrier does not carry the virus after treatment or autoimmunity and can no longer spread to others. The self-healing probability of the incubation period and the successful treatment probability of infectious patients belong to recovery probability. Figure 6 shows a simulation chart of the impact of recovery probability γ on the epidemic spread.

As can be seen from the aforementioned figure, the higher the probability of recovery, the quicker the epidemic will end; the peak value of the infiltrator and infected people will decrease tremendously, and the time to reach the peak value will be delayed, and the number of dead people will also decrease significantly. Therefore, it can be concluded that under the condition of a relatively high recovery rate, all groups in the spread of the epidemic are developing toward a more ideal situation. From this figure, it can be concluded that constantly studying more effective therapeutic drugs and encouraging the general public to vaccinate are all aiming at improving the self-healing and healing abilities so that we can take more initiative in epidemic prevention and control.

4.6 Influence of re-positive probability θ on the epidemic spread

The repositive rate [29] refers to the probability that patients are re-infected with viruses and become virus carriers after a

FIGURE 5
Simulation of the impact of sleeper contact probability on the epidemic. **(A)** General plot of simulated trends in the probability of latent exposure for different populations for different parameter values; **(B)** trends in the number of susceptible persons for different parameter values of the probability of latent exposure; **(C)** trends in the number of latent persons for different parameter values of the probability of latent exposure; **(D)** trends in the number of infected persons for different parameter values of the probability of latent exposure; and **(E)** trends in the number of convalescent persons for different parameter values of the probability of latent exposure. **(F)** trends in the number of deaths for different parameter values of the probability of latent exposure.

period of recovery. In the early stage of the epidemic, the rate of recovery did not attract great attention. With the deepening of research and strict control, it was gradually found that the recovered patients still had the probability of becoming infected after a period of time. Figure 7 is a simulation chart of the influence of repositive probability θ on the epidemic spread.

From the aforementioned figure, it can be concluded that in the early stage of the epidemic, the reactivation rate will not affect the number change of each population, but in the middle stage of the epidemic, with the increase in the number of recovered patients, the reactivation rate begins to affect the number change of the population. The higher the recovery rate, the number of recovered patients will gradually decrease, and the peak value of recovered patients will be advanced and reduced. For susceptible people, the number of this population will increase in the later period, but it can be seen that the repositive rate has little impact on the lurker and infected people and will only slightly increase the number of infected people in the later period, which also shows from the side that the repositive and the first-time infected people have almost the same impact in epidemic prevention and control. Therefore, mapped to the actual epidemic prevention, even if there are some antibodies in the recovered patients, they still carry out the same management as ordinary susceptible people in the epidemic control.

5 Parametric optimization method based on the genetic algorithm

5.1 Adaptive genetic algorithm

The genetic algorithm (GA) was first proposed by John Holland. It is an algorithm that helps find the optimal solution or approximate optimal solution to complex problems by simulating the process of natural evolution. The algorithm is designed according to the evolution of organisms in nature. Through mathematical methods and computer simulation operations, the algorithm converts the problem solving process into processes similar to the crossover and variation of chromosome genes in biological evolution. When solving more complex combinatorial optimization problems, compared with some conventional optimization algorithms, better optimization results can usually be obtained relatively quickly. At present, genetic algorithms have been widely used in various fields.

Compared with traditional optimization algorithms, the genetic algorithm uses probability rules instead of certain rules. Therefore, the genetic algorithm has the characteristics of global optimization and simple operation, which is suitable for solving complex optimization problems. In this work, the genetic algorithm is used to analyze the impact of different types of population on disease dynamics, optimize model parameters, and consider the changes of objective factors such as the gradual improvement of
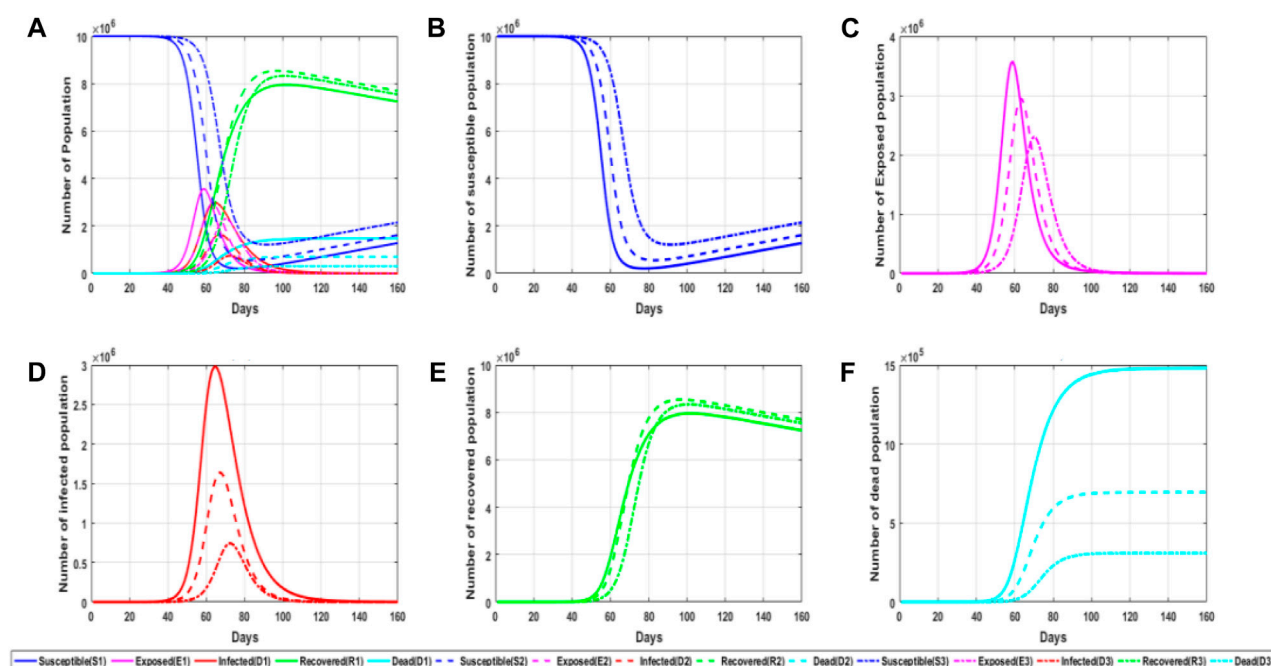
FIGURE 6
Simulation diagram of the influence of recovery probability on an epidemic situation. **(A)** General graph of simulated trends in the probability of recovery for different populations at different parameter values; **(B)** trends in the number of susceptible persons at different parameter values of the probability of recovery; **(C)** trends in the number of latent persons at different parameter values of the probability of recovery; **(D)** trends in the number of infected persons at different parameter values of the probability of recovery; and **(E)** trends in the number of recovered persons at different parameter values of the probability of recovery. **(F)** trends in the number of deaths at different parameter values of the probability of recovery.

isolation measures in the early and late stages of the epidemic. Using the simulation software application MATLAB, an improved SEIRD epidemic prediction model was built. First, we consider that the incubation period is contagious and rehabilitative, and second, we consider that the recovered person is repositive and the infected person is fatal. Finally, the epidemiological transmission trends with different probability in different periods are simulated so that the prediction results are obtained.
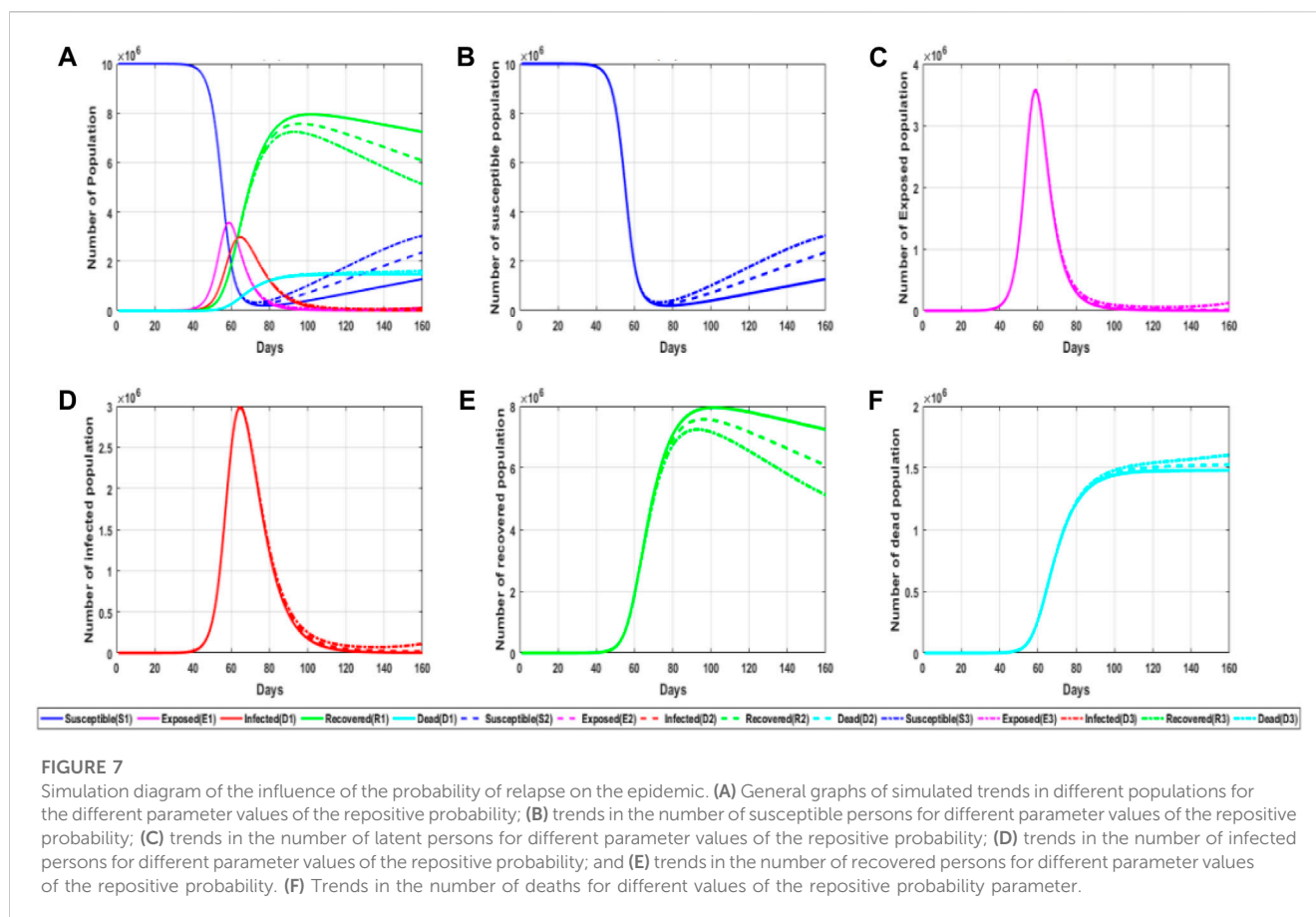
In the face of complex non-linear optimization problems, the traditional genetic algorithm is prone to insufficient optimization ability, causing the algorithm to fall into a local optimal solution. In this article, an improved adaptive genetic algorithm (AGA) is used to change the heterogeneity and crossover rate through the adaptive adjustment of genetic parameters to achieve the retention of excellent individuals of offspring, which not only improves the convergence accuracy of genetic algorithms but also accelerates the convergence speed. In AGA, the cross probability Px and the variation probability Pm are adaptively adjusted according to the following:

$$P_x = \begin{cases} k_1 \dfrac{f_{max} - f'}{f_{max} - f_{avg}}, & f' \gg f_{avg} \\ k_3, & f' < f_{avg}, \end{cases} \quad (33)$$

$$P_m = \begin{cases} k_2 \dfrac{f_{max} - f}{f_{max} - f_{avg}}, & f \gg f_{avg} \\ k_4, & f < f_{avg}. \end{cases} \quad (34)$$

In the formula, f_{max} represents the maximum adaptation value in the population, f_{avg} represents the average adaptation value of each generation of population, f' represents the larger of the adaptation values of two individuals to cross, f represents the adaptation value of the individual to be mutated, and $k1$, $k2$, $k3$, and $k4$ consider the value of the (0,1) interval.

It can be seen from the formula that as the population evolves, the solution may be aggregated to the optimal solution, and f_{avg} gradually approaches f_{max} so that the cross-probability P_x and the variation probability P_m gradually decrease, which helps maintain the excellent structure that the population has formed. In the same generation of populations, the probability of crossover and mutation of different individuals changes linearly with their own adaptation values. The lower the probability of crossover and variation in individuals with higher adaptability, the greater the probability of crossover and variation in individuals with lower adaptability. When the adaptive value of an individual is equal to the optimal adaptation value f_{max} in the contemporary population, its crossover and variation probabilities are calculated to be 0 by a formula, which allows these excellent individuals to be preserved, but it is likely that these excellent individuals will grow exponentially in the evolutionary process, resulting in an excessive convergence. In order to solve this problem, we choose to search for the global optimal solution by individuals with less than average adaptive values in the population.

FIGURE 7
Simulation diagram of the influence of the probability of relapse on the epidemic. **(A)** General graphs of simulated trends in different populations for the different parameter values of the repositive probability; **(B)** trends in the number of susceptible persons for different parameter values of the repositive probability; **(C)** trends in the number of latent persons for different parameter values of the repositive probability; **(D)** trends in the number of infected persons for different parameter values of the repositive probability; and **(E)** trends in the number of recovered persons for different parameter values of the repositive probability. **(F)** Trends in the number of deaths for different values of the repositive probability parameter.

5.2 Algorithm steps

1) Algorithm steps. Randomly select an initial group and represent each individual in the population with a string, and then evaluate the adaptation value of the randomly generated initial group, according to the adaptability function. If the optimal individual in the group does not improve for several consecutive generations, let the individual's adaptability be the optimal adaptation value, and if the optimal adaptation value is not reached, it will enter the next round of evolution. When selecting the operation, select individuals from the population to inherit according to the optimal preservation strategy and the rules of roulette wheel selection, and pass on excellent individuals directly to the next generation or cross-generate new individuals through pairing and then to the next generation. In the crossover operation, choose two as parents in the population and randomly set an intersection point. The structure behind the point is interchangeable to generate two new individuals until the crossover stops after reaching the best. During the mutation operation, an individual in the population is randomly selected and the gene values on some locus in the individual chromosome coding string are replaced with other alleles of the locus until the mutation process stops after reaching the best value, forming a new individual. Calculate the adaptability function value of individuals in the new generation of population and replace the individuals with the worst adaptive individuals. If the best adaptation value is not reached, the improvement strategy will return to continue to evolve, and if the best adaptation value is reached, the best results will be output.

The main steps and flowchart of the genetic algorithm are shown in Figure 8 below:

Input: M individuals, number of iterations t, and initial group $P(t)$.

Output: New group $P^*(t)$.

1) Express the individual as a string, randomly generate the initial biological group $P(t)$ comprising M individuals, and set the number of iterations t.
2) Assess the adaptability of each individual in the initial group.
3) Choose the best solution for improvement (selection, crossover, and variation).
4) Perform selection operations to inherit optimized individuals directly to the next generation or generate new individuals to the next generation by pairing intersections.
5) Perform cross-operations and act on the cross-operations on the group.
6) Carry out mutation operations and act on the mutation operator on the group. After selection, crossover, and mutation operations, group P(t) obtains the next-generation group $P(t + 1)$.
7) Set the termination condition. If $t = T$, then use the individuals with maximum adaptability obtained during the evolutionary process as the optimal solution output to form a new group $P^*(t)$, and terminate the calculation.

2) Determination of adaptability function. In the evaluation of the adaptability function, in order to reflect the individual's adaptability, it is necessary to introduce an adaptability function that can measure the individual's adaptability. In the genetic algorithm for solving the parameters of the infectious disease
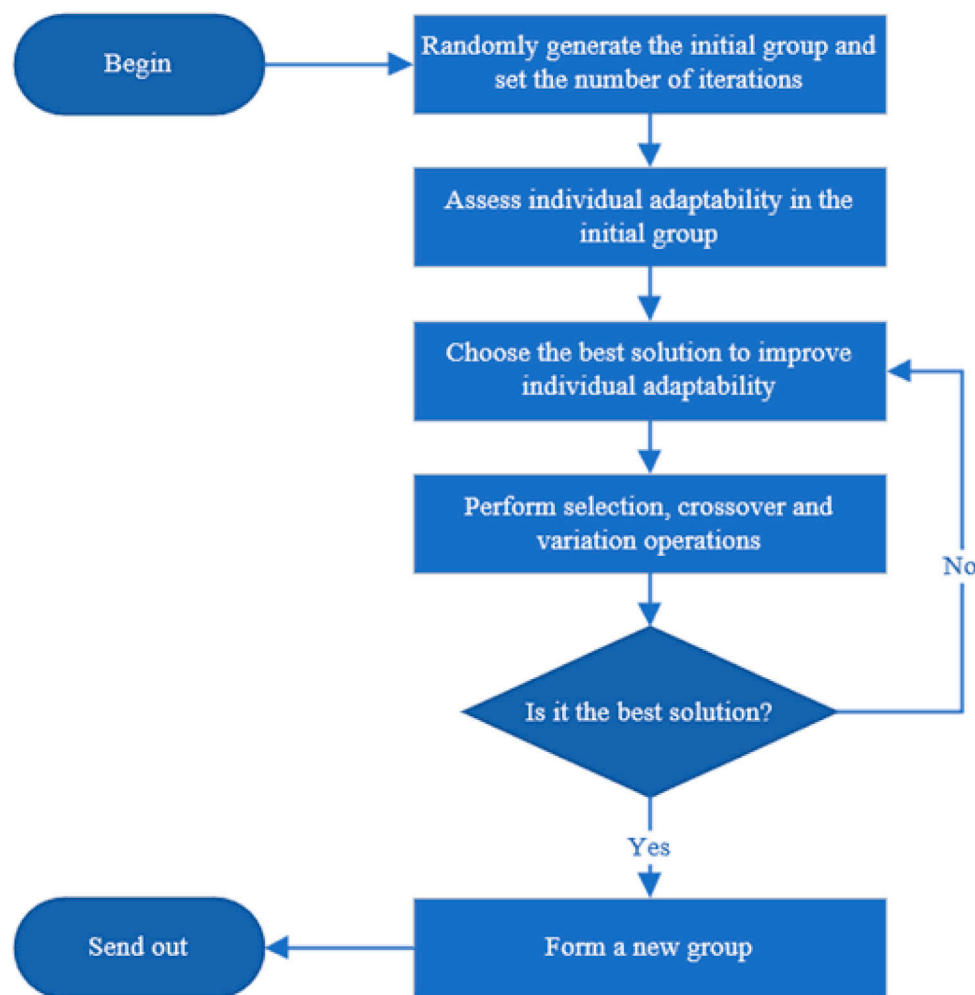
FIGURE 8
Algorithm step flowchart.

model, the sum of the error square of the predicted and real values of the number of infected people infected in the infectious disease model is $F = \sum_{i=1}^{r} \sum_{j=1}^{n_i} (X_{ij} - \overline{X_i})^2$ is the adaptation objective function, and the least square method is used to ensure that the feasible solution and actual solution errors of the number of infected people are minimal.

3) Select the determination of the operator. The purpose of the selection is to inherit optimized individuals directly to the next generation or cross-generate new individuals through pairing and cross-generation so as to improve the global computing efficiency and adaptability. In this paper, a wide range of optimal storage strategies and roulette wheel selection are selected. The roulette gambling method selects a new population based on the probability proportional to the adaptability value (that is, the probability of each individual being selected is directly proportional to the value of its adaptability function). Each individual has the opportunity to be selected, which can improve the average adaptability value of the whole population without destroying the diversity of the population. However, this method is based on probability selection, with statistical errors. Sometimes even individuals with high

adaptability are eliminated, and it is easy to converge to a local maximum. Another choice is the optimal preservation strategy, which sorts the individuals in the population according to the adaptability size, and then selects the most adaptive individuals to maintain them. This behavior can ensure that the optimal individual is not eliminated by random operations. However, because the selection of individuals is determined according to the sorting value, the optimization efficiency depends on the optimal individual.

The specific implementation step of the selection operator is a combination of roulette and optimal selection. Let the initial group size be n (even), and the adaptability function value of individual i is $F(i)$. In the process of selecting individuals to inherit to the next generation, the idea of the optimal preservation strategy is adopted to sort individuals from high to low according to $F(i)$, and the first $n/2$ individuals in the ranking are directly copied to the next-generation population. At the same time, the roulette selection method is used to select $n/2$ individuals from all individuals to inherit to the next generation so that the probability of individual i being selected to be inherited to the next-generation group is

$P_i = \text{Fi}/\sum(i = 1)^n F_i$, and then, a random number between 0 and 1 is generated and matches the probability of each individual inherited to the next generation and finally determines whether the individual is inherited to the next-generation group until $n/2$ individuals are selected. This method uses the scientific probability method to maintain a good diversity of individuals in the population in iteration and also ensures that the best individuals can evolve to the next generation without being eliminated by the randomness of genetic operations, that is, by adding the optimal retention operation to randomness to ensure the convergence of the algorithm. Compared with the simple roulette selection method, this combination strategy runs slightly faster and shows better performance.

4) The selection of crossover and variability. When applying the genetic algorithm, the reasonable selection of the crossover rate and variability is an important factor affecting the efficiency of the algorithm. However, most genetic algorithms give an interval range when setting the crossover and mutation rates, of which the crossover rate is generally greater than 0.9 and between 0.9 and 0.99, and the mutation rate is relatively low, generally below 0.1, between 0.0001 and 0.1, but there is a lot of uncertainty and blindness in determining the approximate range of the cross rate and variability based on the empirical method.

5.3 Evaluation indicators

In order to compare the influence of the application of the parameter optimization method of the adaptive genetic algorithm on the prediction accuracy of the propagation model, it is necessary to evaluate the prediction accuracy of the propagation model. In this paper, three indicators, namely, root mean square error ($RMSE$), average absolute error (MAE), and decision coefficient (R^2), are used to evaluate the predictive accuracy of the model.

$RMSE$ is another commonly used evaluation indicator, indicating that in the process of model fitting, it reflects the gap between the model prediction results and the actual results. The lower the $RMSE$, the more accurate the model is. However, it reflects an objective standard deviation. $RMSE$ can be calculated according to the following formula:

$$RMSE = \sqrt{\frac{1}{m} \sum_{i=1}^{m} (y_i - \hat{y}_i)^2}. \tag{35}$$

MAE is another indicator used to evaluate the accuracy of model prediction results, which represents the gap between model prediction results and the actual results. MAE can be calculated by the following formula:

$$RMSE = \frac{1}{m} \sum_{i=1}^{m} |(y_i - \hat{y}_i)|. \tag{36}$$

Among them, the value range of MAE is $(0, +)$, which is equal to 0 when the predicted value exactly matches the real value, which is the perfect model; the greater the error, the greater the value.

The deciding coefficient (R^2) indicates the fitting optimization of the regression model coefficient evaluated after linear regression. R^2 reflects the proportion of all variations of model-dependent variables being interpreted by independent variables through the

regression model. The larger the value of R^2, the greater the variation in linear return model interpretation. R^2 can be calculated according to the following formula:

$$R^2 = \left[\frac{\sum_{i=1}^{n} \left((y_e^i - \overline{y_e}) (y_0^i - \overline{y_0}) \right)}{\sqrt{\sum_{i=1}^{n} (y_e^i - \overline{y_e})^2} \sqrt{\sum_{i=1}^{n} (y_e^i - \overline{y_0})^2}} \right]^2. \tag{37}$$

When R^2 is 1, it shows that there is no error between the prediction and the real observation values of the model, indicating that the interpretation of the independent variable to the dependent variable in the regression analysis is better; when R^2 is 0, each prediction value of the sample in the model is equal to the mean; when R^2 is close to 0, it indicates that the prediction ability of the model is poor, and the prediction effect is close to using the average of the observed value as the model prediction value. This means that the wrong model may have been used or the assumptions of the model are unreasonable.

5.4 Results and analysis

By consulting the parameters of relevant case data in Wuhan, we set the number of people in close contact with normal people every day at $p = 20$. Because the infected person will have some symptoms, only half of the number of people are seen to be in close contact with normal people. In the process of simulation of the model by the adaptive genetic algorithm, the values of each parameter are set within a certain dynamic range, and then, the value of the model parameters is continuously optimized and improved through the algorithm to achieve the best prediction effect. The value of the model parameters is finally determined as follows:

$\eta = 0.01$, $\lambda = 0.03$, $\lambda_1 = 0.02$, $\alpha = 0.14$,
$\gamma = 0.1$, $\theta = 0.02$, $\beta = 0.005$, and $\omega = 0.02$.

At the same time, in order to verify the effectiveness of the method on the model, the text compares the actual data on the 2020 Wuhan epidemic [30] officially released by the China Health Commission with the trend based on the status of $SEIRD$ nodes to further analyze the difference between the predicted and real values. Figure 9 shows a trend chart that shows the state of each node under real data based on the $SEIRD$ model.

From the figure, it can be seen that the data changes of the number of confirmed cases, and the number of recovered people and deaths in real situations are very similar to the trend of our prediction trend, so it can be shown that after the optimization of adaptive genetic algorithms, the $SEIRD$ model can be applied to the spread of the real epidemic.

At the same time, it can be seen from the figure that the number of confirmed cases increased rapidly in the early stage, and the change trend was evident. However, with a series of measures, such as isolation and wearing masks, the number of confirmed cases gradually decreased, and the number of recovered cases gradually increased, and finally, the number of confirmed cases gradually returned to 0. The trend curve of the recovered patients is also in line with our prediction, and the number of recovered patients is gradually increasing, but in the end, due to the existence of the recovered patients, there will be a slight decline in the end. The trend of death tolls is basically consistent with our predicted results, which first increases slowly and finally tends to be stable. By comparing the
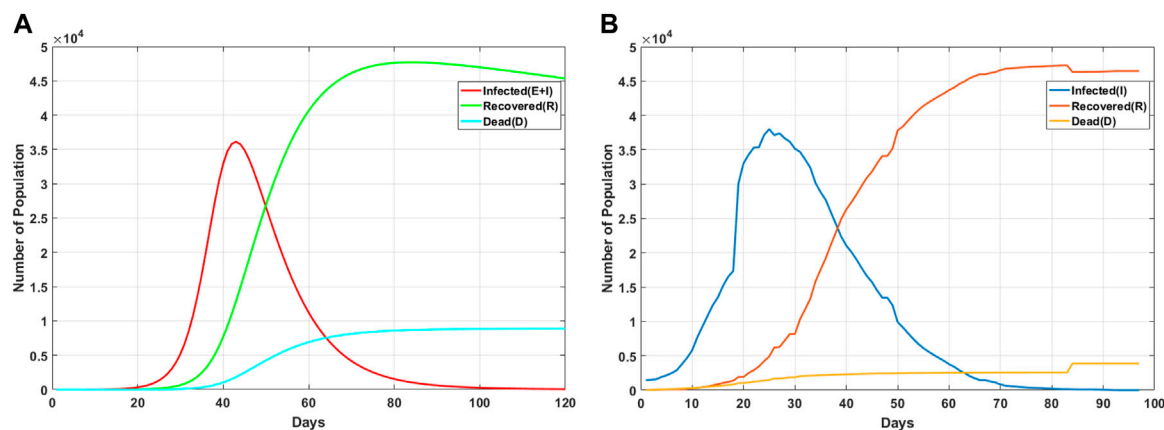
FIGURE 9
Change trend of nodes with different states over time. **(A)** Trend diagram of state nodes based on the SEIRD model. **(B)** Chart of epidemic trends in the real dataset.

actual data with the predicted data, it can be found that the *SEIRD* model can effectively simulate the spread trend of the actual epidemic situation and provide theoretical support for relevant departments.

5.5 Comparative analysis of models

The different types of infectious diseases each have different characteristics in transmission, and this paper is to establish a model to analyze from the perspective of the transmission mechanism. In order to verify the effect of this model in the transmission of new coronavirus causing pneumonia, this paper optimizes different models on the adaptive genetic algorithm and analyzes the data on the optimized classical model and this model, such as the SIR model, SEIR model, and the basic SEIRD model.

The SIR model is one of the most basic of infectious disease models, where S denotes susceptible, I denotes infected, and R denotes recovered. Transmission mechanism: at first, all nodes are in their susceptible state, some nodes reach the infected state after contacting the information, and the infected nodes infect other nodes or reach the recovered state. According to the system modeling idea, the relationship between different populations in the SIR model can be described by a system of differential equations. The total number of users is set as N and satisfies $N(t) = S(t) + I(t) + R(t)$, and the system of equations of susceptible, infected, and recovered people over time is as follows:

$$\frac{ds}{dt} = -\lambda SI, \tag{38}$$

$$\frac{dI}{dt} = \lambda SI - \gamma I, \tag{39}$$

$$\frac{dR}{dt} = \gamma I. \tag{40}$$

The initial conditions are $S(0) \geq 0, I(0) > 0, R(0) \geq 0$.

The SEIR model is an improvement on the SIR model with the addition of the incubator E. Healthy people who have been in contact with a patient do not get sick immediately but become

carriers of the pathogen. According to the system modeling idea, the relationship between different populations in the SEIR model can be described by a system of differential equations. The total number of users is set as N and satisfies $N(t) = S(t) + E(t) + I(t) + R(t)$, and the system of equations for susceptible, exposed, infected, and recovered people over time is as follows:

$$\frac{ds}{dt} = -\lambda SI, \tag{41}$$

$$\frac{dE}{dt} = \lambda SI - \alpha E, \tag{42}$$

$$\frac{dI}{dt} = \alpha E - \gamma I, \tag{43}$$

$$\frac{dR}{dt} = \gamma I. \tag{44}$$

The initial conditions are $S(0) \geq 0, E(0) \geq 0, I(0) > 0, R(0) \geq 0$.

The basic SEIRD model is also improved on the basis of the SEIR model by adding the number of dead people, i.e., the number of people who died from the infection of the epidemic, and this model is more in line with the spread of the real epidemic. According to the system modeling idea, the relationship between different populations in the SEIRD model can be described by a system of differential equations. The total number of users is set as N and satisfies $N(t) = S(t) + E(t) + I(t) + R(t) + D(t)$, and the system of equations for susceptible, exposed, infected, recovered, and dead people over time is as follows:

$$\frac{ds}{dt} = -\lambda SI, \tag{45}$$

$$\frac{dE}{dt} = \lambda SI - \alpha E, \tag{46}$$

$$\frac{dI}{dt} = \alpha E - \gamma I - \omega I, \tag{47}$$

$$\frac{dR}{dt} = \gamma I, \tag{48}$$

$$\frac{dD}{dt} = \omega I. \tag{49}$$

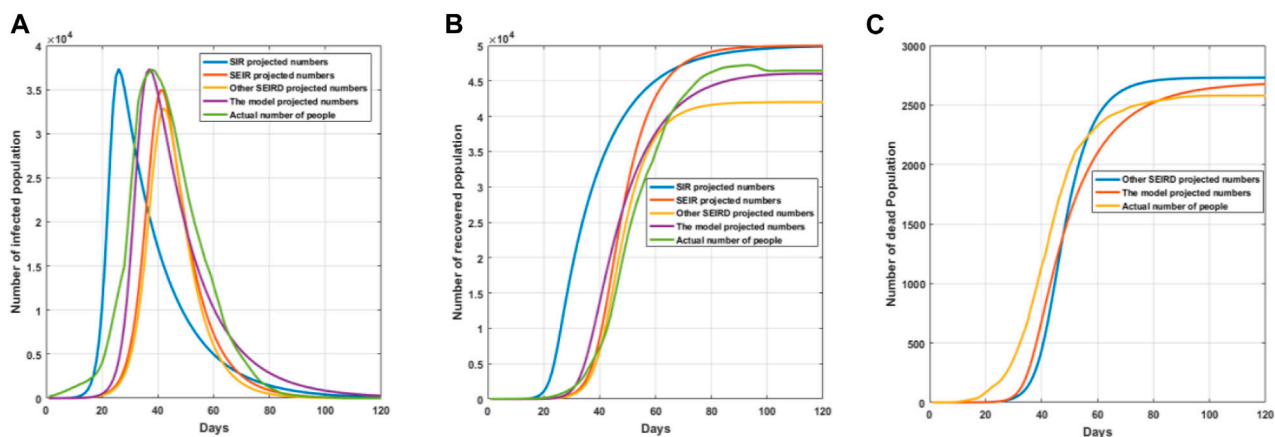The initial conditions are $S(0) \geq 0, E(0) \geq 0, I(0) > 0, R(0) \geq 0, D(0) \geq 0$.

FIGURE 10
Comparative effect graphs of model simulations. **(A)** Trend graph of the number of infections predicted by the model simulation; **(B)** trend graph of the number of recoveries predicted by the model simulation; and **(C)** trend graph of the number of deaths predicted by the model simulation.

This model not only increases the number of dead people but also takes into account the object transmission, the re-positive rate of the recovered people, and the self-healing rate of the latent people, which is very close to the real transmission process of the new coronavirus causing pneumonia.

After the optimization of the adaptive genetic algorithm, the simulation trend of multiple models is shown in Figure 10.

As can be seen in Figure 10A, the trend of infected persons predicted by each model is basically similar, the SIR model does not have an incubation period, and healthy people become infected immediately after contacting infected persons, so it causes the number of infected persons predicted by the SIR model to reach the peak in a relatively short period of time, which leads to the prediction results being very different from the actual infection data. The number of infected persons predicted by the SEIR model is very close to that of the real data, but the number of infected persons has a large gap compared with the real data, which is very close to the real data, but the number of infected people has a large gap compared with the real data, particularly because the SEIR model does not take into account the object transmission and repositive positivity rate, which leads to the actual number of infected people being more than predicted by the model. The underlying SEIRD model also does not take into account object transmission and the repositive positivity rate, and due to the death of some of the infected people, resulting in a lower number of predicted infected people compared to the real infected people. As can be seen from Figure 10B, there is a large difference in the number of recovered persons predicted by each model because the SIR and SEIR models do not take into account those who die, so the number of recovered persons predicted by the model is much higher than the actual number of recovered persons. The underlying SEIRD model also results in a lower number of recovered people than the real data due to the lower number of infected persons predicted by the model. Figure 10C shows that both the base SEIRD model and this model predict the number of deaths which are close to the real number of deaths but both are slightly higher in trend than the real death data; this is because the real data comprise the number of deaths after medical and drug interventions, which results in the predicted data to be higher than the real data. As

can be seen in Figure 10, the improved model in this paper is more accurate in predicting the number of infections, recoveries, and deaths than other models, and is also more in line with the real data compared to the real data.

6 Conclusion

The mechanism of virus transmission is relatively complex in epidemic prevention and control, which requires a more accurate model. In this paper, a SEIRD epidemic transmission model is proposed, which includes factors such as object transmission, self-healing ability, recovery rate, and mortality. Based on this model, this work conducted simulation experiments on each influencing factor to analyze the impact of different factors on the spread of the epidemic. The experimental results show that although the cold chain input probability does not affect the final number of infected people, it will affect the time to reach the peak; the ability to heal is critical in determining the impact of infection, not only affecting the number of infected people but also accelerating the cycle of infection; although the recovery rate will not cause an increase in the number of infected people, it will affect the number of different groups in the later stage of the epidemic; mortality in epidemic prevention and control is closely related to the number of infected people. When the number of infected people is large and treatment is not timely, more deaths will occur. Finally, this work also improves and optimizes the model parameters through the adaptive genetic algorithm, simulates and analyzes the trend of the epidemic from many aspects, and compares and analyzes the real data. The results show that the model optimized by the algorithm can effectively predict the spread of the epidemic, and at the same time, it can bring certain theoretical reference values to epidemic prevention and control.

Data availability statement

The original contributions presented in the study are included in the article/Supplementary Material; further inquiries can be directed to the corresponding author.

Author contributions

Methodology: SH and BC; validation: SH, BC, and XL; data curation: ZL, TC, and MJ; writing—original draft preparation: SH, TC, MJ, and BC; writing—review and editing: SH and BC. All authors contributed to the article and approved the submitted version.

Funding

Conflict of interest

The authors declare that the research was conducted in the absence of any commercial or financial relationships that could be construed as a potential conflict of interest.

Publisher's note

All claims expressed in this article are solely those of the authors and do not necessarily represent those of their affiliated organizations, or those of the publisher, the editors, and the reviewers. Any product that may be evaluated in this article, or claim that may be made by its manufacturer, is not guaranteed or endorsed by the publisher.

Supplementary material

The Supplementary Material for this article can be found online at: https://www.frontiersin.org/articles/10.3389/fphy.2023.1195087/full#supplementary-material

References

1. Zisad SN, Hossain MS, Hossain MS, Andersson K. An integrated neural network and seir model to predict covid-19. *Algorithms* (2021) 14:94. doi:10.3390/a14030094

2. Lacitignola D, Diele F. Using awareness to z-control a seir model with overexposure: Insights on covid-19 pandemic. *Chaos, Solitons & Fractals* (2021) 150:111063. doi:10.1016/j.chaos.2021.111063

3. Verma T, Gupta AK. Network synchronization, stability and rhythmic processes in a diffusive mean-field coupled seir model. *Commun Nonlinear Sci Numer Simulation* (2021) 102:105927. doi:10.1016/j.cnsns.2021.105927

4. Yuan X, Chen S, Yuwen L, An S, Mei S, Chen T. An improved seir model for reconstructing the dynamic transmission of covid-19. In: Proceedings of the 2020 IEEE International Conference on Bioinformatics and Biomedicine (BIBM); December 2020; Seoul, Korea (South). IEEE (2020). p. 2320–7.

5. Husein I, Mawengkang H, Suwilo S, Mardiningsih S. Modeling the transmission of infectious disease in a dynamic network. *J Phys Conf Ser* (2019) 1255:012052. doi:10.1088/1742-6596/1255/1/012052

6. Simha Au., Prasad RV, Narayana S. A simple stochastic sir model for covid 19 infection dynamics for Karnataka: Learning from europe (2020). Available at: https://arxiv.org/abs/2003.11920.

7. Cooper I, Mondal A, Antonopoulos CG. A sir model assumption for the spread of covid-19 in different communities. *Chaos, Solitons & Fractals* (2020) 139:110057. doi:10.1016/j.chaos.2020.110057

8. Gaeta G. A simple sir model with a large set of asymptomatic infectives (2020). Available at: https://arxiv.org/abs/2003.08720.

9. Zakary O, Rachik M, Elmouki I. On the analysis of a multi-regions discrete sir epidemic model: An optimal control approach. *Int J Dyn Control* (2017) 5:917–30. doi:10.1007/s40435-016-0233-2

10. Harko T, Lobo FS, Mak M. Exact analytical solutions of the susceptible-infected-recovered (sir) epidemic model and of the sir model with equal death and birth rates. *Appl Math Comput* (2014) 236:184–94. doi:10.1016/j.amc.2014.03.030

11. Shan C, Zhu H. Bifurcations and complex dynamics of an sir model with the impact of the number of hospital beds. *J Differential Equations* (2014) 257:1662–88. doi:10.1016/j.jde.2014.05.030

12. Zhang J-Z, Jin Z, Liu Q-X, Zhang Z-Y. Analysis of a delayed sir model with nonlinear incidence rate. *Discrete Dyn Nat Soc* (2008) 2008:1–16. doi:10.1155/2008/636153

13. Abdy M, Side S, Annas S, Nur W, Sanusi W. An sir epidemic model for covid-19 spread with fuzzy parameter: The case of Indonesia. *Adv difference equations* (2021) 2021:105–17. doi:10.1186/s13662-021-03263-6

14. Shah NH, Gupta J. *Seir model and simulation for vector borne diseases* (2013).

15. Mwalili S, Kimathi M, Ojiambo V, Gathungu D, Mbogo R. Seir model for covid-19 dynamics incorporating the environment and social distancing. *BMC Res Notes* (2020) 13:352–5. doi:10.1186/s13104-020-05192-1

16. He S, Peng Y, Sun K. Seir modeling of the covid-19 and its dynamics. *Nonlinear Dyn* (2020) 101:1667–80. doi:10.1007/s11071-020-05743-y

17. Artalejo JR, Economou A, Lopez-Herrero MJ. The stochastic seir model before extinction: Computational approaches. *Appl Math Comput* (2015) 265:1026–43. doi:10.1016/j.amc.2015.05.141

18. Kamrujjaman M, Ghosh U, Islam MS. *Pandemic and the dynamics of seir model: Case covid-19* (2020).

19. Li J, Cui N. Dynamic analysis of an seir model with distinct incidence for exposed and infectives. *Scientific World J* (2013) 2013:1–5. doi:10.1155/2013/871393

20. Syafruddin S, Noorani MSM. Lyapunov function of sir and seir model for transmission of dengue fever disease. *Int J Simul Process Model* (2013) 8:177–84. doi:10.1504/ijspm.2013.057544

21. Liu F, Wang J, Liu J, Li Y, Liu D, Tong J, et al. Predicting and analyzing the covid-19 epidemic in China: Based on seird, lstm and gwr models. *PloS one* (2020) 15: e0238280. doi:10.1371/journal.pone.0238280

22. Piccolomini EL, Zama F. Preliminary analysis of covid-19 spread in Italy with an adaptive seird model (2020). Available at: https://arxiv.org/abs/2003.09909.

23. Youssef HM, Alghamdi NA, Ezzat MA, El-Bary AA, Shawky AM. A new dynamical modeling seir with global analysis applied to the real data of spreading covid-19 in Saudi Arabia. *Math Biosci Eng* (2020) 17:7018–44. doi:10.3934/mbe.2020362

24. Mammeri Y. A reaction-diffusion system to better comprehend the unlockdown: Application of seir-type model with diffusion to the spatial spread of covid-19 in France. *Comput Math Biophys* (2020) 8:102–13. doi:10.1515/cmb-2020-0104

25. Intissar A. A mathematical study of a generalized seir model of covid-19. *SciMedicine J* (2020) 2:30–67. doi:10.28991/scimedj-2020-02-si-4

26. Korobeinikov A. Lyapunov functions and global properties for seir and seis epidemic models. *Math Med Biol a J IMA* (2004) 21:75–83. doi:10.1093/imammb/21.2.75

27. Younsi F-Z, Bounnekar A, Hamdadou D, Boussaid O. Seir-sw, simulation model of influenza spread based on the small world network. *Tsinghua Sci Tech* (2015) 20: 460–73. doi:10.1109/tst.2015.7297544

28. Yang F, Zhang Z. A time-delay covid-19 propagation model considering supply chain transmission and hierarchical quarantine rate. *Adv Difference Equations* (2021) 2021:191–21. doi:10.1186/s13662-021-03342-8

29. Zhou X, Cui J. Analysis of stability and bifurcation for an seir epidemic model with saturated recovery rate. *Commun nonlinear Sci Numer simulation* (2011) 16:4438–50. doi:10.1016/j.cnsns.2011.03.026

30. Wan K, Chen J, Lu C, Dong L, Wu Z, Zhang L. When will the battle against novel coronavirus end in wuhan: A seir modeling analysis. *J Glob Health* (2020) 10:011002. doi:10.7189/jogh.10.011002

Burst and Memory-aware Transformer: capturing temporal heterogeneity

Byounghwa Lee*, Jung-Hoon Lee, Sungyup Lee and
Cheol Ho Kim

CybreBrain Research Section, Electronics and Telecommunications Research Institute, Daejeon,
Republic of Korea

Burst patterns, characterized by their temporal heterogeneity, have been observed across a wide range of domains, encompassing event sequences from neuronal firing to various facets of human activities. Recent research on predicting event sequences leveraged a Transformer based on the Hawkes process, incorporating a self-attention mechanism to capture long-term temporal dependencies. To effectively handle bursty temporal patterns, we propose a Burst and Memory-aware Transformer (BMT) model, designed to explicitly address temporal heterogeneity. The BMT model embeds the burstiness and memory coefficient into the self-attention module, enhancing the learning process with insights derived from the bursty patterns. Furthermore, we employed a novel loss function designed to optimize the burstiness and memory coefficient values, as well as their corresponding discretized one-hot vectors, both individually and jointly. Numerical experiments conducted on diverse synthetic and real-world datasets demonstrated the outstanding performance of the BMT model in terms of accurately predicting event times and intensity functions compared to existing models and control groups. In particular, the BMT model exhibits remarkable performance for temporally heterogeneous data, such as those with power-law inter-event time distributions. Our findings suggest that the incorporation of burst-related parameters assists the Transformer in comprehending heterogeneous event sequences, leading to an enhanced predictive performance.

KEYWORDS

burst, temporal heterogeneity, event sequence, timestamp, inter-event time, temporal point process, self-attention, Transformer

1 Introduction

Temporal heterogeneity is frequently referred to as *burst* within the context of complex systems. Numerous natural and social phenomena exhibit bursty temporal patterns such as single-neuron firing (Kemuriyama et al., 2010; Chan et al., 2016; Metzen et al., 2016; Zeldenrust et al., 2018), earthquakes (Corral, 2004; de Arcangelis et al., 2006), solar flares (Wheatland et al., 1998), and human activity (Barabasi, 2005; Karsai et al., 2018). The term temporal heterogeneity rigorously implies that the distribution of inter-event times, which is the time intervals between two consecutive events, exhibits a heavy-tailed distribution such as a power-law distribution. Moreover, when the system is generally temporally heterogeneous, it implies the presence of temporal correlations among inter-event times. For example, the inter-spike interval distribution display temporally heterogeneous patterns, which cannot be simply interpreted as a random or regular process. Numerous studies have addressed temporal correlations between bursty spikes using approaches such as the non-renewal process (Shahi et al., 2016), intensity functions with voltage-dependent terms

(Yamauchi et al., 2011), and transitions between burst and non-burst states (Dashevskiy and Cymbalyuk, 2018). To quantify temporal heterogeneity, two commonly employed single-value metrics are burstiness and memory coefficient.

Figure 1 illustrates the distinction between temporally heterogeneous inter-event times and those that tend toward homogeneity. The event sequences in Figures 1A, D, F serve as examples of temporal heterogeneity with a power-law inter-event time distribution. The event sequences in Figures 1B, C, E, G present instances that exhibit a more homogeneous random characteristic with an exponential inter-event time distribution. Evidently, the bursty event sequence exhibits clustered events within burst trains, in contrast to the non-burst sequence. Such uneven event occurrences can affect the prediction of event sequences. Without properly accounting for the complicated correlation structure and heterogeneity therein, naive models may struggle to effectively discern hidden patterns.

Event sequence data encompass the temporal occurrences of events spanning various domains, ranging from natural phenomena to social activities. Unlike time series data, event sequence data are defined by sequentially ordered timestamps that signify the timing of individual event occurrences. Numerous studies have focused on predicting the timing of subsequent events have been conducted using temporal point processes (TPPs) (Daley and Vere-Jones, 2008). One of the most widely employed TPP is the Hawkes process (Hawkes, 1971). This process embodies a self-exciting mechanism, wherein preceding events stimulate the occurrence of subsequent events. In contrast to the Hawkes process, the self-correcting process provides a feasible method for establishing regular point patterns (Isham and Westcott, 1979).

The Poisson point process can be employed to generate entirely random and memory-less events (Kingman, 1992). In the Poisson process, the inter-event time (IET) follows an exponential distribution. The Cox process is a generalized Poisson process in which the intensity function varies with the stochastic process (Cox, 1955); thus, it is also referred to as a doubly stochastic Poisson process. Cox processes are frequently employed to model and predict the arrival of insurance claims, enabling insurers to assess risk and manage resources effectively (Rolski et al., 2009). If the intensity function is not entirely random, as in the Cox process, but given as a deterministic time-varying function, it is referred to as an inhomogeneous Poisson process.

Leveraging advancements in deep neural networks, recent studies have introduced Hawkes process models based on neural network frameworks. Specifically, the models of Marked Temporal Point Processes (RMTPP) (Du et al., 2016) and Continuous Time LSTM (CTLSTM) (Mei and Eisner, 2017), utilizing Recurrent Neural Networks (RNN) and Long Short-Term Memory (LSTM) (Hochreiter and Schmidhuber, 1997), exhibited better performance than Hawkes processes. More recently, the Transformer Hawkes Process (THP) (Zuo et al., 2020) and the Self-Attentive Hawkes Process (SAHP) (Zhang et al., 2020), both grounded in self-attention mechanisms, have demonstrated improved performance.

Our research was primarily motivated by the idea that incorporating temporal heterogeneous characteristics into event sequence predictions yields a superior performance in forecasting events. We propose a *Burst and Memory-aware Transformer* (BMT) model, signifying its capability to train the Transformer by leveraging insights derived from burstiness and memory coefficient, both of which are associated with temporal heterogeneity. Notably, these two metrics were incorporated as embedding inputs for the Transformer architecture. Moreover, a loss function related to these metrics was formulated and employed, thereby enabling the model to naturally capture
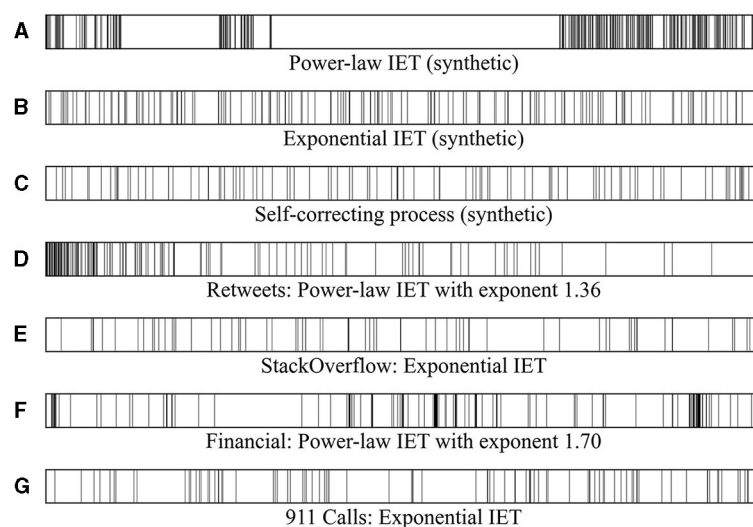

FIGURE 1
(A, D, F) Heterogeneous event sequences with a power-law inter-event time distribution. These event sequences exhibit a high burstiness parameter with significant temporal heterogeneity. (B, C, E, G) Event sequences with an exponential inter-event time distribution. These event sequences have burstiness parameters close to 0 and memory coefficients clustered around 0.
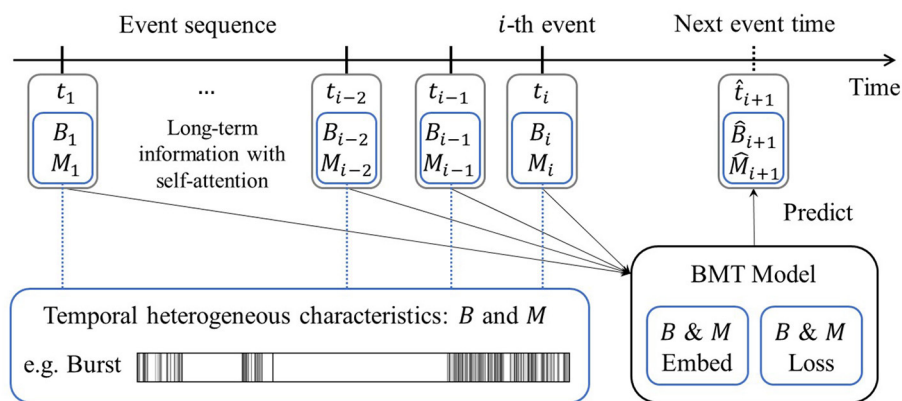
FIGURE 2
Schematic diagram of the Burst and Memory-aware Transformer model. Leveraging information from the preceding events, including burstiness B and memory coefficient M, the model predicts the timing of the next event through B & M embedding and the corresponding B & M loss.

temporal heterogeneity. The overall schematic diagram of the BMT model is depicted in Figure 2.

The main contributions of this paper is summarized as follows:

- The BMT model was developed to integrate insights from the complex systems theory into the Transformer-based temporal point process model, enhancing the capability to incorporate temporal heterogeneity. This study offers a preliminary approach to connect these two distinct disciplines.
- The BMT model surpasses state-of-the-art models by effectively integrating burstiness and memory coefficient into both the embedding procedure and associated loss functions. This is confirmed through extensive numerical experiments across a range of scenarios, including those with and without burstiness and memory coefficient embedding and related loss functions, using real-world datasets and synthetic datasets generated via a copula-based algorithm.
- Our investigation revealed that the BMT model offers particular advantages when dealing with temporally heterogeneous data, such as datasets characterized by a power-law inter-event time distribution, commonly observed in bursty event sequences.
- Our research indicates that excluding either burstiness and memory coefficient embedding or their corresponding loss functions leads to a noticeable reduction in performance. This emphasizes the imperative nature of integrating both elements to achieve optimal performance.

In cases where the inter-event time distribution of the target event sequence exhibits a heavy-tailed distribution, such as a power-law distribution, or where the values of burstiness and memory coefficient significantly deviate from zero, the BMT model ensures superior performance compared to basic Transformer-based models.

The structure of the paper is outlined as follows: Section 2 introduces the background pertaining to the temporal point process, temporal heterogeneity, and generating method

for synthetic datasets; Section 3 introduces our Burst and Memory-aware Transformer model; Section 4 presents numerical experiments on synthetic and real-world datasets; Section 5 presents the performance evaluation results; and Section 6 presents the conclusion.

2 Background

2.1 Temporal point process

A temporal point process (TPP) is a stochastic process involving the occurrence of multiple events as time progresses. The foundational data employed to construct the TPP model consists of event sequence data, encompassing event times $\{t_i\}_{i=1}^n$ along with optional marks $\{\kappa_i\}_{i=1}^n$. For example, spike train sequences of neurons are composed of timings of occurrences, along with action potential as associated marks.

In this study, we examine the unmarked case to specifically investigate the effects of burst and memory phenomena, while excluding the influence of correlations with marks that do not align with the research direction. For the prediction of the marked TPP model, one approach involves the independent modeling of the target's marks by thresholding. Alternatively, based on contextual analysis (Jo et al., 2013), interactions with multiple neighbors within an egocentric network can be considered as marks and subsequently modeled.

TPP encompasses the modeling of the conditional intensity function $\lambda(t|\mathcal{H}_t)$ given the history of event times $\mathcal{H}_t \equiv (t_1, ... t_n)$. The notation for the history of event times, $\mathcal{H}_t$ will be omitted for convenience. The intensity function characterizes the instantaneous event rate at any given time by considering past event occurrences. The probability density function $P(t)$ and cumulative distribution function $F(t)$ can be derived based on the intensity function, as follows (Rasmussen, 2018):

$$P(t) = \lambda(t) \exp\left(- \int_{t_{i-1}}^t \lambda(t')dt'\right), \quad (1)$$

$$F(t) = 1 - \exp\left(-\int_{t_{i-1}}^{t} \lambda(t')dt'\right). \tag{2}$$

2.1.1 Hawkes process

The Hawkes process, also known as the self-exciting point process, is for a situation where a preceding event excites the occurrence of a subsequent event (Hawkes, 1971). The intensity function $\lambda(t)$ of the Hawkes process is defined as

$$\lambda(t) = \zeta + \eta \sum_{t_i < t} \exp\left(-(t - t_i)\right), \tag{3}$$

where the base intensity ζ and η are positive parameters. When a new event occurs during this process, the intensity increases with η and immediately decays exponentially. The probability of the next event occurring is highest immediately following the incidence of the previous event, and it gradually decreases as time elapses. As a result, this process causes events to cluster together. This includes events that happen quickly in a short time and then long times when nothing happens. The generalized Hawkes process is defined as follows:

$$\lambda(t) = \zeta + \eta \sum_{t_i < t} \gamma(t - t_i), \tag{4}$$

where $\zeta \geq 0$, $\eta > 0$, and $\gamma(t)$ is a density on $(0, \infty)$.

2.1.2 Self-correcting process

In contrast to the Hawkes process, the self-correcting process generates regular inter-event time sequences with randomness (Isham and Westcott, 1979). The intensity function $\lambda(t)$ for the self-correcting process is defined as follows:

$$\lambda(t) = \exp\left(\zeta t - \sum_{t_i < t} \eta\right), \tag{5}$$

where ζ and η are positive parameters.

2.1.3 Neural Hawkes process

A limitation of the Hawkes process is that the preceding event cannot inhibit the occurrence of a subsequent event. To overcome these limitations, the neural Hawkes process, which considers the nonlinear relationship with past events using recurrent neural networks, was introduced (Mei and Eisner, 2017). The intensity function $\lambda(t)$ for the neural Hawkes process is defined as follows:

$$\lambda(t) = f\left(\mathbf{w}^{\top}\mathbf{h}(t)\right), \tag{6}$$

where $f(x) = \beta \log\left(1 + \exp(x/\beta)\right)$ is the softplus function with parameter β which guarantees a positive intensity, and $\mathbf{h}(t)$s are hidden representations of the event sequence from a continuous-time LSTM model. Here, the intensity we refer to is not the marked intensity λ_k; Instead, our focus is on the inherent temporal heterogeneity structure, excluding any interference from correlations between event types and times.

2.1.4 Transformer-based Hawkes process

The Transformer is a deep learning architecture for sequence processing such as natural language processing, with a multi-head self-attention module that captures long-range dependencies within sequences (Vaswani et al., 2017). The Transformer is used not only in language models but also in computer vision, audio processing, and time series forecasting (Lim et al., 2021; Wen et al., 2022; Ma et al., 2023). Recently, the Transformer architecture has also been applied to modeling temporal point processes. The Transformer Hawkes Process (Zuo et al., 2020) and the Self-Attentive Hawkes Process (Zhang et al., 2020) were introduced to model the Hawkes process with a self-attention mechanism to capture the long-range correlations underlying both event times and types.

THP and SAHP differ in two aspects: their use of positional encoding and the form of the intensity function. SAHP employs time-shifted positional encoding to address the limitations of conventional methods, which solely account for the sequence order and neglect inter-event times. The intensity function of the THP model is the softplus function of the weighted sum of three terms: ratio of elapsed time from the previous event, hidden representation vector from the encoder, and base. Conversely, the intensity function of the SAHP model is formulated as a softplus of the Hawkes process terms, each of which is derived from the scalar transformation and nonlinear activation function applied to the hidden representation vector from the encoder.

For both the THP and SAHP models, across synthetic and real-world datasets, their performances in event type prediction and event time prediction surpassed that of the baseline model: Hawkes Process as described in Equation (3), Fully Neural Network model (Omi et al., 2019), Log-normal Mixture model (Shchur et al., 2019), Time Series Event Sequence (TSES) (Xiao et al., 2017), Recurrent Marked Temporal Point Processes (Du et al., 2016), and Continuous Time LSTM (Mei and Eisner, 2017). Given the superior performance of THP over the remaining baseline models, this study refrains from direct performance comparison with the SAHP and baseline models (Zuo et al., 2020), opting to concentrate exclusively on performance comparison with the THP model.

2.2 Temporal heterogeneity

Temporal heterogeneity or burst is characterized by various metrics. The most fundamental quantity is the probability density function of the inter-event times. The inter-event time is defined as the time interval between two consecutive events, that is, $\tau_i \equiv t_{i+1} - t_i$, where t_i is i-th event time of the event sequence.

When the inter-event time distribution is heavy-tailed, the corresponding event sequence exhibits temporal heterogeneity. Specifically, the power-law inter-event distribution found in diverse natural and social phenomena is as follows:

$$P(\tau) \sim \tau^{-\alpha}, \tag{7}$$

where a is a constant and α is a power-law exponent.

2.2.1 Burstiness parameter

Several metrics characterize the properties of temporal heterogeneity. Burstiness B measures the burst phenomenon (Goh and Barabási, 2008), and is defined as follows:

$$B \equiv \frac{r-1}{r+1} = \frac{\sigma - \langle\tau\rangle}{\sigma + \langle\tau\rangle}, \qquad (8)$$

where $r \equiv \sigma/\langle\tau\rangle$ is the coefficient of variation (CV) of the inter-event time and σ and $\langle\tau\rangle$ is the standard deviation and average of τs, respectively. Here, $B = -1$ for regular event sequences, $B = 0$ for Poissonian random cases, and $B = 1$ for extremely bursty cases.

When the number of events is sufficiently small, the burstiness parameter causes errors. The fixed burstiness parameter considering the finite-size effect is as follows (Kim and Jo, 2016):

$$B_n \equiv \frac{\sqrt{n+1}\,r - \sqrt{n-1}}{(\sqrt{n+1}-2)r + \sqrt{n-1}}. \qquad (9)$$

We employed the fixed burstiness parameter (9) to handle short-length event sequences throughout this study.

2.2.2 Memory coefficient

The memory coefficient M quantifies the correlations between consecutive inter-event times within a sequence consisting of n inter-event times, that is, $\{\tau_i\}_{i=1,...,n}$, as follows (Goh and Barabási, 2008):

$$M \equiv \frac{1}{n-1}\sum_{i=1}^{n-1}\frac{(\tau_i - \langle\tau\rangle_1)(\tau_{i+1} - \langle\tau\rangle_2)}{\sigma_1\sigma_2}, \qquad (10)$$

where $\langle\tau\rangle_1$ ($\langle\tau\rangle_2$) and σ_1 (σ_2) are the average and standard deviation of the inter-event times $\tau_1, \tau_2, ..., \tau_{n-1}$ ($\tau_2, \tau_3, ..., \tau_n$), respectively. This is the Pearson correlation coefficient between consecutive inter-event times. Here, $M = 0$ indicates no correlation, and $M > 0$ indicates a positive correlation, which means that a large inter-event time follows after a large inter-event time and vice versa for small inter-event time. $M < 0$ indicates a negative correlation, which means small inter-event time follows after the large inter-event time and vice versa for a large inter-event time.

2.2.3 Applications of B and M to BMT model

When plotting M on the x-axis and B on the y-axis for datasets with various inter-event time distributions, it can be observed that event sequences with similar inter-event time distributions tend to cluster at similar positions (Goh and Barabási, 2008). Essentially, if the ranges of B and M values are known, a rough estimate of the inter-event time distribution can be anticipated. Building on this insight, we devised a BMT model to facilitate learning by designing a method in which the values of B and M were combined and fed into the encoder as inputs. Specifically, when the values of B and M exhibit temporal heterogeneity in their ranges, the encoder of the Transformer can produce inter-event time prediction values with a heavy-tailed inter-event time distribution.

Moreover, B and M are not independent: they are intertwined and move in conjunction. For instance, even when attempting to alter only M by shuffling the inter-event times, B can also change. This serves as evidence that embedding both B and M concurrently yields superior performance compared with embedding either one of them individually.

2.3 Copula-based algorithm for generating sequence of inter-event times

To comprehend the impact of burstiness and memory coefficient on the model, we generated synthetic datasets using a copula-based algorithm (Jo et al., 2019). The content of the copula-based algorithm in this study was obtained from Jo et al. (2019). For convenience, we provide a brief overview of the relevant content. The copula-based algorithm models the joint probability distribution of two consecutive inter-event times, that is, $P(\tau_i, \tau_{i+1})$, by adopting the Farlie-Gumbel-Morgenstern (FGM) copula (Nelsen, 2006). The joint probability distribution according to the FGM copula is formulated as follows:

$$P(\tau_i, \tau_{i+1}) = P(\tau_i)P(\tau_{i+1})[1 + rf(\tau_i)f(\tau_{i+1})], \qquad (11)$$

where

$$f(\tau) \equiv 2F(\tau) - 1, \quad F(\tau) \equiv \int_0^\tau d\tau' P(\tau'). \qquad (12)$$

Parameter r is used to control the correlation between τ_i and τ_{i+1} and is in the range of $-1 \leq r \leq 1$. $F(\tau)$ is the cumulative distribution function (CDF) of $P(\tau)$. After applying the transformation method (Clauset and Shalizi, 2009), the next inter-event time τ_{i+1} can be obtained as Jo et al. (2019)

$$\tau_{i+1} = F^{-1}\left[\frac{c_i - 1 + \sqrt{(c_i + 1)^2 - 4c_i x}}{2c_i}\right], \qquad (13)$$

where F^{-1} is the inverse of $F(\tau)$, $c_i \equiv rf(\tau_i)$, and x is a random number sampled from a uniform distribution within interval $0 \leq x < 1$. The copula-based algorithm has the advantage of generating event sequences with independent control of the inter-event time distribution and memory coefficient.

3 Burst and Memory-aware Transformer

3.1 Discretization of B and M

Given that the burstiness parameter and memory coefficient are real numbers within the range of $[-1, 1]$, it is necessary to discretize them for embedding within the Transformer. We adopt the uniform discretization transform; the range $[-1, 1]$ is divided into segments of fixed length by the number of bins b, respectively, and subsequently mapped to a single natural number. The continuous values of the burstiness parameter B and memory coefficient M are discretized into natural numbers d_B and d_M, respectively. For example, when the number of bins is $b = 4$, then $d_B = 3$ if $M = 0.2$, and it $d_B = 1$ if $M = -0.7$. Then, one can obtain the discretized pairs of B and M as (d_B, d_M), where d_B and

d_M are ranging from 1 to b. To map the pair into a unique natural number, the Cantor pairing function was employed. The Cantor pairing function maps discretized d_B and d_M into a unique natural number $d_{B,M}$ as

$$d_{B,M} \equiv \frac{1}{2}(d_B + d_M)(d_B + d_M + 1) + d_M. \quad (14)$$

When the number of discretization bins is b, the number of $d_{B,M}$ is b^2, corresponding to the vocabulary size of the Transformer. Then, we can obtain the one-hot vector of the discretized B & M as $\mathbf{d}_{B,M} \in \mathbb{R}^{b^2}$.

3.2 Embedding event times, and *B* and *M*

The event sequence $\mathcal{S} = \{t_i\}_{i=1}^{n}$ of n events and discretized and one-hot B & M, $\mathbf{d}_{B,M}$ are fed into the self-attention module after proper encoding. First, the event times are transformed using the positional encoding method (Vaswani et al., 2017) to embed the temporal order information into an event sequence. The j-th element of sinusoidal positional encoding for the i-th event time t_i is calculated as:

$$[\mathbf{z}_t(t_i)]_j = \begin{cases} \sin(\omega_k t_i), & \text{if } j = 2k \\ \cos(\omega_k t_i), & \text{if } j = 2k+1, \end{cases} \quad (15)$$

where $\omega_k = 1/10,000^{2k/d}$, the embedding index k is the quotient when dividing j by 2, and $\mathbf{z}_t(t_i) \in \mathbb{R}^d$, where d is the encoding dimension. By multiplying ω_k with the event time t_i, it is converted into an angle, which is then mapped to sine and cosine functions, providing different positional information for each event time.

For the given event times $\{t_i\}_{i=1}^{n}$, the inter-event times are $\tau_i \equiv t_{i+1} - t_i$ for $i = 1, ..., n - 1$. The burstiness parameter (9) and memory coefficient (10) were calculated for all partial sequences. This essentially implies that the input to the encoder is fed sequentially from $t_1, ..., t_i, ..., t_n$, and for each of these instances, the B & M embedding incorporates the calculated B and M values up to t_1 (i.e., B_1 and M_1), ..., up to t_i (i.e., B_i and M_i), ..., and up to t_n ($B_n = B$ and $M_n = M$ for the entire sequence). Note that, during the actual operation of the Transformer, computations are performed in parallel; thus, the sliding B & M embedding vectors form a lower triangular matrix.

The B & M embedding vector $\mathbf{z}_e(B_i, M_i)$ for the one-hot vector of the discretized B_i and M_i, $\mathbf{d}_{B_i,M_i}$, is calculated using a linear embedding layer as follows:

$$\mathbf{z}_e(B_i, M_i) = \mathbf{W}_E \mathbf{d}_{B_i,M_i}, \quad (16)$$

where $\mathbf{W}_E \in \mathbb{R}^{d \times b^2}$ denotes an embedding matrix. Then for the i-th event, the event time embedding vector $\mathbf{z}_t(t_i) \in \mathbb{R}^d$ and the B & M embedding vector $\mathbf{z}_e(B_i, M_i) \in \mathbb{R}^d$ are summed together to acquire the hidden representation of the i-th event $\mathbf{z}_i \in \mathbb{R}^d$ as:

$$\mathbf{z}_i = \mathbf{z}_t(t_i) + \mathbf{z}_e(B_i, M_i). \quad (17)$$

Then the embedding matrix for a whole single event sequence is given by:

$$\mathbf{Z} = [\mathbf{z}_i]_{i=1,...,n}, \quad (18)$$

where $\mathbf{Z} \in \mathbb{R}^{n \times d}$ and n is the length of the event sequence, that is, the number of events in a single sequence.

3.3 Self-attention module

After acquiring the embedding matrix $\mathbf{Z}$ for each event sequence according to Equation (18), we propagated $\mathbf{Z}$ into the input of the self-attention module. The resulting attention output $\mathbf{S}$ is defined as follows:

$$\mathbf{S} = \text{Softmax}\left(\frac{\mathbf{Q}\mathbf{K}^\top}{\sqrt{d_K}}\right)\mathbf{V}, \quad (19)$$

where $\mathbf{Q} = \mathbf{Z}\mathbf{W}^{\mathbf{Q}}$, $\mathbf{K} = \mathbf{Z}\mathbf{W}^{\mathbf{K}}$, $\mathbf{V} = \mathbf{Z}\mathbf{W}^{\mathbf{V}}$, and $\mathbf{S} \in \mathbb{R}^{n \times d_V}$. Here, $\mathbf{Q}$, $\mathbf{K}$, and $\mathbf{V}$ represent the query, key, and value matrices, respectively, obtained by applying distinct transformations to $\mathbf{Z}$. The transformation parameters are $\mathbf{W}^Q \in \mathbb{R}^{d \times d_K}$, $\mathbf{W}^K \in \mathbb{R}^{d \times d_K}$, and $\mathbf{W}^V \in \mathbb{R}^{d \times d_V}$, respectively. In contrast to conventional RNN models, the self-attention mechanism enables an equitable comparison of not only recent values but also the significance of distant past values of the sequence. Consequently, this facilitates the learning of long-term dependencies.

The BMT model employs multi-head attention, similar to other Transformers. Multi-head attention enables the model to manage diverse patterns and contexts of the input sequence. The multi-head attention output $\mathbf{S}$ is given by $\mathbf{S} = [\mathbf{S}_1, ..., \mathbf{S}_i, ..., \mathbf{S}_m]\mathbf{W}_O$, where $\mathbf{S}_i \in \mathbb{R}^{n \times d_V/m}$ is the attention output for the i-th multi-head and $\mathbf{W}_O \in \mathbb{R}^{m \cdot d_V \times d}$ is aggregation parameters.

After the multi-head attention, the resulting attention output $\mathbf{S}$ is subsequently passed into a position-wise feed-forward network, yielding hidden representations $\mathbf{h}(t)$ for the event sequence as:

$$\mathbf{H} = \text{ReLU}(\mathbf{S}\mathbf{W}_{\text{FC1}} + \mathbf{b}_1)\mathbf{W}_{\text{FC2}} + \mathbf{b}_2, \quad (20)$$

where $\mathbf{W}_{\text{FC1}} \in \mathbb{R}^{d \times d_H}$, $\mathbf{W}_{\text{FC2}} \in \mathbb{R}^{d_H \times d}$, $\mathbf{b}_1 \in \mathbb{R}^{d_H}$, and $\mathbf{b}_2 \in \mathbb{R}^d$ are the parameters of each neural network. The i-th event of the event sequence corresponds to the i-th row of the hidden representation matrix $\mathbf{H}$, that is, $\mathbf{h}(t_i) = \mathbf{H}(i, :)$. Furthermore, masks are employed to prevent the model from learning about the future in advance. The hidden representation $\mathbf{H} \in \mathbb{R}^{n \times d}$ encapsulates insights regarding burstiness and memory coefficient for each event within the sequence, acquired through the self-attention mechanism. We further enhanced the incorporation of sequential information by applying LSTM to the hidden representation.

3.4 Training and loss function

The BMT model employs five types of loss functions: (1) squared error of the event time, (2) event log-likelihood loss as described in Equation (22), (3) cross entropy of discretized B & M, (4) squared error of B, and (5) squared error of M.

3.4.1 Event time loss
The most crucial loss function within the model is how accurately it predicts the next event times. The next event time

prediction is $\hat{t}_{i+1} = \mathbf{W}_t \mathbf{h}(t_i)$, where $\mathbf{W}_t \in \mathbb{R}^{1 \times d}$ is the parameter of the event time predictor. To address this, the squared error loss function of the event times for the event sequence is defined as:

$$\mathcal{L}_t = \sum_{i=2}^{n} (t_i - \hat{t}_i)^2, \tag{21}$$

where $\hat{t}_i$ is the predicted event time.

3.4.2 Event log-likelihood

The typical approach for optimizing the parameters of the Hawkes process involves utilizing Maximum Likelihood Estimation (MLE). There are two constraints: (1) no events before time 0, and (2) unobserved event time must appear after the observed time interval. When the observed event sequences are $t_1, ..., t_n \in [0, T)$, then likelihood of an event sequence is given by $\mathcal{L}' = P(t_1) \cdots P(t_{n-1})(1 - F(T))$, where $F(\cdot)$ is the cumulative distribution function, and the last term is for the second constraint. Using (1) and (2), and applying the logarithm function, we obtain the following log-likelihood:

$$\mathcal{L}_\lambda = \sum_{i=1}^{n} \log \lambda(t_i) - \int_0^T \lambda(t') dt'. \tag{22}$$

The first term denotes the sum of the log-intensity functions for the past n events, and the second term represents the non-event log-likelihood.

Here, the intensity function $\lambda(t)$ is defined in the interval $t \in [t_i, t_{i+1}]$ according to the following expression:

$$\lambda(t) = \beta \log\big(1 + \exp(\mathbf{w}_\lambda^\top \mathbf{h}(t_i)\beta^{-1})\big), \tag{23}$$

where β is the softness parameter, $\mathbf{w}_\lambda \in \mathbb{R}^{d \times 1}$ is a parameter that converts the term inside the exponential function into a scalar, and $\mathbf{h}$ is the hidden representation derived from the encoder. The essence of this intensity function aligns with that of the Neural Hawkes Process, as shown in Equation (6). The softplus function formulation was employed to guarantee non-negativity of the intensity.

3.4.3 Discretized B and M loss

The model predicts the discretized $\hat{B}_i$ & $\hat{M}_i$, $\hat{d}_{B_i,M_i}$, based on the hidden representations $\mathbf{h}(t_{i-1})$ as:

$$\hat{\mathbf{p}}_i = \text{Softmax}(\mathbf{W}_{B,M} \mathbf{h}(t_{i-1})), \tag{24}$$

$$\hat{d}_{B_i,M_i} = \arg\max_{d'} \hat{\mathbf{p}}_i(d'), \tag{25}$$

where $\mathbf{W}_{B,M} \in \mathbb{R}^{b^2 \times d}$ is the parameter of the discretized B_i & M_i predictor, and $\hat{\mathbf{p}}_i(d')$ is the d'-th element of $\hat{\mathbf{p}}_i$. To measure the accuracy of B_i & M_i embedding, the following cross-entropy between the ground truth discretized B_i & M_i, d_{B_i,M_i}, and the predicted discretized $\hat{B}_i$ & $\hat{M}_i$, $\hat{d}_{B_i,M_i}$, is calculated:

$$\mathcal{L}_{B,M} = -\sum_{i=2}^{n} \mathbf{d}_{B_i,M_i}^\top \log(\hat{\mathbf{p}}_i), \tag{26}$$

where $\mathbf{d}_{B_i,M_i} \in \mathbb{R}^{b^2}$ is the ground truth one-hot encoding vector.

3.4.4 B loss and M loss

Additionally, the model utilizes the squared errors of the burstiness parameter directly as:

$$\mathcal{L}_B = \sum_{i=2}^{n} (B_i - \hat{B}_i)^2, \tag{27}$$

where B_i and $\hat{B}_i$ are the ground truth and predicted burstiness parameters, respectively. The squared errors of the memory coefficient value can be defined in a similar manner.

$$\mathcal{L}_M = \sum_{i=2}^{n} (M_i - \hat{M}_i)^2, \tag{28}$$

where M_i and $\hat{M}_i$ is ground truth and predicted memory coefficient, respectively.

3.4.5 Overall loss

By aggregating the aforementioned loss functions (21), (22), and (26)–(28), the overall loss function of the model is defined as follows:

$$\mathcal{L} = \mathcal{L}_t + \alpha_1 \mathcal{L}_\lambda + \alpha_2 \mathcal{L}_{B,M} + \alpha_3 \mathcal{L}_B + \alpha_4 \mathcal{L}_M, \tag{29}$$

where α_1 to α_4 are the hyperparameters that balance each loss function determined using the validation datasets. The overall framework of the BMT model is illustrated in Figure 3.

4 Experiments

4.1 Synthetic datasets

We generated synthetic data using the copula-based algorithm for two different inter-event time distributions. The model was tested for the exponential and power-law inter-event time distribution, which also have a different range of memory coefficient and burstiness, to directly understand the impact of temporal heterogeneity on the BMT model and other models. Along with the two synthetic datasets below, we tested the regular event sequences generated by the self-correcting process, as in Equation (5). The statistics of the datasets are displayed in Table 1.

4.1.1 Power-law inter-event time distribution

The power-law inter-event time distribution with a power-law exponent α is defined as $P(\tau) = (\alpha - 1)\tau^{-\alpha}\theta(\tau - 1)$ and the corresponding cumulative distribution function is $F(\tau) = (1 - \tau^{1-\alpha})\theta(\tau - 1)$, where $\theta(\cdot)$ represents the Heaviside step function with a lower bound of 1. After substituting the inter-event time distribution into Equation (13), we obtain the next inter-event time τ_{i+1} from a given previous inter-event time τ_i and random number x in $0 \le x < 1$ as

$$\tau_{i+1} = \left[\frac{2c_i}{c_i + 1 - \sqrt{(c_i + 1)^2 - 4c_i x}}\right]^{1/(\alpha-1)}, \tag{30}$$

where $c_i = \frac{(2\alpha-3)^2}{(\alpha-1)(\alpha-3)} M(1 - 2\tau_i^{1-\alpha})$ (Jo et al., 2019).

A total of 1,000 sequences with a power-law inter-event time distribution were generated with different parameters according to Equation (30). The power-law exponent α, memory coefficient M, and the number of events for each event sequence are randomly and independently drawn from $2.1 \leq \alpha \leq 2.9$, $-1/3 \leq M \leq 1/3$, and $50 \leq n \leq 500$, respectively. The initial inter-event time was randomly drawn from 1 to 2. Depending on the power-law exponent and memory coefficient, the burstiness ranged from 0.297 to 0.962.

As depicted in Figure 4, the power-law inter-event time datasets exhibit pronounced dispersion toward the region of larger burstiness and memory coefficients (B and M scatter plots). Moreover, these datasets show a power-law inter-event time distribution with exponent values $\alpha = 2.4$ close to the average within the range of exponents $2.1 < \alpha < 2.9$.

4.1.2 Exponential inter-event time distribution

The exponential inter-event time distribution with mean μ is defined as $P(\tau) = \mu^{-1} e^{-\tau/\mu}$ and the corresponding cumulative distribution function is $F(\tau) = 1 - e^{-\tau/\mu}$ and the relationship between the parameter and memory coefficient is $r = 4M$. After substituting the inter-event time distribution into Equation (13), we obtain the next inter-event time τ_{i+1} from a given previous inter-event time τ_i and random number x in $0 \leq x < 1$ as follows:

$$\tau_{i+1} = \mu \ln\left[\frac{2c_i}{c_i + 1 - \sqrt{(c_i + 1)^2 - 4c_i x}}\right], \qquad (31)$$

where $c_i = 4M(1 - 2e^{-\tau_i/\mu})$ (Jo et al., 2019).

A total of 1,000 sequences with an exponential inter-event time distribution were generated using different parameters, according to Equation (31). The mean inter-event time μ, memory coefficient M, and the number of events n for each event sequence were randomly and independently drawn from $1 \leq \mu \leq 100$, $-1/3 \leq M \leq 1/3$, and $50 \leq n \leq 500$, respectively. The initial inter-event time was set to μ for each event sequence.

As illustrated in Figure 4, the B and M scatter plots of the exponential inter-event time datasets show that B values are concentrated in the lower range, whereas M values exhibit a broader distribution spread both above and below. This contrasts with the self-correcting process datasets, where the B and M scatter plots show that both B and M clustered at $\sim$0. Although both datasets have an exponential inter-event time distribution, their heterogeneity differs owing to variations in the relationship between B and M. Even with an exponential inter-event time distribution, appropriately shuffling inter-event times can generate event sequences with temporal heterogeneity (i.e., burst) characteristics. We examine this difference further later, as it plays a role in generating variations in performance.

4.2 Real-world datasets

We adopted four real-world datasets to evaluate the models: the *Retweets*, *StackOverflow*, *Financial Transaction*, and *911 Calls*

FIGURE 3
Architecture of the Burst and Memory-aware Transformer model. IET; inter-event time; FF, feed-forward neural network; B, burstiness; M, memory coefficient.
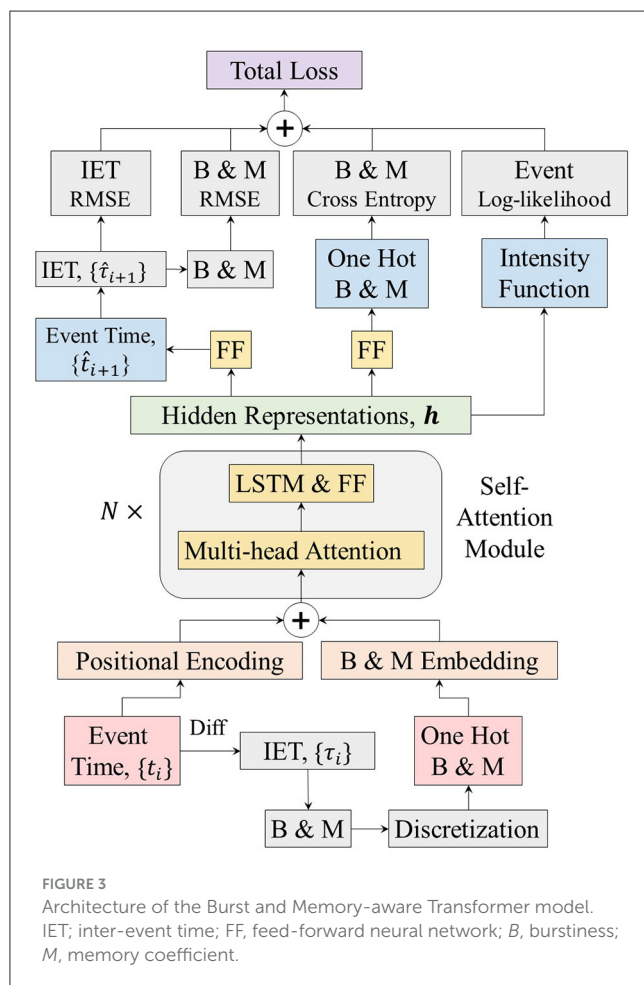
TABLE 1 Datasets statistics.

	Datasets	Power-law	Exponential	Self-correcting	Retweets	Stack Overflow	Financial	911 Calls
IET	Mean	3.4645	57.495	0.20015	2,840.8	0.58677	1.5853	338.14
	S.D.	2.9372	32.938	0.00193	2,157.8	0.16667	5.6152	249.20
B	Mean	0.176	-0.008	-0.048	0.754	0.052	0.522	0.100
	S.D.	0.335	0.068	0.028	0.137	0.083	0.069	0.100
M	Mean	-0.021	-0.059	-0.084	0.442	0.031	0.155	0.009
	S.D.	0.195	0.200	0.058	0.274	0.119	0.078	0.158

IET, inter-event time; B, burstiness; M, memory coefficient; S.D., standard deviation.

FIGURE 4
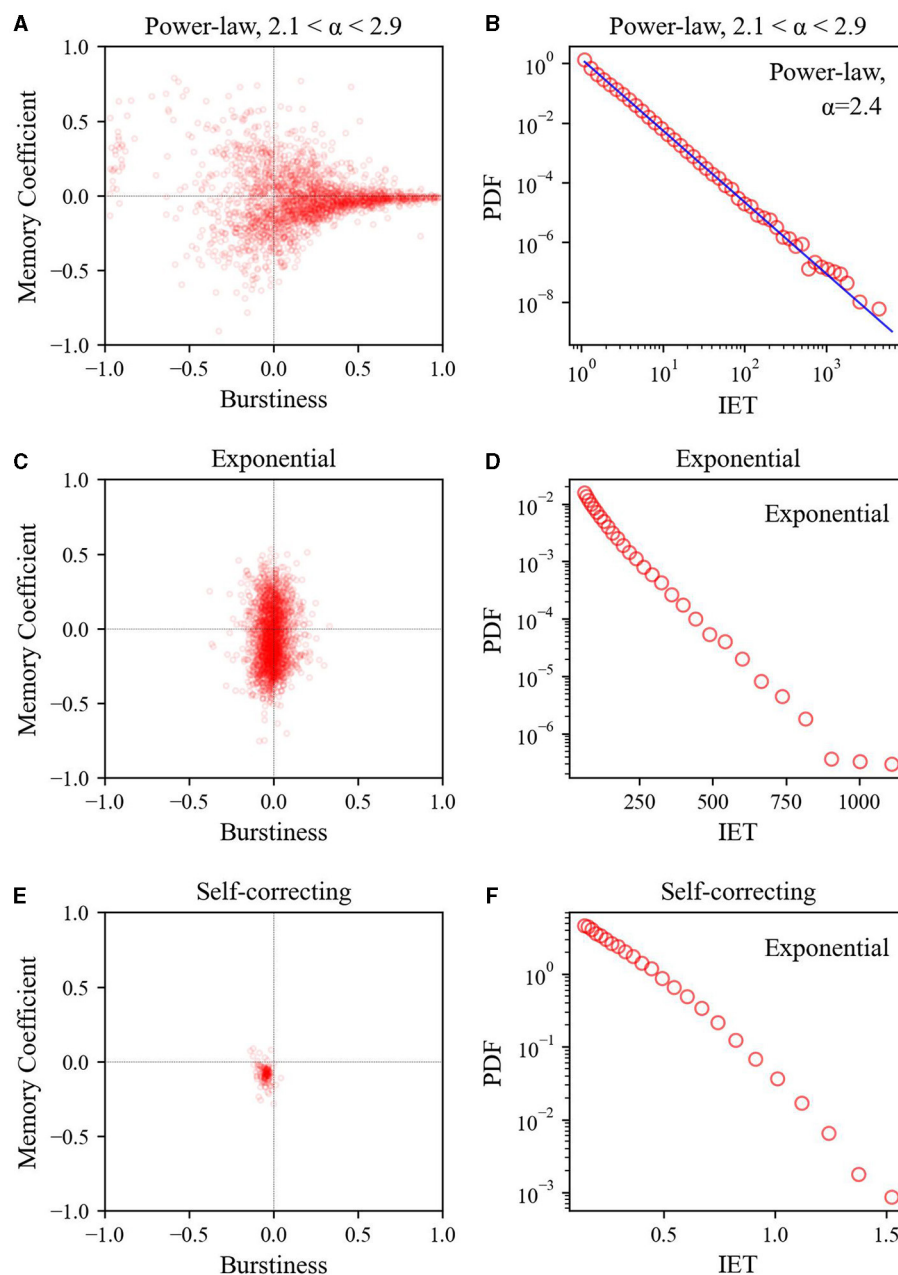Relationship between burstiness and memory coefficient (left) and inter-event time distribution (right) across three synthetic datasets: **(A, B)** power-law inter-event time, **(C, D)** exponential inter-event time, and **(E, F)** self-correcting process. For calculating the inter-event time distribution, logarithmic binning was employed.

datasets. The Retweets dataset (Zhao et al., 2015) contains sequences of tweets and follow-up tweets. The original datasets contained three categories, based on the number of followers. The StackOverflow dataset (Leskovec and Krevl, 2014) contains each user's reward history, that is, the timestamp of users receiving the badge and the type of the badge. The Financial Transaction dataset (Du et al., 2016) includes raw order book records from the New York Stock Exchange (NYSE) for a stock in one day, with a millisecond-level time granularity. The events correspond to two types of actions: buy and sell orders. The 911 Calls

datasets[1] contains emergency phone call records for Montgomery County, PA. This dataset contains information such as calling times and location, and we conducted aggregation based on location, utilizing zip codes as identifiers. The dataset covers a five-year period, which is a relatively extensive time frame for prediction purposes. Therefore, we partitioned the data into monthly intervals. Additionally, to ensure statistical significance, we included only

—————————

1 The dataset is available on https://www.kaggle.com/datasets/mchirico/montcoalert/.

those locations where the number of events exceeded 50 in the data.

Although there are other commonly used datasets, the burst and memory-aware characteristics assumed by the BMT model are applicable when the sequence length is sufficiently long. Furthermore, we sampled event sequences in quantities comparable to synthetic data while concurrently excluding sequences with short lengths. The time units for each dataset are as follows: Retweet and StackOverflow datasets are in days, Financial Transaction datasets are in milliseconds, and 911 Calls datasets are in minutes. The statistics of the datasets are displayed in Table 1.

As shown in Figure 5, when comparing the Retweets datasets (or Financial Transaction datasets) to the StackOverflow datasets (or 911 Calls datasets), it is evident that the Retweets datasets and Financial Transaction datasets are more temporally heterogeneous. In the B and M scatter plots, the Retweets datasets (or Financial Transaction datasets) are concentrated in regions with larger values for both B and M, whereas the StackOverflow datasets (or 911 Calls datasets) are centered around values near 0 for both B and M. However, when compared to the self-correcting process datasets, the StackOverflow (or 911 Calls datasets) datasets exhibit greater dispersion. Additionally, the inter-event time distribution reveals that the Retweets datasets and Financial Transaction datasets follow a power-law distribution (exponent of 1.36 and 1.70, respectively), whereas the StackOverflow datasets and 911 Calls datasets follow an exponential distribution.

4.3 Impact of *B* and *M* embedding and losses

While altering the combination of loss functions during the experimental process, there were five control groups.

1. **BMT-NoE&NoL** (BMT without B & M embedding and without corresponding losses). The simplest scenario occurs when $\alpha_2 = \alpha_3 = \alpha_4 = 0$, utilizing only time and event losses. In this case, only event time and intensity were considered.
2. **BMT-NoE&L** (BMT without embedding for B & M, but with losses for either B or M). To incorporate the effects of the B & M losses, we also consider the case of $\alpha_2 = 0, \alpha_3 > 0$, and $\alpha_4 > 0$ with time and event losses. Note that the case for $\alpha_2 > 0$ relates to predicting the discretized on-hot B & M, and hence it is not applicable in this scenario.
3. **BMT-E&NoL** (BMT without losses related to B & M, but with embedding for B & M). The control group examines the impact of loss for B & M; the representation vector remains consistent with the BMT model, as shown in Equation (18), but without $\mathcal{L}_{B,M}$, $\mathcal{L}_B$, and $\mathcal{L}_M$, that is, $\alpha_2 = \alpha_3 = \alpha_4 = 0$.
4. **BMT-B** (BMT with B embedding only and the corresponding loss). In the case where only B is embedded and the model is trained, the loss is also computed exclusively based on B as $\alpha_2 = 0, \alpha_3 > 0$, and $\alpha_4 = 0$ with time and event losses.
5. **BMT-M** (BMT with M embedding only and corresponding loss). In the case where only M is embedded and the model is trained, the loss is also computed exclusively based on M as $\alpha_2 = \alpha_3 = 0$, and $\alpha_4 > 0$ with time and event losses.

5 Results and discussion

We tested several hyperparameters for both the BMT and THP models and chose the configuration that yielded the best validation performance. The hyperparameters are as follows: the number of bins for discretization (b) is set to 40, mini-batch size is 16, dropout rate is 0.1, embedding dimensions (d and d_H) are both 128, self-attention dimensions (d_K and d_V) are 32, with eight layers in the encoder and 8 heads. For the loss function, hyperparameters were fine-tuned, mainly as follows: $\alpha_1 = 1e3, \alpha_2 = 4e3, \alpha_3 = \alpha_4 = 1e4$. We employed the ADAM (adaptive moment estimation) optimizer with hyperparameters β set to (0.9, 0.999). Regarding the learning rate, we utilized PyTorch StepLR, initializing it at 1e-4 and reducing the learning rate by a factor of 0.9 every 15 steps.

The performance evaluation results for different models across diverse datasets are presented in Table 2. The results indicate that BMT achieves superior performance compared to THP and other control models in terms of the root mean squared error (RMSE) of the event times and log-likelihood. The main metric, RMSE, is a unit-adjusted value obtained by taking the square root of Equation (21). It measures how much predicted event times of the model differ from the actual event times. However, RMSE has a drawback, especially in the case of heterogeneous data, where it can perform well by accurately predicting large values while potentially struggling with smaller ones. To address this limitation, we introduce the event log-likelihood, defined in Equation (22), as a second metric. This metric arises when probabilistically modeling event sequences using the intensity function λ derived from Equation (1). A higher likelihood of the intensity function calculated with predicted event times of the model indicates that the model better probabilistically mimics the actual event sequence. Consequently, larger values of this metric correspond to better performance. Additionally, when considering the B and M losses in Equation (26), they represent how well the model captures discretized burstiness and discretized memory coefficients. Smaller values of these losses indicate better performance in replicating these aspects.

In particular, as the data became more heterogeneous, performance improvement became more pronounced. In synthetic datasets, the performance enhancement of the BMT model was greater for power-law inter-event time data than for self-correcting data, which is a less heterogeneous exponential inter-event time distribution (see Figure 4). Similarly, in real-world datasets, the overall performance of the BMT model was superior in the Retweets dataset, which exhibited a more power-law inter-event time distribution, compared to the StackOverflow datasets with a less heterogeneous exponential inter-event time distribution (see Figure 5).

When compared to the BMT-NoE&L model with respect to the RMSE of the event times, the BMT model shows that superior performance across all datasets except StackOverflow. This suggests that the inclusion of B & M embedding processes aids in augmenting the performance of the model by enabling the encoder to grasp the burst structure of event sequences. Compared with the BMT-E&NoL model, the BMT model demonstrates enhanced performance across all datasets, indicating that the integration of B & M losses into the overall loss function contributes to the
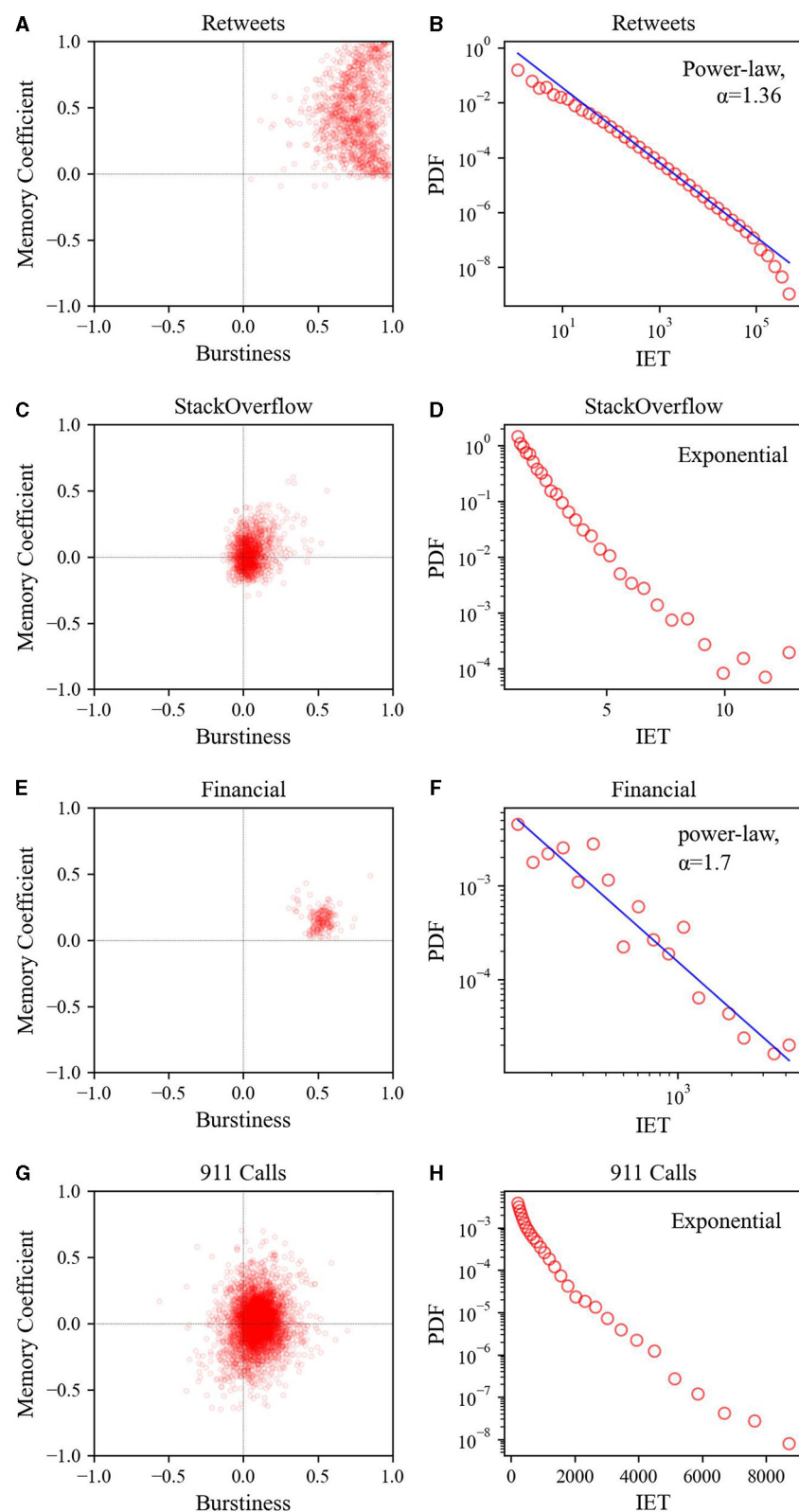
FIGURE 5
Relationship between burstiness and memory coefficient (left) and inter-event time distribution (right) for four real-world datasets: **(A, B)** Retweets, **(C, D)** StackOverflow, **(E, F)** Financial Transaction, and **(G, H)** 911 Calls. For calculating the inter-event time distribution, logarithmic binning was employed.

Dataset	Model	RMSE of time	LL	CE of BM
Power- law	THP	238.0	−2.303	N/A
	BMT-NoE&NoL	66.6	−2.451	N/A
	BMT-NoE&L	68.2	−2.493	N/A
	BMT-E&NoL	82.0	−2.348	12.46
	BMT-B	107.6	−2.712	N/A
	BMT-M	52.3	−2.730	N/A
	BMT	**40.5**	**−2.302**	**8.05**
Exponential	THP	1,973.7	−19.910	N/A
	BMT-NoE&NoL	158.7	−6.486	N/A
	BMT-NoE&L	208.8	−15.640	N/A
	BMT-E&NoL	102.2	−5.633	12.70
	BMT-B	106.1	−7.201	N/A
	BMT-M	140.8	−9.912	N/A
	BMT	**80.1**	**−5.171**	**5.77**
Self-correcting	THP	0.184	0.200	N/A
	BMT-NoE&NoL	0.192	−0.281	N/A
	BMT-NoE&L	0.185	0.329	N/A
	BMT-E&NoL	0.183	0.592	7.30
	BMT-B	0.198	−0.425	N/A
	BMT-M	0.209	−0.456	N/A
	BMT	**0.181**	**0.605**	**5.43**
Retweets	THP	36,080.8	−9.01	N/A
	BMT-NoE&NoL	16,360.8	−111.13	N/A
	BMT-NoE&L	16,362.9	−110.95	N/A
	BMT-E&NoL	16,257.7	**−8.14**	28.92
	BMT-B	16,090.8	−16.21	N/A
	BMT-M	16,266.5	−11.19	N/A
	BMT	**15,825.8**	−11.28	**2.70**
Stack Overflow	THP	127.0	−0.373	N/A
	BMT-NoE&NoL	0.658	**−0.266**	N/A
	BMT-NoE&L	**0.643**	−0.277	N/A
	BMT-E&NoL	0.726	−0.339	17.81
	BMT-B	0.858	−0.718	N/A
	BMT-M	3.969	−0.505	N/A
	BMT	0.663	−0.358	**6.38**
Financial	THP	38.13	−1.826	N/A
	BMT-NoE&NoL	44.26	−11.843	N/A
	BMT-NoE&L	62.72	−11.759	N/A
	BMT-E&NoL	38.39	−2.104	7.39
	BMT-B	37.93	−1.848	N/A
	BMT-M	77.58	−1.796	N/A

(Continued)

Dataset	Model	RMSE of time	LL	CE of BM
	BMT	**37.92**	**−1.775**	**4.41**
911 Calls	THP	6,183.4	−7.190	N/A
	BMT-NoE&NoL	358.3	−17.662	N/A
	BMT-NoE&L	469.3	−41.818	N/A
	BMT-E&NoL	342.4	**−6.608**	28.49
	BMT-B	353.4	−6.832	N/A
	BMT-M	364.8	−6.835	N/A
	BMT	**339.6**	−6.883	**8.56**

RMSE, root mean squared error; LL, log-likelihood; CE, cross entropy; B, burstiness; M, memory coefficient. The bold value indicates the metric of the model with the best performance for each individual dataset.

improved performance of the model. Even in the prediction of one-hot discretized B & M, it can be observed that including B & M losses contributes to a reduction in cross entropy. No significant differences in performance were observed between the BMT-NoE&NoL and BMT-NoE&L models. This suggests that the incorporation of B & M losses is less significant in the absence of B & M embedding.

Summarizing the aforementioned findings, it is evident that both B & M embedding and B & M losses contribute to performance enhancement. Excluding either of these components would likely impede the attainment of a substantial performance improvement, comparable to that observed with the BMT model. If either of the B embedding or M embedding is omitted, a significant performance improvement comparable to that of the BMT model cannot be expected. This was substantiated by comparing the BMT model with the BMT-B and BMT-M models, which revealed the superior performance of the BMT model across all datasets. These results can also be observed in the training curves shown in Figure 6.

We also conducted experiments on mixed synthetic datasets, the results of which are presented in Table 3. The mixed synthetic datasets comprised a combination of three individual datasets: power-law, exponential, and self-correcting datasets. However, when separately examining the RMSE of event time and log-likelihood, the performance of the original BMT model appeared slightly inferior compared to some of the control BMT models, demonstrating an overall superior performance when considering both metrics together.

In summary, the BMT model demonstrates improved performance on heterogeneous data owing to its capability to capture heterogeneous characteristics through the embedding of B & M, combined with the inclusion of corresponding loss functions.

The BMT model has two limitations. First, in cases where the event sequence length is short, the incorporation of B and M into the BMT model may result in reduced effectiveness. This aspect originates from the statistical characteristics of B and M, because their meaningful representation is hindered by fluctuations and noise, particularly when the number of events is small. In the BMT model, during the calculation of sliding
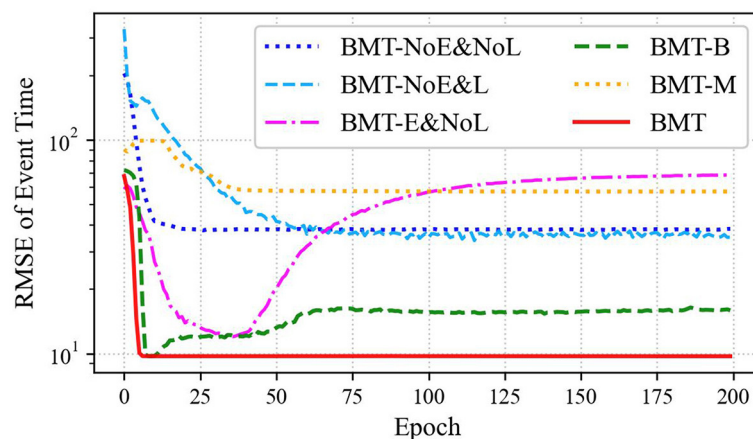
FIGURE 6
Training curves of RMSE for event times fitted on Financial Transaction datasets are presented for various BMT model scenarios: BMT-NoE&NoL, BMT-NoE&L, BMT-E&NoL, BMT-B, BMT-M, and the standard BMT model.

TABLE 3 Performance evaluation results for the mixed synthetic datasets: power-law, exponential, and self-correcting datasets.

Model	RMSE of time	LL	CE of BM
THP	1,338.65	−14.190	N/A
BMT-NoE&NoL	261.20	−9.015	N/A
BMT-NoE&L	**64.19**	−8.228	N/A
BMT-E&NoL	77.14	**−4.414**	12.593
BMT-B	64.74	−7.439	N/A
BMT-M	71.31	−10.476	N/A
BMT	66.98	−4.748	**6.269**

The bold value indicates the metric of the model with the best performance for each individual dataset.

B and M values, masking was applied to exclude the first three events. However, considering that temporal heterogeneity becomes a meaningful characteristic only when the length of the event sequence is sufficiently long, this limitation can be viewed as unavoidable.

The second limitation is the inability to consider event types, which will be addressed in future studies. To account for event types, it is necessary to reflect the correlation structure between inter-event times and event types to generate synthetic data and subsequently test the model using these data. In the context of performance enhancement, the improvement of the BMT model over the THP model can also be attributed to the fact that the BMT model does not embed event types. This allows the model to focus more on predicting the event times. Because the BMT-NoE&NoL model is analogous to a version of the THP model that does not consider event types, comparing the performance of the BMT-NoE&NoL model with the BMT model would provide a more equitable assessment. However, upon comparing the BMT-NoE&NoL model with the BMT model, it becomes evident that the BMT model exhibits superior performance across all datasets, except for StackOverflow.

6 Conclusion

Our study addresses the challenges presented by bursty temporal patterns in event sequences across various domains. By leveraging recent advancements in predicting event sequences using Transformer models based on the Hawkes process with self-attention mechanisms, we introduced a Burst and Memory-aware Transformer (BMT) model. This model effectively captures the nuances of burst patterns by embedding burstiness and memory coefficient within its self-attention module. The incorporation of a specialized loss function tailored for burstiness and memory coefficient further refines the model's predictive capabilities.

Through comprehensive numerical experiments conducted on a diverse array of synthetic and real-world datasets encompassing various scenarios, we validated the outstanding performance of the BMT model by comparing it with the existing models and control groups. This is particularly evident in scenarios involving heterogeneous data, such as power-law inter-event time distributions. Hence, the explicit consideration of burst-related parameters within the Transformer contributes to a deeper comprehension of complex event sequences, ultimately leading to an enhanced predictive performance. In future work, we will focus on integrating a multitude of insights from complex systems into the development of deep neural network models for temporal data.

Data availability statement

The datasets presented in this study can be found in online repositories. The names of the repository/repositories and accession number(s) can be found in the article/supplementary material. The synthetic data can be found here: https://github.com/bh0903lee/BMT-synthetic-datasets.

Author contributions

BL: Conceptualization, Data curation, Formal analysis, Investigation, Methodology, Resources, Software, Validation,

Visualization, Writing—original draft, Writing—review & editing. J-HL: Formal analysis, Resources, Software, Writing—review & editing. SL: Formal analysis, Resources, Software, Writing—review & editing. CK: Formal analysis, Resources, Software, Writing—review & editing.

Conflict of interest

The authors declare that the research was conducted in the absence of any commercial or financial relationships that could be construed as a potential conflict of interest.

Publisher's note

All claims expressed in this article are solely those of the authors and do not necessarily represent those of their affiliated organizations, or those of the publisher, the editors and the reviewers. Any product that may be evaluated in this article, or claim that may be made by its manufacturer, is not guaranteed or endorsed by the publisher.

References

Barabasi, A.-L. (2005). The origin of bursts and heavy tails in human dynamics. *Nature* 435, 207–211. doi: 10.1038/nature03459

Chan, H. K., Yang, D.-P., Zhou, C., and Nowotny, T. (2016). Burst firing enhances neural output correlation. *Front. Comput. Neurosci.* 10, 42. doi: 10.3389/fncom.2016.00042

Clauset, A., and Shalizi, C. R. (2009). Power-law distributions in empirical data. *SIAM Rev.* 51, 661–703. doi: 10.1137/070710111

Corral, Á. (2004). Long-term clustering, scaling, and universality in the temporal occurrence of earthquakes. *Phys. Rev. Lett.* 92, 108501. doi: 10.1103/PhysRevLett.92.108501

Cox, D. R. (1955). Some statistical methods connected with series of events. *J. R. Stat. Soc. Ser.* 17, 129–157. doi: 10.1111/j.2517-6161.1955.tb00188.x

Daley, D. J., and Vere-Jones, D. (2008). *An Introduction to the Theory of Point Processes: Volume II: General Theory and Structure.* New York, NY: Springer.

Dashevskiy, T., and Cymbalyuk, G. (2018). Propensity for bistability of bursting and silence in the leech heart interneuron. *Front. Comput. Neurosci.* 12, 5. doi: 10.3389/fncom.2018.00005

de Arcangelis, L., Godano, C., Lippiello, E., and Nicodemi, M. (2006). Universality in solar flare and earthquake occurrence. *Phys. Rev. Lett.* 96, 051102. doi: 10.1103/PhysRevLett.96.051102

Du, N., Dai, H., Trivedi, R., Upadhyay, U., Gomez-Rodriguez, M., and Song, L. (2016). "Recurrent marked temporal point processes: Embedding event history to vector," in *Proceedings of the 22nd ACM SIGKDD International Conference on Knowledge Discovery and Data Mining* (New York, NY: ACM), 1555–1564.

Goh, K.-I., and Barabáasi, A.-L. (2008). Burstiness and memory in complex systems. *Europhys. Lett.* 81, 48002. doi: 10.1209/0295-5075/81/48002

Hawkes, A. G. (1971). Spectra of some self-exciting and mutually exciting point processes. *Biometrika* 58, 83–90. doi: 10.1093/biomet/58.1.83

Hochreiter, S., and Schmidhuber, J. (1997). Long short-term memory. *Neural Comput.* 9, 1735–1780. doi: 10.1162/neco.1997.9.8.1735

Isham, V., and Westcott, M. (1979). A self-correcting point process. *Stochast. Process. Appl.* 8, 335–347. doi: 10.1016/0304-4149(79)90008-5

Jo, H.-H., Lee, B.-H., Hiraoka, T., and Jung, W.-S. (2019). Copula-based algorithm for generating bursty time series. *Phys. Rev. E* 100, 022307. doi: 10.1103/PhysRevE.100.022307

Jo, H.-H., Pan, R. K., Perotti, J. I., and Kaski, K. (2013). Contextual analysis framework for bursty dynamics. *Phys. Rev. E* 87, 062131. doi: 10.1103/PhysRevE.87.062131

Karsai, M., Jo, H.-H., and Kaski, K. (2018). *Bursty Human Dynamics.* Cham: Springer.

Kemuriyama, T., Ohta, H., Sato, Y., Maruyama, S., Tandai-Hiruma, M., Kato, K., et al. (2010). A power-law distribution of inter-spike intervals in renal sympathetic nerve activity in salt-sensitive hypertension-induced chronic heart failure. *BioSystems* 101, 144–147. doi: 10.1016/j.biosystems.2010.06.002

Kim, E.-K., and Jo, H.-H. (2016). Measuring burstiness for finite event sequences. *Phys. Rev. E* 94, 032311. doi: 10.1103/PhysRevE.94.032311

Kingman, J. F. C. (1992). *Poisson Processes, Vol. 3.* New York, NY: Oxford University Press Inc.

Leskovec, J., and Krevl, A. (2014). *Snap Datasets: Stanford Large Network Dataset Collection.* Ann Arbor, MI. Available online at: http://snap.stanford.edu/data

Lim, B., Arık, S. Ö., Loeff, N., and Pfister, T. (2021). Temporal fusion transformers for interpretable multi-horizon time series forecasting. *Int. J. Forecast.* 37, 1748–1764. doi: 10.1016/j.ijforecast.2021.03.012

Ma, Y., Tang, Y., Zeng, Y., Ding, T., and Liu, Y. (2023). An n400 identification method based on the combination of soft-dtw and transformer. *Front. Comput. Neurosci.* 17, 1120566. doi: 10.3389/fncom.2023.1120566

Mei, H., and Eisner, J. M. (2017). The neural hawkes process: a neurally self-modulating multivariate point process. *Adv. Neural Inf. Process. Syst.* 30, 6754–6764.

Metzen, M. G., Krahe, R., and Chacron, M. J. (2016). Burst firing in the electrosensory system of gymnotiform weakly electric fish: mechanisms and functional roles. *Front. Comput. Neurosci.* 10, 81. doi: 10.3389/fncom.2016.00081

Nelsen, R. B. (2006). *An Introduction to Copulas.* New York, NY: Springer.

Omi, T., Ueda, N., and Aihara, K. (2019). Fully neural network based model for general temporal point processes. *Adv. Neural Inf. Process. Syst.* 32, 2120–2129.

Rasmussen, J. G. (2018). Lecture notes: temporal point processes and the conditional intensity function. *arXiv* [preprint]. doi: 10.48550/arXiv.1806.00221

Rolski, T., Schmidli, H., Schmidt, V., and Teugels, J. L. (2009). *Stochastic Processes for Insurance and Finance.* West Sussex: John Wiley & Sons.

Shahi, M., Van Vreeswijk, C., and Pipa, G. (2016). Serial spike time correlations affect probability distribution of joint spike events. *Front. Comput. Neurosci.* 10, 139. doi: 10.3389/fncom.2016.00139

Shchur, O., Biloš, M., and Günnemann, S. (2019). "Intensity-free learning of temporal point processes," in *International Conference on Learning Representations* (Addis Ababa).

Vaswani, A., Shazeer, N., Parmar, N., Uszkoreit, J., Jones, L., Gomez, A. N., et al. (2017). Attention is all you need. *Adv. Neural Inf. Process. Syst.* 30, 5998–6008.

Wen, Q., Zhou, T., Zhang, C., Chen, W., Ma, Z., Yan, J., et al. (2022). Transformers in time series: a survey. *arXiv* [preprint]. doi: 10.24963/ijcai.2023/759

Wheatland, M., Sturrock, P., and McTiernan, J. (1998). The waiting-time distribution of solar flare hard x-ray bursts. *Astrophys. J.* 509, 448. doi: 10.1086/306492

Xiao, S., Yan, J., Yang, X., Zha, H., and Chu, S. (2017). "Modeling the intensity function of point process via recurrent neural networks," in *Proceedings of the AAAI Conference on Artificial Intelligence* (Palo Alto, CA: AAAI Press), Vol. 31.

Yamauchi, S., Kim, H., and Shinomoto, S. (2011). Elemental spiking neuron model for reproducing diverse firing patterns and predicting precise firing times. *Front. Comput. Neurosci.* 5, 42. doi: 10.3389/fncom.2011.00042

Zeldenrust, F., Wadman, W. J., and Englitz, B. (2018). Neural coding with bursts—current state and future perspectives. *Front. Comput. Neurosci.* 12, 48. doi: 10.3389/fncom.2018.00048

Zhang, Q., Lipani, A., Kirnap, O., and Yilmaz, E. (2020). "Self-attentive hawkes process," in *International Conference on Machine Learning* (PMLR), 11183–11193.

Zhao, Q., Erdogdu, M. A., He, H. Y., Rajaraman, A., and Leskovec, J. (2015). "Seismic: a self-exciting point process model for predicting tweet popularity," in *Proceedings of the 21th ACM SIGKDD International Conference on Knowledge Discovery and Data Mining* (New York, NY: ACM), 1513–1522.

Zuo, S., Jiang, H., Li, Z., Zhao, T., and Zha, H. (2020). "Transformer hawkes process," in *International Conference on Machine Learning* (PMLR), 11692–11702.

Check for updates

Mathematical model of physicochemical regulation of precipitation of bone hydroxyapatite

Hossein Poorhemati[1,2] and Svetlana V. Komarova[1,2,3]*

[1]Department of Biological and Biomedical Engineering, McGill University, Montreal, QC, Canada,
[2]Shriners Hospital for Children, Montreal, QC, Canada, [3]Faculty of Dental Medicine and Oral Health
Sciences, McGill University, Montreal, QC, Canada

Introduction: Formation of hydroxyapatite in bone, dentin, and enamel occurs at restricted molecular sites of specific extracellular matrix proteins and is controlled by multiple mineralization inhibitors. However, the role of physicochemical factors, such as the availability of required ions and the saturation status of the aqueous environment in biological mineralization, is not fully understood. The goal of this study was to use mathematical modeling to describe the complex physicochemical environment permissive to the precipitation of biological hydroxyapatite.

Methods: We simulated the processes occurring in the bone interstitial fluid (ISF) defined as an aqueous environment containing seven chemical components (calcium, phosphate, carbonate, sodium, potassium, magnesium, and chloride) that form 30 chemical species. We simulated reversible equilibrium reactions among these chemical species, and calculated supersaturation for hydroxyapatite and its precipitation rate using kinetic theory.

Results and Discussion: The simulated ISF was of correct ionic strength and predicted the equilibrium component concentrations that were consistent with the experimental findings. Supersaturation of physiological ISF was ∼15, which is consistent with prior findings that mineralization inhibitors are required to prevent spontaneous mineral precipitation. Only total calcium, total phosphate and to a lesser degree total carbonate affected ion availability, solution supersaturation and hydroxyapatite precipitation rate. Both calcium and phosphate levels directly affected hydroxyapatite precipitation, and phosphate was affected by pH, which additionally influenced hydroxyapatite precipitation. Integrating mathematical models capturing the physiochemical and biological factors regulating bone mineralization will allow in silico studies of complex clinical scenarios associated with alterations in ISF ion composition, such as rickets, hypophosphatemia, and chronic kidney disease.

KEYWORDS

bone, mineralization, mathematical modeling, physiochemistry, hydroxyapatite

1 Introduction

Bone is a biological composite material including three different phases, a mineral phase, an organic phase, and water [1]. The mature bone mineral phase is made up of nanosized crystalline hydroxyapatite (HAP) with chemical formula of $Ca_{10}(PO_4)_6(OH)_2$ [1]. The mineral phase of bone provides a strong structure for the mechanical resistance for the tissue [2], and an abundant number of ions (particularly calcium and phosphate) for whole body homeostasis [3]. The organic phase of the bone consists of almost 90% type I collagen, 5% non-collagenous proteins (NCPs), and 2% lipids by weight [1]. Finally, the

aqueous phase is responsible for cell and matrix nutrition, mediating interactions between collagen fibrils and minerals, and controlling ion flux [3]. Bone formation starts with deposition of organic matrix by osteoblasts, which happens at a much faster rate than bone mineralization [4]. The unmineralized bone matrix, osteoid, is mineralized through physicochemical processes regulated by the presence of nucleation centers that can be provided by matrix vesicles [5] and can arise with the maturation of extracellular matrix [6], and the concentrations of mineralization inhibitors produced by osteoblasts or present in the circulation. Thus, complex biological and physicochemical phenomena are involved in regulating hydroxyapatite mineralization.

Mathematical models provide a deeper understanding of how different components interact and influence each other in complex environments [7]. We have previously modeled the role of biological factors in bone mineralization [8], and have examined a simplified model of pH regulation in bone microenvironment [9]. Building on the concept of simulated interstitial fluid (ISF) introduced in the previous work [9], in the current study, we aimed to develop a mathematical model describing the complex physicochemical environment permissive to the precipitation of biological hydroxyapatite. The aqueous environment of ISF was defined to contain seven commonly reported chemical components (calcium, phosphate, carbonate, sodium, potassium, magnesium, and chloride) that form 30 chemical species. Computing the outcomes of reversible equilibrium reactions among these chemical species allowed us to calculate solution supersaturation for HAP and assess HAP precipitation rate using kinetic theory.

2 Model development and simulations

2.1 Model assumptions

In this study, we have simulated the processes occurring in the interstitial fluid (ISF) in the bone vicinity. It is assumed that the environment is homogenous, and ions are immediately distributed evenly in the environment. The following assumptions regarding the biological components of the system were made: [1] the effects of biological factors on equilibrium reactions in ISF are minimal; [2] the presence of biological inhibitors of mineralization increases the precipitation threshold [10]; [3] the nucleation of biological mineral is controlled by biological processes [11], and physicochemical aspects are involved in crystal growth. Efforts have been made to keep the model working with the minimum number of components and complexity while ensuring the predictions are reliable and close enough to the actual processes happening in the body.

Figure 1 provides a map of the model, its different compartments, and the flow of data in the model. A detailed description of how the model is constructed is provided in the following sections.

2.2 Simulated ISF

Previously, we developed the model of the ISF reactions that focused on four components involved in pH regulation,

calcium (Ca^{2+}), phosphate (PO_4^{3-}), carbonate (CO_3^{2-}), and hydrogen(H^+) [9]. However, the ionic strength of the solution containing four components is 0.017, which is notably lower than 0.15–0.16 reported experimentally [12]. Since ionic strength directly affects the calculation of activity coefficients and thus the equilibrium concentrations, to improve model precision, we included the additional chemical components and examined how their inclusion affected the ionic strength of the ISF (Table 1). The resulting ISF was defined as a solution containing seven major components: calcium (Ca^{2+}), phosphate (PO_4^{3-}), carbonate (CO_3^{2-}), sodium (Na^+), chloride (Cl^-), magnesium (Mg^{2+}), and potassium (K^+) (Table 1). These components interact through reversible reactions forming 22 different chemical species listed here: H_3PO_4, $H_2PO_4^-$, HPO_4^{2-}, $H_2CO_3(aq)$, HCO_3^-, $CaHCO_3^+$, $CaCO_3(aq)$, $CaOH^+$, $CaH_2PO_4^+$, $CaHPO_4(aq)$, $CaPO_4^-$, $NaHPO_4^-$, $NaH_2PO_4(aq)$, $MgHCO_3^+$, $MgCO_3(aq)$, $MgOH^+$, $MgH_2PO_4^+$, $MgHPO_4(aq)$, $MgPO_4^-$, $NaCl$, $KHPO_4^-$, OH^-. The equilibrium constants for the 22 reactions were obtained from experimental studies; where reported, we used the value at the body temperature of 37 °C (Table 2). Seven equations for the principle of mass conservation for total amounts of calcium (TCa), phosphate (TPO4), carbonate (TCO3), magnesium (TMg), sodium (TNa), potassium (TK), and chloride (TCl) in addition to pH value completed the description of ISF (Table 2). The total amounts of these components were matched to those reported in human plasma [12](Table 1). The ISF is an ionic solution which requires the inclusion of activity coefficients in calculating its equilibrium concentrations. Ionic strength of a solution is defined as:

$$I = \frac{1}{2} \sum_{i=1}^{n} c_i \cdot z_i^2 \qquad (1)$$

where c_i is the molar concentration of ion i, z_i is its valence, and n is the number of different ions in the solution. The activity coefficients were calculated as follows:

$$\log \gamma_i = -Az_i^2 \left(\frac{\sqrt{I}}{\left(1 + \sqrt{I}\right)} - 0.3I \right) \qquad (2)$$

γ_i is the activity coefficient of ion i, which depends on ionic strength I of the solution, ion valence z_i, and temperature and the dielectric constant of the solvent expressed in parameter A. This parameter was previously approximated [23] for a solution with water as the solvent as:

$$A = 0.486 + 6.07 \times 10^{-4} T_C + 6.43 \times 10^{-6} T_C^2 \qquad (3)$$

where T_C is temperature in Celsius (37 °C in this study). Equation 2 is only valid for I ≤ 0.5 M [18], which is applicable in this case (Table 1). Finally, equilibrium concentrations are calculated as:

$$Q_i = c_i \cdot \gamma_i \qquad (4)$$

where Q_i, the corrected concentration is a product of nominal concentration c_i of each ion and its activity coefficient γ_i.

For the calculation of the equilibrium concentrations a system of non-linear equation had to be formed and solved. Using the reaction rate law and equilibrium constants for the 22
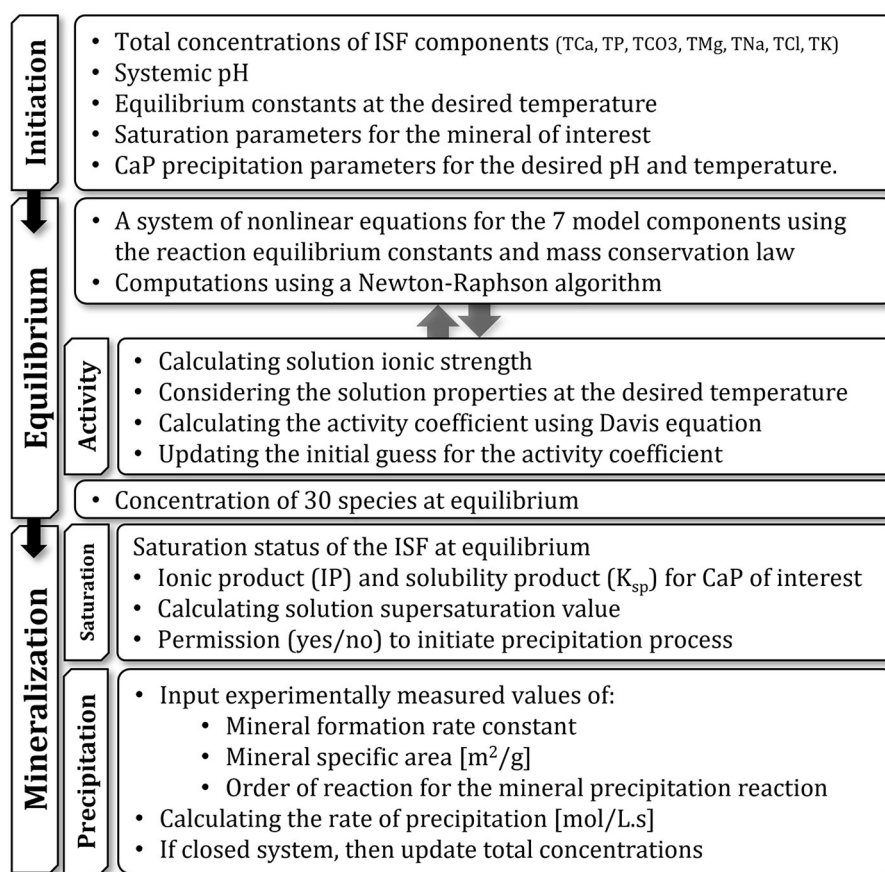
FIGURE 1
Schematic representation of the model and its different compartments and their functions. Arrows show the flow of data between compartments.

reactions (Table 2), one equation from pH definition, in addition of 7 equations derived from mass conservation law for total concentration of calcium (TCa), phosphate (TPO$_4$), carbonate (TCO$_3$), magnesium (TMg), sodium (TNa), potassium (TK), and chloride (TCl), a system of 30 equations was formed. Using the definition of equilibrium constants, the system was later simplified to a system of 7 non-linear equations with 7 variables (the components in Table 1). The system of equation was solved for these 7 variables and the rest of chemical species were later calculated by reversing the simplifying step using equilibrium constants.

2.3 Saturation

The simulated ISF includes the possibility of mineral formation. Physicochemically speaking, mineral formation requires the solution to be at a supersaturated state, meaning that there must be more solute available than the amount that can be dissolved in the solvent at a defined physical condition (temperature and pressure). To investigate the state of saturation, the minerals of interest must be known. Although there have been many studies on the formation of intermediate calcium phosphate precipitates prior to or simultaneous with the formation of hydroxyapatite

TABLE 1 Model components and their effect on the ionic strength of the solution.

Solution components	Total concentration	Physiological concentration (mM)	Solution ionic strength
CO_3^{2-}	TCO$_3$	27	0.017
PO_4^{3-}	TPO$_4$	1.0	
Ca^{2+}	TCa	1.6	
Na^+	TNa	142	0.089
Cl^-	TCl	103	0.140
K^+	TK	5	0.143
Mg^{2+}	TMg	1	0.145

Reported are solution components in their ionic forms, nomenclature for their total concentrations, physiological total plasma concentrations and ionic strength of the solution following the inclusion of the specific component from top to down of the list. The reported ionic strength of human plasma is 0.15–0.16 [12]. Systemic pH was set to 7.4.

[24], in the current model we did not take into account the intermediate precipitates and their gradual transition into the stable hydroxyapatite form. In this study we assumed that hydroxyapatite with the chemical formula of $Ca_{10}(PO_4)_6(OH)_2$ is the only form of mineral that could be formed. With that, to investigate

TABLE 2 ISF Reactions and their equilibrium constants.

Reaction	Equilibrium constants	References
$H_2CO_3(aq) \rightleftharpoons 2H^+ + CO_3^{2-}$	$10^{-6.31}$	[13]
$HCO_3^- \rightleftharpoons H^+ + CO_3^{2-}$	$10^{-10.25}$	[13]
$H_3PO_4 \rightleftharpoons H^+ + H_2PO_4^-$	$10^{-2.196}$	[13]
$H_2PO_4^- \rightleftharpoons H^+ + HPO_4^{2-}$	$10^{-7.185}$	[13]
$HPO_4^{2-} \rightleftharpoons H^+ + PO_4^{3-}$	$10^{-12.19}$	[13]
$Ca^{2+} + HCO_3^- \rightleftharpoons CaHCO_3^+$	$10^{1.16}$	[13]
$Ca^{2+} + CO_3^{2-} \rightleftharpoons CaCO_3(aq)$	$10^{3.38}$	[13]
$Ca^{2+} + OH^- \rightleftharpoons CaOH^+$	25.12	[14]
$Ca^{2+} + H_2PO_4^- \rightleftharpoons CaH_2PO_4^+$	31.9	[15]
$Ca^{2+} + HPO_4^{2-} \rightleftharpoons CaHPO_4(aq)$	6.81×10^2	[15]
$Ca^{2+} + PO_4^{3-} \rightleftharpoons CaPO_4^-$	3.46×10^6	[15]
$Mg^{2+} + HCO_3^- \rightleftharpoons MgHCO_3^+$	$10^{0.62}$	[16]
$Mg^{2+} + CO_3^{2-} \rightleftharpoons MgCO_3(aq)$	$10^{1.87}$	[16]
$Mg^{2+} + OH^- \rightleftharpoons MgOH^+$	$10^{2.19}$	[16]
$Mg^{2+} + H_2PO_4^- \rightleftharpoons MgH_2PO_4^+$	$10^{0.4}$	[17]
$Mg^{2+} + HPO_4^{2-} \rightleftharpoons MgHPO_4(aq)$	$10^{1.8}$	[17]
$Mg^{2+} + PO_4^{3-} \rightleftharpoons MgPO_4^-$	$10^{3.3}$	[17]
$Na^+ + HPO_4^{2-} \rightleftharpoons NaHPO_4^-$	0.21	[18]
$Na^+ + H_2PO_4^- \rightleftharpoons NaH_2PO_4(aq)$	$10^{-6.82}$	[19]
$Na^+ + Cl^- \rightleftharpoons NaCl(aq)$	3.41×10^{-2}	[20]
$K^+ + HPO_4^{2-} \rightleftharpoons KHPO_4^-$	2.5	[21]
$H_2O \rightleftharpoons H^+ + OH^-$	10^{-14}	[22]

the state of saturation we calculated supersaturation using the following equation:

$$S = \left(\frac{IP}{K_{SP}} \right)^{1/9} \qquad (5)$$

S in Equation 5 is the solution supersaturation which depends on the ionic product and the solubility product of hydroxyapatite. Ionic product is calculated as:

$$IP = (C_{Ca} \times \gamma_{Ca})^5 \left(C_{PO_4} \times \gamma_{PO_4} \right)^3 (C_{OH} \times \gamma_{OH})^1 \qquad (6)$$

where C and γ stand for the equilibrium concentration and the activity coefficient for each ion in the mineral structure. Solubility product, K_{SP}, is the equilibrium constant for a chemical reaction in which a solid ionic compound dissolves to yield its ions and is measured experimentally. K_{SP} for hydroxyapatite at 37°C is reported $2.03 \times 10^{-59} \frac{mol^9}{L^9}$ [12]. For other precipitates, we used the following K_{SP}: brushite (DCPD) 10^{-7} [25], octacalcium phosphate (OCP) 1.05×10^{-47} [26], β-tricalcium phosphate (TCP) 2.83×10^{-30} [27], and calcium carbonate (CaCO₃) 3.36×10^{-9} [28]. Supersaturation, S, >1 in a solution indicates a supersaturated state where mineral precipitation occurs until S = 1 (or IP = K_{SP}) and the system rests at equilibrium. In a biological system

like the human body, availability of mineralization inhibitors can affect this behavior. For example, this threshold at human urine is estimated at ~10 [29], while for human plasma it is calculated in the range of 1.5 to 13 [12, 18]. The difference in the reported values comes also from the fact that different studies considered different values for plasma concentrations and did the calculations with different levels of simplification. In the current study, supersaturation S was calculated at 14.9 for the concentrations introduced at Table 1.

It is worth noting here that different studies report the saturation state of the solution using slightly different methods, although they are all addressing the same phenomenon. Some studies use solution supersaturation defined as $\left(\frac{IP}{K_{SP}} \right)^{\frac{1}{\vartheta}}$, where ϑ is the sum of stochiometric coefficients of cations and anions involved in the mineral, some other use the saturation index defined as $\log \left(\frac{IP}{K_{SP}} \right)$, and in some cases, they just looked at the saturation ratio defined by $\frac{IP}{K_{SP}}$. It is obvious that the interpretation of the values calculated differs depending on the method used, for example while solution supersaturation of 1 means the solution is in equilibrium, the saturation index of value of 0 means the same state. In this study we used the solution supersaturation method.

2.4 Mineral precipitation

A supersaturated solution proceeds with mineral precipitation. Calcium phosphates and among them biologically important ones like hydroxyapatite have been studied over the years and different theoretical and experimental studies tried to address their rate of precipitation [30, 31]. In the current study, we relied on experimental study of hydroxyapatite precipitation rate at a solution with pH 7.4 to 8.4 [30] considering human physiology. The precipitation rate equation was reported as:

$$R = k_f s \gamma_2 \gamma_3 \left[Ca^{2+} \right] \left[PO_4^{3-} \right] \qquad (7)$$

where R is rate of hydroxyapatite precipitation ($mol\ HAP\ L^{-1}s^{-1}$), k_f is the rate constant ($L^2 mol^1 m^{-2} s^{-1}$), s is surface area ($m^2 L^{-1}$), γ_2 and γ_3 are the divalent and trivalent activity coefficients, and brackets are the concentrations of Ca^{2+} and PO_4^{3-} ($mol\ L^{-1}$).

2.5 Model simulation and analysis (numerical solution)

Due to the high level of non-linearity and large number of variables, the Newton-Raphson (NR) method was used to solve the system of equations.

To avoid divergence in the NR solver, as proposed by Morel and Morgan [32], in cases that $[X_j]^n + \Delta X_j^n < 0$, the next iteration would be calculated using $[X_j]^{n+1} = \frac{[X_j]^n}{10}$. The initial guess of equal concentrations and equal activity coefficients of 0.5 was made to initiate solving the system. During an iterative process, the calculated concentrations and coefficients of each iteration were used to initiate the next iteration of calculations. This iterative process was repeated to the point where the maximum difference between the last two iterative values of activity coefficients were

TABLE 3 Physiological and pathophysiological levels of total calcium, total phosphate, total carbonate.

	Normal (mM)	References	Hypo (mM)	References	Hyper (mM)	References
Ionized calcium	1–1.4	[33]	Mild: > 0.8 Sever: <0.62	[34]	Mild: 1.4 – 2 - Mod: 2–2.5 Severe: 2.5–3	[33]
Inorganic phosphorous	0.8 – 1.45	[35]	Mild: 0.65– 0.8 Mod: 0.32–0.65 Severe: <0.32	[35]	Mild to mod: >1.45 Severe: >2	[35]
Carbonate	22–28	[36]	Mild: 18–21 Mod: 10–17 Severe: <10	[36]	Mild: 28–32 Mod: 32–36 Severe: > 36	[36]

FIGURE 2
Effect of physiological and pathophysiological total concentration of calcium (A, B), phosphate (B, D), and carbonate (E, F) on the equilibrium concentration of ionized calcium (A, C, E), and ionized phosphate (B, D, E) at physiological pH7.4 (solid line), low pH 7.3 (dashed line) and high pH 7.55 (dished-dotted line). The vertical lines are the mild and severe levels for low and high total concentrations (Table 3).

smaller than an arbitrary value of $\varepsilon_{act} = 10^{-8}$. At this point, the equilibrium concentrations of all chemical species in the solution were calculated.
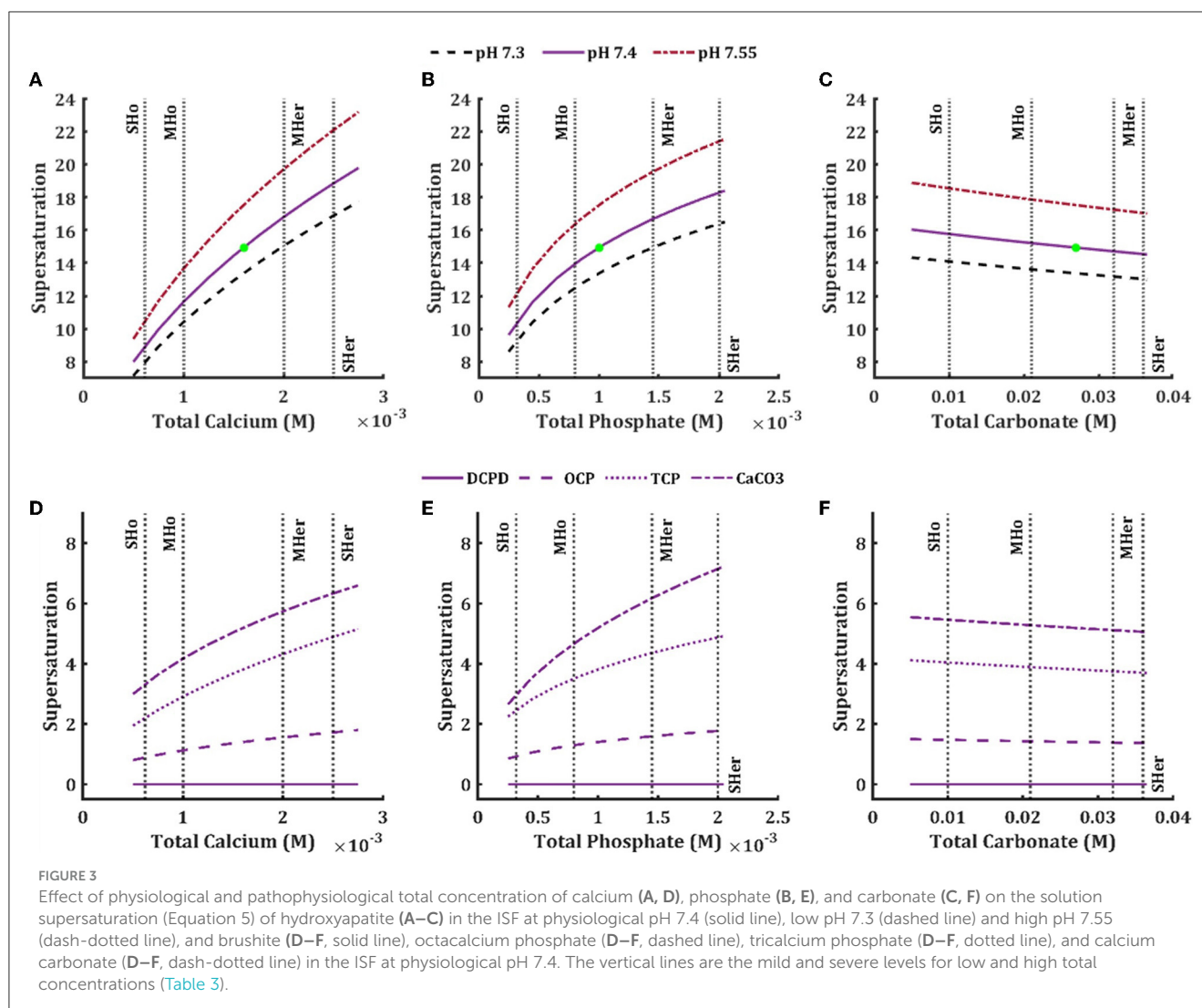
3 Results

We investigated how the changes in total concentrations of 7 model components, TCa, TPO$_4$, TCO$_3$, TMg, TNa, TK, TCl (Table 1), affect ISF composition, hydroxyapatite saturation and hydroxyapatite precipitation. We explored the range of changes corresponding to physiologically reported mild and severe decreases and increases in individual components (Table 3). In

addition, we studied the effect of physiological variation in systemic pH from pH7.3 to pH7.55 [37] on ions distribution.

3.1 Distribution of ions

We focused on the effect of total concentrations of individual components on the concentrations of ions relevant to hydroxyapatite precipitation, i.e., Ca^{2+} and PO_4^{3-} (Figure 2). Changes in TCa positively correlated with ionized calcium concentration (Figure 2A) and negatively correlated with ionized phosphate level (Figure 2B), although the effect of TCa on PO_4^{3-} was less prominent than on Ca^{2+}. The TPO$_4$ positively

FIGURE 3
Effect of physiological and pathophysiological total concentration of calcium (A, D), phosphate (B, E), and carbonate (C, F) on the solution supersaturation (Equation 5) of hydroxyapatite (A–C) in the ISF at physiological pH 7.4 (solid line), low pH 7.3 (dashed line) and high pH 7.55 (dash-dotted line), and brushite (D–F, solid line), octacalcium phosphate (D–F, dashed line), tricalcium phosphate (D–F, dotted line), and calcium carbonate (D–F, dash-dotted line) in the ISF at physiological pH 7.4. The vertical lines are the mild and severe levels for low and high total concentrations (Table 3).

correlated with ionized phosphate concentration and negatively correlated with ionized calcium and had a stronger effect on ionized phosphate (Figures 2C, D). Changes in total concentrations of other components in the model had minimal effect on ionized calcium and phosphate with the exception of carbonate that demonstrated negative association with ionized calcium and no association with ionized phosphate (Figures 2E, F). The effect of systemic pH was negligible for the ionized calcium, while ionized phosphate level was considerably influenced by pH level (Figure 2).

3.2 Saturation

We next examined how total concentrations of individual components affect hydroxyapatite solution supersaturation (Equation 5). Solution supersaturation for HAP at the physiological levels of ions was 14.9, which is consistent with previously reported values [12, 38] and demonstrates that the action of mineralization inhibitors is critical for preventing precipitation in biological fluids [6]. The HAP solution supersaturation was positively associated with the levels of total calcium (Figure 3A) and total phosphate

(Figure 3B). It was also mildly affected by total carbonate (negative association) (Figure 3C), but not by any other model components. Mild and severe hypercalcemia and hyperphosphatemia showed a similar effect in increasing the HAP solution supersaturation. Mild and severe hypocalcemia and hypophosphatemia lead to a decrease in HAP solution supersaturation, with total calcium having a more prominent effect (Table 4). We also considered the solution supersaturation for other mineral species, including DCPD, OCP, TCP and CaCO3 (Figures 3D–F). For all these components the level of solution supersaturation was lower than that of HAP, and for DCPD specifically, it was below 1 in the physiological ranges of total calcium, phosphate, and carbonate.

3.3 Precipitation

Precipitation starts with nucleation and proceeds with crystal growth [39]. In the biological context of bone mineralization, the nucleation step is mostly controlled biologically by the extracellular matrix proteins including collagens [11], while the physicochemical processes are involved in the growth phase. Thus, we assumed that

TABLE 4 Percentage of saturation ratio changes in hypo/hyper levels of blood calcium, phosphate, and carbonate compared to normal concentrations at physiological pH (7.4).

	Severe hypo (%)	Mild hypo (%)	Mild hyper (%)	Severe hyper (%)
TCa	−39.88	−22.14	12.40	26.14
TPO$_4$	−30.31	−6.63	11.71	22.39
TCO$_3$	5.61	1.88	−1.50	−2.65

FIGURE 4
Effect of physiological and pathophysiological total concentration of calcium (A), phosphate (B), and carbonate (C) on the precipitation rate of hydroxyapatite in the ISF, at physiological pH7.4 (solid line), low pH 7.3 (dashed line) and high pH 7.55 (dished-dotted line). The vertical lines are the mild and severe levels for low and high total concentrations (Table 3).
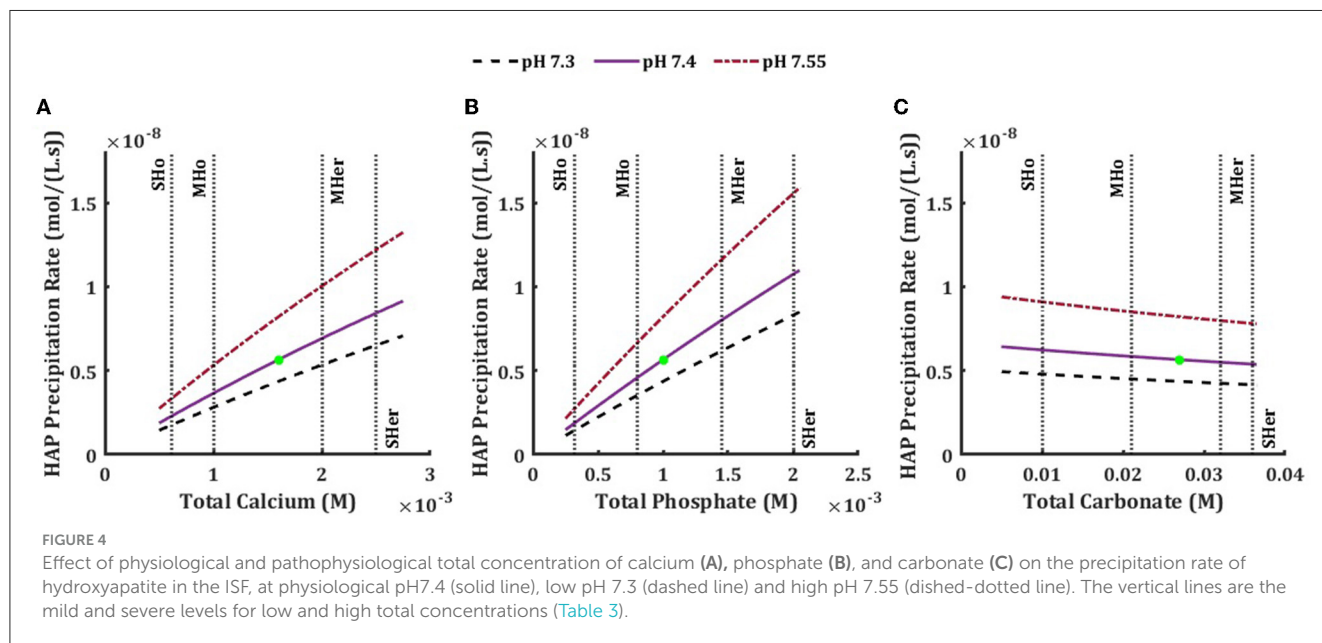
TABLE 5 Percentage of hydroxyapatite precipitation rate change in hypo/hyper levels of blood calcium, phosphate, and carbonate compared to normal concentrations at physiological pH (7.4).

	Severe hypo (%)	Mild hypo (%)	Mild hyper (%)	Severe hyper (%)
TCa	−59.07	−35.39	22.33	48.94
TPO$_4$	−67.02	−19.20	41.74	90.17
TCO$_3$	10.45	3.46	−2.72	−4.80

the number of nucleators were not limiting and examined how hydroxyapatite precipitation rate was affected by change in the ISF total concentrations of different components (Figure 4). Increase in total calcium (Figure 4A) and total phosphate (Figure 4B) concentrations led to higher hydroxyapatite precipitation rate and this increase was considerably influenced by the pH of the ISF. A more basic environment favored higher precipitation rate, while an acidic environment decreased the precipitation rate, although the lower physiological pH limit caused less change in the rate compared to the higher physiological limit. While both hypercalcemia and hyperphosphatemia caused the precipitation rate to increase, hyperphosphatemia (both mild and severe) led to an almost two-fold higher increase in the rate compared to hypercalcemia (Table 5). Hypocalcemia and hypophosphatemia led to decrease of the precipitation rate (Table 5). Changes in total concentrations of other model components did not affect the hydroxyapatite precipitation rate, except for total carbonate (Figure 4C, Table 5) which showed a mild negative association with the precipitation rate.

Since from seven model components, only two, total calcium and total phosphate, considerably influenced the hydroxyapatite precipitation in ISF, we examined how simultaneous changes in these two components affect hydroxyapatite supersaturation and precipitation rate. The simultaneous changes of TCa and TPO$_4$ had non-linear effect on both hydroxyapatite supersaturation and especially on the hydroxyapatite precipitation rate, which increased synergistically when both TCa and TPO$_4$ increased, but was only mildly affected when both TCa and TPO$_4$ decreased (Figure 5).

3.4 The case of isolated ISF

So far in this study, we investigated the behavior of the system under the assumption that ISF is in constant contact with the blood circulation, and the ions involved in the mineral formation will be immediately replenished. This assumption is supported by the fact that the rate of precipitation is much
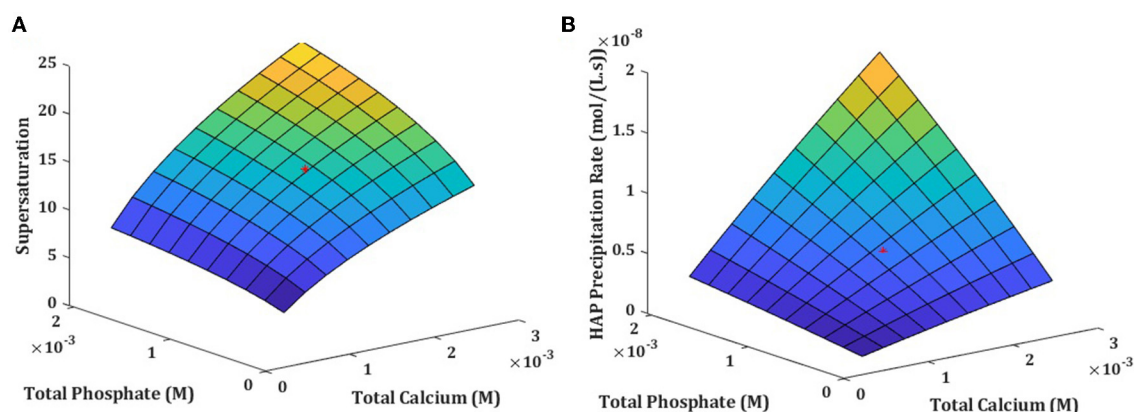
FIGURE 5
Solution supersaturation **(A)** and precipitation rate **(B)** influenced by simultaneous changes in total calcium and total phosphate concentration in physiologically relevant cncentrations at normal 7.4 pH.

slower than the rate of ion delivery to the ISF. Nonetheless, many experimental studies are performed in a closed environment, where there is no continuous delivery of ions consumed in mineral formation. Thus, we adapted the model to simulate such scenarios by employing the following modifications. We assumed that an ISF unit has the volume of 1 μm^3 and the smallest time step to measure changes in the ISF was equal to 1 s. Given the initial total concentrations of model components, we calculated the equilibrium concentrations, supersaturation, and precipitation rate (Equations 4, 5, and 7). Then, the amounts of ions that would have been removed by precipitation in the defined time step (1 s) were calculated and subtracted from the initial total concentrations of model components to produce the updated total concentrations of model components for the next iteration. This process was repeated to investigate the model behavior for a desired time length. This modified model was used to examine the temporal dynamics of hydroxyapatite precipitation in the closed system under different pH levels and initial component concentrations (Figure 6). Initial precipitation rate in closed system strongly depended on pH, resulting in more hydroxyapatite precipitation at alkaline pH, which is similar to experimental observations [40].
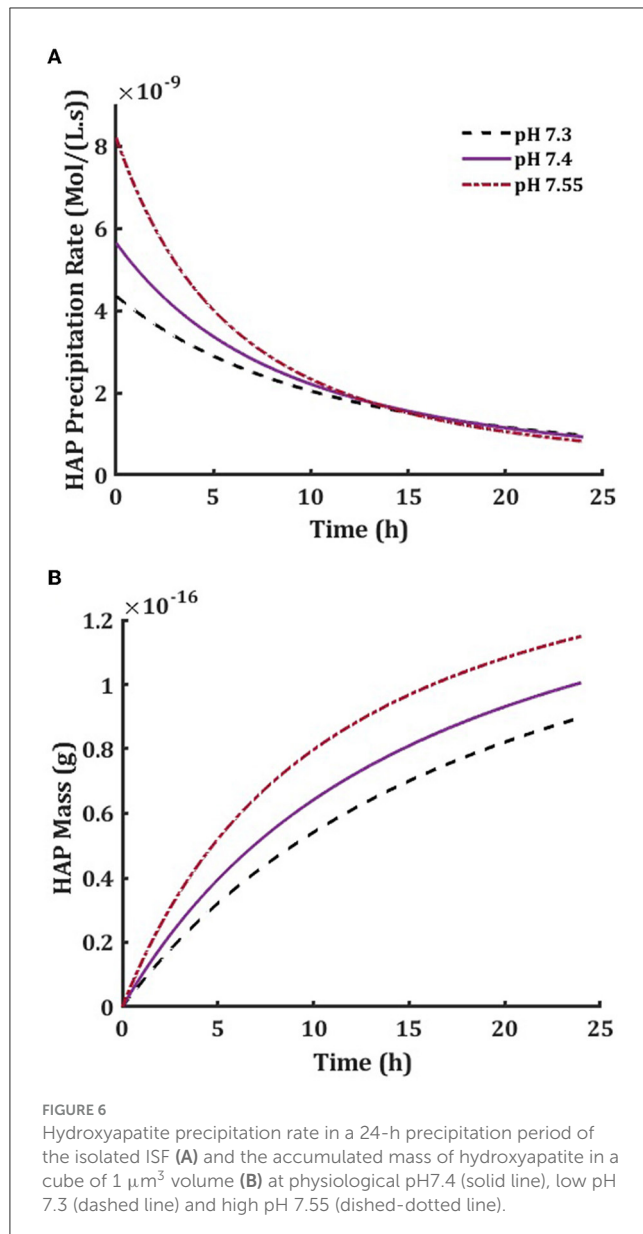
Next, we compared our model predictions to previously published experimental data. First, we modeled the dependence of ionized calcium on pH reported by Miyajima et al. [41]. We used in the model the reported values of component concentrations and pH for the experimental study and calculated the concentration of Ca^{2+} as a function of pH (Figure 7A). Our model agreed well with the experimental values at pH 7.4–7.8 but deviated at higher pH levels. Next, we modeled the pH dependence of ion distributions reported by Boistelle et al. [42]. We have similarly used the experimental values reported in the paper and calculated the resulting ionic concentrations of model species (Figure 7B), and the solution supersaturation for hydroxyapatite (Figure 7C). Our findings were consistent with reported experimentally for pH 5–8 and deviated from reported values at higher pH. Thus, our model predictions were consistent with experimental findings for pH values in the physiological range.

4 Discussion

The goal of this study was to investigate the role of physicochemical factors in the precipitation of bone hydroxyapatite in an environment that resembles bone interstitial fluid. We demonstrate that of the 7 components taken into consideration, only total calcium, total phosphate and to a lesser degree total carbonate affected ion availability, solution supersaturation and hydroxyapatite precipitation rate. Strong effect of systemic pH on solution supersaturation and hydroxyapatite precipitation was due to its effect on ionized phosphate level since ionized calcium was not affected by pH. Hydroxyapatite precipitation was more strongly affected by availability of phosphate than availability of calcium within physiological range of changes in these components. Simultaneous change in total calcium and phosphate had synergetic effect on hydroxyapatite precipitation rate. Thus, while both calcium and phosphate levels affected hydroxyapatite precipitation directly, phosphate also demonstrated susceptibility to changes in pH, which additionally influenced hydroxyapatite precipitation.
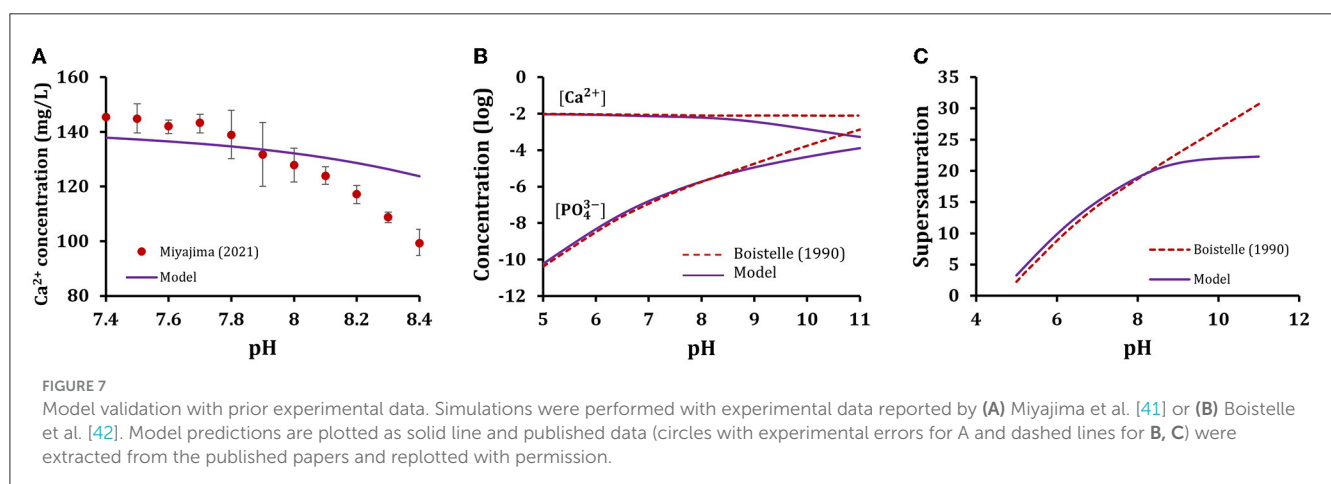
Building a chemically sound model of interactions among different chemical species present in the ISF allowed us to investigate their effect on ionized calcium and phosphate, which are critical for hydroxyapatite formation. While it was challenging to find experimental or computational works that had the exact same solution parameters as the ones implemented in the model, using values from similar experimental studies, we were able to reproduce experimentally observed ion distribution for physiological levels of pH [41, 42]. The negative association between total phosphate and pH with ionized calcium observed previously [43], was also confirmed by the model. Our study suggests that only levels of total calcium and phosphate and to a lesser degree total carbonate affect availability of ionized calcium and phosphate relevant for hydroxyapatite precipitation. However, the chemical complexity of ISF should still be taken into account to obtain correct predictions of the ionic strength and interactions in the solution.

The distribution of ions matters not only because they define the properties of the ISF, but also as they can affect the precipitation

FIGURE 6
Hydroxyapatite precipitation rate in a 24-h precipitation period of the isolated ISF **(A)** and the accumulated mass of hydroxyapatite in a cube of 1 μm^3 volume **(B)** at physiological pH7.4 (solid line), low pH 7.3 (dashed line) and high pH 7.55 (dished-dotted line).

behavior by modifying the solution saturation status. Building on previous findings that total calcium, phosphate and carbonate influence the ionized calcium and phosphate availability, we investigated their consequent effect on saturation state of the ISF. At physiological levels of model components, the model predicted the solution supersaturation of 14.9, which is close to reported experimental values [12]. While the model confirmed the state of supersaturation normally observed in human plasma [44], it also provided a broader understanding of how this supersaturation state could be influenced when total concentration of model components (i.e., their plasma or ISF levels) change. Moreover, the model predicts and explains the previously reported [40, 45] relationship of increased supersaturation values when pH increases at constant calcium and phosphate levels. In the future, the model predictions can be improved by a more precise incorporation of different parameters, such as accounting for the variability in K_{SP} due to pH, temperature, and solution composition [46]. Investigating the effect of ion distribution and saturation status on hydroxyapatite precipitation behavior demonstrated that precipitation rate is driven by the values of ionized calcium and phosphate, which in turn depend on pH. Model predictions were consistent with previous findings that an increase in ionized phosphate at high pH levels increases the deposition rate of hydroxyapatite and that decrease in phosphate availability interferes with hydroxyapatite precipitation [47]. Thus, our findings are consistent with the well-recognized role of phosphate in regulating bone mineralization in physiological condition and in hypophosphatemic osteomalacia.

While many simplifications are implemented in constructing this model, the fact that its findings are in line with experimental works and current understanding of human physiology reassure us that the findings are reliable and that the model is suitable further developed. Combining this model with models of bone mineralization that account for biological factors such as collagen maturation [48] and bone cells-derived regulators [49] will provide a powerful tool in studying the formation of bone hydroxyapatite or other biological mineralized tissues. Another field of modeling that could potentially benefit from the combined physicochemical and biological model is the whole-body calcium and phosphate

FIGURE 7
Model validation with prior experimental data. Simulations were performed with experimental data reported by **(A)** Miyajima et al. [41] or **(B)** Boistelle et al. [42]. Model predictions are plotted as solid line and published data (circles with experimental errors for A and dashed lines for **B, C**) were extracted from the published papers and replotted with permission.

homeostasis models. Bone is a major component of calcium and phosphate homeostasis, and its behavior is regulated by hormonal regulation by PTH, vitamin D, FGF23, calcitonin which directly or indirectly affect calcium and phosphate concentration in the body [50].

Taken together, we developed a mathematical model that captures the physiochemical factors involved in hydroxyapatite precipitation. We demonstrated how factors such as availability of ions in the environment and their distribution of these ions, as well as pH levels affect hydroxyapatite precipitation. Integrating this model with biological models of bone mineralization will allow in silico studies of complex clinical scenarios associated with alterations in ISF ion composition, such as osteomalacia, osteogenesis imperfecta, rickets, hypophosphatemia, and chronic kidney disease. Moreover, with minor adaptations, it could be used to understand mineralization in other physiological tissues, such as dentin and enamel, and in pathological conditions such as kidney stones and atherosclerotic plaques [51].

5 Additional resources

Implementation of current bone physicochemical model in MATLAB is available on GitHub: https://github.com/Hosseinpoorhemati/bone_physicochemical_regulation.git.

Data availability statement

The original contributions presented in the study are included in the article, further inquiries can be directed to the corresponding author.

Author contributions

HP: Conceptualization, Formal analysis, Investigation, Methodology, Software, Validation, Visualization, Writing—original draft, Writing—review & editing. SVK: Conceptualization, Funding acquisition, Methodology, Project administration, Writing—review & editing.

Funding

Conflict of interest

The authors declare that the research was conducted in the absence of any commercial or financial relationships that could be construed as a potential conflict of interest.

Publisher's note

All claims expressed in this article are solely those of the authors and do not necessarily represent those of their affiliated organizations, or those of the publisher, the editors and the reviewers. Any product that may be evaluated in this article, or claim that may be made by its manufacturer, is not guaranteed or endorsed by the publisher.

References

1. Boskey AL. Bone composition: relationship to bone fragility and antiosteoporotic drug effects. *BoneKEy Rep*. (2013) 2:181. doi: 10.1038/bonekey.2013.181

2. Willie BM, Zimmermann EA, Vitienes I, Main RP, Komarova SV. Bone adaptation: Safety factors and load predictability in shaping skeletal form. *Bone*. (2020) 131:115114. doi: 10.1016/j.bone.2019.115114

3. Boskey AL, Robey PG. The composition of bone. *Primer Metab Bone Dis Disord Miner Metab*. (2013) 15:49–58. doi: 10.1002/9781118453926.ch6

4. Vassiliou V, Chow E, Kardamakis D. *Bone Metastases: A Translational and Clinical Approach*. Cham: Springer Science & Business Media (2013).

5. Ambre AH, Katti DR, Katti KS. Biomineralized hydroxyapatite nanoclay composite scaffolds with polycaprolactone for stem cell-based bone tissue engineering. *J Biomed Mater Res A*. (2015) 103:2077–101. doi: 10.1002/jbm.a.35342

6. Murshed M. Mechanism of Bone Mineralization. *Cold Spring Harb Perspect Med*. (2018) 8:12. doi: 10.1101/cshperspect.a031229

7. Collin CB, Gebhardt T, Golebiewski M, Karaderi T, Hillemanns M, Khan FM, et al. Computational models for clinical applications in personalized medicine—guidelines and recommendations for data integration and model validation. *J Pers Med*. (2022) 12:166. doi: 10.3390/jpm12020166

8. Komarova SV, Safranek L, Gopalakrishnan J, Ou MJ, McKee MD, Murshed M, et al. Mathematical model for bone mineralization. *Front Cell Dev Biol*. (2015) 3:51. doi: 10.3389/fcell.2015.00051

9. Poorhemati H, Komarova SV. Mathematical modeling of the role of bone turnover in pH regulation in bone interstitial fluid. *Comput Biol Chem*. (2021) 94:107564. doi: 10.1016/j.compbiolchem.2021.107564

10. Hunter GK, Kyle CL, Goldberg HA. Modulation of crystal formation by bone phosphoproteins: structural specificity of the osteopontin-mediated inhibition of hydroxyapatite formation. *Biochem J*. (1994) 300:723–8. doi: 10.1042/bj3000723

11. Olszta MJ, Cheng X, Jee SS, Kumar R, Kim Y-Y, Kaufman MJ, et al. Bone structure and formation: a new perspective. *Mat Sci Eng R Rep*. (2007) 58:77–116. doi: 10.1016/j.mser.2007.05.001

12. Söhnel O, Grases F. Supersaturation of body fluids, plasma and urine, with respect to biological hydroxyapatite. *Urol Res*. (2011) 39:429–36. doi: 10.1007/s00240-011-0387-5

13. Oyane A, Kim HM, Furuya T, Kokubo T, Miyazaki T, Nakamura T. Preparation and assessment of revised simulated body fluids. *J Biomed Mater Res A*. (2003) 65:188–95. doi: 10.1002/jbm.a.10482

14. Koutsoukos P, Nancollas G. Crystal growth of calcium phosphates-epitaxial considerations. *J Cryst Growth*. (1981) 53:10–9. doi: 10.1016/0022-0248(81)90051-8

15. Chughtai AR, Marshall R, Nancollas GH. Complexes in calcium phosphate solutions. *J Phys Chem*. (1968) 72:208–11. doi: 10.1021/j100847a039

16. Butler JN. *Ionic Equilibrium: Solubility and pH Calculations*. London: John Wiley & Sons (1998).

17. Childs C. Potentiometric study of equilibriums in aqueous divalent metal orthophosphate solutions. *Inorg Chem*. (1970) 9:2465–9. doi: 10.1021/ic50093a017

18. Granjon D, Bonny O, Edwards A. Coupling between phosphate and calcium homeostasis: a mathematical model. *Am J Physiol Renal Physiol*. (2017) 313:F1181–F99. doi: 10.1152/ajprenal.00271.2017

19. Salaun F, Mietton B, Gaucheron F. Influence of mineral environment on the buffering capacity of casein micelles. *Milchwissenschaft Milk Sci Int.* (2007) 62:20–3.

20. Crundwell FK. Path from reaction control to equilibrium constraint for dissolution reactions. *ACS Omega.* (2017) 2:4845–58. doi: 10.1021/acsomega.7b00344

21. Guynn RW. Equilibrium constants under physiological conditions for the reactions of choline kinase and the hydrolysis of phosphorylcholine to choline and inorganic phosphate. *J Biol Chem.* (1976) 251:7162–7. doi: 10.1016/S0021-9258(17)32957-5

22. Silverstein TP, Heller ST. pK_a values in the undergraduate curriculum: What is the real pK_a of water? *J Chem Educ.* (2017) 94:690–5. doi: 10.1021/acs.jchemed.6b00623

23. Drake F, Pierce G, Dow M. Measurement of the dielectric constant and index of refraction of water and aqueous solutions of KCl at high frequencies. *Phys Rev.* (1930) 35:613. doi: 10.1103/PhysRev.35.613

24. Castro F, Ferreira A, Rocha F, Vicente A, Teixeira JA. Characterization of intermediate stages in the precipitation of hydroxyapatite at 37 C. *Chem Eng Sci.* (2012) 77:150–6. doi: 10.1016/j.ces.2012.01.058

25. Nancollas G, Tomazic B. Growth of calcium phosphate on hydroxyapatite crystals. Effect of supersaturation and ionic medium. *J Phys Chem.* (1974) 78:2218–25. doi: 10.1021/j100615a007

26. Moreno EC, Brown WE, Osborn G. Stability of dicalcium phosphate dihydrate in aqueous solutions and solubility of octocalcium phosphate. *Soil Sci Soc Am J.* (1960) 24:99–102. doi: 10.2136/sssaj1960.03615995002400020010x

27. Gregory T, Moreno E, Patel J, Brown W. Solubility of β-Ca3 (PO4) 2 in the System Ca (OH) 2-H3PO4-H2O at 5, 15, 25, and 37° C. *J Res Nat Bureau Standards Sec A Phys Chem.* (1974) 78:667. doi: 10.6028/jres.078A.042

28. Gal J-Y, Bollinger J-C, Tolosa H, Gache N. Calcium carbonate solubility: a reappraisal of scale formation and inhibition. *Talanta.* (1996) 43:1497–509. doi: 10.1016/0039-9140(96)01925-X

29. Herbert FK, Miller H, Richardson G. Chronic renal disease, secondary parathyroid hyperplasia, decalcification of bone and metastatic calcification. *J Pathol Bacteriol.* (1941) 53:161–82. doi: 10.1002/path.1700530202

30. Inskeep WP, Silvertooth JC. Kinetics of hydroxyapatite precipitation at pH 7. 4 to 84. *Geochimica et Cosmochimica Acta.* (1988) 52:1883–93. doi: 10.1016/0016-7037(88)90012-9

31. Yun J, Holmes B, Fok A, Wang Y, A. kinetic model for hydroxyapatite precipitation in mineralizing solutions. *Cryst Growth Des.* (2018) 18:2717–25. doi: 10.1021/acs.cgd.7b01330

32. Morel F, Morgan J. A numerical method for computing equilibria in aqueous chemical systems. *Environ Sci Technol.* (1972) 21:1–14. doi: 10.1021/es60060a006

33. Carroll MF, Schade DS. A practical approach to hypercalcemia. *Am Fam Physician.* (2003) 67:1959–66.

34. Pepe J, Colangelo L, Biamonte F, Sonato C, Danese VC, Cecchetti V, et al. Diagnosis and management of hypocalcemia. *Endocrine.* (2020) 69:485–95. doi: 10.1007/s12020-020-02324-2

35. Koumakis E, Cormier C, Roux C, Briot K. The causes of hypo- and hyperphosphatemia in humans. *Calcified Tissue Int.* (2021) 108:41–73. doi: 10.1007/s00223-020-00664-9

36. Narins RG Emmett M. Simple and mixed acid-base disorders: a practical approach. *Medicine.* (1980) 59:161–82. doi: 10.1097/00005792-198005000-00001

37. Mehta AN, Emmett M. *Approach to Acid-Base Disorders. National Kidney Foundation Primer on Kidney Diseases.* Amsterdam: Elsevier (2018), 120–9.

38. Aleš H, Lenka J, Ludvík Š. The influence of simulated body fluid composition on carbonated hydroxyapatite formation. *Ceram-Silik.* (2002) 46:9–14.

39. Eanes ED. Dynamics of calcium phosphate precipitation. *Calcif Biol Syst.* (2020) 21:1–17. doi: 10.1201/9781003068396-2

40. Lei Y, Song B, van der Weijden RD, Saakes M, Buisman CJ. Electrochemical induced calcium phosphate precipitation: importance of local pH. *Environ Sci Technol.* (2017) 51:11156–64. doi: 10.1021/acs.est.7b03909

41. Miyajima H, Touji H, Iijima K. Hydroxyapatite particles from simulated body fluids with different pH and their effects on mesenchymal stem cells. *Nanomaterials.* (2021) 11:2517. doi: 10.3390/nano11102517

42. Boistelle R, Lopez-Valero I. Growth units and nucleation: the case of calcium phosphates. *J Cryst Growth.* (1990) 102:609–17. doi: 10.1016/0022-0248(90)90420-P

43. Lehmann M, Mimouni F. Serum phosphate concentration. Effect on serum ionized calcium concentration *in vitro. Am J Dis Child.* (1989) 143:1340–1. doi: 10.1001/archpedi.1989.02150230098031

44. Zhu P, Masuda Y, Yonezawa T, Koumoto K. Investigation of apatite deposition onto charged surfaces in aqueous solutions using a quartz-crystal microbalance. *J Am Ceram Soc.* (2003) 86:782–90. doi: 10.1111/j.1151-2916.2003.tb03375.x

45. Nancollas GH, Zhang J. *Formation and Dissolution Mechanisms of Calcium Phosphates in Aqueous Systems. Hydroxyapatite and Related Materials.* London: CRC Press (2017), 73–81.

46. Ito A, Maekawa K, Tsutsumi S, Ikazaki F, Tateishi T. Solubility product of OH-carbonated hydroxyapatite. *J Biomed Mat Res Biomat.* (1997) 36:522–8. doi: 10.1002/(SICI)1097-4636(19970915)36:4<522::AID-JBM10>3.0.CO;2-C

47. Bhadada SK, Rao SD. Role of phosphate in biomineralization. *Calcified Tissue Int.* (2021) 108:32–40. doi: 10.1007/s00223-020-00729-9

48. Oosterlaken BM, Vena MP, de With G. *In vitro* mineralization of collagen. *Adv Mat.* (2021) 33:2004418. doi: 10.1002/adma.202004418

49. Staines KA, Zhu D, Farquharson C, MacRae VE. Identification of novel regulators of osteoblast matrix mineralization by time series transcriptional profiling. *J Bone Miner Metab.* (2014) 32:240–51. doi: 10.1007/s00774-013-0493-2

50. Case RM, Eisner D, Gurney A, Jones O, Muallem S, Verkhratsky A. Evolution of calcium homeostasis: from birth of the first cell to an omnipresent signalling system. *Cell Calcium.* (2007) 42:345–50. doi: 10.1016/j.ceca.2007.05.001

51. Hinterdobler J. Schott, Simin, Jin H, Meesmann A, Steinsiek A-L, Zimmermann A-S, et al. Acute mental stress drives vascular inflammation and promotes plaque destabilization in mouse atherosclerosis. *Eur Heart J.* (2021) 42:4077–88. doi: 10.1093/eurheartj/ehab371

Evaluation of personal protective equipment to protect health and safety in pesticide use

Güler Aksüt[1] and Tamer Eren[2]*

[1]Ministry of Education, TOKI Mevlana Primary School, Yozgat, Türkiye, [2]Departmant of Industrial Engineering, Kırıkkale University, Kırıkkale, Türkiye

Introduction: Agriculture emerges as one of the most dangerous industries in the world, considering injury and illness rates. After the service sector in Turkey, the next large-scale sector is the agricultural sector, which constitutes 20% of the general employment. The exposure of farmers to pesticides, used to increase the quality and productivity of agricultural products, causes health risks via the mouth, respiration, skin, and eyes. Pesticide use in Turkey is increasing; the annual average increase is estimated at 1.2%. Exposure to pesticides can be reduced by wearing personal protective equipment to protect against health and safety hazards.

Objective: This study aimed to determine the importance of personal protective equipment using the multi-criteria decision-making method to prevent the risk of injury and disease resulting from pesticide use.

Materials and methods: The Analytical Hierarchy Process (AHP) method was used to find the weights of the criteria determined by expert opinion and a literature review. The Preference Ranking Organization Method for Enrichment Evaluation (PROMETHEE) was used to rank personal protective equipment.

Results: Personal protective equipment includes masks, gloves, overalls, safety shoes, glasses, and hats. The use of multi-criteria decision-making methods in health and safety in the agricultural sector will contribute to the literature.

Conclusion: Emphasizing the use of personal protective equipment, especially when using pesticides, will increase the rate of use of protective measures.

KEYWORDS

agriculture, analytical hierarchy process and the preference ranking organization method for enrichment evaluation, occupational health and safety, personal protective equipment, pesticide

1 Introduction

Compared to other sectors, the injury and illness rates of agricultural workers in the agricultural sector emerge as one of the most dangerous sectors worldwide. Its full extent is unknown due to inconsistencies in data collection and reporting (1). The agricultural sector constitutes 20% of the general employment in Turkey. It is the largest sector after the service sector (2).

There are significant risks of disease and injury in public health and agriculture associated with pesticide use (3). Most pesticides are very harmful to both human and animal health. It can cause serious, irreversible effects on the environment. This situation causes significant

contamination in all ecosystems (4). Exposure to pesticides occurs mainly via the skin and inhalation. It can also occur by consuming contaminated food, oral contact with contaminated hands, or ingestion. Another important source of exposure is contaminated clothing (5). According to the World Health Organization's (WHO) estimation, 25 million agricultural workers are exposed to acute pesticide poisoning cases each year (3). Risk perception variables of pesticide use that threaten the environment and human health can play an essential role in farmers' taking safety measures (6). WHO classifies pesticides as moderately hazardous toxicity class II, which can lead to health risks if unsafe equipment is used by farmers (7). WHO and the International Labor Organization (ILO) recommend that farmers use personal protective equipment (PPE) to protect their health by reducing their exposure to pesticides (8).

Employee-specific clothing or equipment worn by employees to avoid exposure to health and safety hazards is called PPE. Various PPEs have been designed to protect many body parts, such as the eyes, hands, feet, head, ears, and face (9). Although its use is the least preferred solution, it should be considered in solving professional problems within a systematic and integrated vision. For this reason, the effectiveness of the entire occupational health and safety system and the balanced selection of alternatives for prevention, protection, and control are closely related (10). There are chemical, biological, and physical hazards in working environments. It is a known fact that the quality of workplaces increases with environmental management measures and engineering approaches that protect their employees by reducing or eliminating the danger factors. However, it is not disputed that many fields of study also need to implement such decisive, practical measures. In such cases, a business management approach using PPE is considered an alternative and essential tool to protect the health and safety of employees (11).

In this study, the importance of ranking PPE using Multi-Criteria Decision-Making (MCDM) methods was discussed to prevent the risk of injury and disease caused by pesticide use. The criterion weights of PPE were determined using the AHP method and ranked using the PROMETHEE method.

There are studies on pesticides in the literature. Clark et al. (12) investigated the attitudes, knowledge, and practices of 123 agricultural workers regarding the safe use of pesticides at three irrigation project sites in the Accra Plains, Ghana. Gomes et al. (13) investigated the use of PPE and the application of hygiene and safety procedures to process pesticides in agriculture. Nordin et al. (14) studied the effects of pesticide use-related safety behaviors on the onset of acute organ symptoms in 101 female and 395 male tobacco-growing Malaysian farmers. Mekonnen and Agonafir (15) presented data on pesticide use, PPE use, attitudes, applications, and knowledge of pesticide sprayers on large Ethiopian farms. Reed (16) conducted studies to determine the self-protective work behaviors, risk exposures, and use of personal protective equipment of children on farms. Reed emphasized the need to be informed about personal protective equipment. Atreya (17) studied how pesticide use affects the health of farmers in Nepal. The study aimed to understand acute health symptoms and estimate health costs in rural Nepal concerning pesticide exposure. The study revealed that pesticide use had acute effects on health. Weerasinghe et al. (18) aimed to receive detailed user notifications regarding the differences in pesticide storage, evaluate the use of pesticide-safe storage devices, and identify problems related to crucial protection. Fenske (19) provided field demonstrations and discussions on traumatic and

musculoskeletal injuries in orchards, mobile work platforms, and new pest control technologies. Levesque and Shen (20) aimed to investigate the relationship between the housing conditions of agricultural workers, pesticide safety practices, and PPE use. Meirelles et al. (21) examined the efficiency of using PPE in agriculture through a theoretical framework. They developed an analysis of PPE design by controlling the unhealthy conditions of rural workers. Almeida et al. (22) examined the inadequacy of PPE used in tomato crops, especially thermal comfort. Their study showed that insufficient use of PPE may pose a risk of thermoregulation for rural workers. Basilicata et al. (23) investigated agricultural workers' general working conditions and pesticide exposure in tomato-growing farms in southern Italy during the mixing/loading and applying of pesticides to the fields. Lekei et al. (24) aimed to explain farmers' knowledge of pesticide hazards, pesticide exposure profiles, unsafe practices that cause acute poisoning, the extent to which acute poisoning was reported, and previous poisoning experiences. Al Zadjali et al. (25) conducted their studies to investigate the differences between farm types in PPE use, identify the key people responsible for pesticide applications, and store pesticides safely. In their study, Andrade-Rivas and Andrea Rother (26) aimed to analyze the risk perceptions related to the socio-cultural context, working conditions, and herbicide use to understand the employees' low PPE compliance. The study results revealed that although workers were informed about herbicide exposure risks, PPE use continued at a low rate due to workers being affected by working conditions, herbicide risk perceptions, and workers' social status and gender dynamics. Rudolphi (27) aimed to determine agricultural educators' attitudes, needs, and practices about agricultural safety and health. Ngowi et al. (28) aimed to reveal that national pesticide regulations need to be revised to solve the health and safety problems encountered by agricultural workers in Tanzania in the use of pesticides on a small scale. Sawada et al. (11) aimed to present the latest information on the development and evaluation. Akter et al. (29) aimed to examine the behavioral activities of farmers regarding their pesticide use and determine the relevant factors affecting the use. Yarpuz-Bozdogan (30) emphasized the importance of using PPE in pesticide applications in agriculture. Reynolds et al. (31) obtained descriptive findings regarding pesticide use from 1,191 participants who completed occupational surveys in the study, which included an in-depth evaluation of injuries, respiratory diseases, and other health consequences related to environmental and occupational exposures. Rezaei et al. (32) aimed to fill the gap with healthy spread theory and planned behavior theory, which include perceived sensitivity and severity structures for the factors affecting Iranian farmers' PPE use. Sapbamrer and Thammachai (33) reviewed the existing literature on PPE use by pesticide processors in different regions of the world. Joko et al. (34) investigated the symptoms of poisoning caused by farmers' pesticide exposure. Jakob et al. (35) defined and classified the national occupational health and safety mechanisms in Europe for agricultural workers and aimed to exemplify the scope of implementation of the safety regulation by evaluating the responsible institution for health and safety initiatives. Zhang et al. (36) investigated the work-related risk factors and prevalence level of acute pesticide poisoning among farmers in southern China. Those who experienced work-related acute pesticide poisoning constituted 8.8% of the total pesticide applicators. Paschoalin et al. (37) reported on a non-enzymatic wearable electrochemical sensor that can detect bipyridinium and carbamate pesticides on the surface of food and agricultural samples.

TABLE 1 AHP method steps.

Method steps	Description of method steps
Step 1	Defining the problem clearly and determining its purpose.
Step 2	Establishing a hierarchical structure by determining relative priorities for the main criteria and their sub-criteria.
Step 3	Creation of pairwise comparisons/matrices of defined criteria.
Step 4	Normalization of pairwise comparison matrices and calculation of relative importance weights.
Step 5	Measuring the consistency of comparisons between criteria.

TABLE 2 PROMETHEE method steps.

Method steps	Description of method steps
Step 1	By defining alternatives and criteria, the importance weights of the criteria are determined, and a data matrix is created for the alternatives.
Step 2	Depending on the structure and interrelationship of the determined criteria, preference functions are defined.
Step 3	For pairs of alternatives, common preference functions are determined based on the preference functions.
Step 4	Preference indices are determined for each pair of alternatives using common preference functions.
Step 5	Negative and positive advantages are determined for alternatives.
Step 6	Partial priorities are set with PROMETHEE I.
Step 7	With PROMETHEE II, exact priorities are calculated.

This sensor can detect diquat and carbendazim in apple and cabbage skins without the interference of other pesticides and determine in what proportion they are present. They stated that this type of wearable sensor, including active bio(sensing) layers, could be extended to other agrochemicals and monitor all agri-foods and products online.

To the best of our knowledge, no study was found to determine the importance of PPE for preventing diseases and injuries associated with pesticide use using the MCDM method as a result of the literature research. Its contribution to the literature will be applying these methods to the agricultural sector. Emphasizing the use of PPE in the processing of pesticides in agriculture will increase the tendency of agricultural workers to use protective measures.

2 Materials and methods

Criteria were determined based on a literature review and expert opinion. The criteria weights were calculated with the AHP method, which is one of the MCDM methods, and the importance of the alternatives was ranked using the PROMETHEE method.

2.1 AHP method

When applied to decision-making, the AHP method, one of the most well-known MCDM methods, helps define the general decision process by decomposing a complex problem into a hierarchical structure as the target, criterion, subcriteria, and alternative (38). Pairwise comparisons are made to obtain priority scales based on experts' judgments. Comparisons are made using an absolute judgment scale relative to a particular attribute, representing how much one element dominates another (38). In AHP, the relative importance of decision criteria is evaluated through pairwise comparisons. The decision-maker examines the two alternatives to create a priority value (aij) for each criterion and expresses a preference. In AHP, the standard numerical scale is 1–9, which ranges from "extremely important" to "equally important." A value of "1" indicates that one factor is equally important as another, while a "9" indicates that one factor is highly less critical than the other. An n*n square matrix is obtained at each level of the criterion hierarchy, where n is the number of elements of the level (39).

The method steps are listed in Table 1 (38, 40).

2.2 PROMETHEE method

The PROMETHEE method is one of the MCDM methods and has a significant place. PROMETHEE I, developed by Jean Pierre Brans in 1982, offers partial prioritization. PROMETHEE II, on the other hand, offers clear prioritization (41). The PROMETHEE method, developed based on the difficulties of the prioritization methods applied in the existing literature, has become a frequently used method today (42).

With the PROMETHEE methodology, successful applications in many areas, such as investments, workforce planning, industrial location, banking, water resources, chemistry, medicine, health services, dynamic management, tourism, and ethics in the operating room, have been discussed. The methodology can be applied in many fields due to its ease of use and mathematical properties (41).

Method steps are listed in Table 2 (43).

3 Results

Figure 1 shows the problem flow chart.

3.1 Problem definition

Occupational death, injury, and disease are high among agricultural workers. Agricultural workers risk work-related injuries and illnesses more than most other occupations. The three most dangerous sectors are agriculture, construction, and mining (44). Eurostat statistics reported that in 2013, in EU agriculture, 1.5 non-fatal injuries occurred per 100 workers, while 4.1 fatal injuries occurred per 100,000 workers. However, these rates are represented at a lower level than the actual rates. Because people outside the family do 25% of the work, reporting occupational injuries is optional for the self-employed (1). Pesticide use in agriculture is significant as it adversely affects the health of farmers (14, 17, 28, 34). A significant risk of disease and injury in public health and agriculture is associated with pesticide use. According to WHO estimates, 25 million agricultural workers in developing countries are exposed to acute pesticide poisoning every year (3).

Statistical results revealed that 25 million farmers are poisoned every year, with a mild degree of poisoning. In addition, nearly three million
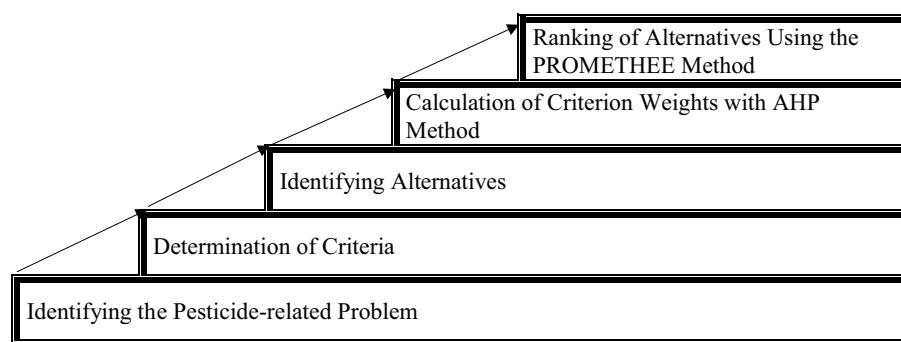
farmers, especially those living in rural areas of developing countries, are exposed to severe pesticide poisoning (29). As a result, 180,000 people, including various agricultural workers, experience fatal events every year (36). In particular, the lack of use of PPE and the lack of appropriate safety behaviors by farmers before, during, and after pesticide application are the most important reasons for the high incidence rate (15, 20, 29, 33). Wearing PPE can reduce the possibility of poisoning by approximately 44% (45). Although it is the least preferred solution, PPE for professional problems should be considered within an integrated and systematic vision. Therefore, the effectiveness of the entire occupational health and safety system for prevention, protection, and control is closely related to the balanced selection of alternatives (10).

This study discusses the problem of sequencing the use of PPEs with the MCDM method to prevent the risk of injury and disease related to pesticide use. Personal protective equipment is worn or used to protect people from various hazards, eliminating and reducing the risk of fatal and non-fatal unintentional work injuries (46).

3.2 Determination of criteria

Pesticides are biologically active chemicals widely used by many agricultural workers and those involved in vector control. Occupational exposure occurs during the mixing, dilution, transport, application, and disposal of pesticides, as well as during the processing of crops and the cleaning of containers (5). Pesticides can enter the body through skin absorption, ingestion, and inhalation. To reduce exposure to pesticides and maintain health, the ILO and WHO recommend that farmers use PPE during pesticide application (8). This study addressed the importance of employees using PPE as a risk reduction measure. The criteria determined by considering the literature and expert opinion were respiratory, skin, swallowing, and eye (5, 8, 47).

3.3 Identifying alternatives

There are various hazards in the workplace, such as chemical, physical, and biological. It is indisputable that protecting employees from these existing dangers, reducing or eliminating harmful factors, improving the quality of workplaces with an engineering approach, and taking environmental management measures are priority solutions. However, it is a fact that such decisive and effective measures

cannot be implemented in many fields of study. In such cases, a work management approach using PPE is considered an alternative and essential tool to protect the safety and health of employees (11). Among pesticide handlers, the most basic PPE coveralls are safety shoes, respirators, gloves, masks, boots, aprons, hats, long-sleeved pants, long-sleeved shirts, face shields, and goggles. In this study, alternatives were determined as masks (face visors), overalls (long-sleeved trousers and shirts), safety shoes (boots), gloves, glasses, and hats. Alternatives were determined based on expert opinions and literature (15, 20, 25, 33, 34, 48).

3.4 Finding criterion weights with the AHP method

The visual PROMETHEE Academic Version Program was used to perform AHP calculations. Figure 2 shows the hierarchical structure.

The group comprising eight experts included two academicians who are industrial engineers, a doctor in the field of occupational health and safety, a class A occupational health and safety specialist, a class B occupational health and safety specialist, a class C occupational health and safety specialist, an occupational health and safety technician, and a medical doctor. The experts were selected based on their experience in the health and safety field. Pairwise comparisons were made based on expert opinions. Saaty's 1–9 scale was used in pairwise comparisons as shown in Table 3 (40). The consistency ratio, which is less than 0.1, was met. Figure 3 shows the pairwise comparison.

Criterion weights were found using the Super Decision Program. The obtained criterion weights are given in Table 4.

3.5 Ranking of alternatives using the PROMETHEE method

Alternatively, the mask, overalls, safety shoes, gloves, glasses, and hat will be ordered using the PROMETHEE method. The criterion weights obtained by the AHP method were entered into the Visual PROMETHEE Academic Version Program. The preference functions to be used in problem-solving are listed in Table 5 (41). In our study, the Fourth Type (Level) Function was used. While the login screen is shown in Figure 4, the ranking of the alternatives is given in Table 6.
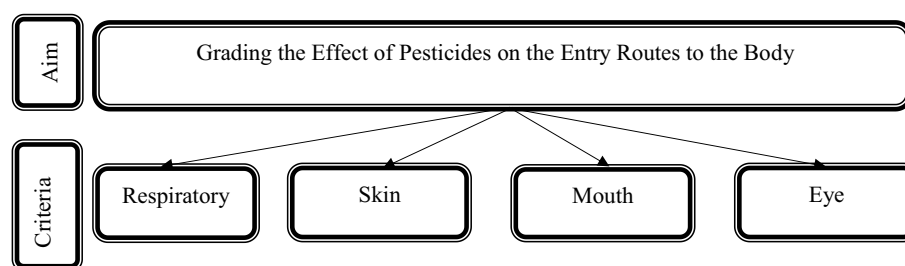
FIGURE 2
Hierarchical structure of the decision problem.

TABLE 3 Significance scale values and definitions.

Value	Definition	Explanation
1	Equally important	Equally important in both options.
3	A little important	Experience and judgment make one criterion slightly superior to the other.
5	Too important	Experience and judgment make one criterion highly superior to the other.
7	Too much important	One criterion is considered superior to the other.
9	Extremely important	Evidence demonstrating that one criterion is superior to the others has great credibility.
2, 4, 6, 8	Intermediate values	Values between two consecutive judgments to be used when reconciliation is needed.

FIGURE 3
Pairwise comparison.

TABLE 4 Criterion weights.

Criteria	Criterion weights	Consistency rate
Respiratory	0.32	0.03475
Skin	0.51	
Mouth	0.07	
Eye	0.10	

Table 6 shows the results of ranking the alternatives using the PROMETHEE method. When obtaining the Phi net priority value, the difference between th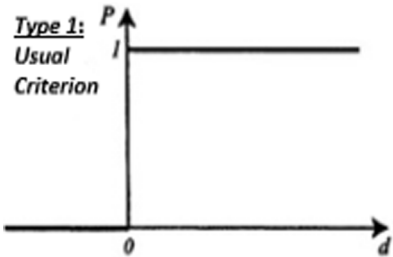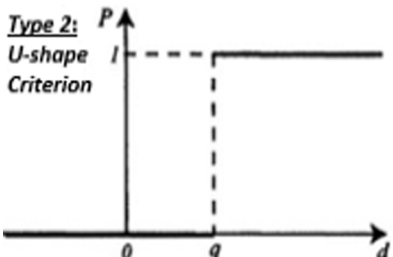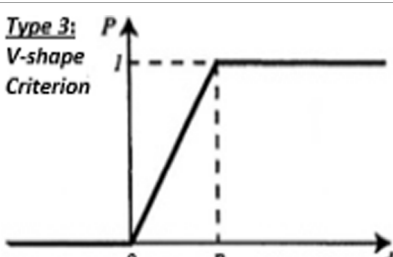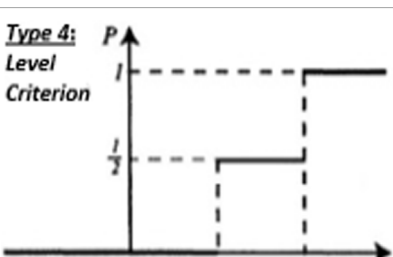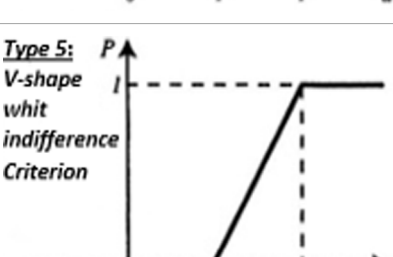e positive superiority Phi+ value and the negative superiority Phi-values is taken. Alternatives are ranked according to their net priority values. According to the results of the PROMETHEE flow table, the order of PPE is listed as masks, gloves, overalls, safety shoes, glasses, and hats.
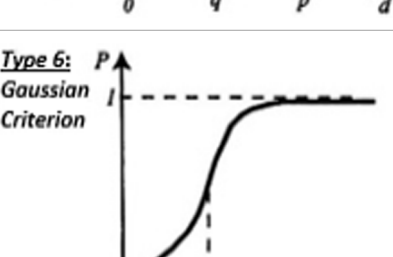
4 Discussion

The order of the PPE used to prevent the risk of injury and disease related to pesticide use using AHP and PROMETHEE methods is listed as a mask, gloves, coveralls, safety shoes, glasses, and hat.

Respiratory protective masks should be used in spraying operations and should be comfortable and breathing resistance

TABLE 5 Preference functions (41).

Generalized criterion		Definition	Parameters to fix
Type 1: Usual criterion		$P(d) = \begin{cases} 0 & d \leq 0 \\ 1 & d > 0 \end{cases}$	–
Type 2: U-shape criterion		$P(d) = \begin{cases} 0 & d \leq q \\ 1 & d > q \end{cases}$	q
Type 3: V-shape criterion		$P(d) = \begin{cases} 0 & d \leq 0 \\ \dfrac{d}{p} & 0 \leq d \leq p \\ 1 & d > p \end{cases}$	p
Type 4: Level criterion		$P(d) = \begin{cases} 0 & d \leq q \\ \dfrac{1}{2} & q < d \leq p \\ 1 & d > p \end{cases}$	p, q
Type 5: V-shape whit indifference criterion		$P(d) = \begin{cases} 0 & d \leq q \\ \dfrac{d-q}{p-q} & q < d \leq p \\ 1 & d > p \end{cases}$	p, q
Type 6: Gaussian criterion		$P(d) = \begin{cases} 0 & d \leq 0 \\ 1 - e^{-\frac{d^2}{2s^2}} & d > 0 \end{cases}$	s

FIGURE 4
PROMETHEE data entry.

TABLE 6 PROMETHEE flowchart of PPE in pesticide use.

Rank	Alternatives	Phi	Phi+	Phi-
1	Mask	0.3571	0.3764	0.0193
2	Gloves	0.1739	0.2580	0.0841
3	Overalls	0.0953	0.2056	0.1103
4	Safety shoes	−0.1103	0.0000	0.1103
5	Glasses	−0.2000	0.0966	0.2966
6	Hat	−0.3159	0.0000	0.3159

appropriate when worn on the face. Goggles should prevent the chemicals used during spraying from getting into the eyes and the chemical vapors from entering the eyes. Various accidents are encountered with chemicals in liquid form after splashing and spilling on the feet or legs. Work boots and shoes should be used to prevent accidents. Hygiene rules should be observed in shoes and boots, and necessary ventilation rules should be applied. Appropriate gloves must

be used, as chemicals will damage the skin in manual spraying applications. Contact with and absorption of chemicals on the skin should be prevented. Gloves should be decontaminated before removal, whenever possible. Overalls (work clothes) are the clothes that employees wear while working. It is essential to use it so that employees can protect themselves against chemical risks. The work clothes used should be removed in a separate section at the end of the work. Removed clothes should be appropriately disinfected (49). The hat used by farmers while spraying effectively prevented the symptoms significantly (14).

Pesticides are biologically active chemicals commonly used by agricultural workers and those involved in vector control. The most commonly used pesticides are organophosphate, carbamate, and pyrethroid insecticides (34). Occupational exposure also occurs during mixing, transporting, diluting, applying, and disposing of pesticides while processing crops and cleaning containers. Exposure occurs mainly through dermal and inhalation routes. Ingestion can occur through oral contact with contaminated hands or consuming

contaminated food. A significant source of exposure is contaminated clothing (5). In the study, the criterion weights were skin 0.51, respiration 0.32, eye listed 0.10, and mouth 0.07. Since pesticide exposure mainly occurs through the dermal route during the preparation of sprays and through dermal and inhalation during application (50), dermal intake has the highest weight in the ranking, followed by breathing, eyes, and mouth intake. PPE use during spraying can reduce pesticide inhalation and contact with pesticides, potentially reducing the chronic and acute health hazards of pesticides for sprayers (15). Recently, smart devices such as Internet of Things (IoT)-based drones, wireless sensors, and robots have been able to identify the crop enemies of the growers precisely, reducing the use of pesticides significantly (51, 52).

5 Conclusion

The agricultural sector constitutes 20% of the general employment in Turkey (2). Pesticide use negatively affects the health of farmers in this significant sector (14, 17, 28, 34). PPE provides additional protection against exposure to hazardous conditions in agricultural production when workers' safety is not addressed by controlling the risk at the source, eliminating the hazard, or minimizing the risk (53). This study discusses the problem of ranking the PPEs with the MCDM method to prevent the risk of injury and disease related to pesticide use. The weights of the criteria determined according to the literature review and expert opinion were calculated with the AHP method, and the PPE determined as an alternative was ranked using the PROMETHEE method. In the ranking, the order of PPE was included as a mask, gloves, overalls, safety shoes, glasses, and hat.

In future, studies can be carried out on using products based on Internet of Things (IoT) technology to prevent pesticide exposure and protect the health and safety of workers.

Data availability statement

The original contributions presented in the study are included in the article/supplementary material, further inquiries can be directed to the corresponding author.

Author contributions

Funding

Conflict of interest

The authors declare that the research was conducted in the absence of any commercial or financial relationships that could be construed as a potential conflict of interest.

Publisher's note

References

1. Merisalu E, Leppälä J, Jakob M, Rautiainen R. Variation in Eurostat and national statistics of accidents in agriculture. *Agron Res*. (2019) 17:1969–83. doi: 10.15159/ar.19.190

2. Akyıldız S, Çakmak B, Alayunt F, Karakitapoğlu N. In the agricultural sector, the impact of media on the development of occupational health and safety cultures. *J Eng Sci Design*. (2017) 5:257–61. doi: 10.21923/jesd.37308

3. Jeyaratnam J. Acute pesticide poisoning: a major global health problem. *World Health Stat Q*. (1990) 43:139–44.

4. Carvalho F. Pesticides, environment, and food safety. *Food Energy Sec*. (2017) 6:48–60. doi: 10.1002/fes3.108

5. ILO. *Banning hazardous pesticides: recommendations for Myanmar*. Myanmar: ILO (2021).

6. Bhandari G, Atreya K, Yang X, Fan L, Geissen V. Factors affecting pesticide safety behaviour: the perceptions of Nepalese farmers and retailers. *Sci Total Environ*. (2018) 631-632:1560–71. doi: 10.1016/j.scitotenv.2018.03.144

7. Atreya K, Johnsen F, Sitaula B. Health and environmental costs of pesticide use in vegetable farming in Nepal. *Environ Dev Sustain*. (2012) 14:477–93. doi: 10.1007/s10668-011-9334-4

8. ILO. *Safety and health in the use of agrochemicals: a guide, Geneva*. Geneva: ILO (1991).

9. Aderaw Z, Engdaw D, Tadesse T. Determinants of occupational injury: a case control study among textile factory workers in Amhara regional state, Ethiopia. *J Trop Med*. (2011) 2011:1–8. doi: 10.1155/2011/657275

10. ILO. *African newsletter on occupational health and safety 11, Helsinki*. Helsinki: ILO (2001).

11. Sawada SI, Kuklane K, Wakatsuki K, Morikawa H. New development of research on personal protective equipment (PPE) for occupational safety and health. *Ind Health*. (2017) 55:471–2. doi: 10.2486/indhealth.55-471

12. Clarke E, Levy L, Spurgeon A, Calvert I. The problems associated with pesticide use by irrigation workers in Ghana. *Occup Med*. (1997) 47:301–8. doi: 10.1093/occmed/47.5.301

13. Gomes J, Lloyd O, Revitt D. The influence of personal protection, environmental hygiene and exposure to pesticides on the health of immigrant farm workers in a desert country. *Int Arch Occup Environ Health*. (1999) 72:40–5. doi: 10.1007/s004200050332

14. Nordin R, Araki S, Sato H, Yokoyama K, Wan Muda WM, Win KD. Effects of safety behaviours with pesticide use on occurrence of acute symptoms in male and female tobacco-growing Malaysian farmers. *Ind Health*. (2002) 40:182–90. doi: 10.2486/indhealth.40.182

15. Mekonnen Y, Agonafir T. Pesticide sprayers knowledge, attitude and practice of pesticide use on agricultural farms of Ethiopia. *Occup Med*. (2002) 52:311–5. doi: 10.1093/occmed/52.6.311

16. Reed D, Browning S, Westneat S, Kidd P. Personal protective equipment use and safety behaviors among farm adolescents: gender differences and predictors of work practices. *J Rural Health*. (2006) 22:314–20. doi: 10.1111/j.1748-0361.2006.00052.x

17. Atreya K. Health costs from short-term exposure to pesticides in Nepal. *Soc Sci Med*. (2008) 67:511–9. doi: 10.1016/j.socscimed.2008.04.005

18. Weerasinghe M, Pieris R, Eddleston M, Hoek W, Dawson A, Konradsen F. Safe storage of pesticides in Sri Lanka – identifying important design features influencing community acceptance and use of safe storage devices. *BMC Public Health*. (2008) 8:1–10. doi: 10.1186/1471-2458-8-276

19. Fenske R. New technologies and worker safety in western agriculture. *J Agromedicine*. (2009) 14:417–20. doi: 10.1080/10599240903260592

20. Levesque D, Arif A, Shen J. Association between workplace and housing conditions and use of pesticide safety practices and personal protective equipment among North Carolina farmworkers in 2010. *Int J Occup Environ Med*. (2012) 3:53–67.

21. Meirelles L, Veiga M, Duarte F. Efficiency of personal protective equipment used in agriculture. *Work*. (2012) 41:14–8. doi: 10.3233/WOR-2012-0129-14

22. de Almeida RA, Veiga MM, De Costa Moura Duarte FJ, Meirelles LA, Veiga BEL. Thermal comfort and personal protective equipment (PPE). *Work*. (2012) 41:4979–82. doi: 10.3233/WOR-2012-0042-4979

23. Basilicata P, Sımonell A, Sılvestre A, Lambert M, Pedata P, Feola D, et al. Evaluation by environmental monitoring of pesticide absorption in farm workers of 18 Italian tomato cultivations. *Int J Immunopathol Pharmacol*. (2013) 26:517–23. doi: 10.1177/039463201302600226

24. Lekei EE, Ngowi AV, London L. Farmers' knowledge, practices and injuries associated with pesticide exposure in rural farming villages in Tanzania. *BMC Public Health*. (2014) 14:1–13. doi: 10.1186/1471-2458-14-389

25. Al Zadjali S, Morse S, Chenoweth J, Deadman M. Personal safety issues related to the use of pesticides in agricultural production in the Al-Batinah region of Northern Oman. *Sci Total Environ*. (2015) 502:457–61. doi: 10.1016/j.scitotenv.2014.09.044

26. Andrade-Rivas F, Rother HA. Chemical exposure reduction: factors impacting on South African herbicide sprayers' personal protective equipment compliance and high risk work practices. *Environ Res*. (2015) 142:34–45. doi: 10.1016/j.envres.2015.05.028

27. Rudolphi J, Retallick M. Agricultural safety and health education: practices, attitudes, and needs of Iowa agricultural educators. *NACTA J*. (2015) 59:174–9.

28. Ngowi A, Mrema E, Kishinhi S. Pesticide health and safety challenges facing informal sector workers: a case of small-scale agricultural workers in Tanzania. *New Solut*. (2016) 26:220–40. doi: 10.1177/1048291116650262

29. Akter M, Fan L, Rahman M, Geissen V, Ritsema C. Vegetable farmers' behaviour and knowledge related to pesticide use and related health problems: a case study from Bangladesh. *J Clean Prod*. (2018) 200:122–33. doi: 10.1016/j.jclepro.2018.07.130

30. Yarpuz-Bozdogan N. The importance of personal protective equipment in pesticide applications in agriculture. *Curr Opin Environ Sci Health*. (2018) 4:1–4. doi: 10.1016/j.coesh.2018.02.001

31. Reynolds SJ, Tadevosyan A, Fuortes L, Merchant JA, Stromquist AM, Burmeister LF, et al. Keokuk County rural health study: self-reported use of agricultural chemicals and protective equipment. *J Agromedicine*. (2018) 12:45–55. doi: 10.1080/10599240801887850

32. Rezaei R, Seidi M, Karbasioun M. Pesticide exposure reduction: extending the theory of planned behavior to understand Iranian farmers' intention to apply personal protective equipment. *Saf Sci*. (2019) 120:527–37. doi: 10.1016/j.ssci.2019.07.044

33. Sapbamrer R, Thammachai A. Factors affecting use of personal protective equipment and pesticide safety practices: a systematic review. *Environ Res*. (2020) 185:109444. doi: 10.1016/j.envres.2020.109444

34. Joko T, Dewanti N, Dangiran H. Pesticide poisoning and the use of personal protective equipment (PPE) in Indonesian farmers. *J Environ Public Health*. (2020) 2020:1–7. doi: 10.1155/2020/5379619

35. Jakob M, Santa D, Holte K, Sikkeland I, Hilt B, Lundqvist P. Occupational health and safety in agriculture-a brief report on organization, legislation and support in

selected European countries. *Ann Agric Environ Med*. (2021) 28:452–7. doi: 10.26444/aaem/140197

36. Zhang LS, Li J, Wang F, Shi JD, Chen W, Tao XM. Flexible stimuli-responsive materials for smart personal protective equipment. *Mater Sci Eng*. (2021) 146:100629. doi: 10.1016/j.mser.2021.100629

37. Paschoalin R, Gomes N, Almeida G, Bilatto S, Farinas C, Machado S, et al. Wearable sensors made with solution-blow spinning poly (lactic acid) for non-enzymatic pesticide detection in agriculture and food safety. *Biosens Bioelectron*. (2022) 199:113875. doi: 10.1016/j.bios.2021.113875

38. Saaty TL. The analytic hierarchy process in conflict management. *Int J Conf Manag*. (1990) 1:47–68. doi: 10.1108/eb022672

39. Benmoussa K, Laaziri M, Khoulji S, Kerkeb M, El Yamam A. AHP-based approach for evaluating ergonomic criteria. *Proc Manufact*. (2019) 32:856–63. doi: 10.1016/j.promfg.2019.02.294

40. Saaty TL. Decision making with the analytic hierarchy process. *Int J Serv Sci*. (2008) 1:83–98. doi: 10.1504/IJSSCI.2008.017590

41. Brans JP, Mareschal B. Promethee methods. In: *Multiple criteria decision analysis: state of the art surveys. international series in operations research & management science*, J Figueira, S Greco, M Ehrogott editors. vol. *78*. New York, NY: Springer (2005). 163–86.

42. Dağdeviren M, Eraslan E. Supplier selection with PROMETHEE sorting method. *J Gazi Univ Fac Eng Archit*. (2008) 23:69–75.

43. Brans JP, Vinck P. Note—a preference ranking organisation method: (the PROMETHEE method for multiple criteria decision-making). *Manag Sci*. (1985) 31:647–56. doi: 10.1287/mnsc.31.6.647

44. Lessenger JE. *Agricultural medicine*. Porterville: Springer (2006).

45. Dasgupta S, Meisner C, Wheeler D, Xuyen K, Lam N. Pesticide poisoning of farm workers–implications of blood test results from Vietnam. *Int J Hyg Environ Health*. (2007) 210:121–32. doi: 10.1016/j.ijheh.2006.08.006

46. Bhattacharjee S, Joshi R, Chughtai A, Macintyre C. Graphene modified multifunctional personal protective clothing. *Adv Mater İnter*. (2019) 6:1900622. doi: 10.1002/admi.201900622

47. Eddleston M. Poisoning by pesticides. *Medicine*. (2020) 48:214–7. doi: 10.1016/j.mpmed.2019.12.019

48. Chughtai A, Macintyre C. Risk of self-contamination during doffing of personal protective. *Am J Infect Control*. (2018) 46:1329–34. doi: 10.1016/j.ajic.2018.06.003

49. Özdemir F, Bulduk İ, Karakaş K. Chemical risk factors in agricultural sector olive growing. *Ohs Academy*. (2020) 3:35–40. doi: 10.38213/ohsacademy.703878

50. WHO. *Preventing disease through healthy environments: exposure to highly hazardous pesticides: a major public health concern*. Geneva: World Health Organization (2019).

51. Kim S, Lee M, Shin C. IoT-based strawberry disease prediction system for smart farming. *Sensors*. (2018) 18:4051. doi: 10.3390/s18114051

52. Venkatesan R, Kathrine G, Ramalakshmi K. Internet of things based pest management using natural pesticides for small scale organic gardens. *J Comput Theor Nanosci*. (2018) 15:2742–7. doi: 10.1166/jctn.2018.7533

53. ILO. *Code of practice on safety and health in agriculture*. Geneva: ILO (2010).

frontiers | Frontiers in Applied Mathematics and Statistics

Check for updates

*CORRESPONDENCE
Dereje Tarekegn Nigatu
✉ tekgem@yahoo.com

Convergence analysis of particle swarm optimization algorithms for different constriction factors

Dereje Tarekegn Nigatu[1]*, Tekle Gemechu Dinka[1] and
Surafel Luleseged Tilahun[2]

[1]Department of Applied Mathematics, Adama Science and Technology University, Adama, Ethiopia,
[2]Department of Applied Mathematics, Addis Ababa Science and Technology University, Addis Ababa,
Ethiopia

Particle swarm optimization (PSO) algorithm is an optimization technique with
remarkable performance for problem solving. The convergence analysis of the
method is still in research. This article proposes a mechanism for controlling the
velocity by applying a method involving constriction factor in standard swarm
optimization algorithm, that is called CSPSO. In addition, the mathematical
CSPSO model with the time step attractor is presented to study the convergence
condition and the corresponding stability. As a result, constriction standard
particle swarm optimization that we consider has a higher potential to balance
exploration and exploitation. To avoid the PSO premature convergence, CSPSO
modifies all terms of the PSO velocity equation. We test the effectiveness of
the CSPSO algorithm based on constriction coefficient with some benchmark
functions and compare it with other basic PSO variant algorithms. The theoretical
convergence and experimental analyses results are also demonstrated in tables
and graphically.

KEYWORDS

PSO algorithms, convergence and stability, constriction factor, Markov chain, Monte
Carlo

1 Introduction

The optimization techniques are fundamentally important in engineering and scientific
computing. The PSO algorithm was first introduced by Kennedy and Eberhart [1] as a
stochastic optimization technique of swarm particles (population). The motivation was
primarily to model the social behavior of birds flocking. The meta-heuristic optimization
algorithms (PSO) work effectively in many areas such as robotics, wireless networks,
power systems, job-shop schedules, human healthcare, and classifying or training of ANN
(artificial neural network) [2]. In PSO, the potential solutions, called particles, fly through
the problem space (domain) by applying their intelligent collective behaviors.

The PSO algorithm is competitive in performance with the well-known huge numbers
of variants such as SPSO and CPSO algorithms and is also an efficient optimization
framework [3, 4].

Lately, researches on PSO mainly intended on algorithmic implementations,
enhancements, and engineering applications with interesting findings derived under the
system that assumes a fixed attractor [5]. Nevertheless, a comprehensive mathematical
explanation for the general PSO is still quite limited. For instance, the works on stability
and convergence analyses are two key problems of great significance that need to be
investigated in depth because many of the works have given attention for standard PSO.

The PSO algorithm depends on three parameters (factors): the inertia, cognitive and social weight to guarantee the stability of PSO.

Stability analysis of PSO is mainly motivated by determining which combination of these parameters encourages convergence [6].

The working rule of PSO method is closely tied with the stability analysis, which investigates how the essential factors affect the swarms dynamics, and under what conditions particle swarm converges to some fixed value. For the first time, stability analysis of the particle dynamics was carried out by Clerc and Kennedy [7]. The study indicates that [8] particle trajectories could converge to a stable point. A more generalized stability analysis of the particle dynamics was conducted using the Lyapunov stability theorem [9]. Recently, based on a weak stagnation assumption, Liu [10] studied the order-2 stability of PSO, and a new definition of stability was proposed with an order-2 stable region. Dong and Zhang [11] analyzed order-3 recurrence relation of PSO kinematic equations based on two strategies to obtain the necessary and sufficient conditions of its convergence.

The convergence analysis determines whether a global optimum solution can be achieved when a particle swarm converges. Using stochastic process theory, Jiang et al. [12] presented a stochastic convergence analysis on the standard PSO. Combining with the finite element grid technique, Poli and Langdon [13] set up a discrete model of Markov chain of the bare-bones PSO. An absorbing Markov process model of PSO was developed in Cai et al. [14]. Cai et al. [14] suggested the main factor of convergence analysis is the attaining-state set and proposed an improved method of convergence in terms of the attaining-state set theorem of expansion. The basic PSO is neither a global nor a local search algorithm, based on the convergence criterion of the pure random search algorithm [15, 16]. To yield a lower bound for the time required to optimize any pseudo-Boolean functions with a unique optimum and to justify upper bounds, Dirk et al. [17] assigned an optimum-level argument that is deep-rooted for evolutionary algorithms of particle swarm optimization. The study in Sun et al. [18] discussed the convergence of the quantum-behaved particle swarm optimization (QBPSO) and proved that it is a global convergent algorithm.

As discussed in Per and Carsten [19], stagnation of the convergence properties for basic PSO may be disadvantageous to finding a sufficiently good solution within a logical time, and it may have infinite expected first hitting time on some functions.

Recently, the existing work on the convergence analyses of PSO including documents from 2013 was surveyed by Tarekegn et al. [6]. The stochastic approximation technique on the PSO algorithm was use to prove convergence of swarm in Yuan and Yin [20]. The global convergence of PSO [21] was investigated by introducing the transition probability of particles. Several properties related to the Markov chain were investigated, and it was found that the particle state space is not repeated and PSO is not globally convergent from the viewpoint of the transition probability [22]. Based on the different models of PSO examined [23], the Markov properties of the state sequences of a single particle and swarm one determine the transition probability of a particle. The transition probability of the optimal set is deduced by combining the law of total probability with the Markov properties [24], which proves that SPSO can reach

the global optimum in probability. Although many methods in Poli and Langdon [13] have proposed PSO convergence analysis, most analyses are based on the assignment of stochastic systems of the Markov process, which strongly depends on the transition matrix and their eigenvalues. Therefore, when the population size is large, current PSO convergence analyses are very refined and investigate different PSO variants algorithms to obtain a solution that converges to global minimum.

Motivated by our recent study in Tarekegn et al. [6], this article proposes a PSO variant known as CSPSO, an algorithm for optimization problem solving.

A constriction factor integrated with an inertia weight are used for the construction. Fast convergent method to an optimal solution within the search space in a small time of iterations was obtained.

The rest of this study is organized as follows: Section 2 presents related works that include the basic PSO algorithm and its existing variants. In Section 3, the proposed CSPSO algorithm analysis is described in detail, while Section 4 presents comparison results on some variants of PSO such as SPSO and CPSO (implementing with test functions) and provides an in-depth discussion, with a conclusion in Section 5.

2 The PSO algorithm and some related studies

In the PSO with K particles in which each particle is treated as an individual in the D-dimensional space, the position and velocity vectors of the i-th particle at the t-th iteration are

$X_i^t = (X_{i1}^t, X_{i2}^t, \ldots, X_{iD}^t)$ and
$V_i^t = (V_{i1}^t, V_{i2}^t, \ldots, V_{iD}^t)$, respectively.

In SPSO algorithm [25], at iteration t, the d th dimension of particle i's velocity and position P_i^t is local best position, x_i^t is current position, and g^t is global best position. Both are updated as

$$V_i^{t+1} = \omega V_i^t + c_1 r_1^t (P_i^t - X_i^t) + c_2 r_2^t (g^t - X_i^t),$$
$$X_i^{t+1} = X_i^t + V_i^{t+1}, \tag{1}$$

for $1 \leq i \leq K$; ω is an inertia weight; and c_1 and c_2 are called acceleration coefficients in real-space, R.

Vector $P_i^t = (P_{i1}^t, P_{i2}^t, \ldots, P_{iD}^t)$ is the best previous position of particle i called personal best (Pbest) position and vector $g^t = (g_1^t, g_2^t, \ldots, g_D^t)$ is the position of the best particle among all the particles in the population and called global best (gbest) position. The parameters r_1^t and r_2^t are sequences of two different random positive numbers in the uniform random distribution in (0, 1) i.e., $U(0, 1)$.

Generally, the value of V_{id}^t is restricted within the interval $[-V_{max}, V_{max}]$, for each $d \in \{1, 2, \ldots, D\}$. Without loss of generality, we consider the minimization problem:

Minimize $f(X)$, such that

$$X \in S \subset \mathbb{R}^D, \tag{2}$$

where $f(X)$ is an objective function continuous almost everywhere and S is a feasible solution space. From (1),

the non-homogeneous recurrence relation (NHRR) is obtained as follows: [8]

$$X_i^{t+1} = -\omega x_i^{t-1} + (1+\omega)x_i^t + \\ \varphi_1^t(P_i^t - x_i^t) + \varphi_2^t(g^t - x_i^t),$$ (3)

where $\varphi_1^t = c_1 r_1^t$, $\varphi_2^t = c_2 r_2^t$.

From NHRR, P^t and g^t, for $1 \leq i \leq K$, are updated, respectively, as follows:

$$P_i^{t+1} = \begin{cases} x_i^{t+1} : for\, f(x_i^{t+1}) < f(P_i^t) \\ P_i^t \quad : otherwise; \end{cases}$$ (4)

$$g^0 = arg\, \min_{1 \leq i \leq k}\{f(x_i^o)\}, \\ g^{t+1} = arg\, \min_{1 \leq i \leq k}\{f(x_i^{t+1}), f(g^t)\}.$$

From (2), (3), the process of the particle's velocity and position change can be obtained, respectively, as follows. They are a second-order difference equations

$$V_i^{t+2} + (\varphi^t - \omega - 1)V_i^{t+1} + \omega V_i^t = 0$$ (5)

$$X_i^{t+1} + (\varphi^t - \omega - 1)x_i^t + \omega x_i^{t-1} = \varphi_1^t P_i^t + \varphi_2^t g^t \\ = \varphi^t O_i^t$$ (6)

where, $\varphi^t = \varphi_1^t + \varphi_2^t$

$$O_i^t = \frac{\varphi_1^t p_i^t + \varphi_2^t g^t}{\varphi^t}.$$ (7)

The terms $(\varphi^t - \omega - 1)x_i^t$ and ωx_i^{t-1} on the left side of (6), both memorize the past values of position (i.e, the memory item of position). The value of the item $\varphi^t O_i^t$ on the right side of (6) is obtained from the previous experience of particles (i.e, the learning item of position) and, in particular, O_i^t is the attractor at the t th iteration in (7).

Now, let

$$Q_x = \max_{x^t \in S_x \subset R} | x(t) |.$$ (8)

For p^t, $g^t \in S_x$, $|p^t| \leq Q_x$, and $|g^t| \leq Q_x$. From (8), $O^t \in S_o$ means $|O^t| \leq Q_o$ for all t.

Introducing a constriction coefficient in SPSO controls the balance between the cognitive component $(p_i^t - x_i^t)$ and social component $(g^t - x_i^t)$ in the velocity equation. The coefficient restricts the particle velocities within a certain range to prevent excessive exploration or exploitation.

$$V_i^{t+1} = \chi * \left(\omega V_i^t + \varphi_1^t(P_i^t - x_i^t) + \varphi_2^t(g^t - x_i^t)\right)$$

2.1 Convergence of some PSO variants

The importance of a hybrid method is to combine different optimization methods to take advantage of the virtues of each of the methods. In addition to standard PSO, several variants of the PSO in Kumar et al. [5] were constructed to improve the performance of PSO.

The SPSO

$$X_i^{t+1} = X_i^t + V_i^{t+1},$$

has a scalar function of position if $x_i^t = p_i^t = g_i^t$ for a particle, that is particle's update depends only on its previous velocity. This can make the algorithm to stop to flow on the swarm's global best position, even if that position is not a local optimum. For instance, based on (4), the guaranteed convergence PSO, GCPSO, overcomes this problem by using a modified position and velocity update equation for the global best particle, which forces that particle to search for a better position in a confined region around the global best position.

The GCPSO can be used with neighborhood topologies such as star, ring, and Von Neumann. Neighborhoods have a similar effect in the GCPSO [16, 19] as they do in the SPSO. Shi and Eberhart [25] introduced the concept of linearly decreasing inertia weight with generation number into PSO to improve the algorithmic performance.

Particles converge to a weighted average (O_i^t) between their personal and local best positions [8], referred to as a so-called theoretical attractor point (ATP). Kennedy [26] has proposed that the entire velocity update equation is replaced by a random number sampled from a Gaussian distribution (Gd) around the ATP, with a deviation of the magnitude of the distance between the personal and global best. The resultant algorithm is called the bare bones PSO (BBPSO). Kennedy also proposed an alternative bare bones PSO (aBBPSO) [26], where the particle sampled from the previous Gd is reunited with the particle's personal best position. The performance of PSO with a small and a larger nearby region might be better on multimodal and unimodal problems, respectively [27]. Changing dynamically the neighborhood structures has been proposed to avoid insufficiencies in fixed nearby regions [28].

The quantum-behaved particle swarm optimization was proposed to show many advantages to the traditional PSO. Fang et al. [24] proposed a quantum-behaved particle swarm optimization (QBPSO) algorithm and discuss the convergence of QBPSO within the framework of random algorithm's global convergence theorem. Inspired by natural speciation, some researchers have introduced evolution methods into PSO [29, 30]. The problem of premature convergence was studied on a perturbed particle swarm algorithm presented based on the new particle updating strategy [31]. To solve optimization problems, Tang et al. [32] developed a feedback-learning PSO algorithm with quadratic inertia weight, ω. Hybridized PSO with a local search technique for locating optimal solutions for multiple global and local solution in physical fitness of more than one global optimal solution for optimization problem using a memetic algorithm can be referred in Wang et al. [33]. An example-based learning PSO was proposed in Huang et al. [34] to overcome the failures of PSO by retaining a balance between swarm diversity and convergence speed. A

variation of the global best PSO where the velocity update equation does not hold a cognitive component is called social PSO, expressed as

$$V_i^{t+1} = \omega V_i^t + \varphi_2(g_i^t - x_i^t), \tag{9}$$

The individuals are only supported by the global best position and their previous velocity. The particles are attracted toward the global best position, instead of a weighted average between global best and their personal best positions, leading to very fast convergence [19].

3 Relations of CSPSO and Markov chain

In this section, the global convergence of CSPSO is analyzed based on properties of Markov Chain and the transition probabilities of particle velocity and position are also computed.

$$V_i^{t+1} = \begin{cases} \chi * (V_i^t + \varphi_1^t(P_i^t - x_i^t) + \\ \qquad \varphi_2^t(g^t - x_i^t)), \text{ for } \omega = 1 \\ \chi * (\omega V_i^t + \varphi_1^t(P_i^t - x_i^t) + \\ \qquad \varphi_2^t(g^t - x_i^t)), \text{ otherwise} \end{cases} \tag{10}$$

In (10), the velocities of particles are updated using two main components: the cognitive component and the social component. The cognitive component guides a particle toward its personal-best position, while the social component directs a particle toward the best position found by the entire swarm.

We introduce some useful definitions, variables and propositions (based on single particle model) which may be important in this article [22, 23, 35, 36].

The following definitions provide a formal description of this property based on single particle model [22, 23, 35, 36].

Definition 1. (Stochastic process and Markov property). Assume all the variables are defined within the context of a common probability space or probability measure.

1. The random variables $Y = (Y^0, Y^1, \dots, Y^t)$ in a sequence are called a stochastic processes.
2. Let Y^t be a value in state space S, and the sequence $\{Y^t\}_{t \geq 0}$ is a discrete stochastic process.
   For every $t \geq 0$ and $i^l \in S(l - 1 \leq t)$.
3. The discrete stochastic process is a Markov Chain.
   If the probability $Pr\{Y^{t+1} = i^{t+1} \mid Y^0 = i^0, Y^1 = i^1, \dots, Y^t = i^t\} = Pr\{Y^{t+1} = i^{t+1} \mid Y^t = i^t\} > 0.$ and $Pr\{Y^0 = i^0, Y^1 = i^1, \dots, Y^t = i^t\} > 0$

Definition 2. (State of particle). The state of particle $\kappa_i^t = (x_i^{t-1}, x_i^t, p_i^t, g^t)$ at the t-th iteration for particle i in (3).

The state of particle space is a set of all possible states of particle, denoted as S. κ_i^t, the update probability of the state of the particle can be calculated based on proposition-1.

Proposition 1. If the accelerating factors φ_1^t and φ_2^t in CSPSO satisfy $\varphi_1^t, \varphi_2^t \in U(0, c)$, then the probability for particle i changes from the position x_i^t to the spherical region centered at x_i^{t+1} with radius $\varrho_t > 0$. The event $A_i = \{\kappa_i^{t+1} \mid \kappa_i^t\}$, defining the state of

particle i at the t-th iteration is updated to the state at the $(t + 1)$-th iteration, for each $i \in \{1, 2, \dots, K\}$ can be computed as

$$Pr(A_i) = \frac{\varrho_t^3}{\chi \omega \parallel x_i^t - X_i^{t-1} \parallel c\chi \parallel p_i^t - X_i^t \parallel c\chi \parallel g^t - X_i^t \parallel}, \tag{11}$$

c is a constant within $U(0, c)$ and $\delta \to 0$, where

$$\varrho = c\chi * \begin{cases} \parallel p_i^t - X_i^t \parallel, \text{ for } f(x_i^t) - \delta \leq f(P_i^t) \leq f(x_i^t) + \delta \\ \parallel g^t - X_i^t \parallel, \text{ for } f(x_i^t) - \delta \leq f(g^t) \leq f(x_i^t) + \delta \end{cases} \tag{12}$$

Proof. The 1-step transition probability of the i th state of particles, P_i^{t+1} and g^{t+1}, are determined by x_i^{t+1} for transferring κ_i^t to κ_i^{t+t} based on the following SPM-Single Particle Model [36]

$$x_i^{t+1} = x_i^t + \chi * (\omega(x^t - x_i^{t-1}) + \\ \qquad \varphi_1^t(P_i^t - x_i^t) + \varphi_2^t(g^t - x_i^t)), \tag{13}$$

x_i^{t+1} determined by $\chi \omega$, $\chi \varphi_1$, and $\chi \varphi_2$.

Three conditions in 1-step transition probability are:

1. $f(x_i^t) - \delta \leq f(P_i^t), f(g^t) \leq f(x_i^t) + \delta$. $x_i^{t+1} = x_i^t + \chi \omega(x_i^t - x_i^{t-1})$ is determined uniquely by $\chi \omega$, where $\chi \omega$ is unknown constant, having

$$P(x_i^{t+1} \mid \kappa_i^t) = \frac{\int_{x_i^{t+1} - \frac{1}{2}\varrho}^{x_i^{t+1} + \frac{1}{2}\varrho} dy}{\int_{x_i^t}^{x_i^t - \chi \omega(x_i^t - x_i^{t-1})} dy} \\ = \frac{\varrho}{\chi \omega \parallel x_i^t - x_i^{t-1} \parallel} \tag{14}$$

2. $f(x_i^t) - \delta \leq f(P_i^t), f(g^t) \leq f(x_i^t) + \delta$.
   Ordering implies $g^t \in \{p_i^t, g^t\}$

$$x_i^{t+1} = x_i^t + \chi \omega(x^t - x_i^{t-1}) + \\ \qquad \chi \varphi_2^t(g^t - x_i^t) \tag{15}$$

Here, φ_2^t is random variable because x_i^{t+1} is determined by $\chi \omega(x^t - x_i^{t-1})$ and $\chi \varphi_2^t(g^t - x_i^t)$

$$P(x_i^{t+1} \mid \kappa_i^t) = \frac{\int_{x_i^{t+1} - \frac{1}{2}\varrho}^{x_i^{t+1} + \frac{1}{2}\varrho} dy}{\int_{x_i^t}^{x_i^t + \chi \omega(x_i^t - x_i^{t-1})} dy} * \frac{\int_{\varphi_1^t - \frac{1}{2}\varrho}^{\varphi_2^t + \frac{1}{2}\varrho} dy}{\int_{x_i^t}^{x_i^t + \chi c(g^t - x_i^{t-1})} dy} \tag{16}$$
$$= \frac{\varrho}{\chi \omega \parallel x_i^t - x_i^t \parallel} * \frac{\varrho}{\chi c \parallel g^t - x_i^t \parallel}$$

3. $f(x_i^t) + \delta < f(P_i^t), f(g^t) < f(x_i^t) - \delta$.

$$x_i^{t+1} = x_i^t + \chi \omega(x^t - x_i^{t-1}) + \chi \varphi_1^t(P_i^t - x_i^t) \\ \qquad + \chi \varphi_2^t(g^t - x_i^t)) \tag{17}$$

when $x_i^{t+1} \in \mathbb{R}$, x_i^{t+1} is determined by $\chi * (\omega, \varphi_1, \varphi_2)$

$$P(x_i^{t+1} \mid \kappa_i^t) = \frac{\int_{x_i^{t+1} - \frac{1}{2}\varrho}^{x_i^{t+1} + \frac{1}{2}\varrho} dy}{\int_{x_i^t}^{x_i^t + \chi \omega(x_i^t - x_i^{t-1})} dy} * \frac{\int_{\varphi_1 - \frac{1}{2}\varrho}^{\varphi_1 + \frac{1}{2}\varrho} dy}{\int_{x_i^t}^{x_i^t + \chi c(g^t - x_i^{t-1})} dy} *$$

$$\frac{\int_{\varphi_2^t - \frac{1}{2}\varrho}^{\varphi_2^t + \frac{1}{2}\varrho} dy}{\int_{x_i^t}^{x_i^t + \chi c(g^t - x_i^{t-1})} dy} \quad (18)$$

$$= \frac{\varrho}{\chi \omega \parallel x_i^t - x_i^{t-1} \parallel} *$$

$$\frac{\varrho}{\chi c \parallel P_i^t - x_i^t \parallel} *$$

$$\frac{\varrho}{\chi c \parallel g^t - x_i^t \parallel}$$

From conditions in $1 - 3$,

$$\lim_{P_i^t \to x_i^t} \frac{\varrho}{\chi \omega \parallel P_i^t - x_i^t \parallel} = 1$$

$$\lim_{g^t \to X_i^t} \frac{\varrho}{\chi c \parallel g_i^t - x_i^t \parallel} = 1.$$

$$P(A_i) = \frac{\varrho^3}{\chi (\omega \parallel x_i^t - x_i^{t-1} \parallel c \parallel P_i^t - x_i^t \parallel c \parallel g^t - x_i^t \parallel} \quad (19)$$

δ is a vector approaching to zero. When

I. ϱ is the radius of x_i^{t+1}
II. $f(x_i^t) - \delta \leq f(P_i^t) \leq f(x_i^t) + \delta$,
$\varrho = c\chi \parallel P_i^t - x_i^t \parallel$
III. $f(x_i^t) - \delta \leq f(g^t) \leq f(x_i^t) + \delta$,
$\varrho = c\chi \parallel g^t - x_i^t \parallel$

Definition 3. (State of swarm). The state of swarm in (3), at iteration t, denoted as η^t, is defined as $\eta^t = (\kappa_1^t, \kappa_2^t, \ldots, \kappa_K^t)$.
The state of swarm space is a set of all possible states of swarm, denoted as ϖ [22].

Proposition 2. (Markov chain). The set of collection of swarm state $\{\eta^t\}_{t \geq 1}$ is a Markov chain [23].

Proof. The proof follows by referring to equation of position that the state of swarm $\eta^{t+1} = (\kappa_1^{t+1}, \kappa_2^{t+1}, \ldots, \kappa_m^{t+1})$ at iteration $t + 1$ depends on only the state of swarm $\eta^t = (\kappa_1^t, \kappa_2^t, \ldots, \kappa_K^t)$. at iteration t. Therefore, $\{\eta^t\}_{t \geq 1}$ is a Markov chain.

Definition 4. Let Γ_1^n denote the σ-field generated by particles state $\kappa_1^t, \kappa_2^t, \ldots, \kappa_n^t$, $(K \geq n)$ and define

$$\phi((\Gamma_1^n, \kappa_{n+1}^t) = sup\{\mid Pr(B \backslash A) - Pr(B) \mid : \\ A \in \Gamma_1^n, B \in \sigma(\kappa_{n+1}^t)\}, \quad (20)$$

$$\phi = \sup_{1 \leq n \leq K-1} \phi(\Gamma_1^n, \kappa_{n+1}^t) \quad (21)$$

Due to the weak interdependent relationship among the particles, ϕ is approximately small.

Proposition 3. The transition probability from η^t to η^{t+1} satisfies

$$\mid Pr(\eta^{t+1} \mid \eta^t) - \prod_{i=1}^K Pr(\kappa_i^{t+1} \mid \kappa_i^t) \mid \leq \mu \quad (22)$$

where μ can be made small enough, therefore, $\mu = (2^{K-1} - 1)\phi$.

Proof. Based on the Definition 4, one has $\mid Pr(B \backslash A) - Pr(B) \mid \leq \phi$.

The event $\{\kappa_i^{t+1} \mid \kappa_i^t\}$ denoted as A_i means that the state of particle i at the t-th iteration is changed to the state at the $(t+1)$-th iteration, for each $i \in \{1, 2, \ldots, K\}$.

$$Pr(\prod_{i=1}^K A_i) = Pr(\eta^{t+1} \mid \eta^t) \quad (23)$$

is the transition probability from η^t to η^{t+1}.

Because g^{t+1} depends on x_i^t and P_i^t for all $1 \leq i \leq K$, $A_1, A_2, \ldots, A_K$ are not independent random events. According to (6) and the conditional probability, one has the following cases:

Case 1: $Pr(A_1 A_2) = Pr(A_1) Pr(A_2 \mid A_1) \leq Pr(A_1)[P(A_2) + \phi]$
$$\leq Pr(A_1) Pr(A_2) + \phi,$$

Case 2: $Pr(A_1) Pr(A_2) - \phi \leq Pr(A_1)[Pr(A_2) - \phi]$
$$\leq Pr(A_1) Pr(A_2 \mid A_1) = Pr(A_1 A_2).$$

This implies

$$Pr(A_1) Pr(A_2) - \phi \leq Pr(A_1 A_2) \leq Pr(A_1) Pr(A_2) + \phi \quad (24)$$

Case 3: $Pr(A_1 A_2 A_3) = Pr(A_1) Pr(A_2 \mid A_1) Pr(A_3 \mid A_1 A_2)$
$$\leq Pr(A_1)[Pr(A_2) + \phi][Pr(A_3) + \phi]$$
$$\leq Pr(A_1) Pr(A_2) Pr(A_3) + 3\phi,$$

Case 4: $Pr(A_1) Pr(A_2) Pr(A_3) - 3\phi \leq$
$$Pr(A_1)[Pr(A_2) - \phi][Pr(A_3) - \phi]$$
$$\leq Pr(A_1) Pr(A_2 \mid A_1) Pr(A_3 \mid A_1 A_2)$$
$$= Pr(A_1 A_2 A_3)$$

Similarly, we can get

$$Pr(A_1) Pr(A_2) P(A_3) - 3\phi \leq Pr(A_1 A_2 A_3) \leq \\ Pr(A_1) Pr(A_2) Pr(A_3) + 3\phi \quad (25)$$

Then,

$$\prod_{i=1}^K Pr(A_i) - (2^{K-1} - 1)\phi \leq Pr(\prod_{i=1}^K A_i) \leq \\ \prod_{i=1}^K Pr(A_i) - (2^{K-1} - 1)\phi \quad (26)$$

is the transition probability from η^t to η^{t+1}. Let $\mu = (2^{K-1} - 1)\phi$. We have

$$\mid Pr(\eta^{t+1} \mid \eta^t) - \prod_{i=1}^{K} P(\kappa_i^{t+1} \mid \kappa_i^t) \mid \le \mu \qquad (27)$$

From (1), the interdependent relationship among the particles is weak, ϕ in (11) is sufficiently small so that the fact that K is finite implies that μ is a small enough positive number.

3.1 Probabilistic convergence analysis of CSPSO

In this subsection, we present the convergence analysis for the version of the standard PSO with constriction coefficient (CSPSO), by analogy of the method of analyzing convergence of the PSO convergence of the PSO in Kennedy and Mendes [27]. We also based on concepts of definitions and results in Section 3 above. Our analysis has the advantage of providing a much easier method to realize the convergence of the PSO with constriction coefficient (χ) in comparison to the original analysis [12]. To conduct the convergence analysis of the SPSO with constriction coefficient (CSPSO), we consider the time step value $\Delta \tau$ to describe the dynamics of the PSO, and rewrite the velocity and position update formulas in (1) as follows:

$$V_i^{t+1} = \chi * \{\omega V_i^t + \varphi_1 \frac{(P_i^t - x_i^t)}{\Delta \tau} + \\ \varphi_2 \frac{(g_i^t - x_i^t)}{\Delta \tau}\}, \qquad (28)$$

$$X_i^{t+1} = X_i^t + V_i^{t+1} \Delta \tau, \qquad (29)$$

By replacing (28) into (29), we obtain the following probabilistic CSPSO:

$$X_i^1 = X_i + \chi * \{\omega V_i + \varphi_1 \frac{(P_i - x_i)}{\Delta \tau} + \\ \varphi_2 \frac{(g_i - x_i)}{\Delta \tau}\} \Delta \tau, \qquad (30)$$

$$X_i^1 = X_i + \chi \omega V_i \Delta \tau + \\ \chi \varphi \left(\frac{\chi \varphi_1 P_i + \chi \varphi_2 g_i}{\chi \varphi} - x_i \right) \qquad (31)$$

By rearranging the terms in (31), we obtain

$$X_i^1 = (1 - \chi \varphi) X_i + \chi \omega \Delta \tau V_i + \\ \chi \varphi_1 P_i + \chi \varphi_2 g_i. \qquad (32)$$

In addition, by rearranging the terms in (29), we obtain

$$V_i^1 = - \frac{\chi \varphi}{\Delta \tau} X_i + \chi \omega V_i + \\ \chi \varphi_1 \frac{P_i}{\Delta \tau} + \chi \varphi_2 \frac{g_i}{\Delta \tau}. \qquad (33)$$

We combine the above two (32), (33) to have the following matrix form:

$$\begin{pmatrix} X_i^1 \\ V_i^1 \end{pmatrix} = \begin{pmatrix} 1 - \chi \varphi & \chi \omega \Delta \tau \\ - \frac{\chi \varphi}{\Delta \tau} & \chi \omega \end{pmatrix} \begin{pmatrix} X_i \\ V_i \end{pmatrix} + \\ \begin{pmatrix} \chi \varphi_1 & \chi \varphi_2 \\ \frac{\chi \varphi_1}{\Delta \tau} & \frac{\chi \varphi_2}{\Delta \tau} \end{pmatrix} \begin{pmatrix} P_i \\ g_i \end{pmatrix} \qquad (34)$$

which can be thought of as a discrete dynamic system representation for the PSO in which $(X \ V)^T$ is the state subject to an external input $(P_i \ g_i)^T$, and the two terms on the right side of the equation correspond to the dynamic and input matrices, respectively [37].

Supposing that no external excitation exists in the dynamic system, $[P_i, g_i]^T$ is constant, i.e., other particles cannot find better positions. Then, a convergent behavior could be maintained. If it converges as $\tau \to \infty, (X_i^1 \ V_i^1)^T \to (X_i \ V_i)^T$. That is, the dynamic system becomes:

$$\begin{pmatrix} 0 \\ 0 \end{pmatrix} = \begin{pmatrix} 1 - \chi \varphi & \chi \omega \Delta \tau \\ - \frac{\chi \varphi}{\Delta \tau} & \chi \omega \end{pmatrix} \begin{pmatrix} X_i \\ V_i \end{pmatrix} + \\ \begin{pmatrix} \chi \varphi_1 & \chi \varphi_2 \\ \frac{\chi \varphi_1}{\Delta \tau} & \frac{\chi \varphi_2}{\Delta \tau} \end{pmatrix} \begin{pmatrix} P_i \\ g_i \end{pmatrix}$$

which holds only when $V_i = 0$ and $X_i = P_i = g_i$, where the convergent point is an equilibrium point if there is no external excitation, but better points are found by the optimization process with external excitation. For (34), Tarekegn et al. [6] has mentioned a sufficient strategies of improved convergence via theoretical analysis to get the relationship among χ, ω, and φ at the condition of convergence.

The derived probabilistic CSPSO can utilize any probabilistic form of prior information in the optimization process and, therefore, the benefits from prior information can lead probabilistic CSPSO to more probable search region and help optimize more quickly with hierarchical use of parameters [40].

By substituting (28) into (29), is transformed into (35)

$$V_i^1 = \chi \omega V_i + \frac{\chi \varphi}{\Delta \tau} \left[P(i) - x_i \right] \qquad (35)$$

where $P(i) = \frac{\varphi_1 P_i + \varphi_2 g_i}{\varphi}$.

Let $y_i = P(i) - x_i$, then (32), (35) can be transformed into (37), (38)

$$V_i^1 = \chi \omega V_i + \frac{\chi \varphi}{\Delta \tau} y_i \qquad (36)$$

$$Y_i^1 = \chi \omega V_i + \left(1 + \frac{\chi \varphi}{\Delta \tau} \right) y_i \qquad (37)$$

Combining (36) an iterative equation in the form of vector is obtained as (38)

$$\begin{pmatrix} V_i^1 \\ Y_i^1 \end{pmatrix} = \begin{pmatrix} \chi \omega & \frac{\chi \varphi}{\Delta \tau} \\ \chi \omega & 1 + \frac{\chi \varphi}{\Delta \tau} \end{pmatrix} \begin{pmatrix} V_i \\ y_i \end{pmatrix} \qquad (38)$$

which can be viewed as a general forecasting model of Markov chain as follows: $\eta^t = PK_i^t$, where, K_i^t is a vector as presented below

$$(\eta^t)^T = \begin{bmatrix} V_i^1 & Y_i^1 \end{bmatrix}$$

$$P^T = \begin{bmatrix} \chi\omega & \chi\omega \\ \frac{\chi\varphi}{\Delta\tau} & 1 + \frac{\chi\varphi}{\Delta\tau} \end{bmatrix},$$

$$(K_i^t)^T = \begin{bmatrix} V_i & y_i \end{bmatrix}$$

(38) is the model with no external excitation, which is useful in studying the evolution of certain systems over repeated trials as a probabilistic (stochastic) model [37].

Using the Markov chain method, the position $(\eta^t)^T(t+1)$ of the d th element of the i th particle at the $(t+1)$ th iteration in CSPSO can be computed using the following formula:

$$(\eta^t)^T(t+1) = [(k_i^t)^T(t)]XP^T \tag{39}$$

superscript T denotes the transposition.

Based on [20, 41] the CSPSO algorithm analysis in Markov chain theory, the algorithm satisfies the context of almost sure convergence as follows:

1. As the algorithm progresses and more iterations are performed, it will converge to an optimal solution with a probability of 1 and
2. Given sufficient time and iterations, it will find the globally optimal solution.

3.2 Stability analysis of CSPSO

We further get insight into the dynamic system in (39). First, we solve the characteristic equation of the dynamic system as follows:

$$\lambda^2 - (1 + \chi\omega + \frac{\chi\varphi}{\Delta\tau})\lambda + \chi\omega = 0.$$

The eigenvalues are obtained as follows:

$$\lambda_{1,2} = \frac{(1 + \chi\omega + \frac{\chi\varphi}{\Delta\tau} \pm \gamma)}{2},$$

$$\gamma = \sqrt{(1 + \chi\omega + \frac{\chi\varphi}{\Delta\tau})^2 - 4\chi\omega}$$

with $\lambda_1 \geq \lambda_2$. The explicit form of the recurrence relation (29) is then given by

$$Y_i^1(t) = r_1 + r_2\lambda_1^t + r_3\lambda_2^t$$

where r_1, r_2, and r_3 are constants determined by the initial conditions of the system. From updated velocity

$$V_i^1(t+1) = \frac{Y_i^1(t+1) - Y_i(t)}{\Delta\tau} \tag{40}$$

result in

$$V_i^1(t+1) = \frac{r_2(\lambda_1^{t+1} - \lambda_1^t) + r_3(\lambda_2^{t+1} - \lambda_2^t)}{\Delta\tau}$$

$$V_i^1(t+1) = (r_2\frac{\lambda_1 - 1}{\Delta\tau})\lambda_1^t + (r_3\frac{\lambda_2 - 1}{\Delta\tau})\lambda_2^t$$

$k_1 = \frac{r_1(\lambda_1-1)}{\Delta\tau}$ and $k_2 = \frac{r_2(\lambda_2-1)}{\Delta\tau}$

$$\lim_{t\to\infty} V_i^1(t+1) = \lim_{t\to\infty} k_1\lambda_1^t + \lim_{t\to\infty} k_2\lambda_2^t$$

$$\lim_{t\to\infty} X_i^1(t+1) = \begin{cases} \lim_{t\to\infty} x_i^1(t) \ if \ max(||\lambda_1||, ||\lambda_2||) < 1, \\ (k_1 \ or \ k_2 \ or \ k_1 + k_2) + \lim_{t\to\infty} x_i^1(t) \ if \\ max(||\lambda_1||, \ ||\lambda_2||) = 1 \end{cases} \tag{41}$$

(41) implies that if the CSPSO algorithm is convergent, then velocity of the particles will decrease to zero or stay unchanged until the end of the iteration.

3.3 Constriction factor and its impact

When the PSO algorithm is run without controlling the velocity, the system explodes after a few iterations. To control the convergence properties of a particle swarm system, an important model having constriction factor and ω together is shown below:

$$V_i^{t+1} = \chi * \{\omega V_i^t + \varphi_1(P_i^t - x_i^t) + \\ \varphi_2(g_i^t - x_i^t)\}, \tag{42}$$

$$2\kappa = \chi \mid 2 - \varphi - \sqrt{\varphi^2 - 4\varphi} \mid,$$

$\varphi_1 + \varphi_2 = \varphi \geq 4, \ 0 \leq \kappa \leq 1.$

Under these assumption conditions, the particle's trajectory in the CSPSO system is stable [6].

$$\omega^{t+1} = \omega_{max} - \left(\frac{\omega_{max} - \omega_{min}}{t_{max}}\right)t, \tag{43}$$

$$\omega_{max} > \omega_{min}$$

where, ω_{max} and ω_{min} are the predefined initial and final values of the inertia weight, respectively, t_{max} is the maximum iteration number, and t is the current iteration number for a linearly decreasing inertia weight scheme.

3.4 Global convergence analysis of QBCSPSO

A sequence generated by the iterative PSO algorithm converges to a solution point. Several PSO variants were proposed to enhance convergence performance of PSO [5, 24], which combines quantum results with CSPSO, denoted as QBCSPSO. In this subsection, the global convergence of QBCSPSO is investigated.

From the Monte Carlo method, the current velocity for the position x_i^{t+1} of the d th element of the i th particle at the $(t+1)$ th iteration in QBCSPSO can be obtained using the following formula:

$$V_i^{t+1} = Y_i^t \pm L_i^t \, ln(u_i^{-(t+1)}),$$
$$u_i^{t+1} \sim U(0,1) \qquad (44)$$

where $U_i^t \in (0, 1)$. Referring to Sun et al. [18, 24], where δ the (wave) function

$$\delta(Y_i^{t+1}) = \frac{1}{\sqrt{L_i^t}} \, exp(-Y_i^{t+1}/L_i^t)$$

with $Y_i^{t+1} = | \, x_i^{t+1} - P_i^t \, |$, and

the characteristic length L_i^t is obtained by

$$L_i^t = \gamma |x_i^t - C^t| \qquad (45)$$

the term C^t used in (45) is $C^t = \frac{1}{K} \sum_{i=1}^{K} P_i^t$. [24].

The contraction-expansion coefficient γ can be adjusted to balance the trade-off between global and local exploration ability of the particles during the optimization process for two main purposes [38]:

- a larger γ value enables particles to have a stronger exploration ability but a less exploitation ability.
- a smaller γ allows particles a more precise exploitation ability.

Notice that in this article, most of the (1)-(45) represent velocities or positions or both of them.

4 Results and discussions

To demonstrate the working of the CSPSO algorithm, two well-known test functions in a global optimization were widely used in evaluating performance of evolutionary methods, and have the global minimum at the origin or very close to the origin. We compare the performance of PSO, SPSO, CPSO, and CSPSO. Example 1. Unimodal function

$$min \, f(x_i) = \sum_{i=1}^{K} x_i^2 \qquad (46)$$
$$Subject \, to - 10 \leq x_i \leq 10.$$

Example 2. Multi modal function

$$min \, f(x) = \sum_{i=1}^{K} -x_i sin(\sqrt{| \, x_i \, |}) \qquad (47)$$
$$Subject \, to - 10 \leq x_i \leq 10.$$

In the experiments, inertia weight decreases from 0.9 to 0.4 and the generation stops when $E_i = | \, Fg^t(x_i) - Fp^t(x_i) \, | \leq tolerance$ satisfied. Here, Fp is the function value of the best personal in current iteration and Fg denotes the global optimum and $c_1 = c_2 = 1.49$ and $c_1 = c_2 = 2$ are used in PSO and CSPSO, respectively.

For all algorithms, results are averaged over 100 independent runs and iterations while the population size is 50.

Following the recommendations of the original references, the best function value settings of some compared algorithms are summarized in Table 1.

The mean velocity v^{t+1} of (46) is shown using Table 1 and graphically (Figures 1–3) for the algorithms in Table 1. Figure 1 shows the convergence of PSO without controlling factor inertia weight exploded. One of the main limitations of PSO is that particles prematurely converge toward a local solution.

The evaluation results of the compared algorithms are shown in Figures 2, 3 for decreasing and increasing inertia weight, respectively. Figure 2 shows the evolution of inertial weight of the compared algorithms over the running time. The main disadvantage is that once the inertia weight is decreased, the

FIGURE 1
Basic PSO with no inertia weight for (46) on example 1.
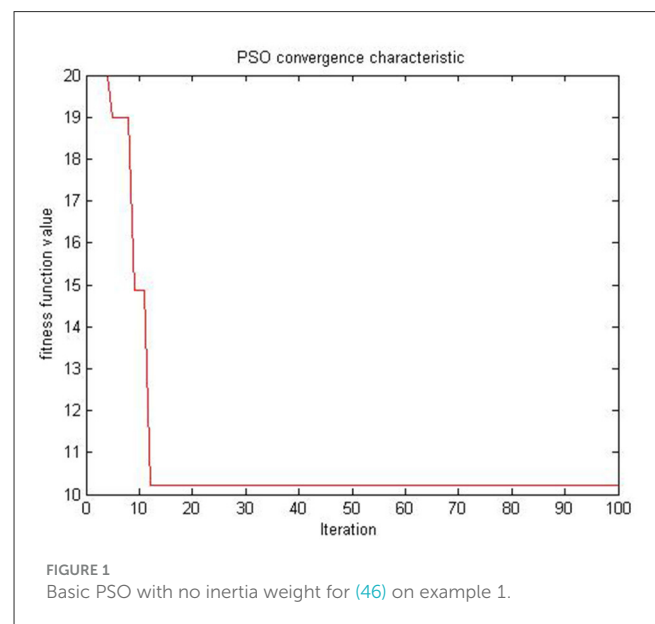
TABLE 1 Comparison of algorithms on optimization test functions.

No	Best fun	Algorithm	Best run	Best variables	$\omega \in range$
1.	10.2213	Basic PSO	35	[0.3809, 1.4531, 3.1164]	
2.	9.3944	SPSO	4	[0.4381, 1.4566, 3.1052]	[0.9, 0.4]
3.	9.3945	SPSO	27	[0.4384, 1.4564, 3.1051]	[0.4, 0.9]
4.	9.3941	CSPSO	29	[0.4379, 1.4568, 3.1053]	[0.9, 0.4]
5.	9.3941	CSPSO	28	[0.4381, 1.4567, 3.1052]	[0.4, 0.9]

swarm loses its ability to search new areas [39]. Figure 3 shows the evolution of convergence characteristic for CSPSO based on inertial weight during the run. CSPSO can avoid premature convergence by performing efficient exploration that can help to find better solutions as the number of iterations increases and can avoid premature convergence by balancing exploration and exploitation. The algorithm CSPSO has shown fast convergence speed on unimodal functions.

In order to confirm the performance on multi-modal functions, we carry out a similar simulation by using (47).

The same set of parameters is assigned for all algorithms of Table 2 as in (46). Where in this function the number of local minima increases exponentially with the problem dimension. Its

global optimum value is approximately −5.74, as we see from Table 2.

FIGURE 4
CPSO when $\omega = 1$ for (47) on example 2.

FIGURE 2
Evaluation of SPSO for (46) on example 1.

FIGURE 3
Evaluation of CSPSO for (46) on example 1.

FIGURE 5
Evaluation of SPSO for (47) on example 2.
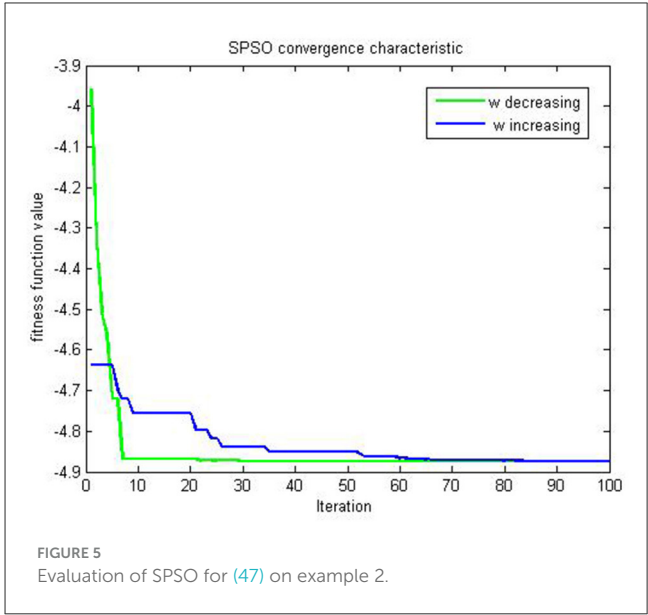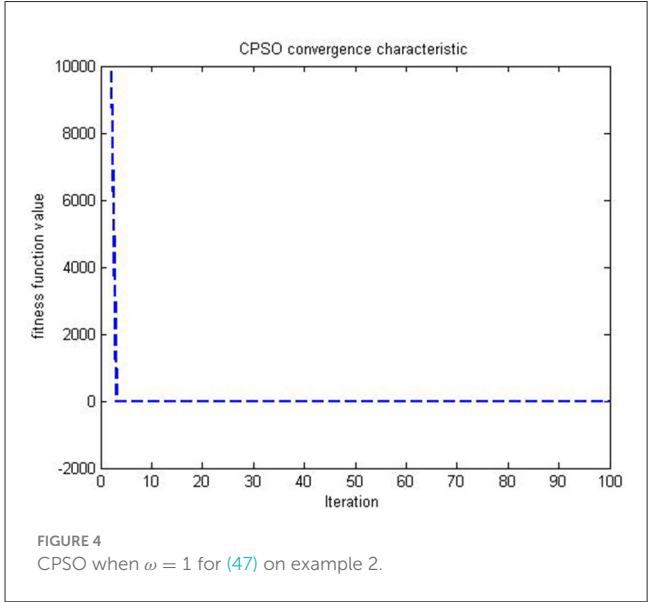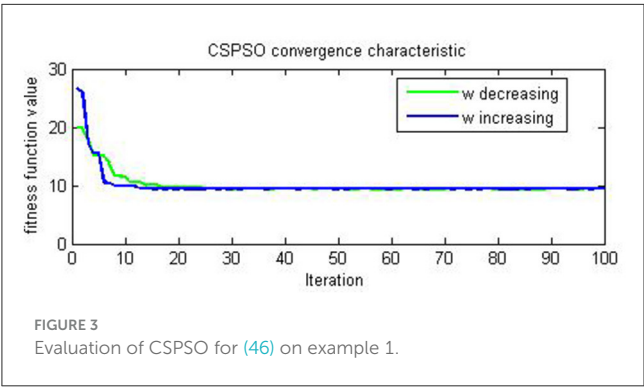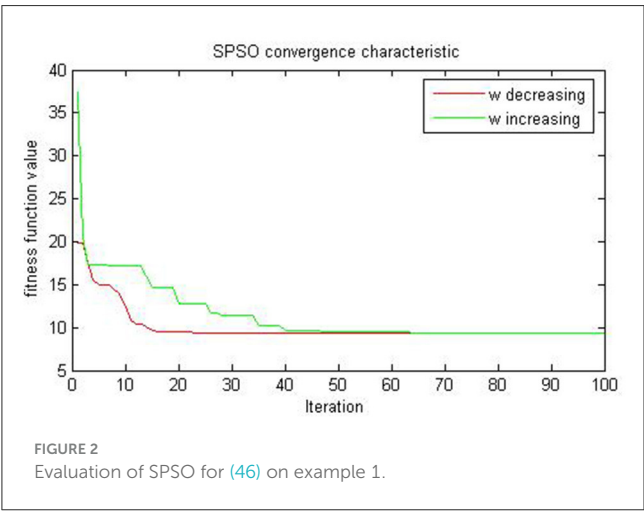
TABLE 2 Comparison of algorithms on optimization test functions of multi-modal.

No	Algorithm	Best fun	Best run	Best variables	$\omega \in range$
1.	CPSO	−6.12	01	[1.79, 0, 3.20]	$\omega = 1$
2.	SPSO	−6.73	32	[1.79, 0, 3.21]	[0.4, 0.9]
3.	SPSO	−8.133	89	[1.79, 0, 3.21]	[0.9, 0.4]
4.	CSPSO	−11.83	69	[5.23, 5.23, 5.23]	[0.9, 0.4]
5.	CSPSO	−5.74	39	[1.79, 0, 3.21]	[0.4, 0.9]

FIGURE 6
Evaluation of CSPSO for (47) on example 2.
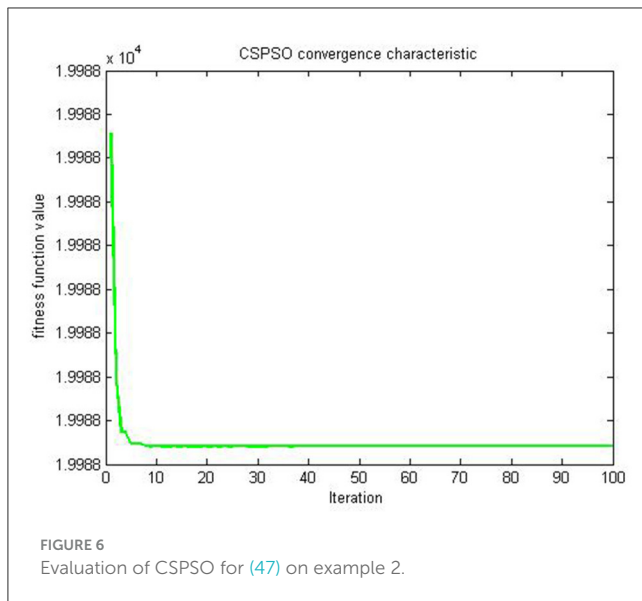
Figures 4, 5 are simulations obtained from Table 2 results, and all the figures meet the objective of the CSPSO algorithm for the optimization problem given in (47) and its evaluation in Figure 6.

5 Conclusion

This article mainly concerns the convergence and stability analysis of the CSPSO algorithm and its performance improvement for different constriction coefficients. We first investigated the convergence of the SPSO algorithm by relating it to the Markov chain in which the stochastic process and Markov properties employ quantum behaviors to improve the global convergence and prove Markov chain transition probability, showing that the CSPSO algorithm converges to the global optimum in probability. We also compared the proposed algorithm with basic PSO, SPSO, and CPSO algorithms evaluating the optimal value (fitness value) based on the range of ω. The proposed algorithm is fast and efficient, and the run plans of CSPSO for ω linearly decreasing from 0.9 to 0.4 are easy to implement. The CSPSO algorithm performs better because it regenerated those results to minimize the test functions. On the other hand, the proposed heuristic algorithm did not seek solutions that minimized the delay time or cost function, and the adjustment process would be stopped if no ω was identified as regular. The CSPSO algorithm is verified to be a global convergent algorithm.

These promising results motivate other researchers to apply CSPSO to solve optimization problems. And in the future we will make further investigations on convergence and stability of PSO variants.

Data availability statement

The original contributions presented in the study are included in the article/supplementary material, further inquiries can be directed to the corresponding author.

Author contributions

DT: Formal analysis, Writing—original draft, Software, Investigation, Project administration. TG: Supervision, Methodology, Validation, Project administration, Writing—review & editing. SL: Conceptualization, Supervision.

Funding

Acknowledgments

Conflict of interest

The authors declare that the research was conducted in the absence of any commercial or financial relationships that could be construed as a potential conflict of interest.

Publisher's note

All claims expressed in this article are solely those of the authors and do not necessarily represent those of their affiliated organizations, or those of the publisher, the editors and the reviewers. Any product that may be evaluated in this article, or claim that may be made by its manufacturer, is not guaranteed or endorsed by the publisher.

References

1. Kennedy J, Eberhart RC. Particle swarm optimization. In: *Proceedings of the IEEE International Conference on Neural Networks*, (1995). p. 1942–1948.

2. Ahmed G. GadParticle swarm optimization algorithm and its applications: a systematic review. *Arch Comput Methods Eng.* (2022) 29:2531–61. doi: 10.1007/s11831-021-09694-4

3. Banks A, Vincent J, Anyakoha CA. A review of particle swarm optimization. Part I: background and development. *Nat Comput.* (2007) 6:467–84. doi: 10.1007/s11047-007-9049-5

4. AlRashidi MR, El-Hawary ME. A survey of particle swarm optimization applications in electric power systems. *IEEE Trans Evol Comput.* (2009) 14:913–8. doi: 10.1109/TEVC.2006.880326

5. Kumar A, Singh BK, Patro BD. Particle swarm optimization: a study of variants and their applications. *Int J Comput Applic.* (2016) 135:24–30. doi: 10.5120/ijca2016908406

6. Tarekegn D, Tilahun S, Gemechu T. A review on convergence analysis of particle swarm optimization. *Int J Swarm Intell Res.* (2023) 14:328092. doi: 10.4018/IJSIR.328092

7. Clerc M, Kennedy J. The particle swarm-explosion, stability and convergence in a multidimensional complex space. *IEEE Trans Evol Comput.* (2002) 6:58–73. doi: 10.1109/4235.985692

8. van den Bergh F, Engelbrecht AP. A study of particle swarm optimization particle trajectories. *Inform Sci.* (2006) 178:937–71. doi: 10.1016/j.ins.2005.02.003

9. Kadirkamanathan V, Selvarajah K, Fleming PJ. Stability analysis of the particle dynamics in particle swarm optimizer. *IEEE Trans Evol Comput.* (2006) 10:245–55. doi: 10.1109/TEVC.2005.857077

10. Liu QF. Order-2 stability analysis of particle swarm optimization. *Evol Comput.* (2015) 23:187–216. doi: 10.1162/EVCO_a_00129

11. Dong WY, Zhang RR. Order-3 stability analysis of particle swarm optimization. *Inf Sci.* (2019) 503:508–20. doi: 10.1016/j.ins.2019.07.020

12. Jiang M, Luo YP, Yang SY. Stochastic convergence analysis and parameter selection of the standard particle swarm optimization algorithm. *Inform Process Lett.* (2007) 102:8–16. doi: 10.1016/j.ipl.2006.10.005

13. Poli R, Langdon WB. Markov chain models of bare-bones particle swarm optimizers. In: *Proceedings of the 9th Annual Conference on Genetic and Evolutionary Computation.* (2007). p. 142–149. doi: 10.1145/1276958.1276978

14. Cai ZQ, Huang H, Zheng ZH, Luo W. Convergence improvement of particle swarm optimization based on the expanding attaining-state set. *J Huazhong Univ Sci Technol.* (2009) 37:44–7.

15. Solis F, Wets R. Minimization by random search techniques. *Math Oper Res.* (1981) 6:19–30. doi: 10.1287/moor.6.1.19

16. van den Bergh F, Petrus Engelbrecht A. A convergence proof for the particle swarm. *Optimiser Fund Inform.* (2010) 105:341–74. doi: 10.3233/FI-2010-370

17. Dirk S, Carsten W. Runtime analysis of a binary particle swarm optimizer. *Theor Comput Sci.* (2010) 411:2084–100. doi: 10.1016/j.tcs.2010.03.002

18. Sun J, Wu X, Palade V, Fang W, Lai CH, Xu W. Convergence analysis and improvements of quantum-behaved particle swarm optimization. *Inf Sci.* (2012) 193:81–103. doi: 10.1016/j.ins.2012.01.005

19. Per KL, Carsten W. Finite first hitting time versus stochastic convergence in particle swarm optimization. *Adv Metaheur.* (2013) 53:1–20. doi: 10.1007/978-1-4614-6322-1_1

20. Yuan Q, Yin G. Analyzing convergence and rates of convergence of particle swarm optimization algorithms using stochastic approximation methods. *IEEE T Automat Contr.* (2015) 60:1760–73. doi: 10.1109/TAC.2014.2381454

21. Ren ZH, Wang J, Gao Y. The global convergence analysis of particle swarm optimization algorithm based on Markov chain. *Control Theory Applic.* (2011) 28:462–6.

22. Xu G, Yu G. On convergence analysis of particle swarm optimization algorithm. *J Comput Appl Math.* (2017) 333:65–73. doi: 10.1016/j.cam.2017.10.026

23. Feng P, Xiao-Ting LI, Qian ZH, Wei-Xing LI Qi GA. Analysis of standard particle swarm optimization algorithm based on Markov Chain. *Acta Autom Sinica.* (2013) 39:381–9. doi: 10.1016/S1874-1029(13)60037-3

24. Sun J, Feng B, Xu WB. Particle swarm optimization with particles having quantum behavior. In: *Proceedings of the 2004 Congress on Evolutionary Computation, CEC04,* Portland, USA (2004). p. 326–331.

25. Shi YH, Eberhart RC. Empirical study of particle swarm optimization. In: *Proceedings of the Congress on Evolutionary Computation,* (1999). p. 1945–1950.

26. Kennedy J. Bare bones particle swarms. In: *Proceedings of the 2003 IEEE Swarm Intelligence Symposium,* IEEE (2003). p. 80–87.

27. Kennedy J, Mendes R. Population structure and particle swarm performance. In: *Proceedings of the Congress on Evolutionary Computation.* (2002). p. 1671–6.

28. Liang JJ, Suganthan PN. Dynamic multi-swarm particle swarm optimizer. In: *Proceedings of the IEEE Swarm Intelligence Symposium.* (2005). p. 124–129.

29. Parrott D, Li X. Locating and tracking multiple dynamic optima by a particle swarm model using speciation. *IEEE Trans Evol Comput.* (2006) 10:440–58. doi: 10.1109/TEVC.2005.859468

30. Brits R, Engelbrecht AP, van den Bergh F. Locating multiple optima using particle swarm optimization. *Appl Math Comput.* (2007) 189:1859–83. doi: 10.1016/j.amc.2006.12.066

31. Zhao X. A perturbed particle swarm algorithm for numerical optimization. *Appl Soft Comput.* (2010) 10:119–24. doi: 10.1016/j.asoc.2009.06.010

32. Tang Y, Wang ZD, Fang JA. Feedback learning particle swarm optimization. *Appl Soft Comput.* (2011) 11:4713–25. doi: 10.1016/j.asoc.2011.07.012

33. Wang HF, Moon I, Yang SX, Wang DW. A memetic particle swarm optimization algorithm for multimodal optimization problems. *Inform Sci.* (2012) 197:38–52. doi: 10.1016/j.ins.2012.02.016

34. Huang H, Qin H, Hao Z, Lim A. Example-based learning particle swarm optimization for continuous optimization. *Inform Sci.* (2012) 182:125–38. doi: 10.1016/j.ins.2010.10.018

35. Lawler GF. Introduction to Stochastic Processes, second edition. London: Chapman and Hall/CRC Press. (2006).

36. Xiao XY, Yin HW. Moment convergence rates in the law of logarithm for moving average process under dependence. *Stochastics.* (2014) 86:1–15. doi: 10.1080/17442508.2012.748057

37. Hu D, Qiu X, Liu Y, Zhou X. Probabilistic convergence analysis of the stochastic particle swarm optimization model without the stagnation assumption. *Inf Sci.* (2021) 547:996–1007. doi: 10.1016/j.ins.2020.08.072

38. Chen J, Xin B, Peng Z, Dou L, Zhang J. Optimal contraction theorem for explorationexploitation tradeoff in search and optimization. *IEEE Trans Syst Man Cybern Part A.* (2009) 39:680–91. doi: 10.1109/TSMCA.2009.2012436

39. Ezugwu AE, Agushaka JO, Abualigah L, Mirjalili S, Gandomi AH. Prairie dog optimization algorithm. *Neural Comput Applic.* (2022) 34:20017–65. doi: 10.1007/s00521-022-07530-9

40. Lee J, Mukerji T. *Probabilistic Particle Swarm Optimization (Pro]PSO) for Using Prior Information and Hierarchical Parameters.* Department of Energy Resources Engineering, Stanford University (2014).

41. Schmitt M, Wanka R. Particle swarm optimization almost surely finds local optima. *Theor Comput Sci.* (2014) 561:57–72. doi: 10.1016/j.tcs.2014.05.017

Appendix

Matlab codes

```matlab
tic
clc
clear all
close all
rng default
LB=[0 0 0]; UB=[10 10 10];
m=3; n=50;
wmin=0.9; wmax=0.4; c1=2; c2=2;
maxite=100; maxrun=100;
for run=1:maxrun
run
for i=1:n
for j=1:m
x0(i,j)=round(LB(j)+(UB(j)-LB(j))*rand());
end
end
x=x0; v=0.1*x0;
for i=1:n
f0(i,1)=ofun(x0(i,:));
end
pbest=x0;
[fmin0,index0]=min(f0);
gbest=x0(index0,:);
ite=1;
tolerance=1;
rho=0.9;
while ite <= maxite && tolerance > 10^{-12}
w =wmax-(wmax-wmin)*ite/maxite;
kappa=1; phi1=2.05; phi2=2.05;
phi=phi1+phi2;
chi = 2 * kappa/abs(2 - phi - sqrt(phi^2 - 4 * phi));
a=1/w;
for i=1:n
for j=1:m
v(i,j)=chi*[w*v(i,j)+c1*rand()*(pbest(i,j)-
x(i,j))+c2*rand()*(gbest(1,j)-x(i,j))];
end
end
for i=1:n
for j=1:m
x(i,j)=x(i,j)+v(i,j);
end
end
for i=1:n
for j=1:m
```

```matlab
if x(i,j)<LB(j)
x(i,j)=LB(j);
elseif x(i,j)>UB(j)
x(i,j)=UB(j);
end
end
end
for i=1:n
f(i,1)=ofun(x(i,:));
end
for i=1:n
if f(i,1)<f0(i,1)
pbest(i,:)=x(i,:);
f0(i,1)=f(i,1);
end
end
[fmin,index]=min(f0);
ffmin(ite,run)=fmin;
ffite(run)=ite;
if fmin<fmin0
gbest=pbest(index,:);
fmin0=fmin;
end
if ite>100;
tolerance=abs(ffmin(ite-100,run)-fmin0);
end
if ite==1;
disp(sprintf('Iteration Best particle objective fun'));
end
disp(sprintf('
ite=ite+1;
end
gbest;
fvalue=-x(1)*sin(sqrt(abs(x(1))))-x(2)*sin(sqrt(abs(x(2))))-
x(3)*sin(sqrt(abs(x(3))));
fff(run)=fvalue;
rgbest(run,:)=gbest;
disp(sprintf('———'));
end
disp(sprintf(''));
disp(sprintf('***********'));
disp(sprintf('Final Results——'));
[bestfun, bestrun] = min(fff)
best_variables = rgbest(bestrun, :)
disp(sprintf('*********'));
toc
plot(ffmin(1:ffite(bestrun),bestrun),'–b','linewidth',2);
xlabel('Iteration ');
ylabel('fitness function value');
title('CSPSO convergence characteristic')
```

Improving passengers' attitudes toward safety and unreliable train operations: analysis of a mathematical model of fractional order

Gizachew Kefelew Hailu* and
Shewafera Wondimagegnhu Teklu

Department of Mathematics, College of Natural and Computational Sciences, Debre Berhan
University, Debre Berhan, Ethiopia

In this study, we aimed to explore the dynamics of rail passengers' negative attitudes that can be influenced by safety concerns and unreliable train operations. We mainly formulated and analyzed a mathematical model of fractional order and derived an optimal control problem considering the Caputo fractional order derivative. In the analysis part of the model, we proved that the solutions of the model for the dynamical system are non-negative and bounded, and determined the passengers' negative attitude-free and negative attitude persistence equilibrium points of the model. Both the local and global stabilities of these equilibrium points were examined. Furthermore, we verified the conditions necessary for the existence of optimal control strategies. We then proceeded to analyze the proposed control strategies, which aim to prevent negative attitudes and improve the attitudes of passengers who have already developed negative attitudes. Finally, we conducted numerical simulations to examine the effects of these control strategies. The results revealed that protecting passengers from developing negative attitudes and improving the attitudes of those who have already developed such attitudes are crucial for improving the overall attitude of railway passengers. These measures can effectively address any negative experiences caused by safety concerns and unreliable train operations.

KEYWORDS

passengers, negative attitude, protection, improvement, fractional order derivative

1 Introduction

Railway transportation plays a significant role in enhancing market accessibility and facilitating efficient travel for both passengers and goods. The progress of railway development in developed countries has been remarkable, with advanced infrastructure, efficient operations, and continuous technological advancements. However, the progress of railway transportation in developing nations encounters notable difficulties due to inadequate operation and maintenance of railway infrastructure (1). These difficulties contribute to a growing concern regarding the escalation in passengers' negative attitudes toward railway services (2). Understanding the control strategies behind these negative attitudes is crucial for improving service quality and addressing passengers' concerns.

The quality of service offered by public transit can be understood by measuring its performance according to the experiences of its riders (3). Several factors influence passengers'

attitudes toward railway transportation, including service quality, safety concerns, a lack of effective communication, frequent breakdowns, overcrowding, and reliability of operation (4). Insufficient communication during disruptions or emergencies can lead to frustration and further dissatisfaction among passengers. Passengers often feel helpless and uninformed, which escalates their dissatisfaction and contributes to negative attitudes toward train services (5).

A decline in passenger satisfaction and an increase in negative attitudes can lead to a decrease in ridership, ultimately affecting the revenue and viability of railway operations (6). Lower customer satisfaction can also lead to a decline in public trust and support, hindering the growth and development of the train industry (7). It is, therefore, crucial to thoroughly examine the dynamics behind passengers' negative attitudes to gain valuable insights for policymakers and railway operators, enabling them to make well-informed decisions and implement effective measures to improve the overall passenger experience.

To better describe and analyze various aspects of a real-world problem in various disciplines, including science and engineering, mathematical modeling can serve as a powerful tool for representing the problem by using mathematical equations, formulas, and algorithms. This can be observed, for instance, by examining its application in various contexts (8–10).

The authors discussed how mathematical modeling can help identify the key factors that contribute to the dynamics of real-life situations by analyzing the stability of equilibrium points. The classic autonomous ordinary differential equations representing evolutionary systems have no memory, as their solution is independent of the previous instant (11). However, the fractional order differential equations, in contrast, incorporate the memory effect of an evolutionary system, such as passengers' attitudes. In the context of rail passengers, memory effects can play a significant role in shaping their attitudes. These effects refer to the influence of past experiences and interactions on the present attitude of individuals. Furthermore, memory effects that impact the dynamics include the persistence of negative experiences, recency bias, confirmation bias, social influence, and expectation formation.

A fractional order model means a representation of a system described by a fractional differential equation or a system of such Equation (12). Mathematicians have developed several approaches for fractional derivatives, such as Grunwald-Letnikov, Riemann-Liouville, and Caputo's fractional derivatives. The Riemann-Liouville method results in initial conditions that include the limiting values of the Riemann-Liouville fractional derivatives at the lower bound $t = a$, and these types of initial conditions lack a recognized physical interpretation. Applied engineering problems require the formulation of a fractional order model with the use of physically interpretable initial conditions, such as $X(a), X'(a), X''(a)$, and so on. Caputo's approach enables the formulation of initial conditions for fractional order differential equations at the lower terminal $t = a$ (12).

The Caputo fractional derivative approach is another mathematical technique that can be employed for evolutionary systems with memory effect. The application of this approach has been dealt with in various contexts (13–17). Bhalekar et al. (18) considered the dynamics of the fractional order systems involving non-local derivative operators on singular points in the solution trajectories of the systems. The study investigated the behavior of the trajectories when the eigenvalues λ are at a specified stable region and examined the existence of singular points in the trajectories of such systems in a given region. Echenausía-Monroy et al. (19) investigated a physical interpretation of fractional-order derivatives in a jerk system using an electronic approach based on unstable dissipative systems (UDSs) and a saturated non-linear function (SNLF). The results of the analysis revealed that, when the orders of the fractional integration are considered, the areas of the generated attractor are modified with respect to the integer-order dynamic. Zhou et al. (20) clarified the physical process for fractional dynamical systems. The dynamics in fractional order systems have been discussed extensively for presenting possible guidance in the field of applied mathematics and interdisciplinary science.

Motivated by the concepts discussed above, in this study, we constructed a Caputo fractional derivative compartmental modeling approach to analyze the dynamics of passengers' negative attitudes toward railway transportation. These advanced analytical techniques enable us to gain insights into the underlying factors contributing to negative attitudes and explore strategies for improving passengers' attitudes.

The remainder of this article is structured as follows: in section 2, we present some basic terminologies necessary for the formulation of mathematical models of fractional order. The formulation of integer and fractional order models is given in section 3. Section 4 presents the optimal control problem, followed by the numerical simulation in section 5. Finally, in section 6, we conclude the article with a summary and discuss future work.

2 Basic terminology of fractional order calculus

The following concepts of fractional order calculus will serve as a foundation for constructing the fractional order model in this study:

Definition 1: The Caputo fractional order derivative of order ϑ for a function $f \in C^n$ is defined by Vargas-De-León (17) and Petrás (21).

$$\mathrm{C}_{D_t^\vartheta} f(t) = \frac{1}{\Gamma(n-\vartheta)} \int_o^t f^n(\zeta) \frac{(t-\zeta)^{n-\vartheta}}{t-\zeta} d\zeta, \; n-1 < \vartheta \le n \in N \tag{1}$$

Note:

$$\mathrm{C}_{D_t^\vartheta} f(t) \text{ tends to } \dot{f}(t) \text{ as } \vartheta \to 1 \tag{2}$$

Definition 2: The Caputo fractional order integral of order $\vartheta > 0$ for a function $f \in C^n$ is defined by Vargas-De-León (17) and Petrás (21).

$$\mathrm{C}_{I_t^\vartheta} f(t) = \frac{1}{\Gamma(\vartheta)} \int_o^t f(\zeta) \frac{(t-\zeta)^\vartheta}{t-\zeta} d\zeta, 0 < \vartheta \langle 1, t \rangle 0 \tag{3}$$

Definition 3: Let $\gamma_1 > 0, \gamma_2 > 0$ be positive parameters, then the Mittag–Leffler function is defined by Mainardi (22), Fernandez and Husain (23), and Özarslan and Fernandez (24).

$$E_{\gamma_1,\gamma_2}(t) = \sum_{m=1}^{\infty} \frac{t^m}{\Gamma(\gamma_1 m + \gamma_2)} \qquad (4)$$

Definition 4: Suppose $\gamma_2 = 1$ is the constant parameter. Then, the Mittag–Leffler function is defined by Mainardi (22) and Özarslan and Fernandez (24).

$$E_{\gamma_1,1}(t) = \sum_{m=1}^{\infty} \frac{t^m}{\Gamma(\gamma_1 m + 1)} = E_{\gamma_1}(t) \qquad (5)$$

Definition 5: A constant number θ^* is identified as an equilibrium point of the Caputo-fractional order model when

$$^C D_t^\vartheta \theta(t) = f(t, \theta(t)), \vartheta \in [0,1] \text{ if and only if } f(t, \theta^*) = 0 \qquad (6)$$

Proposition 1: The Laplace transform of the Caputo fractional order derivative with order ϑ, $n-1 < \vartheta \le n, n \in N$ is given by

$L\left(D_t^\vartheta h\right)(s) = s^\vartheta H(s) - \sum_{k=1}^{n-1} s^{\vartheta-k-1} h^k(0)$, where $H(s)$ is the Laplace transform of the function $h(t)$.

Proposition 2: The Laplace transformation of the two-parameter functions of the Mittag–Leffler case is given by Balatif et al. (25).

$$L\left(t^{\gamma_2-1} E_{\gamma_1,\gamma_2}\left(\pm \gamma t^{\gamma_1}\right)\right)(s) = \frac{s^{\gamma_1-\gamma_2}}{s^{\gamma_1} \mp \gamma}$$

Proposition 3 (Generalized Mean Value theorem): Suppose $h(t) \in \mathcal{L}[0, T_f]$ and $^C D_t^\vartheta h(t) \in \mathcal{L}[0, T_f]$ for $\vartheta \in (0,1]$. Then, the theorem states that $h(t) = h(0) + \frac{1}{\Gamma(\vartheta)} \, ^C D_t^\vartheta h(\zeta) t^\vartheta$, where $\zeta \in [0, t]$ for each t such that $0 < t \le T_f$.

Note: These statements follow from Proposition 3.

a. The function h is non-decreasing for all $t \in [0, T_f]$, if $^C D_t^\vartheta h(t) \ge 0$.
b. The function h is non-increasing for all $t \in [0, T_f]$, if $^C D_t^\vartheta h(t) \le 0$.

Proposition 4: Suppose $g(t) \in L^\infty(\mathbb{R}) \cap \mathcal{F}(\mathbb{R})$ and $\in \mathbb{R}$, $n-1 < \vartheta \le n, n \in N$. Then, the following conditions hold

a.
$$\left(^C D_t^\vartheta I^\vartheta g\right)(t) = g(t).$$

b. $\left(I^\vartheta \, ^C D_t^\vartheta g\right)(t) = g(t) - \sum_{k=0}^{n-1} \frac{t^k}{k!} g^k(0).$

c. Specifically, if $0 < \vartheta < 1$, then $\left(I^\vartheta \, C D_t^\vartheta g\right)(t) = g(t) - g(0).$

d. For a constant function $g(t) = b$ then $^C D_t^\vartheta(b) = 0.$

3 Models' formulation

3.1 Description and assumptions of the models

To analyze the dynamics of the passengers' negative attitudes toward railway transportation, we divided the total number of passengers, denoted by $M(t)$ at a given time t, into five distinct mutually exclusive classes: susceptible passengers who can develop negative attitudes whenever they are exposed, which is denoted by $S(t)$, passengers who are exposed to negative attitudes due to perceived safety concerns and unreliable operation of train services, which is denoted by $E(t)$, passengers who developed negative attitude due to safety concerns, which is denoted by $I_S(t)$, passengers who developed negative attitudes due to unreliable train operation, which is denoted by $I_U(t)$, and passengers whose negative attitudes changed, which is denoted by $R(t)$. The passengers who developed negative attitudes due to unreliable train operation may have encountered trains running late or not adhering to the schedule, leading to frustration and dissatisfaction.

$$M(t) = S(t) + E(t) + + I_S(t) + I_U(t) + R(t). \qquad (7)$$

Acquiring a negative attitude from another passenger is not influenced by the number of passengers around, and susceptible individuals within the population acquire negative attitudes from other passengers at a standard incidence rate given by

$$\lambda_{SC}(t) = \frac{\beta}{M}\left(\rho_1 I_S(t) + \rho_2 I_U(t)\right). \qquad (8)$$

where

ρ_1 is the relative effect of passengers with negative attitudes due to safety concerns;
ρ_2 is the relative effect of passengers with negative attitudes due to unreliable train operation; and
β is the transmission rate of negative attitude.

To construct the Caputo fractional order model for the transmission dynamics of negative attitudes among passengers in a population, certain key assumptions need to be considered.

A portion q of susceptible passengers who were exposed to negative attitude, i.e., $S(t)$ transfers to the $I_S(t)$, a portion of passengers who developed negative attitudes due to safety concerns at a rate ϖ, while the remaining portion $1-q$ joins $I_U(t)$, a portion of passengers who developed negative attitudes due to unreliable train operation at the same rate.

Passengers with negative attitude due to safety concerns $I_S(t)$ and those with negative attitude due to unreliable train operation $I_U(t)$ progress to the portion of passengers whose negative attitudes $R(t)$ at the rates α_1 and α_2, respectively. The rate η is the progression of individuals from the I_S portion to I_U. Other parameters and state variables are stated in Tables 1, 2.

The population flow diagram, which is based on the model descriptions and assumptions given above, illustrates how the negative attitude of passengers disseminates among the population.

TABLE 1 Description of parameters.

Parameter description	
d	Natural mortality rate.
K	Population recruitment rate.
ϖ	Rate at which passengers exposed to negative attitudes develop negative attitudes either due to safety concerns or unreliable train operation.
α_1	Rate of progression from passengers who developed negative attitudes due to safety concerns to the group whose negative attitudes have changed.
η	The progression rate of passengers who developed negative attitudes due to safety concerns to the portion of passengers with negative attitudes due to unreliable train operation.
α_2	Rate of progression from passengers who developed negative attitudes due to unreliable train operation to the group whose negative attitudes changed.
q	Portion of passengers who were exposed to negative attitudes and transferred to passengers' group who developed negative attitudes due to unreliable train operation $I_U(t)$.

TABLE 2 Definitions of state variables.

Variable definition	
S	Passengers who are susceptible to passengers' negative attitude.
E	Passengers who are exposed to negative attitudes.
I_S	Passengers who developed negative attitudes due to safety concerns.
I_U	Passengers who developed negative attitudes due to unreliable train operation.
R	Passengers whose negative attitudes have changed.

3.2 Integer order model

The integer order model, a system of non-linear first-order ordinary differential equations, is based on the population flow diagram given in Figure 1 and represents the evolution of passengers' negative attitudes, which is given by

$$\frac{dS}{dt} = K - (\lambda_{SC} + d)S$$

$$\frac{dE}{dt} = \lambda_{SC}S - (d + \varpi)E$$

$$\frac{dI_S}{dt} = (1-q)\varpi E - (d + \alpha_1 + \eta)I_S$$

$$\frac{dI_U}{dt} = q\varpi E + \eta I_S - (d + \alpha_2)I_U$$

$$\frac{dR}{dt} = \alpha_1 I_S + \alpha_2 I_U - dR \qquad (9)$$

subject to $S(0) > 0,\quad E(0) \geq 0, I_S(0) \geq 0\quad I_U(0) \geq 0$, and $R(0) \geq 0$ (10)

3.3 Fractional order model

In this subsection, we reformulated the transmission dynamics of passengers' negative attitude model (Equation 9). This is done by using Caputo derivatives, which allows us to incorporate memory effects and gain a deeper understanding of the evolution of passengers' negative attitudes. The mathematical representation of this fractional order model can be observed in Equation 11.

$$^C D_t^\vartheta S = K - (\lambda_{SC} + d^\vartheta)S$$

$$^C D_t^\vartheta E = \lambda_{SC} S - (d^\vartheta + \varpi^\vartheta)E$$

$$^C D_t^\vartheta I_S = q^\vartheta \varpi^\vartheta E - (d^\vartheta + \alpha_1^\vartheta + \eta^\vartheta)I_S$$

$$^C D_t^\vartheta I_U = q^\vartheta \varpi^\vartheta E + \eta^\vartheta I_S - (d^\vartheta + \alpha_2^\vartheta)I_U$$

$$^C D_t^\vartheta R = \alpha_1^\vartheta I_S + \alpha_2^\vartheta I_U - d^\vartheta R \qquad (11)$$

The initial data for the proposed fractional order model (Equation 11) is demonstrated by

$$S(0) \geq 0,\ E(0) \geq 0,\ I_S(0) \geq 0,\ I_U(0) \geq 0, R(0) \geq 0 \quad (12)$$

The analysis of the fractional order model given in Equation 11 is presented in the Supplementary material, where theorem 1 shows the non-negativity and boundedness of the model, and theorem 2 demonstrates the existence and uniqueness of solution of the model. The equilibrium points and basic reproduction bombers are calculated

FIGURE 1
The passengers' flow diagram.
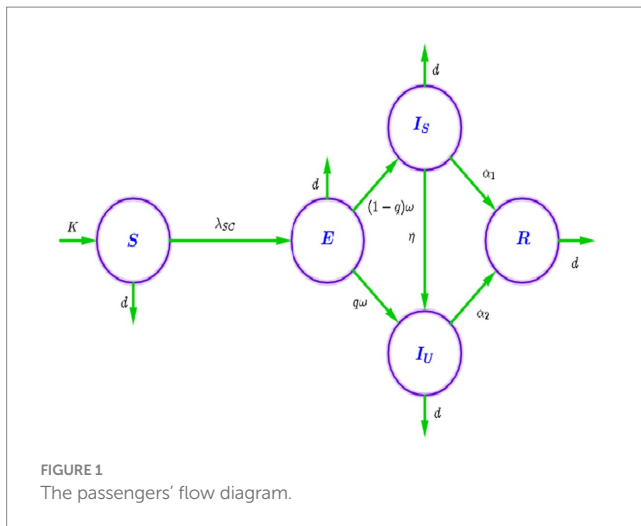
in section 3. The local stability of the negative attitude free equilibrium point is addressed in theorem 3, while the global stability of equilibrium points is illustrated in theorems 5 and 6.

4 Optimal control problem

The negative attitude of rail passengers is a complex behavior that can be influenced by various factors. In the context of unreliable train operations and safety concerns, it is important to address this negative attitude to improve the overall passenger experience.

The prevention control strategy aims to reduce the number of susceptible passengers by addressing the factors contributing to negative attitudes. For example, improving train operations and implementing safety measures can help create a positive passenger experience and reduce the likelihood of developing negative attitudes. By focusing on prevention, the goal is to minimize the number of passengers who become exposed to negative attitudes and subsequently develop negative attitudes.

On the other hand, the improvement control strategy focuses on addressing the negative attitudes of passengers who developed negative attitudes and helping them to change their attitudes. Assisting in the process of changing their negative attitudes can be done through various measures, such as providing information, assistance, and support to passengers who have developed negative attitudes. By actively addressing and improving these negative attitudes, the goal is to facilitate the process of changing their negative attitudes and ultimately reducing the overall number of passengers who develop negative attitudes.

By combining both prevention and improvement control strategies, the researchers proposed a comprehensive approach to managing rail passengers' negative attitudes. This approach acknowledges the importance of addressing the root causes of negative attitudes through prevention while recognizing the need to support and improve the attitudes of those who have already developed negative attitudes. Through this control design, the researchers aimed to create a positive rail travel experience for passengers, which in turn can enhance customer satisfaction and loyalty.

We presented three control strategies that depend on time and are designed to modify the fractional order model (Equation 11). These strategies are represented by the Lebesgue controlling functions $u_1(t)$, $u_2(t)$, and $u_3(t)$, with $0 \le u_1(t), u_2(t), u_3(t) \le 1$.

These functions serve as measures of control and are defined as follows:

1. The measure to prevent passengers' negative attitudes is aimed at minimizing the effective contact rate, and it is represented by the control measure $u_1(t)$. This measure involves taking actions to enhance the management of congestion during train operations and improve the daily operation of trains by ensuring punctuality and regularity.
2. The time-dependent control measures represented by $u_2(t)$ and $u_3(t)$ are improvement strategies for passengers who developed negative attitudes as a result of safety concerns and unreliable train operations, respectively.

The new reformulation of the Caputo fractional order model's optimal control problem (Equation 11) is based on the control variables mentioned earlier.

$$^C D_t^\vartheta S = K^\vartheta - \left(\left(1-u_1(t)\right) \frac{\beta^\vartheta \left(\rho_1^\vartheta I_s + \rho_2^\vartheta I_U\right)}{M} + d^\vartheta \right) S$$

$$^C D_t^\vartheta E = \left(1-u_1(t)\right) \frac{\beta^\vartheta \left(\rho_1^\vartheta I_s + \rho_2^\vartheta I_U\right)}{M} - \left(d^\vartheta + \varpi^\vartheta\right) E$$

$$^C D_t^\vartheta I_s = \left(1-q^\vartheta\right) \varpi^\vartheta E - \left(d^\vartheta + \eta^\vartheta + u_2(t)\alpha_1^\vartheta\right) I_s$$

$$^C D_t^\vartheta I_U = q^\vartheta \varpi^\vartheta E + \eta^\vartheta N_s - \left(d^\vartheta + u_3(t)\alpha_2^\vartheta\right) I_U$$

$$^C D_t^\vartheta R = u_2(t)\alpha_1^\vartheta I_s + u_3(t)\alpha_2^\vartheta I_U - d^\vartheta R \qquad (13)$$

with initial data $S(0) > 0$, $E(0) \ge 0, I_S(0) \ge 0$, $I_U(0) \ge 0$, and $R(0) \ge 0$, and the controlling set is $\Delta_C = \left\{ \left(u_1(t), u_2(t), u_3(t)\right) : 0 \le u_1(t), u_2(t), u_3(t) \le 1, t \in \left[0, T_f\right] \right\}$, where T_f is the final time of implementing control measures.

The aim of the control problem is to minimize the number of people who are exposed to and develop negative attitudes while increasing the number of individuals whose negative attitudes change, taking into account the cost of implementing control strategies. To achieve this, we formulated an objective function that represents the goal of reducing the number of individuals who have already developed negative attitudes in the population.

$$J\left(u_1, u_2, u_3\right) = \int_0^{T_f} \left(\chi_1 E + \chi_2 I_S + \chi_3 I_U + \frac{\Gamma_1}{2} u_1^2 + \frac{\Gamma_2}{2} u_2^2 + \frac{\Gamma_3}{2} u_3^2 \right) dt \qquad (14)$$

To manage the number of individuals who developed negative attitudes and the associated costs of implementing prevention and improvement control strategies, we strived to minimize $u_1(t), u_2(t)$, and $u_3(t)$ while considering the system (Equation 14) as a constraint.

In this section, the value T_f represents the final time, while the coefficients χ_1, χ_2, and χ_3 are positive weight constants. The measures $\frac{\Gamma_1}{2}, \frac{\Gamma_2}{2}$, and $\frac{\Gamma_3}{2}$ represent the relative costs of prevention

and improvement corresponding to the controls $u_1, u_2,$ and u_3, respectively. Additionally, these measures help to balance the units of the integrand.

The objective is to locate the optimal values for the controls $U = (u_1, u_2, u_3)$, denoted as $U^* = (u_1^*, u_2^*, u_3^*)$, to achieve the desired state trajectories $S^*, E^*, I_S^*, I_U^*,$ and R^* that are solutions of (Equation 14) over a given time interval $[0, T_f]$. These state trajectories should also satisfy the initial data and minimize the objective function.

In the cost functional, the term $\chi_1 E$ represents the cost related to individuals exposed to negative attitudes, the term $\chi_2 I_S$ refers to the cost related to individuals who developed negative attitudes due to safety concerns, and the term $\chi_3 I_U$ represents the cost related to individuals who developed negative attitudes due to unreliable train operation.

Additionally, χ_i (where $i = 1, 2, 3$) are positive constants that represent the cost of implementing the three strategies to control, and Γ_i (where $i = 1, 2, 3$) is the corresponding effort made to minimize the dissemination of negative attitudes toward these strategies. T_f represents the duration for which the control measures are applied.

The aim is to determine the optimal control variable $u(t)$ that minimizes the objective function $\min_{\bar{u} \in \bar{U}} J(\bar{u})$, which is subject to the new optimal control dynamical system given in Equation 13 with the initial data.

The vector $\bar{u} = \{u_1, u_2, u_3)$ is the vector that controls the system, and the set

$$\bar{U} = \left\{ \bar{u} \in \left(L^\infty \left([0, T_f] \right) \right)^3, 0 \le u_i \le 1, i = 1, 2, 3, \right\} \quad (15)$$

is a closed and bounded set of controls that are admissible.

4.1 Existence and optimality of the control strategies

The fractional order dynamical system (Equation 11) with (Equation 12) can be rewritten as follows:

$$C_{D_t^\vartheta} Y = G(t, Y(t)) + H(t, Y(t)) \bar{u}, 0 \le t \le T_f,$$

$$Y(t) = Y_0, \quad \text{where} \quad Y(t) = (S(t), E(t), I_S(t), I_U(t), R(t))$$

represents the state variables of the dynamical system, and $u(t) = (u_1(t), u_2(t), u_3(t)$ represents the control functions or variables in the control problem mentioned in Equation 13. The functions G and H are given as follows:

$$G(t, Y(t)) = \begin{bmatrix} K^\vartheta - \left(\dfrac{\beta^\vartheta \left(\rho_1^\vartheta I_S + \rho_2^\vartheta I_U \right)}{M} + d^\vartheta \right) S \\ \dfrac{\beta^\vartheta \left(\rho_1^\vartheta I_S + \rho_2^\vartheta I_U \right)}{M} S - \left(d^\vartheta + \varpi^\vartheta \right) E \\ \left(1 - q^\vartheta \right) \varpi^\vartheta E - \left(d^\vartheta + \eta^\vartheta \right) I_S \\ q^\vartheta \varpi^\vartheta E + \eta^\vartheta I_S - \left(d^\vartheta \right) I_U \\ -d^\vartheta R \end{bmatrix}$$

$$H(t, Y(t)) = \begin{bmatrix} \dfrac{\beta^\vartheta \left(\rho_1^\vartheta I_S + \rho_2^\vartheta I_U \right)}{M} S & 0 & 0 \\ -\dfrac{\beta^\vartheta \left(\rho_1^\vartheta I_S + \rho_2^\vartheta I_U \right)}{M} S & 0 & 0 \\ 0 & -\alpha_1^\vartheta I_S & 0 \\ 0 & 0 & -\alpha_2^\vartheta I_U \\ 0 & \alpha_1^\vartheta I_S & \alpha_1^\vartheta I_S \end{bmatrix}$$

To establish the existence of the three optimal control strategies, we need to verify the following conditions:

- The control trajectories have at least one feasible solution.
- The set of admissible controls is convex, bounded, and closed.
- The function represented by $G(t, Y(t)) + H(t, Y(t))$ is bounded with respect to both the state variables and the controlling variables.
- The expression $\chi_1 E + \chi_2 I_S + \chi_3 I_U + \dfrac{\Gamma_1}{2} u_1^2 + \dfrac{\Gamma_2}{2} u_2^2 + \dfrac{\Gamma_3}{2} u_3^2$ is convex on the set of admissible controls $\bar{U}$.

According to the definitions mentioned in the manuscript, the conditions can be expressed as follows:

If we consider control functions with values $u_1 = 1, \quad u_2 = 0,$ and $u_3 = 0$ within the admissible control set $\bar{U}$ defined in Equation 15 and the solution $Y = (S, E, I_S, I_U, R)$ of the fractional order model (Equation 11) with given initial data, then the set of all feasible solutions for the control problem is not empty. Furthermore, based on the definition of the admissible control set $\bar{U}$, this control set is bounded, closed, and convex. Additionally, according to the existence and uniqueness criteria for model (Equation 11), the solutions of model (Equation 13) are unique and bounded because $0 \le u_i \le 1$, for $i = 1, 2, 3$.

Theorem 7: The function defined by $G(t, Y(t)) + H(t, Y(t)) \bar{u}$ satisfies the solution.

$\bar{Y} = (S, E, I_A, I_C, R)$ such that

$$\| G(t, \bar{Y}) + H(t, \bar{Y}) \| \le \max(k_1, k_2) \left(\| \bar{Y} \| + \| \bar{u} \| \right) \quad (16)$$

where $k_1 = \max \begin{pmatrix} 1 + \beta^\vartheta \left(\rho_1^\vartheta + \rho_2^\vartheta \right) + d^\vartheta, d^\vartheta + \varpi^\vartheta, d^\vartheta \\ + d_1^\vartheta + \eta^\vartheta + \alpha_1^\vartheta, d^\vartheta + d_2^\vartheta + \alpha_2^\vartheta, d^\vartheta \end{pmatrix},$

and $k_2 = \max \left(\beta^\vartheta \left(\rho_1^\vartheta + \rho_2^\vartheta \right), \eta^\vartheta, 1 \right)$.

Proof: Let us consider the matrix $G(t, Y(t))$ in a rewritten form.

$$G(t, Y(t)) = \begin{bmatrix} D & 0 & 0 & 0 & 0 \\ \dfrac{\beta^\vartheta \left(\rho_1^\vartheta I_A + \rho_2^\vartheta I_C \right)}{M} & -\left(d^\vartheta + \varpi^\vartheta \right) & 0 & 0 & 0 \\ 0 & \left(1 - q^\vartheta \right) \varpi^\vartheta & \left(d^\vartheta + d_1^\vartheta + \eta^\vartheta + \alpha_1^\vartheta \right) & 0 & 0 \\ 0 & q^\vartheta \varpi^\vartheta & \eta^\vartheta & \left(d^\vartheta + d_2^\vartheta + \alpha_2^\vartheta \right) & 0 \\ 0 & 0 & \alpha_1^\vartheta & \alpha_2^\vartheta & -d^\vartheta \end{bmatrix} \begin{bmatrix} S \\ E \\ I_S \\ I_U \\ R \end{bmatrix},$$

where $D = \dfrac{K^\vartheta}{S} - \dfrac{\beta^\vartheta\left(\rho_1^\vartheta I_S + \rho_2^\vartheta I_U\right)}{M}$.

Given the definition of the matrix $G\left(t, Y(t)\right)$, we can see that $K^\vartheta \leq S$. Additionally, considering the bounded nature of the solution, we demonstrate that

$$\| G\left(t,\overline{Y}\right)\| \leq \max\begin{pmatrix} 1 + \beta^\vartheta\left(\rho_1^\vartheta + \rho_2^\vartheta\right) + d^\vartheta, d^\vartheta + \varpi^\vartheta, d^\vartheta \\ + d_1^\vartheta + \eta^\vartheta + \alpha_1^\vartheta, d^\vartheta + d_2^\vartheta + \alpha_2^\vartheta, d^\vartheta \end{pmatrix}\|\overline{Y}\|$$

By employing a similar procedure, we can demonstrate the following:

$$\| G\left(t,\overline{Y}\right)\| \leq \max\left(\beta^\vartheta\left(\rho_1^\vartheta + \rho_2^\vartheta\right), \eta^\vartheta, 1\right)\|\overline{u}\|.$$

Theorem 8: The function expressed as $\mathbb{V}\left(t,\overline{Y},\overline{u}\right) = \chi_1 E + \chi_2 I_S + \chi_3 I_U + \dfrac{\Gamma_1}{2}u_1^2 + \dfrac{\Gamma_2}{2}u_2^2 + \dfrac{\Gamma_3}{2}u_3^2$ is convex within the admissible control region $\overline{U}$, and there exists a non-negative constant k such that $\mathbb{V}\left(t,\overline{Y},\overline{u}\right) \geq k\overline{u}$.

Proof: For the function $\mathbb{V}\left(t,\overline{Y},\overline{u}\right)$, we derived the corresponding Hessian matrix given by

$$\mathbb{H} = \begin{bmatrix} 2u_1 & 0 & 0 \\ 0 & 2u_2 & 0 \\ 0 & 0 & 2u_3 \end{bmatrix}.$$

Therefore, the matrix $\mathbb{H}$ is a positive definite matrix in the admissible control region $\overline{U}$ and hence $\mathbb{V}\left(t,\overline{Y},\overline{u}\right)$ is strictly convex in U. Let $k = \min\left(\dfrac{\Gamma_1}{2}, \dfrac{\Gamma_2}{2}, \dfrac{\Gamma_3}{2}\right)$, then

$$\mathbb{V}\left(t,\overline{Y},\overline{u}\right) = \chi_1 E + \chi_2 I_S + \chi_3 I_U + \dfrac{\Gamma_1}{2}u_1^2 + \dfrac{\Gamma_2}{2}u_2^2 + \dfrac{\Gamma_3}{2}u_3^2$$
$$\geq \dfrac{\Gamma_1}{2}u_1^2 + \dfrac{\Gamma_2}{2}u_2^2 + \dfrac{\Gamma_3}{2}u_3^2 \geq k\left(\dfrac{\Gamma_1}{2}u_1^2 + \dfrac{\Gamma_2}{2}u_2^2 + \dfrac{\Gamma_3}{2}u_3^2\right) \quad. \quad \text{Thus,}$$

we established the proof.

Theorem 9: There is an optimal control point $\overline{u}^* = \left(u_1^*, u_2^*, u_3^*\right)$ and the model-associated solutions

$$\overline{Y}^* = \left(S^*, E^*, N_S^*, N_R^*, R^*\right) \text{ that minimize the objective function}$$

$J\left(\overline{u}\right)$ on the admissible control set $\overline{U}$, such that $\min_{\overline{u} \in \overline{U}} J\left(\overline{u}\right) = J\left(\overline{u}^*\right)$.

The optimality necessary condition: The optimality necessary condition, as stated in Teklu and Terefe (26), is required to be fulfilled by the optimal control problem (Equation 13), and Equation 14 is adapted from Pontryagin's maximum principle stated in Mandal et al. (13), Ahmed et al. (16), and Teklu and Terefe (27), and it is also fulfilled by changing into a minimizing Hamiltonian function with respect to the control variables $\left(u_1, u_2, u_3\right)$. The Hamiltonian function corresponding to Equations 13 and 14 is derived as follows:

$$H\left(\overline{Y}, \overline{u}, K^\vartheta\right) =$$
$$\chi_1 E + \chi_2 I_S + \chi_3 I_U +$$
$$\dfrac{\Gamma_1}{2}u_1^2 + \dfrac{\Gamma_2}{2}u_2^2 + \dfrac{\Gamma_3}{2}u_3^2 + \lambda_1$$
$$\left(K^\vartheta - \left(\dfrac{\left(1 - u_1(t)\right)\beta^\vartheta\left(\rho_1^\vartheta I_S + \rho_2^\vartheta I_U\right)}{M} + d^\vartheta\right)S\right)$$
$$+ \lambda_2\left(\dfrac{\left(1 - u_1(t)\right)\beta^\vartheta\left(\rho_1^\vartheta I_S + \rho_2^\vartheta I_U\right)}{M} - \left(d^\vartheta + \varpi^\vartheta\right)E\right)$$
$$+ \lambda_3\left(\left(1 - q^\vartheta\right)\varpi^\vartheta E - \left(d^\vartheta + d_1^\vartheta + \eta^\vartheta + u_2(t)\alpha_1^\vartheta\right)I_S\right)$$
$$+ \lambda_4\left(q^\vartheta\varpi^\vartheta E + \eta^\vartheta I_S - \left(d^\vartheta + d_2^\vartheta + u_3(t)\alpha_2^\vartheta\right)I_U\right)$$
$$+ \lambda_5\left(u_2(t)\alpha_1^\vartheta I_S + u_3(t)\alpha_2^\vartheta I_U - d^\vartheta R\right)$$

$$(17)$$

where $\lambda_1(t), \lambda_2(t), \lambda_3(t), \lambda_4(t)$, and $\lambda_5(t)$ are the co-state variables or adjoint variables.

Theorem 10: Let us give the optimal control solutions u_i^* for $i = 1, 2, 3$ and the solutions of the optimal control problem (Equation 13) that minimize the objective function (Equation 15) in the admissible control region $\overline{U}$, then there are functions $\lambda_1, \lambda_2, \lambda_3, \lambda_4$, and λ_5 such that

$${}^C_{D_t^\vartheta}\lambda_1 = \left(\lambda_1 - \lambda_2\right)\left(1 - u_1\right)\dfrac{\beta^\vartheta\left(\rho_1^\vartheta I_S + \rho_2^\vartheta I_U\right)}{M}\left(1 - \dfrac{S}{M}\right) + d^\vartheta\lambda_1$$

$${}^C_{D_t^\vartheta}\lambda_2 = \left(\lambda_2 - \lambda_1\right)\left(1 - u_1\right)\dfrac{\beta^\vartheta\left(\rho_1^\vartheta I_S + \rho_2^\vartheta I_U\right)S}{M^2} + \lambda_2\left(d^\vartheta + \varpi^\vartheta\right) - \lambda_3\left(1 - q^\vartheta\right)\varpi^\vartheta - \lambda_4 q^\vartheta\varpi^\vartheta - \chi_1$$

$${}^C_{D_t^\vartheta}\lambda_3 = \left(\lambda_2 - \lambda_1\right)\left(1 - u_1\right)\left(\dfrac{\beta^\vartheta\left(\rho_1^\vartheta I_S + \rho_2^\vartheta I_U\right)S}{M^2} - \beta^\vartheta\rho_1^\vartheta\dfrac{S}{M}\right)$$
$$+ \left(\lambda_3 - \lambda_4\right)\left(\eta^\vartheta + u_2\right) + \lambda_3 B + \lambda_4\alpha_1^\vartheta - \chi_2$$

$$C_{D_t^\vartheta} \lambda_4 = (\lambda_2 - \lambda_1)(1 - u_1)\left(\frac{\beta^\vartheta (\rho_1^\vartheta I_S + \rho_2^\vartheta I_U) S}{M^2} - \beta^\vartheta \rho_2^\vartheta \frac{S}{M} \right) + (\lambda_4 - \lambda_5)(\alpha_2^\vartheta + u_3) + \lambda_4 (d^\vartheta) - \chi_3$$

$$C_{D_t^\vartheta} \lambda_5 = (\lambda_2 - \lambda_1)(1 - u_1) \frac{\beta^\vartheta (\rho_1^\vartheta I_S + \rho_2^\vartheta I_U) S}{M^2} + \lambda_5 d^\vartheta \qquad (18)$$

where $B = \left(d^\vartheta + \alpha_1^\vartheta \right)$.

The conditions for the transversality of the system (Equation 18) can be expressed as $\lambda_i^*(T_f) = 0$, $i = 1, 2, \ldots, 5$. These conditions are based on the Hamiltonian function H defined mentioned in Equation 17. Additionally, the optimal control strategy can be determined by

$$u_1^*(t) = \min\left\{ 1, \max[0, \frac{(\lambda_1 - \lambda_2)}{\Gamma_1} \frac{\beta^\vartheta (\rho_1^\vartheta I_S + \rho_2^\vartheta I_U) S}{M} \right\}$$

$$u_2^*(t) = \min\left\{ 1, \max[0, \frac{(\lambda_3 - \lambda_5)}{\Gamma_2} N_S \right\}$$

$$u_2^*(t) = \min\left\{ 1, \max[0, \frac{(\lambda_4 - \lambda_5)}{\Gamma_3} N_R \right\}$$

where $\lambda_1(t), \lambda_2(t), \lambda_3(t), \lambda_4(t), \lambda_5(t)$, and $\lambda_6(t)$ are the co-state variables or adjoint variables and the conditions for transversality that are mentioned earlier.

Proof: The existence of the co-state variables $\lambda_1(t), \lambda_2(t), \lambda_3(t), \lambda_4(t), \lambda_5(t)$ is demonstrated by applying Pontryagin's maximal principle, as shown in reference (15, 28). Furthermore, the characterization of each optimal control strategy outlined in Equation 13 is achieved by solving the following set of partial differential equations within the interior of the admissible control set $\bar{U}$ as follows:

$$\frac{\partial H}{\partial u_1} = \frac{\partial H}{\partial u_2} = \frac{\partial H}{\partial u_3} = 0. \qquad (19)$$

5 Numerical simulation

In this section, we conducted numerical simulations of model (Equation 11) and control problem (Equation 13) to gain a deeper understanding of the system's behavior and pinpoint the most efficient optimal control strategies that influence the evolution of passengers' attitudes. These simulations yield visualizations, enhancing our intuitive grasp of how different factors affect the transmission dynamics and serving as valuable tools for scenario evaluation. We utilized the ODE45 solver in MATLAB 2023a for numerical simulations to capture the dynamics of the passengers' attitude model.

This solver, belonging to the second-order Runge–Kutta family of methods and utilizing either the Euler forward or backward finite difference method, is chosen for its ability to generate accurate and reliable results (29).

5.1 Numerical simulations to show the effect of changing fractional order

Some values of the fractional order ϑ are taken to check the performance of the proposed model. The simulation curve illustrated in Figures 2A-D indicates how changes in fractional order affect the negative attitudes of passengers toward railway transportation. Based on the results of Figure 2, it can be observed that, when the fractional order decreases, there is a decrease in the numbers of exposed passengers and passengers with negative attitudes due to safety concerns and unreliable train operations. These changes are attributed to the memory effect.

Moreover, decreasing fractional order leads to an increase in the number of passengers whose negative attitudes toward railway transportation have changed. This indicates that the fractional order model yields better model accuracy than the integer order model.

5.2 Numerical simulation of the optimal control problem

To assess the effects of controlling strategies and validate the analytical findings of the fractional order optimal control problem, we conducted a numerical simulation (Equation 13) using MATLAB 2023a programming codes.

We employed the Euler forward or/and backward finite difference method for the simulation, using different initial conditions and assuming specific baseline parameter values to be $\chi_1 = \chi_2 = \chi_3 = 32$, $\Gamma_1 = 40$, $\Gamma_2 = 43$, $\Gamma_3 = 48$, $q = 0.5$, $\beta = 0.38$, $\eta = 0.34$, $d_2 = 0.2$, $d = 0.23$, $K = 100$, $\varpi = 0.4$, $\alpha_1 = 0.45$, and $\alpha_2 = 0.38$. In this subsection, we conducted a numerical simulation using the Euler forward method to investigate the impact of controlling strategies on the state variables in the optimal control problem (Equation 13). We assumed that the order of the derivative is $\vartheta = 0.96$.

Figures 3–5 in the numerical simulations demonstrated the importance of control strategies in addressing the dissemination of negative attitudes among passengers in the community. We considered optimal controlling strategies to showcase the impact of protection and improvement measures on reducing transmission rates. The first strategy involves implementing only the protection strategy (u_1). The second strategy focuses solely on the improvement of the attitudes individuals (u_2) who developed negative attitudes due to safety concerns. The third strategy targets the improvement of the attitudes of individuals (u_3) who developed negative attitudes due to unreliable train operation. The fourth strategy combines both improvement strategies (u_2 and u_3) simultaneously, and finally, the fifth strategy involves implementing all of the controlling strategies (u_1, u_2, and u_3) together.

5.2.1 Effect of protection ($u_1 \neq 0$)

In this sub-section, we conducted a numerical simulation under two conditions: one without applying improvement-controlling
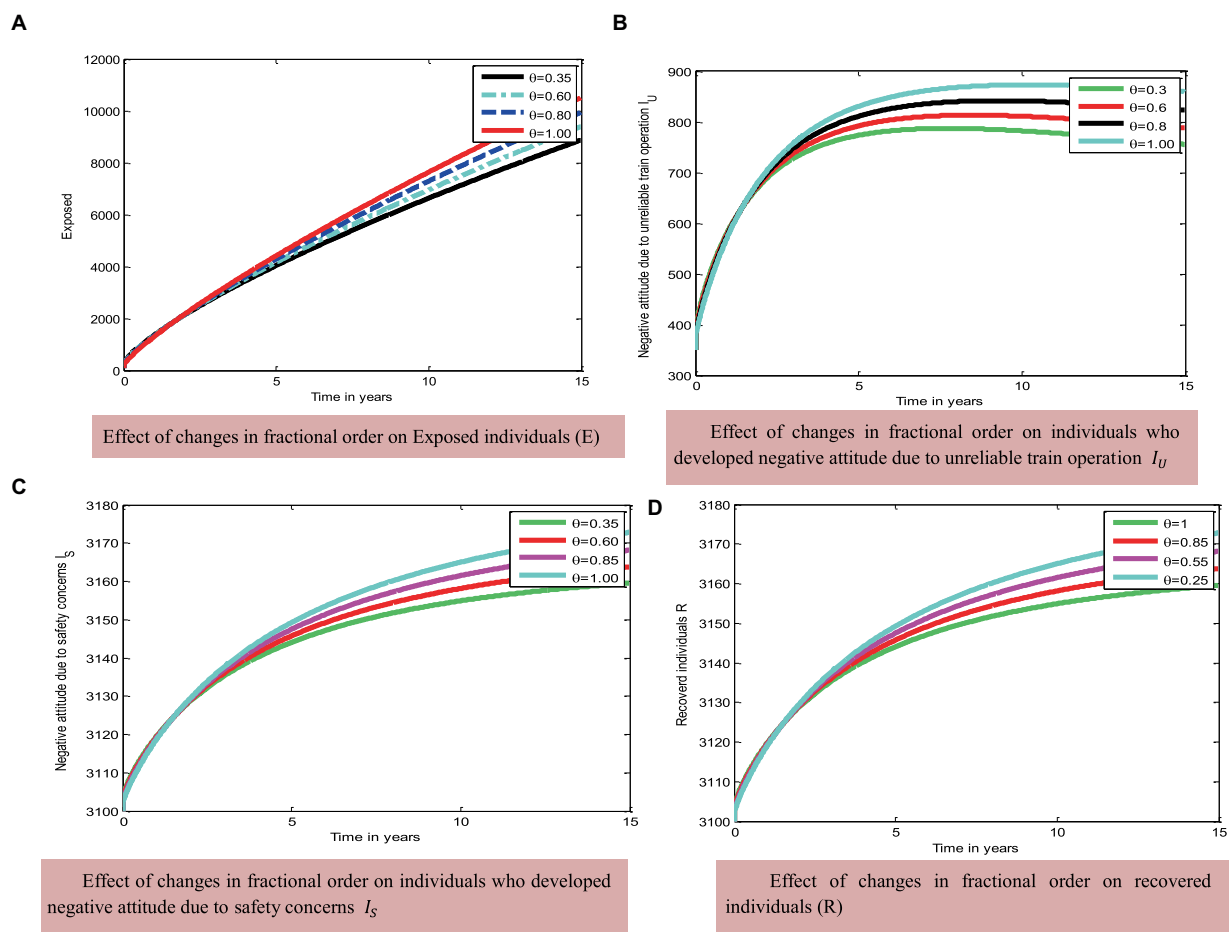
A Effect of changes in fractional order on Exposed individuals (E)

B Effect of changes in fractional order on individuals who developed negative attitude due to unreliable train operation I_U

C Effect of changes in fractional order on individuals who developed negative attitude due to safety concerns I_S

D Effect of changes in fractional order on recovered individuals (R)

FIGURE 2
Effect of fractional order on the status of the state variables.

strategies and the other with the implementation of a preventive strategy (Strategy 1), that is, by setting $u_1 \neq 0$, $u_2 = 0$, and $u_3 = 0$ while also considering the value $\vartheta = 0.96$. The graphical representation in Figure 3 that illustrates the influence of the prevention strategy on the dynamics of passengers' transmission of negative attitudes shows that implementing the controlling strategy u_1 significantly decreases the exposed passengers, the passengers who developed negative attitudes due to safety concerns, and the passengers who developed negative attitudes due to unreliable train operation, while there was an increase in the number of susceptible passengers and in the number of passengers whose negative attitudes changed.

5.2.2 Effect of improvement strategies ($u_2 \neq 0$ and $u_3 \neq 0$)

In this subsection, we performed numerical simulations without applying a protection control strategy (u_1) and applying the improvement strategies ($u_2 \neq 0$ and $u_3 \neq 0$). From the simulation illustrated by Figure 4B shows that individuals in the exposed class are reduced slightly as compared to Figure 3B, but passengers who developed negative attitudes due to safety concerns and the passengers who developed negative attitudes due to unreliable train operation are reduced rapidly compared to the first similar classes.

5.2.3 Effect of protection and improvement strategies ($u_1 \neq 0, u_2 \neq 0$, and $u_3 \neq 0$)

In this subsection, we performed numerical simulations without applying all controlling strategies in place and by applying all possible controlling strategies ($u_1 \neq 0, u_2 \neq 0$, and $u_3 \neq 0$) simultaneously.

Here, we can compare the impact of implementing the different control strategies on the emergence of negative attitudes. Figure 5A demonstrates that implementing all proposed control strategies significantly increases the number of susceptible individuals compared to the numbers shown in Figures 3A, 4A. Additionally, Figure 5B illustrates that all proposed controlling strategies greatly decrease the number of exposed individuals compared to the number of exposed individuals illustrated in Figures 3B, 4B. Furthermore, Figure 5C reveals that all proposed controlling strategies have a considerable impact on reducing the number of passengers who developed negative attitudes compared to the numbers in Figures 3C,D, 4C. Finally, in Figure 5D, implementing all proposed strategies notably increases the number of individuals whose negative attitudes changed compared to the number of individuals whose negative attitudes changed as illustrated in Figures 3E, 4D. Ultimately, it is observed from Figure 5 that applying all possible controlling strategies ($u_1 \neq 0, u_2 \neq 0$, and $u_3 \neq 0$)
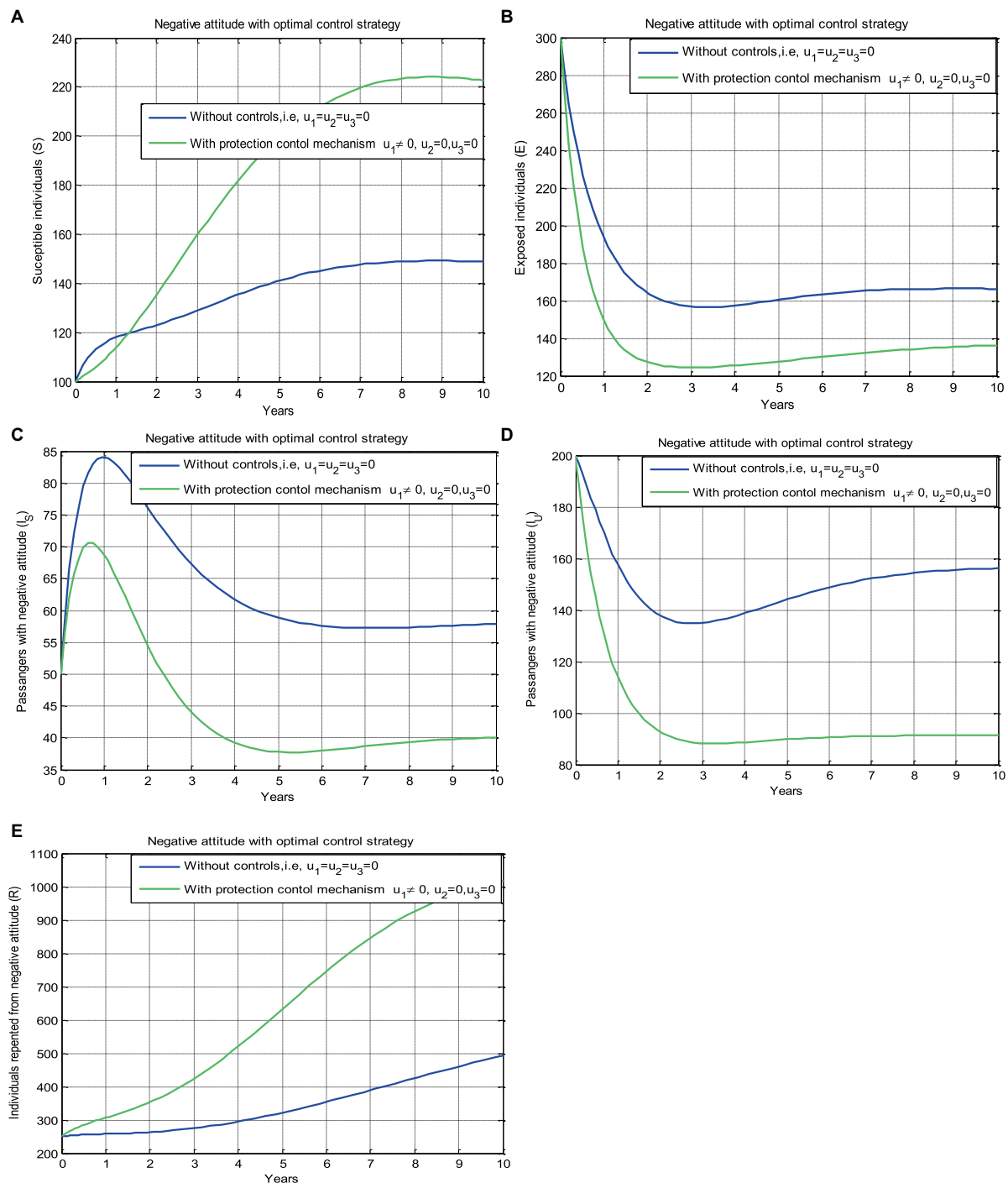
FIGURE 3
Effect of the prevention strategy (u_1) on the negative attitude status of different population groups with $\vartheta = 0.96$.

simultaneously leads to a significant reduction in the number of passengers who develop negative attitudes in the community after 10 years. When compared to other strategies, implementing protection alone or improvement strategies alone, both protection and improvement strategies together is the most effective strategy in addressing the evolution of negative attitudes due to unreliable train operations or safety concerns among passengers in the community.

6 Conclusion

In this study, the dynamics of passengers who developed negative attitudes by applying the Caputo fractional order derivative approach whenever the fractional order $\vartheta = 0.96$ is presented. Some fundamental proprieties of the solutions of the proposed fractional order model, such as existence, uniqueness, positivity, and boundedness, are analyzed. We derived the formula for the model's
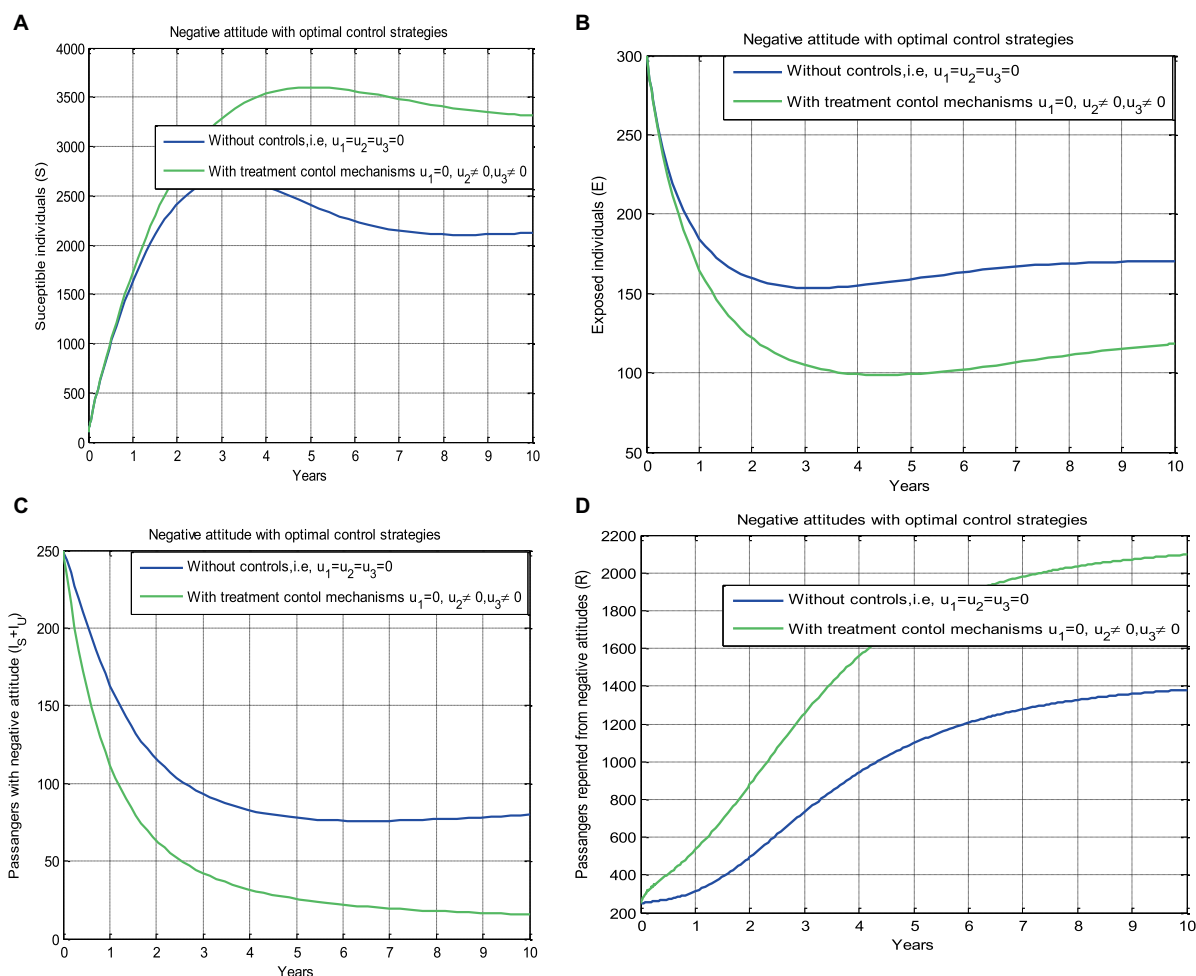
FIGURE 4
Effect of the improvement strategies [u_2 and (u_3)] on the negative attitude status of different population groups with ϑ=0.96.

basic reproduction number using the next-generation operator approach. Using the stability criteria for the fractional order model, we analyzed the results of the stability of the proposed model with respect to the basic reproduction number. We examined the local and global asymptotical stability of the negative attitude-free equilibrium points whenever the corresponding basic reproduction number is less than unity.

Moreover, we carried out the local and global stability of the negative attitude endemic equilibrium point of the model. We formulated and analyzed the corresponding optimal control problem for the fractional order model by incorporating three time-dependent control strategies: prevention measures, improvement measures for negative attitudes due to safety concerns, and improvement measures for negative attitudes due to unreliable train operation by applying the Pontryagin's maximum principle. Moreover, using the well-known Euler's forward or/and backward finite difference numerical methods, we established the results of the numerical simulation of the proposed optimal control problem. From the results of the numerical simulation given in Figure 5, we concluded that applying all possible controlling strategies $(u_1 \neq 0, u_2 \neq 0,$ and $u_3 \neq 0)$ simultaneously greatly decreases the number of passengers who developed negative attitudes in the community after a decade. Strategy 4 is the most

effective strategy to tackle the disseminating rate of passengers' negative attitudes throughout the community compared to other strategies.

Finally, as this study is not comprehensive, other researchers in the field have the opportunity to enhance the proposed model by including additional factors such as a stochastic approach, considering the age structure of passengers and refining the model with relevant real-world data.

Data availability statement

The original contributions presented in the study are included in the article/Supplementary material, further inquiries can be directed to the corresponding author.

Author contributions

GH: Conceptualization, Formal analysis, Investigation, Methodology, Resources, Software, Supervision, Validation, Visualization, Writing – original draft, Writing – review & editing. ST: Conceptualization, Formal analysis, Investigation, Methodology,
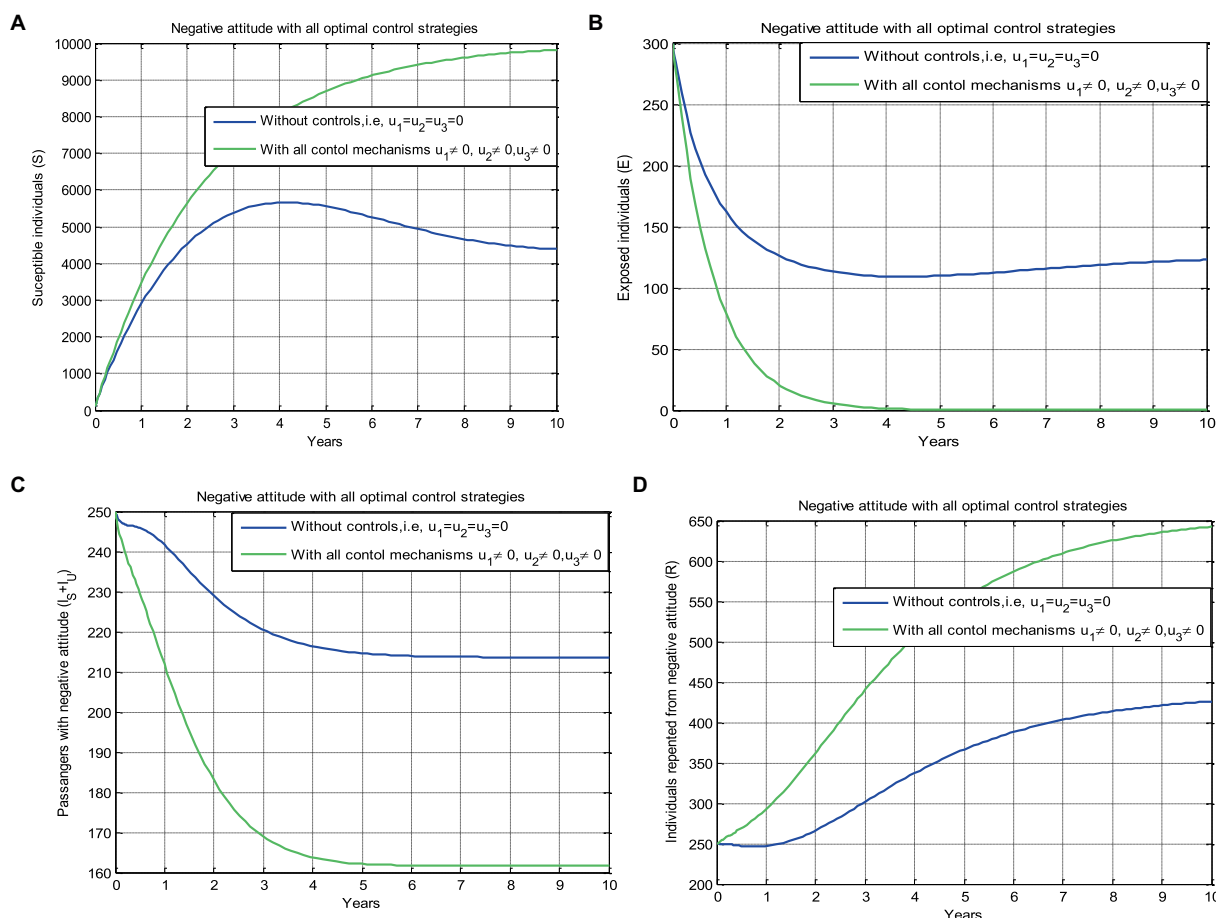
FIGURE 5
Effect of all the control strategies ($u_1 = 0$ $u_2 = 0$ and $u_3 = 0$) simultaneously on the passengers' negative attitude status of different population groups with $\vartheta = 0.96$.

Resources, Software, Supervision, Validation, Visualization, Writing – original draft, Writing – review & editing.

Funding

Conflict of interest

The authors declare that the research was conducted in the absence of any commercial or financial relationships that could be construed as a potential conflict of interest.

Publisher's note

Supplementary material

The Supplementary material for this article can be found online at: https://www.frontiersin.org/articles/10.3389/fams.2024.1290494/full#supplementary-material

References

1. Alemu A. Success factors and challenges of railway megaprojects in Ethiopia. *J Bus Adm Stud* (2016) 8:1.

2. Berger A, Hoffmann R, Lorenz U, Stiller S. Online railway delay management: hardness, simulation and computation. *Simulation* (2011) 87:616–29. doi: 10.1177/0037549710373571

3. Dziekan K. (2008). *Ease-of-use in Public Transportation: A User Perspective on Information and Orientation Aspects*. Stockholm, Sweden: Royal Institute of Technology.

4. Cheng YH. Exploring passenger anxiety associated with train travel. *Transportation* (2010) 37:875–96. doi: 10.1007/s11116-010-9267-z

5. Currie G, Muir C. Understanding passenger perceptions and behaviors during unplanned rail disruptions. *Transp Res Procedia* (2017) 25:4392–402. doi: 10.1016/j.trpro.2017.05.322

6. Marteache N, Bichler G, Enriquez J. Mind the gap: perceptions of passenger aggression and train car supervision in a commuter rail system. *J Public Transp* (2015) 18:61–73. doi: 10.5038/2375-0901.18.2.5

7. Kuo T, Chen CT, Cheng WJ. Service quality evaluation: moderating influences of first-time and revisiting customers. *Total Qual Manag Bus Excell* (2018) 29:429–40. doi: 10.1080/14783363.2016.1209405

8. Din A, Khan FM, Khan ZU, Yusuf A, Munir T. The mathematical study of climate change model under nonlocal fractional derivative. *Partial Differ Equ Appl Math* (2022) 5:100204. doi: 10.1016/j.padiff.2021.100204

9. Sene N. Analytical solutions of a class of fluids models with the Caputo fractional derivative. *Fractal Fract* (2022) 6, 3–8. doi: 10.3390/fractalfract6010035

10. Ghosh U, Pal S, Banerjee M. Memory effect on Bazykin's prey-predator model: stability and bifurcation analysis. *Chaos, Solitons Fractals* (2021) 143, 3–14. doi: 10.1016/j.chaos.2020.110531

11. de Barros LC, Lopes MM, Pedro FS, Esmi E, dos Santos JPC, Sánchez DE. The memory effect on fractional calculus: an application in the spread of COVID-19. *Comput Appl Math* (2021) 40:4–5. doi: 10.1007/s40314-021-01456-z

12. Podlubny I. *Fractional Differential Equations: An Introduction to Fractional Derivatives, Fractional Differential Equations, to Methods of Their Solution and Some of Their Applications*, vol. 198. San Diego, California, USA: Academic Press. (1999).

13. Mandal M, Jana S, Nandi SK, Kar TK. Modelling and control of a fractional-order epidemic model with fear effect. *Energy Ecol Environ* (2020) 5:421–32. doi: 10.1007/s40974-020-00192-0

14. Matignon D. Stability results for fractional differential equations with applications to control processing. *Comput Eng Syst Appl* (1996).

15. Teklu SW. Analysis of fractional order model on higher institution students' anxiety towards mathematics with optimal control theory. *Sci Rep* (2023) 13:6867. doi: 10.1038/s41598-023-33961-y

16. Ahmed E, El-Sayed AMA, El-Saka HAA. On some Routh-Hurwitz conditions for fractional order differential equations and their applications in Lorenz, Rössler, Chua and Chen systems. *Phys Lett Sect A Gen At Solid State Phys* (2006) 358:1–4. doi: 10.1016/j.physleta.2006.04.087

17. Vargas-De-León C. Volterra-type Lyapunov functions for fractional-order epidemic systems. *Commun Nonlinear Sci Numer Simul* (2015) 24:75–85. doi: 10.1016/j.cnsns.2014.12.013

18. Bhalekar S, Patil M. Singular points in the solution trajectories of fractional order dynamical systems. *Chaos* (2018) 28:113123. doi: 10.1063/1.5054630

19. Echenausía-Monroy JL, Gilardi-Velázquez HE, Jaimes-Reátegui R, Aboites V, Huerta-Cuellar G. A physical interpretation of fractional-order-derivatives in a jerk system: electronic approach. *Commun Nonlinear Sci Numer Simul* (2020) 90:105413. doi: 10.1016/j.cnsns.2020.105413

20. Zhou P, Ma J, Tang J. Clarify the physical process for fractional dynamical systems. *Nonlinear Dyn* (2020) 100:2353–64. doi: 10.1007/s11071-020-05637-z

21. Petrás I. (2011). *Fractional-Order Nonlinear Systems. Modeling, Analysis and Simulation*. Springer, Berlin, Heidelberg. doi: 10.1007/978-3-642-18101-6_2

22. Mainardi F. Why the mittag-leffler function can be considered the queen function of the fractional calculus? *Entropy* (2020) 22, 2–3. doi: 10.3390/e22121359

23. Fernandez A, Husain I. Modified mittag-leffler functions with applications in complex formulae for fractional calculus. *Fractal Fract* (2020) 4:1–2. doi: 10.3390/fractalfract4030045

24. Özarslan MA, Fernandez A. On the fractional calculus of multivariate Mittag-Leffler functions. *Int J Comput Math* (2022) 99:247–73. doi: 10.1080/00207160.2021.1906869

25. Balatif O, Boujallal L, Labzai A, Rachik M. Stability analysis of a fractional-order model for abstinence behavior of registration on the electoral lists. *Int J Differ Equa* (2020) 2020:1–8. doi: 10.1155/2020/4325640

26. Teklu SW, Terefe BB. Mathematical modeling analysis on the dynamics of university students animosity towards mathematics with optimal control theory. *Sci Rep* (2022a) 12:11578. doi: 10.1038/s41598-022-15376-3

27. Teklu SW, Terefe BB. Mathematical modeling investigation of violence and racism coexistence as a contagious disease dynamics in a community. *Comput Math Methods Med* (2022b) 2022:1–13. doi: 10.1155/2022/7192795

28. Pontryagin LS, Boltyanskii VG, Gamkrelidze RV, Mishchenko EF, Trirogoff KN, Neustadt LW. L. S. Pontryagin selected works: the mathematical theory of optimal processes. *Angew Chem Int Ed* (1967) 6:951–2.

29. Yang WY, Cao W, Chung TS, Morris J. *Applied Numerical Methods Using MATLAB®*, Hoboken, New Jersey: John Wiley and Sons (2005).

Frontiers in
Applied Mathematics and Statistics

Investigates both applied and applicable mathematics and statistical techniques

Explores how the application of mathematics and statistics can drive scientific developments across data science, engineering, finance, physics, biology, ecology, business, medicine, and beyond

Discover the latest Research Topics

See more →

frontiers

Frontiers in
Applied Mathematics
and Statistics

frontiers | Research Topics